Pramana – journal of physics

RAMAN RESEARCH INSTITUTE
BANGALORE - 80.
CLASS NO.
ACC NO. 26997

Editor

R Nityananda
Raman Research Institute, Bangalore

Associate Editor

H R Krishnamurthy
Indian Institute of Science, Bangalore

Editorial Board

G S Agarwal, *University of Hyderabad, Hyderabad*
V Balakrishnan, *Indian Institute of Technology, Madras*
M Barma, *Tata Institute of Fundamental Research, Bombay*
P Chaddah, *Centre for Advanced Technology, Indore*
B M Deb, *Panjab University, Chandigarh*
P K Kaw, *Institute for Plasma Research, Gandhinagar*
H S Mani, *Indian Institute of Technology, Kanpur*
N Mukunda, *Indian Institute of Science, Bangalore*
T Padmanabhan, *Inter-University Cêntre for Astronomy and Astrophysics, Pune*
J C Parikh, *Physical Research Laboratory, Ahmedabad*
G Rajasekaran, *Institute of Mathematical Sciences, Madras*
V S Ramamurthy, *Institute of Physics, Bhubaneswar*
R Ramaswamy, *Jawaharlal Nehru University, New Delhi*
K R Rao, *Bhabha Atomic Research Centre, Bombay*
Probir Roy, *Tata Institute of Fundamental Research, Bombay*
A K Sood, *Indian Institute of Science, Bangalore*

Editor of Publications of the Academy

V K Gaur
C-MMACS, NAL, Bangalore

Subscription Rates
(Effective from 1989)

All countries except India	1 year	3 years	5 years
(Price includes AIR MAIL charges)	US$ 175	$ 470	$ 700
India	1 year Rs. 100	10 years (1989–1998 only) Rs. 500	

All correspondence regarding subscription should be addressed to the **Circulation Department** of the Academy

---

Editorial Office

Indian Academy of Sciences, C V Raman Avenue,
P.B. No. 8005, Bangalore 560 080, India

Telephone: 334 2546
Telex: 845-2178 ACAD IN
Telefax: 91-80-334 6094

© 1995 by the Indian Academy of Sciences. All rights reserved.

"**Information for contributors**" is printed in the last issue of every volume.

Regd. No. KRN-A 64

Pramana journal of physics Vol. 44 (No. 1), January 1995

Contents

Effect of size and charge on ordering of a highly charged concentrated macroions in suspension .... *R K Pandey and D N Tripathi* 1

Transient currents in discharge mode in cellulose acetate:polyvinyl acetate blend films .... *P K Khare, R S Chandok and A P Srivastava* 9

Microwave conductivity studies on some semiconductors .... *V Subramanian, V R K Murthy and J Sobhanadri* 19

Dielectric relaxation and related studies of 4-ethylphenol-methanol mixtures using time domain reflectometry .... *R H Fattepur, M T Hosamani, D K Deshpande, R L Patil and S C Mehrotra* 33

A comparative study of laser second harmonic generation in some crystals .... *G C Bhar, A M Rudra, P K Datta, U N Roy, V K Wadhawan and T Sasaki* 45

Dynamics of a collisional ion sheath .... *S Mukherjee and P I John* 55

Instrumentation for beam-foil spectroscopic studies in the UV-visible region .... *Tapan Nandi, V Nanal, W A Fernandes, C A Desai, M B Kurup, K G Prasad, P M R Rao and S Padmanabhan* 67

Rapid Communication

Gap states in a doped Mott–Hubbard insulator .... *Prasenjit Sen, Saurabh Basu and Avinash Singh* L77

Indexed in CURRENT CONTENTS ISSN 0304–4289

Edited and published by V K Gaur for the Indian Academy of Sciences, Bangalore 560080. Typeset at Thomson Press (I) Ltd., New Delhi 110001 and printed at Macmillan India Press, Madras 600041.

Regd. No. KRN-A 64

Pramana journal of physics · Vol. 44 (No. 2), February 1995

Contents

A new computation scheme for triangular quantum billiards .... *Paolo Bellomo* 85

On the accuracy of wavefunctions obtained by the Fourier grid Hamiltonian method .... *P Dutta and S P Bhattacharyya* 109

Conversion of a chaotic attractor into a strange nonchaotic attractor in an one dimensional map and BVP oscillator .... *S Rajasekar* 121

Wormholes in higher dimensions with Gauss–Bonnet terms .... *B C Paul, A Beesham and S Mukherjee* 133

Magnetic moments of decuplet baryons in an independent particle potential model .... *N Barik, P Das and A R Panda* 145

A new approach for heavy ion fusion spin distribution .... *S V S Sastry, A K Mohanty and S K Kataria* 153

Momentum- and energy-dependence of J/ψ suppression in relativistic heavy ion collisions .... *R S Kaushal and S K Karn* 167

Deep inelastic collisions of $^{32}S + ^{27}Al$ reaction at 130 MeV bombarding energy.......... *R K Choudhury, D M Nadkarni, V S Ambekar, B V Dinesh, A Saxena, M S Samant, D C Biswas and L M Pant* 177

Trinucleon system with Reid soft core potential by hyperspherical harmonics expansion method .... *Satadal Bhattacharyya and Tapan Kumar Das* 183

7 APR 1995

RAMAN RESEARCH INSTITUTE
LIBRARY
BANGALORE-80.

Indexed in CURRENT CONTENTS

ISSN 0304–4289

Edited and published by V K Gaur for the Indian Academy of Sciences, Bangalore 560 080. Typeset at Thomson Press (I) Ltd., New Delhi 110 001 and printed at Macmillan India Press, Madras 600 041.

RAMAN RESEARCH INSTITUTE
LIBRARY
BANGALORE-80.
2 MAY 1995

Regd. No. KRN-A 64

Pramana journal of physics Vol. 44 (No. 3), March 1995

Contents

Phonons and fractons in sol-gel alumina: Raman study .... *Anushree Roy and Ajay K Sood* 201

Thermally stimulated luminescence and electron paramagnetic resonance studies on uranium doped $K_2Ca_2(SO_4)_3$ .... *T K Seshagiri, V Natarajan and M D Sastry* 211

Structural, spectroscopic and dielectric properties of KVO_3 .... *N K Misra, R N P Choudhary and K L Yadav* 219

Anomalous variation of thermal lens signal with concentration from rhodamine B in methanol solution .... *C V Bindhu, S S Harilal, Riju C Issac, Geetha K Varier, V P N Nampoori and C P G Vallabhan* 225

Pulsed photoacoustic technique to study nonlinear processes in liquids: Results in toluene .... *C V Bindhu, S S Harilal, Riju C Issac, Geetha K Varier, V P N Nampoori and C P G Vallabhan* 231

Analysis of mode-locked internally frequency doubled broad-band continuous wave lasers .... *H K T Kumar, K Appaji Gowda and K P J Reddy* 237

Self tapering and uptapering of a self guided laser beam in an absorbing/gain medium with nonlinearity .... *Sarang Medhekar, S Konar and Rajkamal* 249

The evolution of the resonant mode in plasma-maser interaction .... *Bipuljyoti Saikia and S Bujarbarua* 257

Dynamic sheath expansion and ion current in transient ion sheath experiments .... *S Mukherjee, K Avinash and P I John* 263

Static structure factor of electrons around a heavy positively charged impurity in a one component quantum rare plasma .... *S P Tewari and Hira Joshi* 271

Corrigendum 279

Indexed in CURRENT CONTENTS ISSN 0304–4289

Edited and published by V K Gaur for the Indian Academy of Sciences, Bangalore 560080. Typeset at Thomson Press (I) Ltd., New Delhi 110001 and printed at Macmillan India Press, Madras 600041.

STATEMENT ABOUT OWNERSHIP AND OTHER PARTICULARS OF

Pramana – Journal of Physics

1. Place of Publication .. Bangalore

2. Periodicity of Publication .. Monthly

3. Printer's Name .. V K Gaur
Indian Academy of Sciences
Bangalore 560 080

4. and 5. Publisher and Editor .. V K Gaur

6. Nationality .. Indian

7. Address .. Indian Academy of Sciences
P. B. No. 8005
Bangalore 560 080

8. Name and Address of the Owner .. Indian Academy of Sciences
Bangalore 560 080

I, V K Gaur, hereby declare that the particulars given above are true to the best of my knowledge.

V K Gaur
Signature of Publisher

Dated 1st March 1995

PRAMANA
— journal of
physics

© Printed in India

Vol. 44, No. 1,
January 1995
pp. 1–7

Effect of size and charge on ordering of a highly charged concentrated macroions in suspension

R K PANDEY and D N TRIPATHI
Laser and Spectroscopy Laboratory, Department of Physics, Banaras Hindu University, Varanasi 221 005, India

MS received 15 January 1993; revised 19 October 1994

Abstract. An efficient fast Fourier transform method has been employed to determine correlation function [$g(r^*)$] using the structure factor [$S(Q^*)$] calculated with the rescaled mean spherical approximation (RMSA) and the DLVO potential. Based on this function a parametric (size and charge) study of the ordering in a highly charged and concentrated macroions (an ideal colloid) has been made. The strength of the correlation increases with the increase in the charge on macroions and it saturates after a certain value. Similarly, a critical diameter of the particle depending on the charge on it has been found at which normal feature of the ordering disappears.

Keywords. Correlation function; rescaled mean spherical approximation; DLVO.

PACS Nos **82·70; 61·20**

17 1995

1. Introduction

Colloids define a range of systems containing dispersed particles that are larger than atomic dimensions but small enough to exhibit Brownian motion, which prevents appreciable sedimentation in normal gravity. The particles have typical dimensions in the range 10^2–10^5 Å and have of the order of 10^2–10^4 surface ionizable groups [1, 2]. These ubiquitous dispersions fall into two categories, namely lyophilic (solvent loving) and lyophobic (solvent fearing) [3, 4].

In a recent work [5] we have analyzed the nature of the structure factor for a highly charged concentrated monodisperse macroions in aqueous suspension as obtained using the DLVO interaction potential [3] and rescaled mean spherical approximation (RMSA) [6]. The limitations regarding the applicability of the DLVO model interaction potential and the theoretical framework of RMSA for such a system have been examined.

It is well-known that the number density and hence the volume fraction and the excess ion concentration (counterions + impurity ions) are the two important parameters which govern the ordering process in such systems. Tata *et al* [7] have found that as the impurity ion concentration (n_i) increases the peak height of $g(r^*)$ decreases and its position shifts towards lower values of r^* and finally it becomes zero for $n_i > 3z\rho$. Because, an addition of ionic impurity reduces Coulomb screening length and so the particles can penetrate deeper into the value of r^* at which $g(r^*)$ becomes zero. The influence of the particle concentration on pair distribution function has been studied by Hartl and Versmold [8]. It is pointed out that height of the first peak of $g(r^*)$ increases very slowly and its position also shifts towards lower side of r^*.

However, the number density remaining constant, increase in size of the macroions also results in the increase of the volume fraction η. Further, the increase in the surface charge of the particles is bound to affect the interaction potential. Therefore, these two factors viz the size and the charge of the suspension are also expected to play an important role in the process of ordering. In this work we examine the nature of the radial correlation function (which is a Fourier transform of the structure factor) and hence the ordering process, in respect of these two parameters in the case of an ideal charged colloidal suspension.

2. Theory

An outline of the RMSA method is given by Hayter and Penfold [6]. The radial distribution function is defined as

$$g(r) = 1 + \frac{1}{2\pi^2 r\rho}\int_0^\infty [S(Q) - 1] Q \sin Qr \, dQ \tag{1}$$

where ρ is the number density, Q is the momentum transfer (or scattering wave vector) and $S(Q)$ is the structure factor at Q. Equation (1) may be expressed in terms of dimensionless variable by defining

$$r^* = \frac{r}{\sigma}$$

$$Q^* = Q\sigma \tag{2}$$

where σ is the particle diameter, as

$$g(r^*) = 1 + \frac{1}{12\pi\eta r^*}\int_0^\infty [S(Q^*) - 1] Q^* \sin Q^* r^* \, dQ^* \tag{3}$$

where

$$\eta = \frac{\pi\alpha^3\rho}{6} \tag{4}$$

is the volume fraction. The upper limit of the integration is replaced by a finite value of 128, i.e., nearly 100 times that of the first peak position $Q^*_{\max}$ of the structure factor $S(Q^*)$ to evaluate $g(r^*)$ to sufficient accuracy. In the calculation of $g(r^*)$ we have calculated $S(Q^*)$ (see [5]) at an interval of $dQ^* = 0{\cdot}1$. All calculations are carried out in double precision on Mighty Frame(II) Computer of the Computer Centre, BHU, Varanasi, using a program developed by Hayter and Hansen [9] and Hayter [10].

3. Results and discussion

The radial correlation function $g(r^*)$ for various values of ze viz. 1200, 800, 200, 100, 50 with $\sigma = 600$ Å, 910 Å and 1600 Å for $\rho = 4{\cdot}0 \cdot 10^{18}\ \mathrm{m}^{-3}$ have been shown in figure 1a, 1b and 1c, respectively in order to see the change in its nature and hence the ordering due to the charge on different sizes of macroions. The first peak amplitude in $g(r^*)$ vs. r^* curve increases with the increase of charge on macroions. Its position also shifts slightly towards higher r^* value. The number of peaks increases indicating thereby, the increase in the range as well as strength of the interaction potential and the decrease in isothermal compressibility [11]. This implies that the strength of the interaction potential between nearest neighbor, next-nearest neighbor, next-to-next nearest neighbor and so on, increases with the increase of charge on macroions at a given volume fraction. Further, for $\sigma = 600\,\text{Å}$ and $z \geqslant 200\,\text{e}$ (volume fraction $\eta = 4{\cdot}52{\cdot}10^{-4}$) a peak smaller than the one mentioned above, precedes it at lower value of r^* (see figure 1a). The position of the second and third peaks however, remain unaltered.

The variation of the pair correlation function $g(r^*)$ with r^* for different size (σ) with $z = 500\,\text{e}$, $800\,\text{e}$ and $1000\,\text{e}$ for $\rho = 4{\cdot}0{\cdot}10^{18}\,\text{m}^{-3}$ have been shown in figures 2a, 2b and 2c, respectively. The first peak height increases with size increase of the macroions indicating an increase in the strength of the correlation.

It is important to note that for particles having a critical diameter, which is a function of the charge over the macroion ($\sigma \leqslant 200\,\text{Å}$ for charge $z = 500\,\text{e}$, $\sigma \leqslant 400\,\text{Å}$ for $z = 800\,\text{e}$ and $\sigma \leqslant 800\,\text{Å}$ for $z = 1000\,\text{e}$), the normal shape of the function $g(r^*)$ gets distorted and it acquires an unphysical negative contact values [6]. Except these critical diameter, the position of the first maximum of $g(r^*)$ occurs in the range of r equal to 5 to 10 times of the diameter (σ). In this case RMSA gives reasonably good results with the variation of charge and size. It is to be noted that Hartl and Versmold [8] have also reported a similar result in this range with the different particle densities. However, below the critical size, which is a function of the particles density and charge, the ordering in the colloidal suspension has not been observed. This is a most likely condition of Brownian motion of the suspensions in the medium. This may also be an indication of the failure of the RMSA method for such a system. Further, it is noticed that the number of peaks increases and its position shifts as well towards lower value of r^*. This behavior may be explained in terms of the increase in effective volume fraction [12, 13], i.e., $\eta^* = \eta(1 + (2/k))^3$ and effective charge [14], i.e., $z^* = z/(1 - \eta)$. The centre-to-centre distance between charged macroions remain unaltered at fixed particle concentration (ρ). The interparticle separation however, decreases as size increases. Therefore, an increase in effective volume fraction and effective charge result an increase of the interactions between nearest neighbor next-to-next nearest neighbor and so on. This may be the reason that the peak height as well as number of peaks increase and their positions shift as well towards the lower value of r^*. The effective charge and therefore, the interaction potential increases with the increase in charge and size of the macroions. This causes decrease in the width and increase in the height of the peaks in $g(r^*)$ (see figures 1 and 2). That is the strength of binding between the layer increases and the interlayer spacing decreases.

In both the cases i.e. increase in size as well as charge, the interaction potential causes a change in the shape and size of the pair correlation function $g(r^*)$. The variation in peak $g(r^*)_{\max}$ and dip $g(r^*)_{\min}$ magnitudes and relative shift in their positions may therefore, provide an estimate of the change in it due to a change in these two factors. The variation of $g(r^*)_{\max}$ and $g(r^*)_{\min}$ with charge and size are shown in figure 3. The curves marked $g(r^*)_{\max}(I)$ and $g(r^*)(\text{II})_{\max}$ and $g(r^*)_{\min}(\text{I})$ and $g(r^*)(\text{II})_{\min}$ show the variation of height and depth of first and second peaks of $g(r^*)$ vs r^* with charge and size, respectively. It is noticed that both the height as well as depth of first two peaks increases with the charge up to $z \approx 1000\,\text{e}$ (see figure 3a) which, thereafter acquires a plateau region. That is, the increase in charge in excess of $\sim 1000\,\text{e}$ has no effect on them. This behavior may be understood in terms of the maximum charge [1] at a given volume fraction (η), i.e., $z^{\max} = 7{\cdot}5\sigma/\lambda$; (where

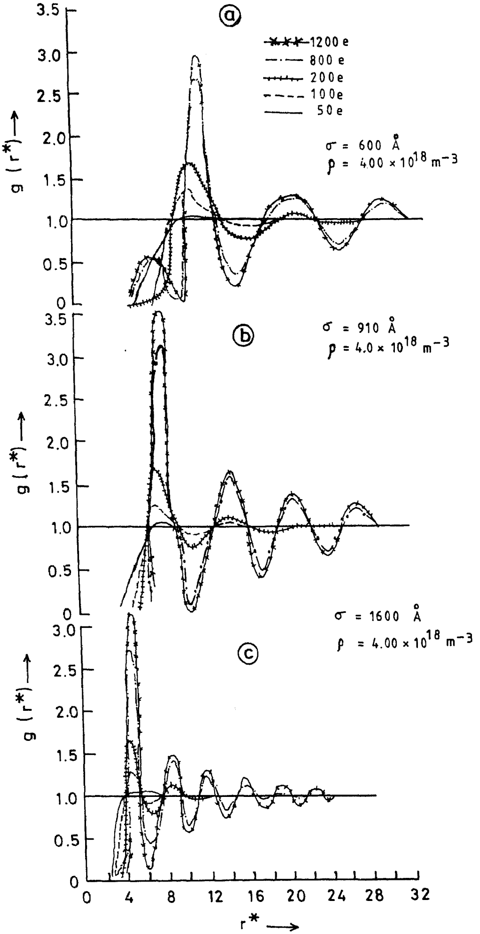

Figure 1. Variation of $g(r^*)$ with r^* for $z = 50$e (———), $z = 100$e (– – – –), $z = 200$e (+ + + + + + +), $z = 800$e (—·—·—), $z = 1200$e (–∗–∗–∗–∗–) at (a) $\sigma = 600$ Å, (b) $\sigma = 910$ Å and (c) $\sigma = 1600$ Å.

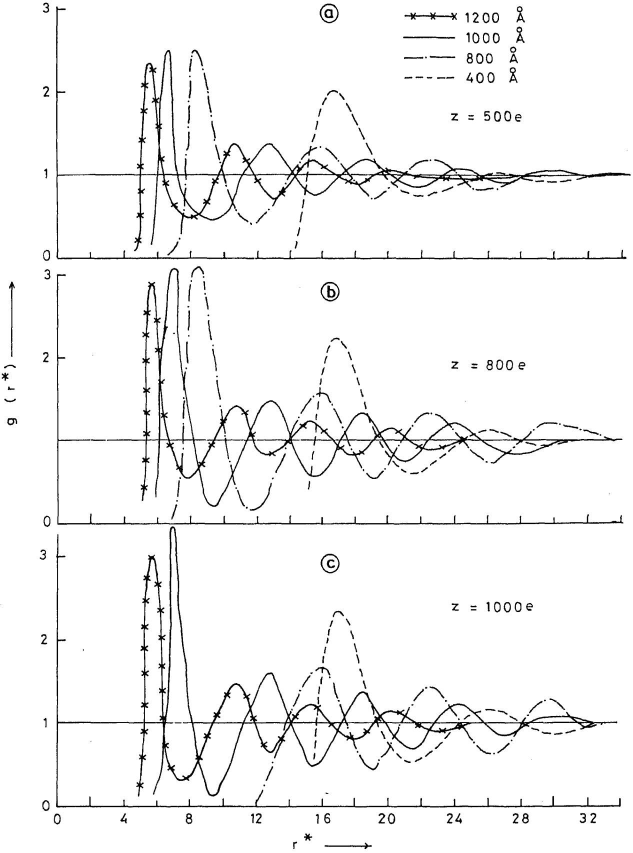

Figure 2. Variation of $g(r^*)$ with r^* for a given charge (a) $z = 500$ e, (b) $z = 800$ e and (c) $z = 1000$ e and size $\sigma = 400$ Å (– – – –), $\sigma = 800$ Å (—·—·—·—), $\sigma = 1000$ Å (———) and $\sigma = 1200$ Å (∗–∗–∗–∗–).

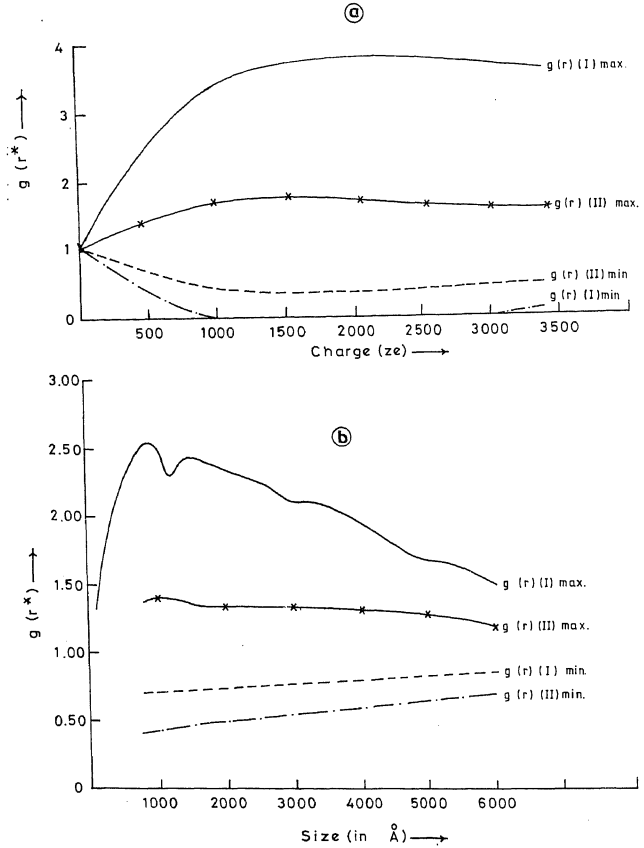

Figure 3. Variation of $g(r^*)_{\max}$ and $g(r^*)_{\min}$ with (a) charge for size $\sigma = 910$ Å and (b) size for $z = 500$ e.

$\lambda = e^2/4\pi\varepsilon_0 \varepsilon k_b T$) on the macroion that is effective in ordering. In the present case the value of $z^{\max}$ is found to be ≈ 975 e. Thus the expression given by Alexander *et al* [1] confirms our results.

$g(r^*)(\mathrm{I})_{\max}$ increases in the beginning with an increase in particles diameter up to $\sigma = 1000$ Å, then after it oscillates (see figure 3b). $g(r^*)(\mathrm{II})_{\max}$ on the other hand, remains nearly constant. The first two dips depth $[g(r^*)_{\min}]$ increases very slowly with size increase of the macroions. All of the heights and dips viz. $g(r^*)(\mathrm{I})_{\max}$, $g(r^*)(\mathrm{II})_{\max}$, $g(r^*)(\mathrm{I})_{\min}$ and $g(r^*)(\mathrm{II})_{\min}$ converge to a value of $g(r^*)$ equal to 1·0 indicating thereby, a decrease in the interaction potential from nearest neighbor to next nearest neighbor and so on amongst the charged particles in suspension.

Acknowledgements

Authors are grateful to Profs D K Rai and K N Upadhyay for fruitful discussions with them. One of the authors (RKP) is thankful to UGC for the financial support during the course of this work.

References

[1] S Alexander, P M Chaikin, P Grant, G J Morales, P Pincus and D Hone, *J. Chem. Phys.* **80**, 5776 (1984)
[2] R D Groot, *J. Chem. Phys.* **94**, 5083 (1991)
[3] E J W Verwey and J Th G Overbeek, *Theory of the stability of lyophobic colloids* (Elsevier 1948)
[4] B V Derjaguin and L D Landau, *Acta Phys. Chim. URSS* **14**, 633 (1941)
[5] R K Pandey and D N Tripathi, *Pramana – J. Phys.* **39**, 589 (1992)
[6] J P Hansen and J B Hayter, *Mol. Phys.* **46**, 651 (1982)
[7] B V R Tata, R Kesavamoorthy and Akhilesh K Arora, *Mol. Phys.* **57**, 369 (1986)
[8] W Hartl and H Versmold, *J. Chem. Phys.* **88**, 7157 (1988)
[9] J B Hayter and J P Hansen, *The structure factor of charged colloidal dispersion at any density* (Institute Lave-Langevin Report, 1982)
[10] J B Hayter, *A program for fast bi-directional transform between g(r) and s(Q)* (Institute Laue-Langevin Report, 1979)
[11] J B Hayter and J Penfold, *Mol. Phys.* **42**, 109 (1981)
[12] J P Hansen, *J. Phys.* **C14**, L151 (1981)
[13] P Pieranski, *Contemp. Phys.* **24**, 25 (1983)
[14] N J Wagner, R Krause, A R Rennie, B D'Aguanno and J M Goodwin, *J. Chem. Phys.* **95**, 494 (1991)

PRAMANA
— journal of
physics

© Printed in India

Vol. 44, No. 1,
January 1995
pp. 9–18

Transient currents in discharge mode in cellulose acetate: polyvinyl acetate blend films

P K KHARE, R S CHANDOK* and A P SRIVASTAVA†
Department of Postgraduate Studies and Research in Physics, Rani Durgavati Vishwavidyalaya, Jabalpur 482 001, India
*Shri Guru Tegh Bahadur Khalasa College, Jabalpur 482 001, India
*39, SBI Colony, SAF Road, Makronia, Sagar 470 003, India

MS received 3 September 1994; revised 14 November 1994

Abstract. The transient currents measured in discharge mode with cellulose acetate (CA): polyvinyl acetate (PVAc) blend films ($\approx 20\,\mu$m thick) as a function of charging field [$(1{\cdot}5$–$4{\cdot}5) \times 10^4$ V/cm], temperatures (323–373 K) and polymer weight ratio (90:10 and 75:25) have been found to follow Curie–von Schweidler law, characterized with two slopes in short and long time regions. Isochronals characteristics (i.e. current/temperature plots at constant times) constructed from these data seemed to reveal a broad peak observed at 363 K. Values of activation energy increase with PAVc content and also with time of observation. Space charge due to trapping of injected charge carriers in energetically distributed traps and induced dipoles created because of the piling up of charge carriers at the phase boundary of heterogeneous structure of blend are considered to account for the observed currents.

Keywords. Transient currents; cellulose acetate; polyvinyl acetate; induced dipoles; space charge; plasticization effect.

PACS Nos 77·30; 81·40; 81·20

1. Introduction

In polymer dielectrics movement of charge carriers has received a good attention because of its importance in science and technology, which include leakage current in electrical insulation [1, 2], charge injection from electrodes which may lead to premature breakdown [3], various forms of photoconduction and of transient pulse drift and induced conductivity. These problems involve the transport and distribution of charged particles which, therefore, be treated as quasi-continuous clouds rather than as individual. However, despite serious efforts [4–6], there remains substantial doubt as to mechanism of charge transport in many insulating polymers which find very wide industrial applications. There are various methods of studying conduction processes [7] which include AC conduction studies, charge particle bombardment, surface voltage decay, trapped charge decay, radiation induced conduction and photo conduction. However, there are uncertainties inherent in each of the above methods. Therefore, fresh attempts were undertaken to study the time dependent dielectric absorption/desorption current flow, following the application of a step voltage.

A systematic study of transient currents can reveal the carrier injection, trapping and polarization proceses which may be operative in a dielectric. The knowledge of transient currents is also necessary to discover the true conductivity of the material.

The transient current data can be converted from time to frequency domain by Fourier transformation to give dielectric loss of the material at low frequencies [8]. The time dependent part of the current is due to polarization of the dielectric under the applied electric field. The polarization of polymeric dielectrics may be due to dipolar orientation, accumulation of charge carriers near the electrodes or trapping in the bulk [5]. Under certain conditions additional charge carriers may be provided by injection from the electrodes which also contribute in space charge polarization [9]. Hopping of charge carriers from one localized state to another [10] and tunnelling from electrode to those trap levels in the dielectric which are close to the Fermi level of the electrode metal [4] have been proposed for the transient currents in dielectrics. The process which actually occurs must be determined by considering the variation of the transient current with temperature, field, time, electrode materials and sample thickness etc.

A lot of work on charge storage has been carried out on cellulose acetate [11–13] and polyvinyl acetate (PVAc) [14–17]. The physical processes leading to electret state of these polymers are clear. However, the effect of blending of these two on charge storage and transport mechanism is still not well understood. Polymer blends are heterogeneous mixtures and the possibility of charge trapping at the grain boundaries of the individual materials is higher in them. It has been shown that polyblend samples are better charge storer [18, 19]. Investigations concerning the dependence of electrical properties on structure are, however, presently very sparse.

In the present paper a polyblend consisting of cellulose acetate and polyvinyl acetate has been studied in detail in two weight proportion under different forming conditions. This particular combination in which the two components have the same functional groups, forms a thermodynamically compatible system [20].

2. Experimental details

Isothermal immersion technique was utilized for preparing films of polyblends. Both the polymers cellulose acetate (CA) and polyvinyl acetate (PVAc), having average molecular weight 80,000 and 50,000 respectively were dissolved separately in dioxane. The two solutions, each of which, with a concentration of 100 g/L were then mixed in proportions of 90:10 and 75:25 by weight proportion of CA and PVAc, designated as A_1 and A_2 respectively. The solution was continuously stirred for half an hour by means of a teflon-coated magnetic stirrer. Thereafter, it was stirred and heated up to 313 K to yield a homogeneous and transparent solution. The glass beaker containing the solution was then immersed in a constant temperature oil bath. Ultrasonically, cleaned vacuum metallized microscopic glass slides were immersed vertically into the solution for about half an hour. The majority of measurements were made with aluminium electrodes except for a limited number of observations which are made on samples provided with copper, silver and lead electrodes. After the deposition of film, the glass slide was taken out and slowly dried in a saturated dioxane atmosphere. Films were further dried for 24 h in a dry atmosphere and were finally kept in an oven at 313 for 24 h to evaporate residual solvent. This was followed by room temperature outgassing at $133{\cdot}33 \times 10^{-5}\,\mathrm{N/m^2}$ for 24 h. Polyblend films of 20 μm thickness were used unless otherwise stated. The thickness which was estimated [21] by measuring the capacitance of fabricated sandwiches taking the dielectric constant ε of CA and PVAc as 3. The transient currents were measured in the discharge mode, as the charging current is a sum of the absorption current and the conduction current. Different steps for the preparation of a thermoelectret are as follows (i) the sample is heated to the desired polarizing temperatures (T_p); it is kept at T_p for some time (in the present case, 2 h) to reach thermal equilibrium; (iii) then, an electric field (E_p) is applied at T_p and kept on for a period of polarizing time (t_p); (iv) it is then cooled slowly under the field application, to room temperature. The field is then removed. The effect of field variation in current was recorded by increasing the voltage in steps of 10 V at fixed temperature, while temperature variation was recorded by keeping the field constant and increasing the temperature in steps of 10 K. In the present study, the samples were thermally polarized with fields of $(1{\cdot}5–4{\cdot}5) \times 10^4$ V/cm at various temperatures (323–373 K) for 10^2 min during which the transient currents in discharging mode has been observed at suitable interval of time, after the removal of the field. The current was recorded, with a Keithley 600 B electrometer which was carefully shielded and grounded to avoid ground loops or extraneous electrical noise, as a function of applied field, temperature and charging time as reported earlier [15, 22].

3. Results and discussion

The time dependence of the discharging current in CA:PVAc blend samples with 90:10 and 75:25, weight % ratio of the two polymers over a time period of $1–10^2$ min, in the temperature range 323–373 K with polarizing field $1{\cdot}5 \times 10^4$ V/cm are shown in figure 1. The observed discharging current has been found to be of the order of $10^{-10}–10^{-7}$ A. Figure 2 depicts such currents for samples A_1 and A_2 at 323 K with various polarizing fields $(1{\cdot}5–4{\cdot}5) \times 10^4$ V/cm. As can be seen from figure 1, the magnitude of the discharge currents at a particular time show a marked dependence of temperature. The various plots have been found to be characterized with two regions; one short time region and the other long time region. The curves become steeper at longer times. The value of n, i.e. of slope for sample A_1 and A_2 become smaller ($\approx 0{\cdot}45$) in the shorter time region, as the time of discharge increases, while that for long time region an increase in the value of n almost approaching to 1·6 is found. There appears to be a process of thermal activation over the whole range of temperature. The observed time dependence of the current transients may be considered to follow Curie-von Schweidler law

$$I_a(t) = A(T)t^{-n} \tag{1}$$

where I_a is the absorption current, t the time and $A(T)$ a temperature-dependence factor. The faster decay of current in long time region for different samples indicates the existence of energetically distributed localized traps in the sample. Trapping of charges can take place at various trapping sites—surface states, chain foldings and molecular disorder [12]. Small irregularities observed in some cases may be due to presence of charge domains inside the material [23]. The polyblend is a heterogeneous mixture and as such has a very large number of trapping sites. It seems that at lower charging temperatures only shallow traps are involved which get emptied at these temperatures. But as the temperature rises, more and more deeper traps are involved. The trapping of charge carriers (holes and electrons) in the deep trap levels may lead to induced dipole formation. The energy required for their disorientation and the release of charge carriers from these trapping sites will be high and as such the discharge current is small [24]. The bulk of the measurements of the transient currents

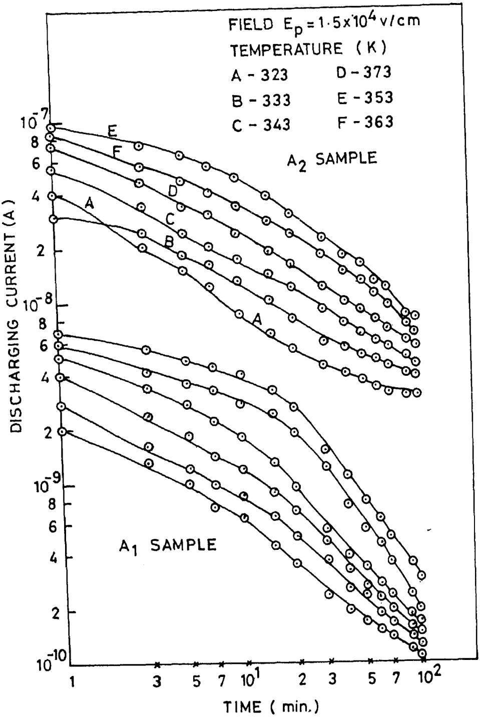

Figure 1. Current transient versus time curves at various temperatures (323, 333, 343, 353, 363 and 373 K) with constant poling field ($1{\cdot}5 \times 10^4$ V/cm) for A_1 and A_2 samples.

in blend sample were made with 20 μm samples. A limited number of measurements, however, were made with samples of 10, 30 and 40 μm thickness over a temperature range with aluminium, copper, silver and lead electrodes (results not shown). These results indicate that the transient current in blend of CA:PVAc may not be dependent on the electrode materials as well as thickness of the samples within the range of fields employed.

The discharge current measured at prescribed times (i.e. isochronals) plotted against temperature for two polyblend samples are shown in figure 3. These plots are characterized by well defined peak at 363 K. The observed broadness of the isochronal peaks may also have been due to overlapping of a number of relaxation mechanisms. The activation energy (E) value obtained from plots (figure 4) of the discharge current

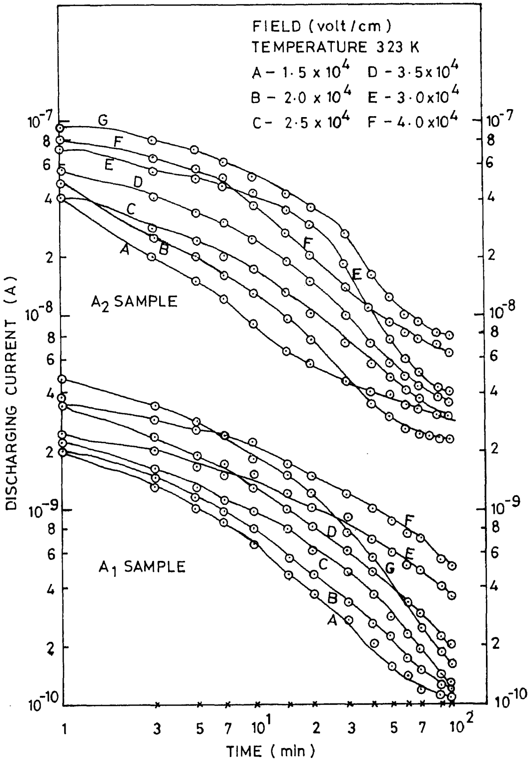

Figure 2. Current transient versus time curves with various poling fields ($1{\cdot}5 \times 10^4$, $2{\cdot}0 \times 10^4$, $2{\cdot}5 \times 10^4$, $3{\cdot}0 \times 10^4$, $3{\cdot}5 \times 10^4$, $4{\cdot}0 \times 10^4$ and $4{\cdot}5 \times 10^4$ V/cm) at 323 K, for A_1 and A_2 samples.

versus $10^3/T$ at various prescribed times (1 min, 5 min, 10 min, 30 min, 70 min and 100 min) for various samples with different ratios of the polymers (A_1 and A_2) are found to vary from 0·61 to 1·21 eV. The value of E agrees well with what obtained from the TSDC results [25]. For samples with a fixed weight ratio of the two polymers, the activation energy value has been found to increase with increase in time of observation of the discharge current. Moreover, at any fixed time the activation energy value increases with increasing concentration of polymer. Increasing concentration of PVAc in the polymer matrix is considered to play an important

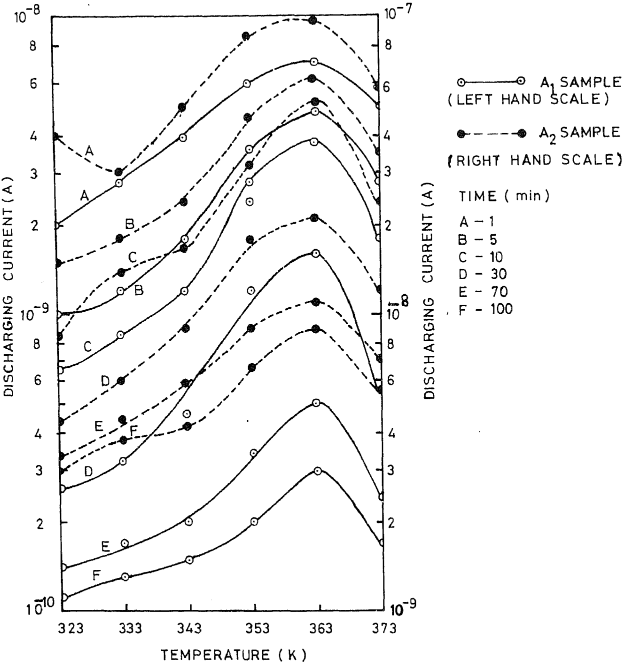

Figure 3. Current transient versus temperature curves at constant times (1 min, 5 min, 10 min, 30 min, 70 min and 100 min) for A_1 and A_2 samples.

role in modifying the trap structure in the sample causing more and more deeper traps, due to which the observed activation energy value is more.

In the segments, mobility may be increased after the complete phase transition and thus the possibility of injection of charge carriers near the electrodes and their drift seem to be possible by self motion of charge carriers/ions above the T_g range. Above T_g of the polymer a sudden change in its volume may occur and thus structural rearrangements of chains (segments) may be possible due to sufficient mobility of segments [26]. It is difficult to say about the contribution of individual homopolymer molecular orientations to this high temperature isochronal peak, since both CA and PVAc are partial polar polymer having T_g around 373 and 333 K respectively. However, the broadness of the peak may be explained by assuming a distributed or multiple dielectric relaxation may be due to distribution in activation energy when the rotation of the dipoles does not proceed in the same environment. Alternatively, it may be due to distribution in relaxation time, when the rotational masses of the

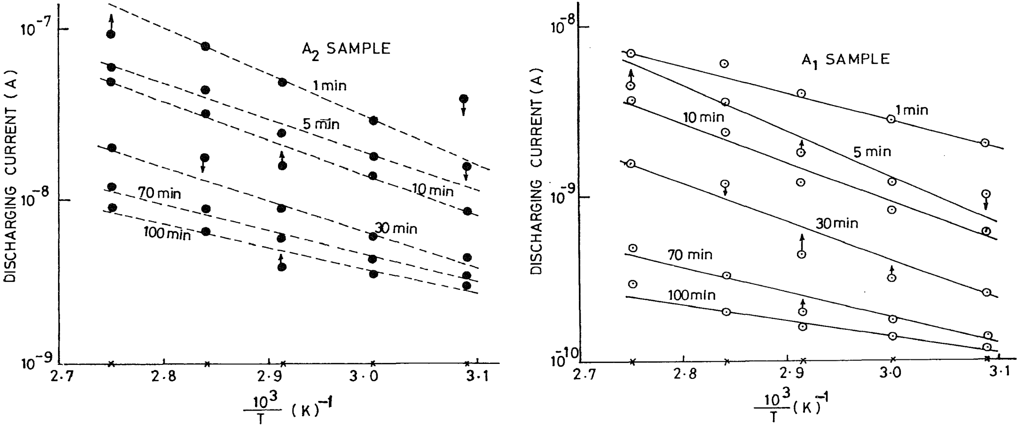

Figure 4. Current transient versus $10^3/T$ curves at constant times (1 min, 5 min, 10 min, 30 min, 70 min and 100 min) for A_1 and A_2 samples.

dipoles are not equal. The broadness of the peak in the present case is, however, most likely to be distribution in relaxation time, because the peak is occurring near T_g of the two polymer, where the side groups move in unison with the main chain, differing in masses [27, 28]. Because the distribution of dipoles in the amorphous phase is most likely to be random, it is expected therefore, this complex process involving both the distribution of the activation energy and relaxation time.

As temperature increases mobility of carriers also increases, hence all the deeper traps are filled. Release of a large number of charge carriers from the traps during the process may then result in high return rate of carriers leading to blocking of electrodes causing a decrease in current. The charge injection from electrodes with subsequent trapping of injected charges in near surface region giving rise to homospace charge and the thermal release of charge carriers from the traps. Before the trapped space charge injected at higher fields, is thermally released, a space charge barrier is presented to the electrode which suppresses the entrance of charge carriers into the sample. Thus, the observed current remains smaller than its corresponding value.

Addition of PVAc in CA produces heterogeneous structure and plasticization effect [19]. Because of the heterogeneous structure, charge carriers injected in the bulk may pile at the phase boundaries. Plasticization causes loosening of the structure and greater mobility of charge carriers resulting in the increase of current. In CA:PVAc matrices containing different percentage at least two phases coexist and discontinuity of structure at such boundary increases. Because of the carrier conductivity in different phases, the carriers get trapped at the interphases of phase boundary. Further, the dipoles may also originate due to trapping of both positive and negative charge carriers in the deep traps in such a way as to form induced dipoles. Such trapped charge carriers may be generated in the bulk from the impurities thus they lead to induced dipole polarization in the polyblend films [12]. It is also possible that contribution of a permanent dipole of the host material is masked due to induced dipoles. In the blends, dipoles of the polar compound are so constrained that under the field, they either do not orient or their contribution to the total polarization is almost negligible as compared to the contribution of induced dipoles, which are formed in the bulk by the deep trapping of charge carriers originating in the bulk. The large value of activation energy may be taken as an indication of induced dipole formation because in this case the energy required to disorient them and subsequently release charge carriers from the trapping sites is expected to be higher [18, 19].

The Curie-von Schweidler type of time dependence has been observed for many polymers with the index "n" close to unity. A number of mechanisms may be invoked to explain such time dependence. It is therefore, not possible to specify the origin of transient currents in blend from analysis of time dependence alone. The polyblend samples used in the present case are expected to possess various dipoles due to the presence of PVAc. Polyvinyl acetate (PVAc) contains polar group C=O in its main chain having a weak permanent dipole moment. The structure of cellulose acetate with a polar main chain with polar side groups enhances formation of the carriers, which accumulate at the electrode during formation. These polar groups form permanent dipoles which can be oriented during the polarization process. These considerations suggest that it is reasonable to ascribe the observed discharge current due to the dipolar mechanism. However, the experimental facts in the present case are not consistent with the behaviour of discharging current. In the case of dipolar mechanism, the discharging current should vary linearly with the field intensity.

However, in the present case, the discharging current depends on field at random manner (figure 2). It was, therefore, unlikely that the dipolar orientation involving the relaxation process was responsible for the isochronal current peak observed at the high temperature range in this work. On the other hand, the observed values of "n" for shorter and longer times as well as the thermal activation of discharging currents at various fixed times counted after the removal of the charging field indicate that the space charge due to accumulation of charge carriers near the electrodes and trapping in the bulk may also be supposed to account for the observed current. In the case of transients governed by space charge, the peak in the current time curve should occur at a time

$$t_m = \frac{0{\cdot}786a^2}{\mu V}$$

where V is the applied voltage, a is the sample thickness and μ the carrier mobility. To have a rough estimate of the time at which this peak should occur we used the values of a, V and μ to be $20\,\mu$m, $2{\cdot}0 \times 10^4$ V/cm and 10^{-11} cm^2/V. It was found that t_m should approximately be equal to $1{\cdot}57 \times 10^3$ s. Thus, there is possibility of space charge relaxation occurring at sufficiently longer times. This may be due to trapping of charge carriers in sufficiently deeper traps. The observed temperature dependence (i.e. thermal activation) and the absence of any significant effects (i) electrode materials and (ii) sample thickness, makes tunneling unlikely as a possible mechanism to explain the nature of transient currents. The process of electrode polarization is also unlikely because of the absence of electrode effects and also because the observed "n" values are significantly different from the theoretically predicted model. The polymer films are known to be a mixture of amorphous and crystalline regions. The presence of localized states may lead to the localization of injected charge carriers giving rise to the accumulation of trapped space charge. The hopping mechanism, such as the one described by Lewis [29] required the existence of localized carrier trapping states, which had a distribution of energies. The observed time-dependence of the transient current would not be incompatible of such a process.

Struik [30] showed that solids like polymers are not in thermodynamic equilibrium at temperatures below their glass transition. For such materials, free volume enthalpy and entropy are greater than those they would be in the equilibrium state. The gradual approach to equilibrium affects many properties for example, free volume of the polymer may be decreased. The decrease in free volume lowers the mobility of chain segments and also charge carriers such as ions. This decrease in mobility may be expected to reduce dc conductivity. At higher electric fields, the changes in mobility may take place faster than at lower fields and also recombination of charge carriers may be more.

4. Conclusion

Considering the effects of charging field, temperature and time on the transient current in CA:PVAc blend, we conclude that the polarization in blend is due to trapping of the bulk charges, produced charges as well as the electrode injected charges in the deeper traps and their subsequent alignment due to step field.

References

[1] R M Hill, *J. Phys.* **D8**, 2488 (1975)
[2] D K Davies, *J. Phys.* **D2**, 149 (1969)
[3] A K Jonscher, *J. Phys.* **D11**, 601 (1978)
[4] H J Wintle, *J. Non. Cryst. Solids* **15**, 471 (1974)
[5] D K Dasgupta and K Joyner, *J. Phys.* **D9**, 829 (1976)
[6] S Nakamura, G Sawa and M Ieda, *Jpn. J. Appl. Phys.* **18**, 995 (1979)
[7] H J Wintle, *IEEE Trans Electr. Insul.* **EJ-12**, 97 (1977)
[8] B V Hamon, *Proc. Inst. Electr. Eng.* London Monographs **27**, (1952)
[9] R H Petridge, *Polym. Lett.* **5**, 205 (1967)
[10] A Servini and A K Jonscher, *Thin Solid Films* **3**, 341 (1969)
[11] A Kumar and R Nath, *Phys. Status Solidi* **A61**, 301 (1980)
[12] P K C Pillai, G K Narula, A K Tripathi and R G Mendirata, *Phys. Status Solidi* **A67**, 649 (1981)
[13] P K Khare, *Indian J. Pure Appl. Phys.* **32**, 160 (1994)
[14] P K Khare, J M Keller and S C Datt, *Indian. J. Pure Appl. Phys.* **29**, 714 (1991)
[15] P K Khare, M S Gaur, Alka Bajpai, R K Pandey and A P Srivastava, *Indian J. Pure Appl. Phys.* **31**, 326 (1993)
[16] P C Mahendru, K Jain, V K Chopra and P Mahendru, *J. Phys.* **D8**, 305 (1975)
[17] P C Mahendru, K Jain and Praveen Mahendru, *J. Phys.* **D11**, 1431 (1978)
[18] P K Khare and A P Srivastava, *Indian J. Pure Appl. Phys.* **30**, 102 (1992)
[19] P K Khare, M S Gaur and A P Srivastava, *Indian J. Pure Appl. Phys.* **31**, 102 (1993)
[20] C Yasile, S Ioan, N Asandei and I A Schneide, *Macromol. Chem.* **6**, 24 (1969)
[21] P K Khare, M S Gaur and A P Srivastava, *Indian J. Pure Appl. Phys.* **32**, 14 (1994)
[22] P K Khare and Ranjeet Singh, *Polymer International* **34**, 407 (1994)
[23] M R Bhide and S Rao, *Pramana – J. Phys.* **4**, 271 (1975)
[24] P K C Pillai, G K Narula, A K Tripathi and R G Mendiratta, *Phys. Status Solidi* **A77**, 693 (1983)
[25] P K Khare, Thesis Ph.D., Study of thermostimulated discharge currents of doped films in organic systems Saugor (MP) India (1989)
[26] P K Khare and R S Chandok, *Polymer International* **35**, (1994)
[27] J Van Turnhout, *Thermally stimulated discharge of polymer electrets* (Elsevier, Amsterdam, 1975), pp. 106–130
[28] Van J derschueren, *J. Polym. Sci. Polym. Phys.* (*USA*), **15**, 873 (1977)
[29] T J Lewis, *Conf. on Electr. properties of organic solids*, (Inst Phys. Chem. Wroclaw Tech Univ Poland Ser No. 7, Conf No. 1, pp. 146–62
[30] L C E Struik, *Physical aging in amorphous polymers and other materials* (Elsevier, Amsterdam, 1978)

PRAMANA
— journal of
physics

© Printed in India

Vol. 44, No. 1,
January 1995
pp. 19–32

Microwave conductivity studies on some semiconductors

V SUBRAMANIAN, V R K MURTHY and J SOBHANADRI
Department of Physics, Indian Institute of Technology, Madras 600 036, India

MS received 21 September 1994

Abstract. The cavity perturbation technique is employed for the characterisation of semiconductors at microwave frequency for its conductivity. Temperature variation of microwave conductivity studies provide the information regarding the band gap, scattering parameter and impurity ionization energy. Change in the real part of the dielectric permittivity with conductivity indicates the change in the momentum relaxation time.

Keywords. Cavity perturbation technique; silicon; microwave conductivity; momentum relaxation time.

PACS Nos 72·20; 77·00

1. Introduction

Application of microwave techniques to characterize semiconductors is steadily gaining importance for variety of reasons. The study of complex dielectric permittivity of semiconductors at microwave frequencies is useful in additionally estimating the momentum relaxation time and effective mass. Though the conventional DC conductivity technique is simpler and easier to characterize the semiconductor for its bandgap, scattering phenomena, activation energy etc., the microwave technique is superior since it removes the contact potential problem, giving all the information that the DC technique provides and also giving information about the relaxation time of the carriers. As early as 1960, microwave techniques have been used to characterize the semiconductors for its conductivity and lifetime. Transmission and reflection techniques have been employed for these studies. Henisch and Zucker [1] in 1956 developed an experimental arrangement to measure the conductivity and lifetime at 9 MHz using a resonant cavity. In 1959, Ramsa *et al* [2] utilized the reflection technique in the microwave frequency region. Employing the cavity resonance technique for semiconductors at microwave frequencies had been proposed by Montgomery [3] in 1947. Recently various versions of microwave measurement technique are reported for the characterization of Si [4–6], GaAs [7], CdS [8], ZnS [9], HgCdTe [10], InP [11] and Zn_3P_2 [12].

The microwave techniques utilized for the characterization of semiconductors can be classified broadly into reflection [13–14], transmission [15] and cavity resonance techniques [16–19]. Among these, cavity resonance technique is considered to be the most sensitive and does not require large amount of samples. Cavity perturbation technique is one such technique and is widely used in the dielectric measurements of liquids and solids [20–21]. This technique is also used for the transient analysis of certain liquid samples like cyclohexanaone to monitor the reaction kinetics [22] and also to monitor the minority carrier lifetime in semiconductors [12].

The analysis of cavity perturbation technique assumes that the cavity is a lumped resonant circuit resembling the parallel or series LCR depending upon reflection or transmission type respectively. Murthy and Raman [21] utilized this assumption on a reflection type TE_{10n} mode cavity and derived an expression for the measurement of dielectric parameter when the sample fully occupies the '*b*' dimension of the rectangular cavity at the electric field maximum. If the sample does not fully occupy the '*b*' dimension of the cavity, the available formulae cannot be used. Recently, Lehndroff [23] has arrived at a correction factor involving the depolarization factor (can be used only for cylindrical samples) due to the reduction in the sample size. But this correction factor cannot be used for semiconductor samples due to the sample size requirement. Therefore the cavity perturbation technique is employed to study the relative variation in conductivity.

In this paper, the cavity perturbation technique is used in the characterization of some semiconductor samples (single and polycrystalline silicon and GaAs) for its temperature variation of conductivity (300–500 K) at 9 GHz. From this data the band gap, scattering mechanism etc. are studied as in the case of temperature variation of DC conductivity. The variation of momentum relaxation time with conductivity is also reported for a single crystal silicon samples.

2. Sample

The samples used in the present study are listed in table 1. The carrier concentration of the silicon samples is in the range of 10^{13}–$10^{16}/\text{cm}^3$. The single crystal gallium arsenide is an *n*-type semi-insulating sample with resistivity around 12000 Ω-cm. Among the six silicon samples, three samples are single crystal and other three are polysilicon of different grain sizes. The silicon samples are prepared by Czeckrolski technique and supplied by Metkem, India.

3. Theory

The carrier motion in a semiconductor acted upon by an electromagnetic field of angular frequency ω is given by Drude–Zener theory [24–25],

$$m^* \frac{\mathrm{d}v}{\mathrm{d}t} = eEe^{-j\omega t} - \frac{m^* v}{\tau(v)} \tag{1}$$

Table 1. List of samples under study.

Sample	Type	ρ(Ω-cm)	Grain size (μm)
Silicon-A	*p*	320	Single
B	*p*	135	Single
C	*n*	80	Single
E	*n*	120	Single
K1	*P*	1·9	150
M2	*n*	120–240	800
GaAs-R	*n*	12000	Single

where $Ee^{-j\omega t}$ is the applied field, m^*, the effective mass, v, the velocity of carrier and $\tau(v)$ is the momentum relaxation time (a function of velocity). The current density due to the application of electromagnetic field is given by,

$$J = J_i + J_o \tag{2}$$

where n is the carrier concentration, σ is the conductivity at microwave frequency,

$$J_i = \sum \frac{ne^2\tau(v)Ee^{j\omega t}}{m^*[1+\omega^2\tau^2(v)]} = \sigma Ee^{j\omega t} \tag{3}$$

and

$$J_o = \sum \omega\epsilon Ee^{j\omega t} - \frac{ne^2\tau^2(v)\omega Ee^{j\omega t}}{m^*[1+\omega^2\tau^2(v)]} \tag{4}$$

J_i is the in-phase component of current density and gives the conductivity at ω. J_o is the out-of-phase component and is the resultant of dielectric current and out-of-phase carrier current. This out-of-phase carrier current changes the effective dielectric permittivity by $\Delta\varepsilon$. The AC conductivity is now given by,

$$\sigma = \sum \frac{ne^2\tau(v)}{m^*[1+\omega^2\tau(v)^2]} = \frac{\sigma_{\mathrm{DC}}}{[1+\omega^2\tau(v)^2]} \tag{5}$$

For τ in the other of 10^{-13} s [25], at 10 GHz, the values of σ and σ_{DC} are same. For a single relaxation time, the complex dielectric permittivity of a semiconductor is given by

$$\varepsilon^* = \varepsilon' - j\varepsilon'' = \varepsilon' - j\sigma\omega\varepsilon_0 \tag{6}$$

where ε' is the dielectric constant and ε'' is the dielectric loss.

The change in the dielectric permittivity due to the out-of-phase carrier current is given by

$$\Delta\varepsilon' = -\frac{\sigma\tau}{\varepsilon_0}. \tag{7}$$

The complex dielectric permittivity therefore gives the value of the conductivity at microwave frequencies and the change in the dielectric constant at DC. Benedict and Shockley [26] showed that the (7) can be used to evaluate the momentum relaxation time of the carriers.

The cavity perturbation technique is used to calculate the complex dielectric permittivity of semiconductors. As mentioned earlier, it is very difficult to measure the absolute value of complex dielectric permittivity and therefore, the relative variation of complex dielectric permittivity is measured by varying the temperature. The complex dielectric permittivity is calculated from the change in the resonance frequency and the quality factor of the cavity due to the introduction of the semiconductor sample in an electric field maximum. While the shift in the resonance frequency is related to ε', the change in the quality factor is attributed to ε''

$$(\varepsilon' - 1) \propto \left(\frac{f_0^2 - f_1^2}{f_1^2}\right) \tag{8}$$

and

$$\varepsilon'' \propto \left(\frac{1}{Q_1} - \frac{1}{Q_0}\right) \tag{9}$$

where f_0 and f_1 are the resonance frequency of the empty and sample loaded cavity, Q_0 and Q_1 are the quality factors of empty and sample loaded cavity. From (6), it is obvious that the conductivity is indirectly proportional to the change in the Q-factor of the cavity

$$\sigma \propto \Delta\left(\frac{1}{Q}\right). \tag{10}$$

4. Experimental

The block diagram of the experimental arrangement is shown figure 1. HP8720A microwave vector network analyser output port is connected to a TE_{103} mode reflection type cavity by means of a flexible coaxial connector. The resonance frequency of the empty cavity is 9·158 GHz and the loaded quality factor is 2800. The resonance curve is shown in figure 2. The samples are loaded in the sample holder made with teflon. The resonance frequency of the cavity with empty sample holder is 9·082 GHz. The cavity has a provision for fixing the sample holder at the centre of the cavity. The sample can be illuminated with light of energy greater than the band gap. The temperature of the cavity is varied from 300 to 550 K and monitored by a computer. Network analyzer and the digital nanovoltmeter (used to monitor the thermocouple voltage) are connected to the computer through IEEE 488 interface bus for the data transfer and temperature controlling.

Network analyser's port parameters are calibrated up to the cavity connection using a standard waveguide calibration kit provided by the Hewlett Packard. The

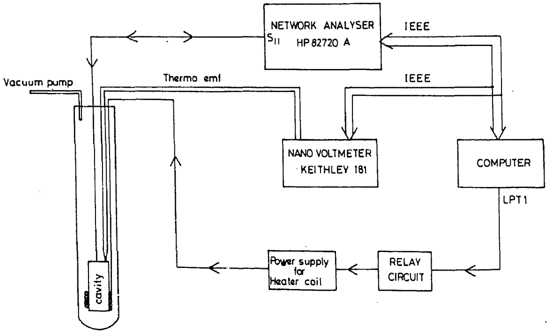

Figure 1. Block diagram of the experimental arrangement to measure the microwave conductivity.

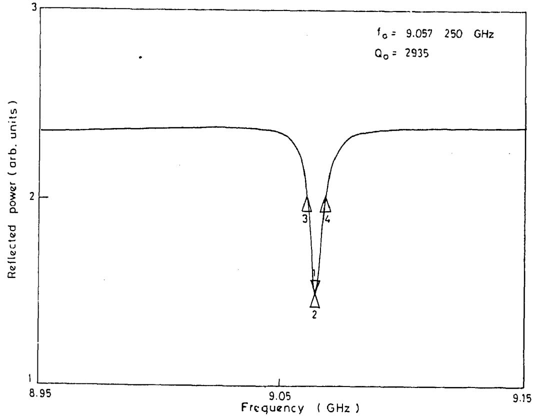

Figure 2. Resonance curve of the empty cavity.

empty cavity (along with the sample holder) is connected and the temperature is varied to get the reference data on the shift in resonance frequency and change in the quality factor with temperature. Figure 3 shows the change in the resonance frequency and quality factor. All the data taken for samples are normalized with these values.

The accuracies in the measurement of resonance frequency and quality factor are ± 10 kHz and ± 10 respectively.

5. Results and discussion

5.1 *Temperature variation of conductivity*

The temperature variation studies on conductivity and dielectric constant are already reported earlier in 1960s and 1970s. But it was not pursued further which may be due to lack of sensitive experimental arrangement and difficulty in the measurement. Bhar [24] had reported the variation of microwave conductivity with temperature in two single crystal silicon samples (1000 and 143 Ω-cm) and similar studies on three single crystal silicon samples (0·5, 40, 170 Ω-cm) are reported by Natarajan *et al* [27]. Both these papers utilized the reflection technique. Though both these papers show similar graphs and give an interpretation with extrinsic and intrinsic conductions, the band gaps from the intrinsic region are not evaluated. The difficulty in getting the band gap value may be due to lack of sensitive experimental arrangement to compensate the variation of reflectivity from the empty waveguide with temperature. With the extension of cavity perturbation technique and availability of vector network

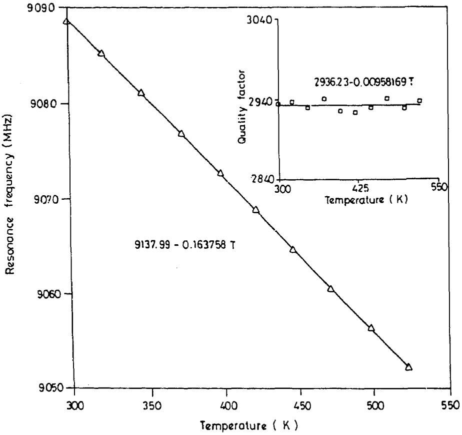

Figure 3. Variation of resonance frequency with temperature. Inset: Variation of quality factor with temperature.

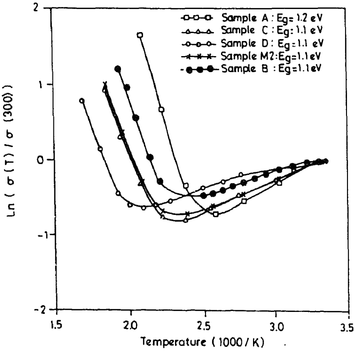

Figure 4. Variation of microwave conductivity with temperature for silicon samples-A, B, C, E, and M2.

analysers, it is possible to study accurately the variation of complex dielectric permittivity with temperature or illumination intensity.

Figures 4–6 give the variation of microwave conductivity with temperature for silicon and gallium arsenide samples. The slope of the plot between $\ln(\sigma(T)/\sigma(300))$ and $1/T$ gives the band gap. Table 2 presents the results on the band gap of silicon and gallium arsenide. The temperature variation of conductivity observed for sample-K1 (figure 6) shows that the sample has not reached the intrinsic region and the region from 300–400 K still exhibits the active nature of deep impurity centre having the activation energy 0·28 eV below conduction band. Paul Marusk *et al* [28] have reported the activation energy of 0·216 eV in a 7 Ω-cm polysilicon sample of grain size 1000 μm using DC resistivity data. The temperature region 400–500 K represents the participation of lattice scattering and impurity centre or may indicate the carrier saturation region.

5.2 *Temperature variation study of dielectric permittivity*

As given by (7), the dielectric permittivity (ε') also changes with the conductivity of the semiconductor. As the conductivity increases, the $\Delta\varepsilon'$ also increases. The negative sign in (7) indicates that the absolute value of the dielectric permittivity decreases with increase in σ or τ. The change in the dielectric permittivity due to carrier motion was experimentally observed by Benedict [29] for a germanium sample as 0·1% having resistivity of 1000 Ω-cm. Cardona *et al* [30] had also observed the change in a 1 MΩ-cm silicon sample as approximately 1% for the change in the temperature from 50 to 200 K and predicted even higher change at temperatures above 300 K.

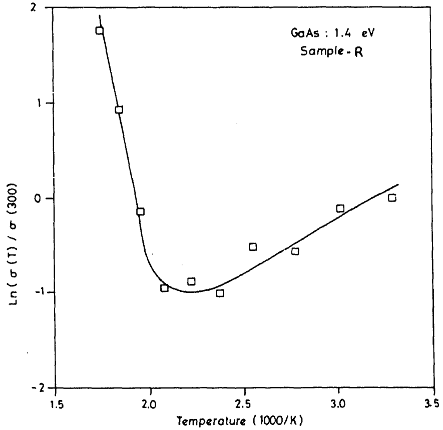

Figure 5. Variation of microwave conductivity with temperature for semi-insulating GaAs sample-R.

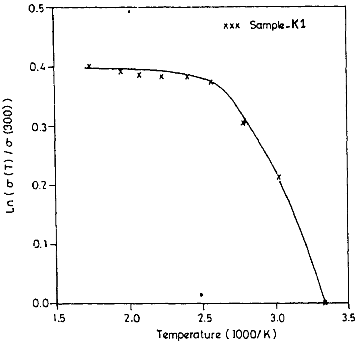

Figure 6. Variation of microwave conductivity with temperature for silicon sample-K1. The variation shows that the extrinsic conduction region due to the impurity centre located at 0·28 eV below the conduction band and the subsequent carrier saturation region.

Table 2. The energy gap calculated in silicon and gallium arsenide samples using the temperature variation of conductivity at microwave frequency.

Sample	Energy gap (eV)
Silicon-A	1·2
Silicon-B	1·1
Silicon-C	1·1
Silicon-E	1·1
Polysilicon-M2	1.1
GaAs-R	1·4

Bhar [24] had also observed a change less than 1% per 100 K for 1000 Ω-cm silicon sample.

Figures 7 and 8 show the variation of $\Delta\varepsilon'$ with temperature evaluated for some silicon samples from the temperature variation of complex dielectric permittivity. As it is not possible to evaluate the absolute value of dielectric permittivity and conductivity, the relative change in $\Delta\varepsilon'$ is calculated. Figures 7 and 8 show that $\Delta\varepsilon'$ remains constant till the sample reaches the intrinsic region and increases thereafter. The variation of $\Delta\varepsilon'$ should be similar to the variation of conductivity, but it is not observed so (see figure 9 for sample-A). In the intrinsic region, though $\Delta\varepsilon'$ increases with increase in conductivity, ε' is observed to increase with increase in temperature instead of getting decreased. Cardona *et al* [30] observed this trend and attributed

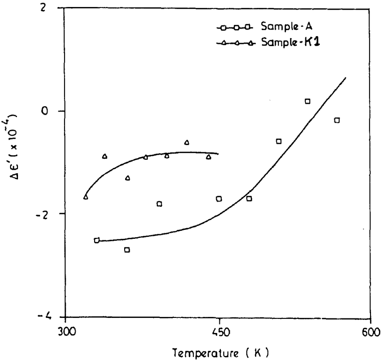

Figure 7. Variation of change in dielectric constant with temperature for samples-A and K1.

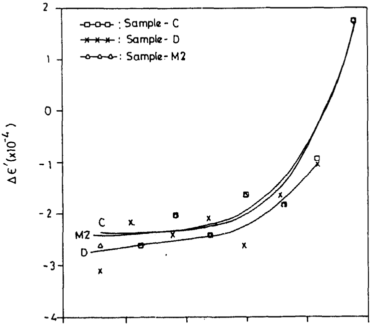

Figure 8. Variation of change in dielectric constant with temperature for samples-C, D, and M2.

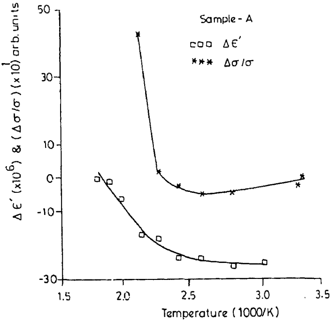

Figure 9. Variation of $\Delta\varepsilon'$ ($\times 10^6$) and ($\Delta\sigma/\sigma$) ($\times 10$) with temperature for sample-A for comparison.

to the change in the dielectric permittivity in a direction opposite to that due to carrier motion. It is also possible to suggest that the increase in ε' is the resultant of decrease in τ. The decrease of τ with increase in conductivity is the resultant of increase in the carrier concentration.

The decrease in τ may be attributed to the increase in the lattice scattering or to the electron–electron scattering or the combined effects of both. If the lattice scattering dominates over τ, then the $\Delta\varepsilon'$ should have decreased in the temperature range 300–450 K (where the conductivity reduces due to the lattice scattering), rather it remained constant. Considering the other possibility, as the carrier concentration increases, the carrier–carrier scattering increases. This decreases the momentum relaxation time. Though the electron–electron scattering is not much significant at lower concentrations of electrons, it affects the momentum relaxation time at higher concentrations ($10^{16}/\text{cm}^3$: in this case) [31]. For an assumed values of ε' as 12, effective mass (m^*) as 0·5 for electron, and the energy of the electron as 0·03 eV, the relation between the momentum relaxation time and carrier concentration may be given by [31],

$$\tau \propto \frac{10^4}{n} \tag{11}$$

where n is the carrier concentration expressed in cm^{-3}.

Therefore, as the carrier concentration remains constant for the temperature range 300-400 K for samples-A, C, E, and M2, $\Delta\varepsilon'$ also remains constant. But in the intrinsic region, (> 450 K), the carrier concentration increases and hence τ decreases.

Similarly, the variation of $\Delta\varepsilon'$ for sample-K1 is attributed to the increase in the carrier concentration (300–400 K) and its subsequent saturation (400–500 K). It is interesting the note that the momentum relaxation does not get affected by the variation in the conductivity but is sensitive to the carrier concentration. The comparison between figures 4 and 6 and 7 and 8 indicates that the change in the $\Delta\varepsilon'$ indirectly gives the change in the carrier concentration.

To ensure this type of trend, instead of increasing the temperature, a 122 mW/cm^2 white light is used to increase the carrier concentration (subsequently the conductivity) of sample-A. The aim is to increase the conductivity of the sample by slowly increasing the intensity of the illumination source, thereby it is possible to study the variation of $\Delta\varepsilon'$ with conductivity. As mentioned earlier, the dielectric permittivity is directly proportional to the measurement of resonance frequency shift and the dielectric loss is proportional to the change in the quality factor. Therefore, for various intensities of the excitation source, the relative change in the permittivity is measured in terms of increase in the resonance frequency shift of the cavity. Similarly, the variation of conductivity is measured in terms of the quality factor. Figure 10 shows the cavity resonance plotted for the cavity under dark and illuminated condition loaded with sample-A showing clearly the shift in the resonance frequency due to the application of illumination intensity. It is observed that the dielectric permittivity increases with intensity and therefore with conductivity. By varying the intensity of the illumination source, the shift in the resonance frequency with the conductivity of the sample is plotted in figure 12. The change in the slope of the plot gives the relative variation of relaxation time. The decrease in τ is calculated as 3% to 87% for an increase in conductivity from 3% to 793% (σ at 300 K is 0·00286 S/cm) and $\Delta\varepsilon'$ up to 17·5%. There is not much change in $\Delta\varepsilon'$ for a change of σ up to 300%, but increase in the conductivity above this value decreases the absolute value of the ε'. This drastically reduces the relaxation time. Figure 12 shows a similar change in the resonance frequency and quality factor of the cavity loaded with sample-M2 under dark and

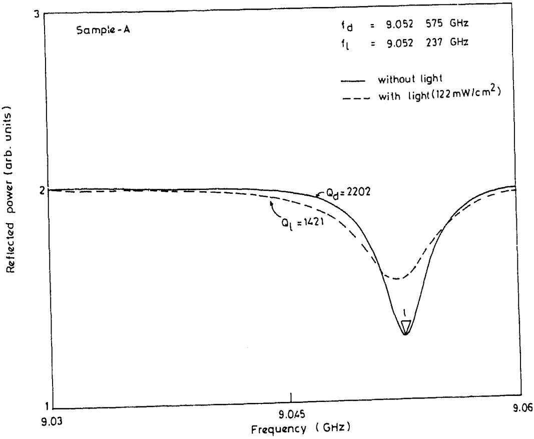

Figure 10. Cavity resonance curve for sample-A under dark and under 122 mW/cm^2 white light illumination.

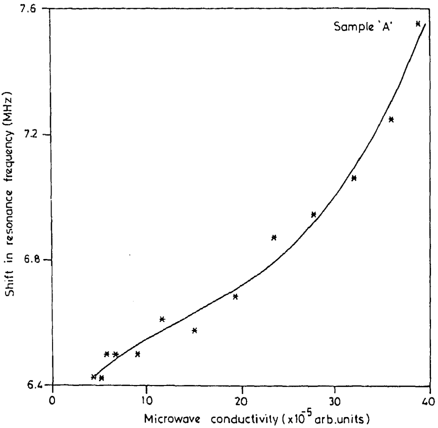

Figure 11. Shift in the resonance frequency with conductivity for sample-A.

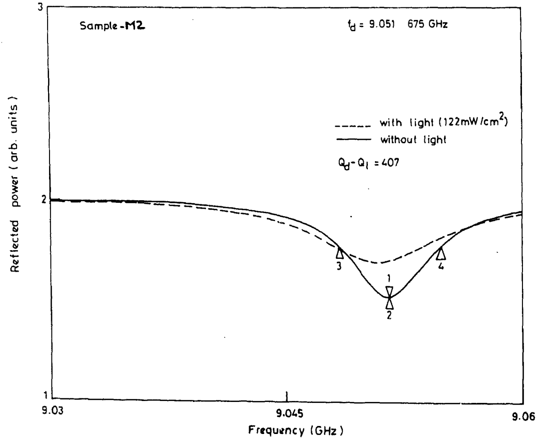

Figure 12. Cavity resonance curve for sample-M2 under dark and under 122 mW/cm^2 white light illumination.

illuminated condition. Therefore, it may be concluded that the change in $\Delta\varepsilon'$ is dominated by the change in the carrier concentration compared to the change in the conductivity.

6. Conclusion

The cavity perturbation technique is employed to observe the temperature variation of conductivity in single and polycrystalline silicon and gallium arsenide at microwave frequencies. Apart from the measurement of band gap, an attempt is made to correlate the variation of dielectric constant with the conductivity. The paper suggests that the increase of dielectric constant with increase in conductivity is due to the increase in carrier–carrier scattering resulting in the decrease of momentum relaxation time of the carriers.

Acknowledgements

One of the authors, (VS) acknowledges CSIR, New Delhi for the financial support provided through a Senior Research Fellowship. The authors wish to acknowledge INDO-US project for providing some of the experimental facilities. The authors wish to thank Mr V Sivasubramanian for useful discussions.

References

[1] H K Henisch and J Zucker, *Rev. Sci. Instrum.* **27**, 409 (1956)
[2] A P Ramsa, H Jacob, and F A Brand, *J. Appl. Phys.* **30**, 1054 (1959)
[3] C A Montgomery, in *Technique of microwave measurements*, MIT Rad. Lab. Ser., (McGraw-Hill, New York, 1947) **11**, 625
[4] G Beck and M Kunst, *Rev. Sci. Instrum.* **57**, 197 (1986)
[5] A Sanders and M Kunst, *Solid State Electron* **34**, 1007 (1991)
[6] M Kunst and A Sanders, *Semicond. Sci. Technol.* **7**, 51 (1992)
[7] K D Cummings, S J Pearton, and G P Vella-Coleiro, *J. Appl. Phys.* **60**, 1676 (1986)
[8] John M Warman, Matthijs P de Haas, Stephan W F M, van Hovell tot Westerflier, Johannes J M Binsma and Zvonimir I Kolar, *J. Phys. Chem.* **93**, 5895 (1989)
[9] B Kramer, S Gelfman and K Kalikstein, *Phys. Rev.* **B6**, 556 (1972)
[10] M C Chen, *J. Appl. Phys.* **64**, 945 (1988)
[11] S Bothra, S Tyagi, S K Ghandhi and J M Borrego, *Solid State Electron* **34**, 47 (1991)
[12] R W Fessenden, J Sobhanadri and V Subramanian, communicated to Thin Solid Films, USA
[13] S Dixon, R F Giordano and H Jacobs, *J. Appl. Phys.* **45**, 2570 (1974)
[14] S Deb and B R Nag, *J. Appl. Phys.* **33**, 1604 (1962)
[15] H Jacobs, A P Ramsa and F A Brand, *Proc. IRE* **48**, 2570 (1974)
[16] J O Artman and P E Tannenwald, *J. Appl. Phys.* **26**, 1124 (1955)
[17] K S Champlin and R R Krongard, *IRE Trans. Microwave Theory Tech.* **MTT-9**, 546 (1961)
[18] V Subramanian, B S Bellubbi and J Sobhanadri, *Rev. Sci. Instrum.* **64**, 231 (1993)
[19] V Subramanian and J Sobhanadri, *Rev. Sci. Instrum.* **65**, 453 (1994)
[20] V Subramanian, B S Bellubbi and J Sobhanadri, *Pramana – J. Phys.* **41**, 9 (1993)
[21] V R K Murthy and R Raman, *Solid State Commun.* **70**, 847 (1989)
[22] Richard W Fessenden, Paul M Carton, Henning Paul, Hiroshi Shimamori, *J. Phys. Chem.* **83**, 1676 (1979)
[23] B Lehndroff, *Meas. Sci. Technol* **3**, 822 (1992)

[24] J N Bhar, *Proc. IEEE*, **51**, 1623 (1963)
[25] F J Blatt, in *Physics of electronic conduction in solids* (McGraw Hill New York, 1968)
[26] T S Benedict and W Shockley, *Phys. Rev.* **89**, 1152 (1953)
[27] R Natarajan, D C Dube and V K Tripathi, *Indian J. Phys.* **52**, 567 (1978)
[28] H Paul Maruska, Amal K Ghosh, Albert Rose and Tom Feng, *Appl. Phys. Lett.* **36**, 381 (1980)
[29] T S Benedict, *Phys. Rev.* **91**, 1565 (1953)
[30] M Cardona, W Paul and H Brooks, in *Solid State Physics* (Academic Press, New York, 1960) vol. 1, pp. 206–214
[31] B K Ridley, in *Quantum processes in semiconductors* (Oxford University Press, New York, 1993) edn. 3, p. 175

RAMAN RESEARCH INSTITUTE
BANGALORE - 80.
CLASS NO.
ACC NO. 26997

PRAMANA
— journal of
physics

© Printed in India

Vol. 44, No. 1,
January 1995
pp. 33–44

Dielectric relaxation and related studies of 4-ethylphenol–methanol mixtures using time domain reflectometry

R H FATTEPUR#, M T HOSAMANI$, D K DESHPANDE@, R L PATIL@ and S C MEHROTRA*
#Basaveshwar Science College, Bagalkot 587 101, India
$P. C. Jabin Science College, Hubli, India
@Department of Physics, Karnatak University, Dharwad 580003, India
*Department of Physics, Dr. Babasaheb Ambedkar Marathwada University, Aurangabad 431 004, India

MS received 13 July 1994; revised 29 October 1994

Abstract. The dielectric relaxation studies of 4-ethylphenol–methanol mixtures have been carried out at various temperatures ranging from 10°C to 40°C using time domain reflectometry in the frequency range 10 MHz to 10 GHz. The relaxation mechanism in these systems is explained by Cole–Davidson model. The excess dielectric parameters, Kirkwood correlation factor and activation energy have been calculated and discussed with respect to molecular arrangements, and microdynamics of the binary mixture composed of both the associative type of liquids.

Keywords. Permittivity; microwaves; relaxation times; 4n-ethylphenol; methanol; binary mixtures.

PACS No. 77·22

1. Introduction

Several workers have reported [1–4] dielectric relaxation studies of pure alcohols and their aqueous solutions to understand hydrogen bond structure in these systems. It is generally observed that hydrogen bond is a strong intermolecular interaction which causes a significant effect upon the structure, thermodynamic properties and macroscopic dielectric properties of the solutions of polar liquids. As noticed by Gestblom and Sjoblom [5] small-chain alcohols like methanol behave in a different way from long-chain alcohols as the former is characterized by faster relaxation and low activation energy whereas the latter by slower relaxation and high activation energy. The dielectric studies of aqueous methanol show ideal mixture behaviour due to the similar self association patterns of the two components. But not much work has been done on the alkyl phenol-methanol systems where the alkyl phenols are characterized by high relaxation time and activation energy but lower macroscopic permittivity compared to methanol. Such studies are expected to yield information about the structural behaviour or self association pattern and intermolecular interactions in the mixture. In view of this we have taken up the dielectric relaxation studies of different *n*-alkylphenols-methanol mixtures using time domain reflectometry (TDR) technique.

The objective of the paper is to study the dielectric relaxation in 4-ethylphenol

(4EP)-methanol (MtOH.) mixtures over entire range of concentration at four different temperatures from 10°C to 40°C using TDR. The excess dielectric properties, thermodynamic properties and Kirkwood correlation factor have been calculated and the results discussed.

2. Experimental details

4-Ethylphenol of 99% purity (Aldrich) and methanol of spectroscopic grade purity obtained commercially were used without further purification. The mixtures were prepared at various volume percentages of 4EP in MtOH in steps of 10 (before mixing) at room temperature.

The complex permittivity spectra were studied using time domain reflectometry (TDR) method as described in [6–8]. The Tektronix 7854 sampling oscilloscope with 7S12 TDR unit has been used. A fast rising step voltage pulse of 200 mV with 25 ps rise time and repetative frequency of 1 kHz generated by a tunnel diode was propagated through a co-axial line system. The sample was placed at the end of co-axial line in standard military application (SMA) coaxial cell of 3·5 mm outer diameter and 1·35 mm effective pin length. The change in the pulse after reflection from the sample placed in the cell was monitored. In our experiment time window of 5 ns was used. The reflected pulse without sample $R_1(t)$ and with sample $R_x(t)$ were digitized into 1024 points and transferred to PC/XT through GPIB. Temperature of the sample was controlled electronically within ± 0·2°C.

Processing of data yielded complex reflection coefficient spectra $\rho^*(\omega)$ over a frequency range of 10 MHz to 10 GHz [6, 7]. The complex permittivity spectra $\varepsilon^*(\omega)$ were obtained from reflection coefficient spectra $\rho^*(\omega)$ by applying the least squares fit method of calibration used for HMPA-Water mixture [8, 9]. A typical reflection coefficient spectrum $\rho^*(\omega)$ (before calibration) and complex dielectric spectrum $\varepsilon^*(\omega)$ (after calibration) are shown in figure 1. The discontinuity at 2 GHz and 6 GHz in

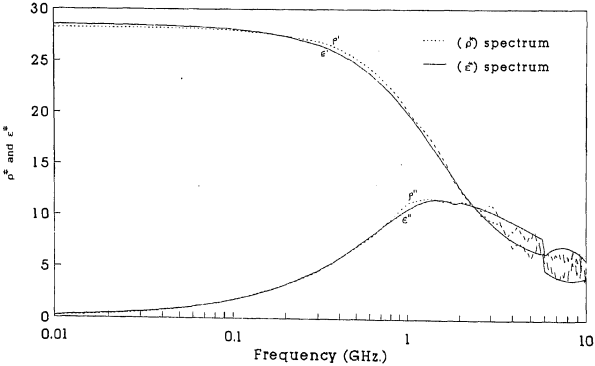

Figure 1. The reflection coefficient spectrum-(ρ^*) and corrected dielectric spectrum (ε^*) for a 4-ethylphenol-methanol mixture.

the $\varepsilon^*(\omega)$ spectrum is due to the numerical error caused by dividing the spectrum into three parts to achieve better accuracy in calibration [8].

3. Results and discussions

The Cole–Davidson equation was used in the least squares fit method as follows,

$$\varepsilon^*(\omega) = \varepsilon_\infty + \frac{\varepsilon_s - \varepsilon_\infty}{(1 + j\omega\tau)^\beta} \tag{1}$$

when ε_s is the static dielectric constant ε_∞, the high frequency dielectric constant τ the relaxation time and β the Cole-Davidson distribution parameter. Values of ε_s, τ and β as a function of 4EP concentration in MtOH at four different temperatures studied are given in table 1 and a graphical representation of ε_s and τ is given in figures 2(a) and 2(b) respectively. The values of ε_s of the mixture decrease from corresponding value of MtOH to that of pure 4EP whereas τ increases from that of

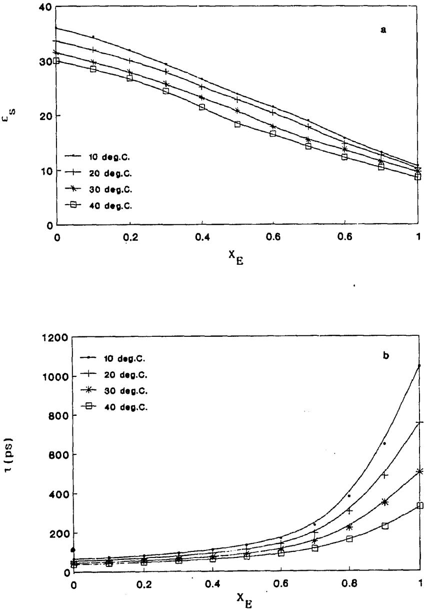

Figure 2. Variation of (**a**) static dielectric constant-(ε_s) and (**b**) relaxation time-(τ) with volume fraction of 4-ethylphenol (X_E) in methanol at various temperatures.

Table 1. Variation of dielectric parameters for 4-ethylphenol-methanol mixture.

Vol.% 4EP	ε_s	τ (ps)	β
10°C			
00	35·72(12)	66·0 (9)	0·948(3)
10	34·67(12)	71·7(11)	0·954(5)
20	32·04(10)	80·7(13)	0·931(3)
30	29·11(10)	93·2(16)	0·907(2)
40	26·09(11)	109·3(19)	0·914(2)
50	23·30 (9)	132·6(24)	0·881(2)
60	20·67 (9)	167·5(31)	0·903(2)
70	18·12 (8)	235·1(39)	0·942(3)
80	15·67 (8)	379·1(40)	0·921(3)
90	13·87 (6)	646·5(48)	0·904(2)
100	12·14 (5)	1045·4(56)	0·896(2)
20°C			
00	33·68(10)	55·8 (6)	0·936(7)
10	32·17 (9)	60·7 (8)	0·904(3)
20	29·72 (8)	68·1 (9)	0·903(3)
30	26·91 (9)	78·4(11)	0·886(2)
40	23·97 (9)	91·6(15)	0·875(2)
50	21·29 (7)	110·6(18)	0·951(6)
60	18·63 (6)	137·7(25)	0·945(5)
70	16·09 (6)	195·1(30)	0·933(3)
80	14·17 (5)	304·7(37)	0·987(8)
90	12·06 (4)	485·4(42)	0·885(3)
100	10·51 (4)	754·1(53)	0·906(3)
30°C			
00	31·53 (9)	45·3 (4)	0·951(5)
10	29·74(7)	49·3 (5)	0·948(4)
20	27·53(7)	55·3 (6)	0·936(4)
30	24·87(6)	65·3 (8)	0·955(6)
40	22·15(5)	73·9(12)	0·941(3)
50	19·53(5)	88·2(15)	0·929(3)
60	17·13(5)	111·5(18)	0·925(2)
70	14·82(3)	152·8(25)	0·908(2)
80	12·73(3)	222·0(30)	0·952(6)
90	11·01(3)	348·4(37)	0·913(3)
100	9·56(3)	502·0(45)	0·902(2)
40°C			
00	29·96 (8)	38·4 (4)	0·938(4)
10	28·08(8)	41·6 (5)	0·941(5)
20	25·92(7)	46·6 (5)	0·926(3)
30	23·33(7)	53·2 (6)	0·951(5)
40	20·73(5)	61·5 (7)	0·936(3)
50	18·27(5)	72·8(10)	0·918(2)
60	16·07(4)	88·0(13)	0·878(2)
70	13·93(4)	112·6(17)	0·893(2)
80	11·90(3)	159·3(23)	0·906(2)
90	10·23(3)	225·4(30)	0·933(4)
100	8·91(3)	328·6(35)	0·925(4)

Numbers in parentheses denote uncertainty in last significant digit obtained by least squares fit method. e.g. 8·91 (3) means 8·91 ± 0·03, 328·6(35) means 328·6 ± 3·5.

MtOH to 4EP. τ increases sharply in the higher concentration of 4EP. Similar trend has been observed in our study on 4n-propylphenol-methanol [10] mixtures where τ is found to be more than in 4EP-MtOH mixtures at all concentrations and temperatures.

The contributions of nonlinear effects due to solute-solvent interactions can be studied by the excess dielectric properties. The excess permittivity ε_s^E and excess inverse relaxation time $(1/\tau)^E$ are determined using the following equations:

$$\varepsilon_s^E = [\varepsilon_{sm} - \varepsilon_{\infty m}] - [(\varepsilon_{sM} - \varepsilon_{\infty M})X_M + (\varepsilon_{sE} - \varepsilon_{\infty E})X_E] \tag{2}$$

$$[1/\tau]^E = [1/\tau]_m - [(1/\tau)_M X_M + (1/\tau)_E X_E] \tag{3}$$

where subscripts m, M, E correspond to the mixture, MtOH and 4n-ethylphenol respectively and X_M and X_E represent the weight fractions of the two components of the mixture. The variation of ε_s^E and $(1/\tau)^E$ with X_E (weight fraction of 4EP) for various temperatures are shown in figures 3(a) and 3(b) respectively. For the mixtures $\varepsilon_{\infty m}$

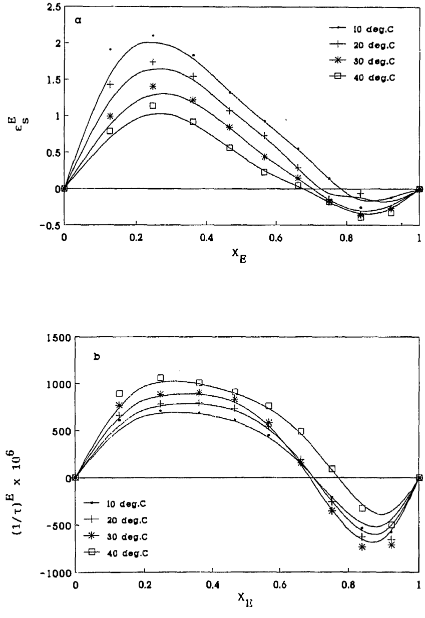

Figure 3. The excess dielectric permittivity-ε_s^E and excess inverse relaxation time-$(1/\tau)^E$ for 4-ethylphenol-methanol mixture as a function of weight fraction of 4-ethylphenol (X_E) at different temperatures.

values are calculated from the corresponding values $\varepsilon_{\infty E}$ and $\varepsilon_{\infty M}$ of the two components using additive rule.

The above models give a good qualitative account to study the solute-solvent interactions. The negative excess ε_s^E is associated with either the disappearance of the polymeric forms, leaving behind the dimers and monomers, or alternatively the creation of new structures of the type depicted above which have essentially zero dipole moment. Either way the net effect is that the permittivity drops below its additive value. The positive values of ε_s^E is interpreted as a formation of monomer structure, whereas the negative ε_s^E implies the formation of multimer structure. The negative excess inverse relaxation time $(1/\tau)^E$ means the creation of an environment such that the solute molecules rotate more slowly in the mixture.

The experimental values of both the excess parameters are fitted to the Redlick–Kister [11, 12] equation,

$$A^E = (X_1 X_2) \sum_j B_j (X_1 - X_2)^j \tag{4}$$

where A is any physical parameter and X_1 and X_2 are the concentrations of the two components. The coefficients B_j's for $j = 0$ to 4 are given in table 2 along with the standard deviation σ. By using these B_j values, A^E values calculated are used as guidelines to draw smooth curves in figures 3(a) and 3(b).

The excess dielectric constant ε_s^E is found to be positive over a wide range of concentration except for small negative values in the higher concentration region of 4EP. The ε_s^E is maximum around 20% of 4EP in MtOH at all temperatures. The positive ε_s^E values suggest that the effective number of dipoles in the mixture might be greater than their corresponding average number in their pure forms probably by creation of monomers.

$(1/\tau)^E$ values are found to be positive in the MtOH-rich region but negative in the 4EP-rich region [figure 3(b)]. The sign inversion of $(1/\tau)^E$ takes place around 70% of 4EP in MtOH. This indicates that the addition of MtOH to 4EP has created a

Table 2. Coefficients B_j's and standard deviation σ of Redlick-Kister equation.

Excess permittivity

t(°C)	B_0	B_1	B_2	B_3	B_4	σ
10	4·92	8·65	3·01	7·47	3·78	0·08
20	3·67	8·90	2·94	1·91	−0·17	0·10
30	2·86	8·19	2·79	−0·05	−4·51	0·04
40	1·81	6·72	4·94	0·75	−8·60	0·04

Inverse relaxation time

t(°C)	$B_0 \times 10^3$	$B_1 \times 10^3$	$B_2 \times 10^3$	$B_3 \times 10^3$	$B_4 \times 10^3$	$\sigma \times 10^3$
10	2·28	2·83	−3·37	8·09	−1·21	0·05
20	2·76	3·24	−5·23	8·95	0·01	0·10
30	3·09	4·18	−7·14	9·41	2·65	0·06
40	3·48	2·61	−0·49	9·99	−3·79	0·09

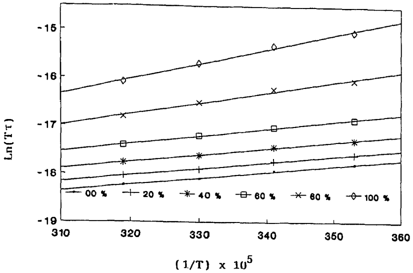

Figure 4. Ln(Tτ) vs 1/T for 4-ethylphenol + methanol mixtures at various volume percentages of 4-ethylphenol.

hindering field such that the effective dipoles rotate slowly in the 4EP-rich region whereas in the MtOH-rich region the effective dipoles rotate faster. This variation of $(1/\tau)^E$ reflects the state of microdynamics of the system under study.

The thermodynamic parameters like molar enthalpy of activation ΔH^* and molar entropy of activation ΔS^* are determined from Eyring's rate equation [13] (eq. 5) utilizing least squares fit method.

$$\tau = \frac{h}{KT}\exp(\Delta H^* - T\Delta S^*)/\mathrm{RT}. \tag{5}$$

The variation of $\ln(T\tau)$ with $(1/T)$ for some of the compositions of the mixture is shown in figure 4 and a good linear fitting was observed in all the cases. The results of ΔH^* and ΔS^* for various volume percentages of 4EP in MtOH are given in table 3.

Table 3. Variation of ΔH^* and ΔS^* for 4-ethylphenol + methanol solution.

Vol.% 4EP	ΔH^* kJ/mol	ΔS^* J/mol/K
00	11·03 (49)	− 10·67
10	11·68 (52)	− 11·25
20	11·19 (49)	− 11·79
30	11·42 (42)	− 12·18
40	11·81 (52)	− 12·13
50	11·41 (59)	− 11·65
60	13·28 (79)	− 10·45
70	15·41 (173)	− 5·62
80	18·95 (181)	2·48
90	23·15 (227)	12·90
100	26·03 (174)	19·10

Numbers in the parentheses indicate errors in the last significant digit.

There is no significant variation in ΔH^* in the MtOH-rich region but it sharply increases above 70% of 4EP in MtOH and in the same concentration region of 4EP $(1/\tau)^E$ is observed to be negative. From this table it can also be noticed that for more than 80% volume fraction of 4EP, ΔS^* is observed to be positive. But as suggested by Hill *et ai* [14] no much significance can be attached to these values in view of the absence of higher accuracy.

The Kirkwood correlation factor g [15] explains the orientation of the electric dipoles in the polar liquids and it is given by the equation,

$$\frac{4\pi N\mu^2\rho}{9KTM}g = \frac{(\varepsilon_s-\varepsilon_\infty)(2\varepsilon_s+\varepsilon_\infty)}{\varepsilon_s(\varepsilon_\infty+2)^2} \tag{6}$$

The two modified forms of the above equation normally used to study the orientation of the electric dipoles in the binary mixture [16, 17] are as follows,

$$\frac{4\pi N}{9kT}\left(\frac{\mu_{\mathrm{M}}^2\rho_{\mathrm{M}}}{\mathrm{M}_{\mathrm{M}}}X_{\mathrm{M}}+\frac{\mu_{\mathrm{E}}^2\rho_{\mathrm{E}}}{\mathrm{M}_{\mathrm{E}}}X_{\mathrm{E}}\right)g_{\mathrm{eff}} = \frac{(\varepsilon_{\mathrm{sm}}-\varepsilon_{\infty\mathrm{m}})(2\varepsilon_{\mathrm{sm}}+\varepsilon_{\infty\mathrm{m}})}{[\varepsilon_{\mathrm{sm}}(\varepsilon_{\infty\mathrm{m}}+2)]^2} \tag{7}$$

where g_{eff} is Kirkwood correlation factor for a binary mixture, X_{M} and X_{E} represent volume fraction of MtOH and 4EP respectively. The value of g_{eff} varies between g_{M}

Table 4. The Kirkwood factors g_{eff} and g_f for 4-ethylphenol + methanol mixtures.

Vol.% 4EP	g_{eff}	g_f	g_{eff}	g_f
	10°C		20°C	
00	3·22 (19)	1·000 (61)	3·14 (19)	1·000 (61)
10	3·20 (19)	1·017 (62)	3·06 (19)	1·004 (61)
20	3·03 (18)	0·991 (60)	2·90 (18)	0·980 (60)
30	2·81 (17)	0·957 (58)	2·69 (16)	0·946 (58)
40	2·61 (16)	0·920 (56)	2·47 (15)	0·907 (55)
50	2·41 (15)	0·892 (54)	2·27 (14)	0·877 (54)
60	2·22 (14)	0·871 (53)	2·06 (13)	0·851 (52)
70	2·03 (12)	0·856 (53)	1·85 (11)	0·829 (51)
80	1·84 (11)	0·850 (53)	1·70 (11)	0·850 (53)
90	1·71 (11)	0·900 (56)	1·52 (9)	0·877 (55)
100	1·59 (10)	1·000 (63)	1·39 (9)	1·000 (63)
	30°C		40°C	
00	3·03 (18)	1·000 (61)	2·97 (18)	1·000 (61)
10	2·92 (18)	0·991 (60)	2·84 (17)	0·985 (60)
20	2·77 (17)	0·971 (59)	2·68 (16)	0·963 (59)
30	2·57 (16)	0·936 (57)	2·48 (15)	0·925 (56)
40	2·35 (14)	0·899 (55)	2·26 (14)	0·887 (54)
50	2·14 (13)	0·865 (53)	2·12 (13)	0·878 (54)
60	1·94 (12)	0·841 (52)	1·80 (11)	0·833 (51)
70	1·75 (11)	0·823 (51)	1·60 (10)	0·819 (51)
80	1·56 (10)	0·824 (52)	1·49 (9)	0·816 (51)
90	1·41 (9)	0·870 (55)	1·34 (8)	0·860 (55)
100	1·29 (8)	1·000 (64)	1·22 (8)	1·000 (65)

Numbers in parentheses denote last significant digit in the errors calculated by assuming 2% error in the values of ε_s and ε_∞.

and g_E. The second form is

$$\frac{4\pi N}{9kT}\left(\frac{\mu_M^2\rho_M g_M}{M_M}X_M+\frac{\mu_E^2\rho_E g_E}{M_E}X_E\right)g_f=\frac{(\varepsilon_{sm}-\varepsilon_{\infty m})(2\varepsilon_{sm}+\varepsilon_{\infty m})}{\varepsilon_{sm}(\varepsilon_{\infty m}+2)^2} \tag{8}$$

where g_M and g_E are the Kirkwood correlation factors of pure MtOH and 4EP respectively, and are assumed to be affected by an amount g_f in the mixture. The value of g_f is unity for an ideal mixture and deviation from unity may indicate interaction between the two components of the mixture.

The values of g_{eff} and g_f for various compositions of the mixture are given in table 4 and are represented graphically in figures 5(a) and 5(b) respectively. The dipole moments of 4EP and MtOH are taken as 1·98 D (calculated from vector method) and 1·69 D respectively. Kirkwood correlation factor g_{eff} decreases from g of MtOH to that of pure 4EP and g of both the components is more than unity i.e. ($g_M > g_E > 1{\cdot}0$) at all temperatures. This confirms the associative nature of both alcohols and phenols with parallel orientations of their electric dipoles. The extent of parallel orientation decreases with concentration of 4EP. From table 4 and figure 5(b) it is observed that

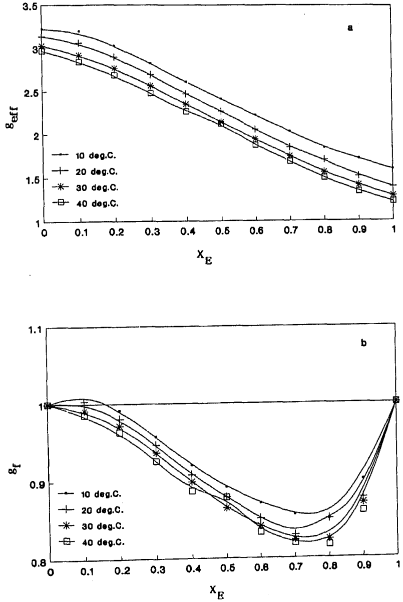

Figure 5. Variation of (**a**) g_{eff} and (**b**) g_f with volume fraction (X_E) of 4-ethylphenol in methanol.

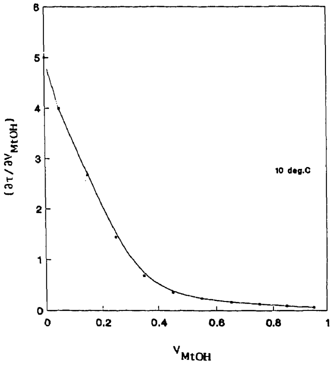

Figure 6. The variation of $(\partial\tau/\partial V_{\mathrm{MtOH}})$ as a function of volume fraction of methanol (V_{MtOH}) for 4-ethylphenol + methanol mixture.

g_f values are less than unity for all compositions and at all temperatures and maximum deviation from unity is observed around 75% of 4EP at all temperatures. This may indicate strong interactions between the molecules of the two components.

In view of the results discussed in the above paragraphs, high relaxation time-τ, negative $(1/\tau)^E$ and high activation energy-ΔH^* in the 4EP-rich region indicate that the effective dipoles in the system may be interacting in such a way that they possess limited ability to reorient. Although both the components of the mixture are associative in nature but the high frequency relaxation of MtOH and low frequency relaxation of 4EP may indicate that the self associating patterns in the two components are totally different. The quantitative trends of the several parameters cited above suggest multimeric structure in the 4EP which breaks down effectively by the addition of MtOH. From figure 6 one can understand the effect of addition of MtOH on the relaxation time in terms of $(\partial\tau/\partial V_{\mathrm{MtOH}})$, the sharp increase in this parameter as (V_{MtOH}) tends to zero indicate strong initial interactions between the molecules of the two components. Similar kind of observation was made by Gestblom and Sjoblom [3, 5] for aqueous solutions of higher alcohols.

According to Bruggeman, static dielectric constants of the mixture and components of the binary mixture can be related to the volume fraction of the solute (4EP in our case) by the following equation [19, 20], assuming an ideal mixture behaviour,

$$f_B = \left[\frac{\varepsilon_{sm} - \varepsilon_{sE}}{\varepsilon_{sM} - \varepsilon_{sE}}\right]\left[\frac{\varepsilon_{sM}}{\varepsilon_{sm}}\right]^{1/3} = (1 - X_E) \tag{9}$$

yielding a linear relationship between Bruggeman factor-f_B and X_E. However, in the present case experimental values of f_B are found to deviate from the linear relationship (figure 7). Several similar observations have been reported [16, 20]. To fit the experimental data the above equation is modified [16] as follows,

$$f_B = 1 - [a - (a - 1)X_E]X_E \tag{10}$$

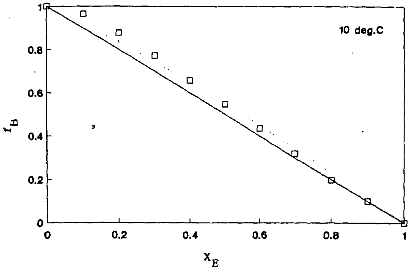

Figure 7. The Bruggeman plot for 4-ethylphenol + methanol mixtures. Open square solid line and dotted curve represent experimental points, original and modified Bruggeman equations respectively.

where a is a numerical fitting parameter and $a = 1$ for an ideal mixture. The values of a are found to be 0·792, 0·820, 0·856 and 0·885 for 10°, 20°, 30° and 40°C respectively. It is found that, the value of a tends to increase towards unity as temperature increases. The value of $a < 1$ indicates that the effective volume fraction of 4EP in MtOH has increased by a factor $[a-(a-1)X_E]$. From figure 7, it can be seen that, the modified Bruggeman equation fits better with the experimental values of f_B than the original Bruggeman equation.

4. Conclusion

Dielectric relaxation parameters, thermodynamic parameters and Kirkwood correlation factor have been reported for 4n-ethylphenol-methanol mixtures for various temperatures and concentrations. These studies suggest that multimeric structure in the 4EP breaks down effectively in the presence of MtOH. The dielectric behaviour of this binary mixture may be better explained by modified Bruggeman equation.

Acknowledgements

Authors thank Prof. G S Raju and Dr P B Patil for helpful discussions. Two of the authors (RHF and MTH) thank University Grants Commission, India for the award of Teacher Fellowship.

References

[1] U Kaatze, M Schhafer and R Pottel, *Z. Phys. Chem. Neue*, **165**, 103 (1989)
[2] R H Cole and D W Davidson, *J. Chem. Phys.* **20**, 1388 (1950)
[3] B Gestblom and J Sjóblom, *J. Acta Chem. Scan.* **A38**, 47 (1984)
[4] A C Kumbharakhane, S M Puranik and S C Mehrotra, *J. Chem. Soc. Faraday Trans.* **87**, 575 (1991)
[5] B Gestblom and J Sjóblom, *J. Acta Chem. Scan.* **A38**, 575 (1984)

[6] R H Cole, J G Barberian, S Mashimo, G Chryssicos, A Burns and E Tombri, *J. Appl. Phys.* **66**, 793 (1989)
[7] S M Puranik, A C Kumbharakhane and S C Mehrotra, *J. Microwave Power and Em. Energy* **26**, 196 (1991)
[8] A C Kumbharakhane, S Doraswamy and S C Mehrotra, *J. Chem. Phys.* **99** 2405 (1993)
[9] S N Helambe, *Ph.D. Thesis*, submitted to Dr Babasaheb Ambedkar University, Aurangabad (India)
[10] R H Fattepur, M T Hosamani, D K Deshpande and S C Mehrotra, *Dielectric relaxation studies of 4n-Propylphenol-Methanol mixture using TDR*" 1994 *J. Mol. Liq.* (Communicated)
[11] M I Aralaguppi, T M Aminabhavi, R H Balundgi and S S Joshi, *J. Phys. Chem.* **95**, 5299 (1991)
[12] S F Al-Azzawi *et al*, *J. Chem. Eng. Data* **35**, 463 (1990)
[13] S Glasstone, K J Laider and H Eyring, *The Theory of Rate Process* (McGraw-Hill, Oxford 1941)
[14] N E Hill *et al*, *Dielectric properties and molecular behaviour* (Van Nost. Reinhold Co., London, 1969)
[15] H Frólhich, *Theory of Dielectrics* (Oxford, London, 1949)
[16] A C Kumbharakhane, S M Puranik and S C Mehrotra, *J. Mol. Liq.* **51**, 261 (1992)
[17] A C Kumbharakhane, S M Puranik and S C Mehrotra, *J. Soln. Chem.* **22**, 219 (1993)
[18] A C Kumbharakhane, S M Puranik and S C Mehrotra, *J. Pure Appl. Phys.* **4**, 1992 (1992)
[19] D A G Bruggeman, *Ann. Phys.* (*Leipzig*) **5**, 636 (1935)
[20] S M Puranik, A C Kumbharakhane and S C Mehrotra, *J. Mol. Liq.* **59**, 173 (1993)

PRAMANA
— journal of
physics

© Printed in India

Vol. 44, No. 1,
January 1995
pp. 45–53

A comparative study of laser second harmonic generation in some crystals

G C BHAR*, A M RUDRA*, P K DATTA*[1], U N ROY[†], V K WADHAWAN[†] and T SASAKI[††]
*Laser Laboratory, Department of Physics, Burdwan University, Burdwan 713 104, India
[†]Crystal Growth Laboratory, Centre for Advanced Technology, Indore 452 013, India
[††]Department of Electrical Engineering, Faculty of Engineering, Osaka University, Yamada-oka, 2-1 Suita, Osaka 565, Japan
*[1] Present address: Centre for Advanced Technology, Indore 452 013, India

MS received 24 May 1994; revised 14 November 1994

Abstract. Comparison of the conversion efficiency for efficient second-harmonic generation of Nd:YAG laser radiation is reported for KDP, LAP, KTP, BBO and LBO crystals. Conversion efficiencies as high as 50% and 46% were obtained for our laboratory-grown KDP and LAP crystals respectively, for power densities well below their damage thresholds.

Keywords. Nonlinear optics; frequency conversion; crystal growth.

PACS Nos 81·10; 42·65

1. Introduction

With the advent of advanced solid state laser technology, laser radiation in the near infrared, with high average power and good beam quality, has become available. Frequency doubling in a nonlinear-optical crystal is a commonly used technique for generating coherent radiation in a frequency regime where direct laser sources do not exist. Second-harmonic generation of Nd:YAG laser radiation has been moderately efficient. Crystals with high conversion efficiencies for second-harmonic generation are desirable in various fields. Since the first generation of the second harmonic of ruby laser radiation in a quartz crystal by Franken *et al* [1] in 1961, the search for crystals with good frequency-conversion properties continues to this day. In this paper we report a comparative study of the energy-doubling efficiency of a number of crystals for Nd:YAG laser radiation. The measurements were carried out at Burdwan University. The crystals investigated are: potassium dihydrogen phosphate (KDP), 1-arginine phosphate monohydrate (LAP), potassium titanyl phosphate (KTP), beta barium borate (BBO), and lithium triborate (LBO). KDP and LAP crystals were grown in our laboratory at Indore, and KTP crystals were grown in our laboratory at Osaka. BBO and LBO crystals were procured from commercial sources.

2. Crystal growth

KDP crystals were grown from aqueous solution by the temperature-reduction method. Analytical grade KDP powder was further purified by repeated crystallization in deionized water of 18 MΩcm resistivity. The crystals were grown from solutions of different *p*H values, ranging from 2·8 to 4·9. At lower *p*H values the crystals were found to be tapered heavily. In order to reduce tapering, the higher *p*H value solutions were used for growing these crystals. At an optimum *p*H the crystals were found to be not only taper-free, but also had minimum growth along **a** and **b** directions. Any further increase in *p*H led to excessive growth in **a** and **b** directions, apart from causing the occurrence of many cracks in the growing crystals. The crystals were grown by reducing the temperature of the solution from ~ 50°C to room temperature at a rate of 0·2° to 0·5°C/day. The temperature stability of the water bath was ± 0·02°C. In order to reduce the presence of inclusions in the growing crystals, different speeds of seed rotation, up to 60 rpm, were tried to find out the optimum rotation range; it was found to be between 20–30 rpm. Small amounts of H_2O_2 were added to the solution to inhibit the growth of microbes, which create scattering centres in the crystals and consequently lower the damage threshold value. We are now growing good quality crystals routinely, with sizes up to $4{\cdot}5 \times 4{\cdot}5 \times 19\,\mathrm{cm}^3$, at growth rates of 2–3 mm/day.

LAP crystals were also grown from aqueous solution by the temperature-reduction method. LAP was first synthesized by dissolving stoichiometric amounts of AR grade orthophosphoric acid and L-arginine in triple-distilled water. The synthesized material was then further purified by repeated crystallization. The purified LAP was then dissolved in freshly prepared triple-distilled water. The crystals were grown in the temperature range ~ 40°C to room temperature. Self-nucleated crystals were used as seed crystals. The seed was rotated in clockwise and anticlockwise directions at a speed between 20–30 rpm. The major problem encountered in the growth of LAP crystals is the growth of fungus in the solution. In order to restrict the growth of fungus, hexane was used by other workers to encapsulate the surface of the LAP solution, as it floats on the surface [2]. This technique is found to be very effective for inhibiting the growth of fungus. But we observed heavy nucleation of LAP crystals at the interface of the LAP solution and hexane, which afterwards fall to the bottom of the growth vessel and continue to grow there, thus reducing the growth rate of the main crystal. Our alternative method of adding H_2O_2 (0.1% by volume) and Hg was found to be very effective in delaying the growth of fungus in the LAP solution. Using this technique, large, clear, LAP crystals of size up to $4{\cdot}5 \times 4{\cdot}5 \times 1{\cdot}6\,\mathrm{cm}^3$ were grown.

Large sized KTP crystals were grown by the top seeded flux method [3, 4]. A furnace of diameter 35 cm and height 50 cm was used. The flux used was $K_6P_4O_{13}(K_6)$. It was prepared by dehydration of a mixture of KH_2PO_4 and K_2HPO_4. The total weight of the charge was ~ 5 kg, placed in a platinum crucible of diameter 15 cm and height 15 cm. The temperature was raised to 950°C. The charge was stirred well with a platinum stirrer for proper mixing of the charge. A seed was then inserted into the solution. It was rotated at 60 rpm in clockwise and anticlockwise directions for intervals of 30 s each. The melt temperature was then lowered at a rate of 3°C/day. Large, inclusion-free KTP crystals of size $\sim 3{\cdot}2 \times 4{\cdot}2 \times 8{\cdot}7\,\mathrm{cm}^3$ were grown after a period of ~ 40 days.

3. Theoretical considerations

Second harmonic efficiency is defined as the ratio of the energy in the second-harmonic beam after it leaves the crystal to the input fundamental beam energy. The conversion efficiency depends on the peak intensity of the incident input beam.

Therefore, to get higher efficiencies, higher input intensities are required. But the damage threshold of the crystal, defined as the maximum possible energy density per pulse which can be impinged on the crystal without inducing damage, limits the use of high input intensities required for high conversion efficiencies. Other factors which help attain high conversion efficiency are: large effective nonlinear coefficient of the crystal, small residual absorption and scattering loss, and favorable phase-matching properties like small temperature sensitivity of birefringence. For a focused Gaussian beam the conversion efficiency η is given by [5]:

$$\eta = \tanh^2\left[\frac{52{\cdot}2 d^2 l T_1^2 T_2 P_1}{n_1^2 n_2 \lambda_1^2}\right]^{1/2} h(\sigma, B, a, \mu, \xi) \tag{1}$$

where $h(\sigma, B, a, \mu, \xi)$ is the focusing correction factor involving crystal absorption, phase-mismatch etc.

Phase-mismatch parameter $\sigma = b\Delta k/2$, b being the confocal parameter.
walk-off parameter, $B = \rho(lk_1)^{1/2}/2$, ρ being the work off angle
absorption parameter, $a = \alpha b/2$; $\alpha = \alpha_1 + \alpha_2/2$
focal position parameter, $\mu = (l - 2f)/l$
focusing parameter, $\xi = l/b$.

The above expression holds only when the crystal is placed within the Rayleigh range of the focused Gaussian beam. When the crystal is placed well away from the Rayleigh range the expression that holds good is given by [6]

$$\eta = \tanh^2\left[\frac{52{\cdot}2 d^2 l^2 F T_1^2 T_2 P_1}{n_1^2 n_2 \lambda_1^2}\right]^{1/2} \tag{2}$$

where F is the correction factor for absorption loss in the crystal, and is given by [6b]

$$F = \frac{(1 - 2e^{-\alpha l/2} + e^{-\alpha l})e^{-\alpha_2 l}}{(\alpha l/2)^2} \tag{3}$$

here $\alpha = \alpha_1 + \alpha_2/2$, and α_i's are the absorption coefficients at wavelengths λ_i's. T_1 and T_2 are the single surface power transmission coefficients at the fundamental and second-harmonic wavelengths respectively. d is the effective nonlinear coefficient. l is the effective crystal length. P_1 is the input power density in units of watt/cm^2.

In the situation when eq. (2) applies, only the divergence of the focused beam limits the conversion. We use a long focal length lens in our experiment and as such the divergence effect does not enter as a major factor in our experimental situation.

For a conversion efficiency less than 10%, (2) simplifies to

$$\eta = \frac{52{\cdot}2 d^2 l^2 F T_1^2 T_2 P_1}{n_1^2 n_2 \lambda_1^2}. \tag{4}$$

4. Experimental

The laser system used for the comparative study of the five crystals is a Q-switched Nd:YAG laser (Spectra Physics DCR-II) with filled-in beam optics, having output at 1064 nm of pulse width 8 ns and energies up to 180 mJ. The laser spectral line

Table 1. Relevant parameters for the conversion efficiency measurement experiments.

Crystal	:	KDP	LAP	KTP	BBO	LBO
Crystal length (cm)	:	3·5	1·6	0·5	0·6	0·5
Distance between lens and crystal (cm)	:	48·0	61·5	unfo-cused	50·0	70·0
Beam radius at the crystal (ω_0:cm.)	:	0·06	0·116	0·15	0·07	0·12
Double refraction (ρ deg.)	:	1·8	2·2	1·0	3·2	0·43
Aperture length (1 cm)	:	3·39	5·35	15·2	2·2	28·3
Effective length (cm)	:	3·39	1·6	0·5	0·6	0·5

width is less than 1·0 cm^{-1}. The divergence of the output beam is less than 0·5 mrad, and the laser is operated at a repetition rate of 10 pps. The diameter of the laser beam is 6 mm.

To improve the energy conversion ratio, a long (100 cm) focal length lens was used to focus the fundamental beam. The distance between the lens and the crystal for the various crystals studied is shown in table 1. Since the distance between the focal point and the crystal is quite large, the Boyd–Kleinman focusing correction (1) is neglected. This introduces a small error in the calculation. However, the double-refraction effect limits the interaction length in the crystal.

Crystals having the following effective lengths, and sufficient transverse extent, were used: KDP 3·5 cm, LAP 1·6 cm, KTP 0·5 cm, BBO 0·7 cm and LBO 0·5 cm. KDP and LAP crystals were used in their as-grown shapes. KTP was of $\theta = 90°$, $\phi = 59°$ cut, BBO was of type-I cut (for SHG of 1064 nm), while LBO was of xyz cut.

To determine the conversion efficiency, we measured the pulse energies of the fundamental and the second harmonic by a pyroelectric energy meter (Scientech make). The vertically polarized Nd:YAG laser beam was weakly focused on the nonlinear-optical crystal being investigated. Type-1 configuration for LAP, BBO and LBO crystals, and type-II configuration for KDP and KTP crystals were chosen for maximum interaction. The xy-plane ($\theta = 90°$) of the LBO and KTP crystals coincided with the laboratory horizontal plane. The effective nonlinear coefficients for these two crystals are:

$$d_{\text{eff}} = d_{32} \cos\phi \quad \text{for} \quad \text{LBO (type-I)}, \tag{5}$$

$$d_{\text{eff}} = d_{31} \sin^2\phi + d_{32} \cos^2\phi \quad \text{for} \quad \text{KTP (type-II)}, \tag{6}$$

Here ϕ is the phase matching angle.

The generated second harmonic was separated from the fundamental by a glass filter having 74% transmission at 532 nm, while blocking completely the 1064 nm radiation. The conversion efficiency was calculated from the measured pulse energies, taking into account the filter transmission loss. The energy of the second-harmonic pulse was measured for fundamental beam pulses of different energies, staying well within the respective damage thresholds of the crystals.

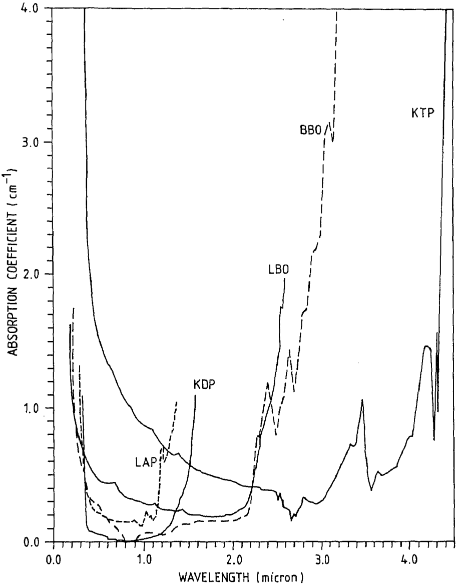

Figure 1. Absorption spectra for 3·5 cm long KDP, 0·7 cm long BBO, 1·6 cm long LAP, 0·5 cm long LBO and 0·5 cm long KTP crystals.

The optical transmission characteristics of the five crystals were measured with a UV–VIS–IR spectrophotometer and are shown in figure 1.

5. Results and discussion

As can be seen from figure 1, KDP, LAP and BBO crystals are of better optical quality than KTP and LBO crystals. The relevant optical parameters of all the five crystals are given in table 2 [7–10]. The phase matching angles are defined with reference to the dielectric polar axis. We have earlier reported efficient (32%) second harmonic generation in BBO by focusing of the laser beam [11]. Data from that study are used for comparison with the results obtained in the present study. Large birefringence of BBO makes its performance highly angle sensitive.

Potassium titanyl phosphate has the widest transparency range, extending from 350 nm to the infrared region. But LBO transmits deep down to 160 nm in the UV region. KTP has the largest nonlinear coefficient of the five crystals investigated.

We compare the measured conversion efficiencies with the calculated values obtained using the measured optical parameters, including transmittance of the

Table 2. Linear and nonlinear optical properties of the studied nonlinear crystals.

Crystal	KDP	LAP	KTP	BBO	LBO
Symmetry	42m	2	mm2	3m	mm2
Transparency (um)	0·2–1·5	0·24–1·3	0·35–4·5	0·19–3·4	0·16–2·6
Damage threshold (GW/cm^2)	1·0	14–19	0·44	8·0	—
Birefringence	0·034	0·07	0·0077	0·113	0·039
Phase-matching angle (deg·)	$\theta = 60·5$	$\theta = 58·8$ $\phi = 15·6$	$\theta = 90$ $\phi = 23$	$\theta = 22·8$	$\theta = 90$ $\phi = 11$
Absorption coefficient (cm^{-1}) at					
1·064 μm	0·02	0·07	0·74	0·07	0·27
0·532 μm	0·05	0·02	1·39	0·26	0·46
d_{eff}(pm/V)	0·33	0·78	5·26	1·72	1·40
ΔT.L(°C.cm)	11·5	11·9	25	55	3·90
ΔA.L(mrad.cm)	0·84	0·53	15–68	1·5	9·0
$\Delta\lambda$.L(Å.cm)	116	11	5·6	9·8	11

crystal, and the beam quality and power density of the laser. The measured efficiency of type I SHG of 1064 nm Nd:YAG laser radiation for LAP, BBO and LBO crystals, and type II SHG for KDP and KTP crystals, is plotted as a function of the power density of the fundamental beam (figure 2). The maximum conversion efficiencies obtained are 50%, 46%, 34%, 24% and 22·4%, for the fundamental power densities 196 MW/cm^2, 143 MW/cm^2, 130 MW/cm^2, 268 MW/cm^2 and 116 MW/cm^2, for KDP, LAP, LBO, BBO and KTP crystals respectively. The solid curves in figure 2 represent the calculated efficiencies, whereas the measured values are shown as dots of distinct character, alongwith the estimated probable errors of measurement. Reflection losses at the crystal surface are accounted for before plotting the experimental points. The agreement between theory and experiment is good at lower power densities, but the two tend to depart considerably at higher power densities. There are several reasons for this: (a) The detailed nature of the mode structure in the focused laser beam is not known. In fact, the raw laser beam is not perfectly Gaussian in nature. (b) The intensity is not uniform in the beam cross section. (c) There are pencil rays in the beam which are nearly completely converted, whereas other pencil rays, notably those near the circumference of the beam, undergo little or no conversion. The situation is aggravated by the anisotropic nature of the medium. (d) Not all directions in a beam of finite aperture can have perfect phase-matching. (e) Local heating of the crystal is a more serious problem at higher power densities, leading to a larger detuning of the phase-matching arrangement. And (f) at high power operation the Nd:YAG laser radiation itself gets somewhat depolarized. Out of the five crystals, LBO shows the maximum deviation in its experimental conversion efficiency as compared to the theoretical counterpart. The LBO crystal used in our experiment is of xyz cut and as such it has to be rotated by a large angle to realise phase-matching for second harmonic generation of 1064 nm radiation, thereby introducing large

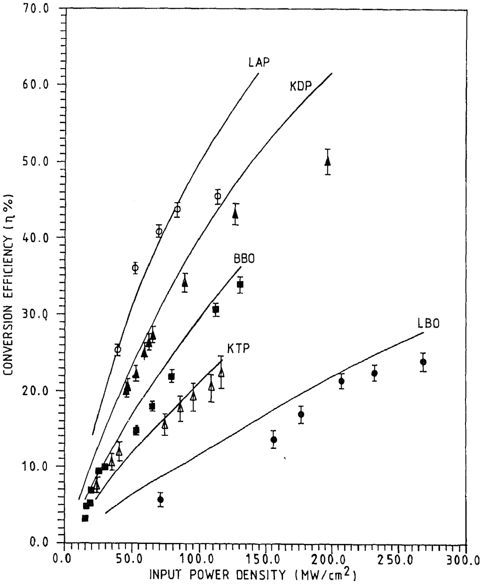

Figure 2. Conversion efficiency for SHG in KDP, LAP, KTP, BBO and LBO crystals as a function of the power density of the input Nd:YAG laser pulses. The smooth curves represent the calculated values.

reflection losses. Secondly LBO is somewhat more temperature sensitive, which may also have enhanced the deviation of experimental values from the theoretical ones. Since the laser beam is not only weakly focused, but also the crystal is placed at a considerable distance from the focal point, the conversion efficiency is expected to be proportional to l^2. Established reported data for second harmonic generation of 1064 nm radiation in these crystals by other authors are reproduced in table 3 for comparison purposes.

Though the effective nonlinear coefficient of KTP is higher than that of other crystals, its conversion efficiency is seen to be rather low. This is because of its larger absorption coefficient, and also because the surface quality of the crystal investigated is not very good, causing considerable reflection of the input beam. By comparison, the as-grown KDP and LAP crystals have good surface quality and a large effective interaction length. These two factors result in higher conversion efficiencies.

For LBO also, because of its smaller effective length and poorer surface quality, the conversion efficiency shown in figure 2 is small, in spite of the fact that it has a higher nonlinear coefficient compared to KDP and LAP.

Table 3. Some selected literature values of conversion efficiency data for second harmonic generation (1064 nm → 532 nm).

Crystal	KDP	KTP	BBO	LBO	LAP
Type of interaction	ooe	eoe	ooe	oeo	ooe
Phase-matching angle, θ_{pm}(deg.)	41	30	22·8	90	—
Input power density I_0(MW/cm^2)	400	100	190	127	—
Pulse width τ_p(ns)	20	30	14	10	—
Crystal length L(mm)	—	8	6	—	—
Conversion efficiency (η%)	30	50	47	60	—
Ref.	[12]	[13]	[14]	[15]	[9]

The damage threshold of four of the crystals (KDP, LAP, BBO and KTP) for Q-switched Nd:YAG laser radiation was measured to be about 1·0 GW/cm^2, 14–19 GW/cm^2, 8 GW/cm^2 and 440 MW/cm^2 respectively.

Damage threshold puts a practical upper limit on the use of higher energy pumping for obtaining higher conversion efficiency. At high intensities, the crystals are damaged either on the surface or within the bulk. Our studies were for surface damage threshold (although for KTP bulk damage was also observed). Surface damage is said to occur if, on irradiation, a pit is visible on the surface [16].

Damage threshold in transparent dielectrics is influenced by a wide range of material properties, preparation and handling techniques, and variations in the laser pulses. Our damage threshold values are somewhat lower than those reported in the literature. This probably reflects the poorer surface quality of the crystal specimens investigated.

6. Conclusions

Our study indicates clearly the superior capability of the laboratory-grown KDP, LAP and KTP crystals for efficient second-harmonic generation of 1064 nm laser radiation. Frequency-conversion efficiency is a multiparameter problem. A high value of the nonlinear optical coefficient cannot be the sole consideration in practical situations. Cost of production, as well as the effort required for growing large, high optical quality crystals are some of the other important considerations.

Acknowledgements

Authors acknowledge Directorate of Aeronautics (R & D) for partial financial support. One of the authors (AMR) acknowledges the CSIR for a maintenance fellowship. We are also thankful to Dr D D Bhawalkar for his useful suggestions and guidance.

References

[1] P A Franken, A E Hill, C W Peters and G Weinreich, *Phys. Rev. Lett.* **7**, 118 (1961)
[2] G Dhanaraj, T Sripathi and H L Bhat, *J. Cryst. Growth*, **113**, 456 (1991)
[3] A Miyamoto, T Sasaki and S Nakai, *Rev. Laser Engg.* (*Japan*) **20**, 86 (1992)
[4] T Sasaki, *Rev. Laser Engg.* **20**, 207 (1992)
[5] G D Boyd and D A Kleinman, *J. Appl. Phys.* **39**, 3957 (1968)
[6a] C L Tang (Ed.), *Methods of experimental physics – quantum electronics*, (Academic Press, New York, 1979) vol. 15 Part B
[6b] R L Aggarwal and B Lax, *Nonlinear infrared generation* edited by Y R Shen (Springer Verlag, 1977) p. 29
[7] D Eimerl, L Davis, S Velsko, E K Graham and A Zalkin, *J. Appl. Phys.* **62**, 1968 (1987)
[8] D Eimerl, *Ferroelectrics* **72**, 95 (1987)
[9] D Eimerl, S Velsko, L Davis, F Wang, G Loiakono and G Kennedy, *IEEE J. Quantum Electron.* **25**, 179 (1989)
[10] J D Bierlein and H Vanherzeele, *J. Opt. Soc. Am.* **B6**, 622 (1989)
[11] G C Bhar, S Das and P K Datta, *Phys. Status Solidi* **A119**, K173 (1990)
[12] Walter Koechner, Solid State Laser Engineering (2nd Edn) (Springer Verlag, 1988) p. 502
[13] T A Driscoll, H J Hoffman, R E Stone and P E Perkins, *J. Opt. Soc. Am.* **B3**, 683 (1986)
[14] R S Adhav, S R Adhav and J M Pelaprat, *Laser focus* **23**, 88 (1987)
[15] J T Lin, J L Montgomery and K Koto, *Opt. Commun.* **80**, 159 (1990)
[16] H Kildal and G M Iseler, *Appl. Opt.* **15**, 3062 (1976)

PRAMANA
— journal of
physics

© Printed in India

Vol. 44, No. 1,
January 1995
pp. 55–66

Dynamics of a collisional ion sheath

S MUKHERJEE and P I JOHN
Institute for Plasma Research, Bhat, Gandhinagar 382 424, India

MS received 23 September 1994

Abstract. Experiments on collisional ion sheaths are carried out by applying a pulsed negative bias on a disc electrode immersed in a collisional plasma. The pulse is characterized by a linear rise, followed by a constant voltage phase and then exponential decay. The measured currents to the electrode are compared to predictions from a dynamic collisional ion sheath model which is developed from the basic two fluid equations. The parameter determining the degree of collisionality is also defined. The agreement between the two in the rising and the flat top phases of the pulse is found to be good. Some residual discrepancies as well as the disagreement in the decay phase are discussed.

Keywords. Collisional ion sheaths; constant mean free path; dynamic collisional sheath thickness; secondary electron emission.

PACS No. 52·40

1. Introduction

The dynamics of collisional ion sheaths is receiving increasing attention these days. Several recent experiments [1–3] have demonstrated that more analysis of the collisional sheaths are required. The essential feature that makes the study of collisional dynamic ion sheaths interesting is that the ions in the sheath cannot get the entire energy from the field. A significant portion of the energy is lost by collisions with the neutrals. The validity of using a quasistatic Child's law when the sheath is in evolution is therefore not justified and there exists a need to derive a proper dynamic collisional law.

On the other hand, the dynamics of collisionless sheaths has been extensively studied, partly due to its importance in many applications [4–10]. For example, in plasma immersion ion implantation (PIII) [4], which is a relatively new and non-line-of-sight technique for surface modifications of materials, the collisionless sheath plays a crucial role in accelerating the ions and getting them implanted. Some features are common to both collisional and collisionless sheaths [10, 11]. In both the cases the current demanded by the electrode is given by sheath expansion. This exposes more ions to the potential and permits them to respond to it.

At lower operating pressures (10^{-4} torr) [4–10] the mean free path of ion neutral collisions is generally larger than the typical sheath dimensions making the sheath essentially collisionless. Among the ion neutral collisions that take place in the sheath, charge exchange collisions have the highest cross section. Also for a large energy range their cross sections remain fairly constant [1–3, 11]. Collisional sheath experiments are carried out at higher pressures (~ 50 m torr) which makes the mean free path of ion neutral collisions smaller than the sheath dimensions. Hence an ion may lose a significant portion of its energy by collisions, before reaching the electrode.

In this paper we report on experiments, carried out on a disc electrode immersed in a collisional plasma, and to which a negative pulse is applied. The negative pulse is characterized by a linear rise time, followed by a flat top phase and an exponential decay. The current collected by the electrode during the pulse duration is measured. The measured currents are compared to the prediction from a theoretical model. The model is developed from the fluid equations with the inclusion of appropriate collisional terms to permit the study of collisional sheaths. The model is found to yield generally good results in the rising and the flat top phase of the pulse. The small residual discrepancies as well as the disagreement during the decay region are discussed in terms of the shortcomings of the model.

2. Experimental set up

The experiments are performed (figure 1) in a cylindrical chamber made of stainless steel of diameter 50 cm and length 120 cm. The chamber is pumped down to $1{\cdot}0 \times 10^{-5}$ torr and is brought to the operating pressure by filling with argon. Two sets of filaments at the ends of the chamber are heated using two separate power supplies. Thermoionic electrons emitted from the filaments are accelerated into the chamber, where they undergo collisions with argon atoms producing a plasma. The filament current and the discharge current can be adjusted to get a uniform plasma in the experimental region. In the pressure range (1–100 mtorr) in which the experiments are carried out, $T_e \approx 3\,\text{eV}$ and n_i can be varied between $1{\cdot}0$–$10{\cdot}0 \times 10^8$ per cc. The ions are assumed to be at room temperature.

In the center of the cylindrical chamber a stainless steel disc electrode of diameter 20 cm is kept with its surface normal to the axis of the chamber. Negative pulses of magnitude 400 V and pulse duration of 12 μs are applied on the disc. The rise time of the pulse is about $1{\cdot}4\,\mu$s and is linear, with a flat top phase of $3{\cdot}6\,\mu$s and an exponential decay with time constant of $2{\cdot}52\,\mu$s (figure 2). The pulse satisfies the criterion that the applied bias is much larger than T_e and each section of the pulse is larger than the ion plasma period. The pulses are produced [12] by discharging a previously charged LC network across the characteristic resistance of the LC line. The drop across the resistance is connected to the disc electrode through a capacitor (figure 3). This arrangement keeps the electrode at the floating potential in the absence of the pulse. The current collected by the electrode is measured by a Pearson current transformer and the current is noted during the entire pulse period. The capacitor also prevents any dc current to flow through the current transformer.

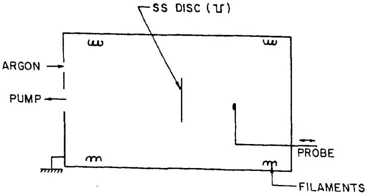

Figure 1. Experimental set up.

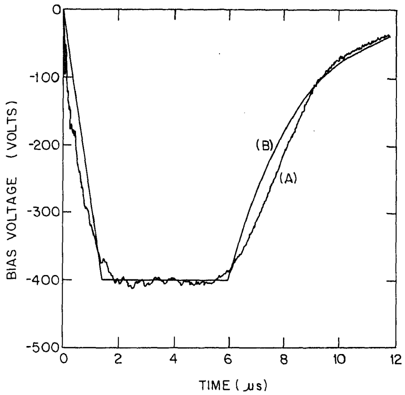

Figure 2. Pulse shapes used in: [A] Experiment [B] Calculation (eq. 15). $\phi_0 = 400\,\mathrm{V}$ and $\tau = 2{\cdot}52\,\mu\mathrm{s}$.

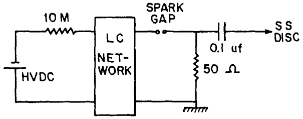

Figure 3. Schematic diagram of the pulse forming circuit.

The experimental current is shown in figure 5 (trace A) and figure 6 (trace A). Both the traces indicate identical overall behaviour. During the rise time of the applied bias the current increases. In the flat top phase the current starts decreasing from its value at the end of the rise time. During the decay phase of the pulse, the current further decreases and becomes negative and then goes to zero at the end of the pulse.

3. Collisional sheath model and its application

For a more quantitative understanding of the experimental results a theoretical model is developed. The model is based on the fluid treatment of the ions and the electrons. We begin with the static model and then extend it to include time evolution so that the dynamics of the ion sheaths can be understood.

3.1 *Derivation of the static collisional sheath model*

The derivation of the collisional sheath model is made by using the fluid equations for the ions and electrons. The electrons are assumed to satisfy a Boltzman distribution. This assumption is valid when the time scales of interest are much longer than the electron plasma time scales. Hence the electron density can be written as,

$$n_e = n_0 \exp(e\phi/kT_e) \tag{1}$$

where e is the electronic charge, k is the Boltzman's constant and T_e denotes the electron temperature. As shown in [3] the dominant collisions in the sheath are ion neutral collisions, specially charge exchange. These collisions are source free, hence conserving ion flux and are also characterized by the property of constant mean free path. We will be restricting ourselves to one dimensional planar calculations. The time stationary ion continuity and momentum equation is

$$\partial_x(n_i v_i) = 0 \tag{2}$$

$$M_i v_i \partial_x v_i = -e\partial_x \phi - M_i n_n \sigma v_i^2 \tag{3}$$

where M_i, v_i, n_i are the ion mass, velocity and density respectively. σ and ϕ are the cross section and potential respectively. Poisson's equation completes the set of model equations, and the self consistent potential in the collisional sheath is obtained

$$\varepsilon_0 \partial_x^2 \phi = -e(n_i - n_e). \tag{4}$$

We make the equations dimensionless by using the following transformations. [$\eta = -e\phi/kT_e, \xi = x/\lambda_d, u = v_i/c_s$ and $\alpha = \lambda_d n_n \sigma = \lambda_d/\lambda_{mfp}$]. The dimensionless set of equations are

$$\eta' = u u' + \alpha u^2 \tag{5}$$

$$\eta'' = u_0/u - \exp(-\eta). \tag{6}$$

The boundary conditions at the sheat plasma interface are at $\xi = 0$, $u = u_0$, $\eta = 0$ and $\eta' = 0$ and at the electrode $\xi = d, \eta = \eta_w$. Equations (5) and (6) have been used before [13]. These nonlinear equations are difficult to solve analytically except in some simpler limits. However it is straightforward to solve them numerically. The numerical

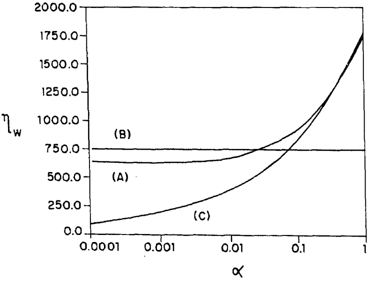

Figure 4. Dependence of η_w (dimensionless wall potential) on α (ratio of debye length to the charge exchange mean free path) for [A] exact equations (eqs 5 and 6) [B] collisionless (eqs 7 and 8) and [C] collisional (eqs 10 and 11). The sheath thickness $d = 100$ debye lengths.

solutions of (5) and (6) are carried out by keeping the sheath thickness fixed but by changing α. Each value of α gives a value of the dimensional electrode potential (η_w) such that a $\xi = 0$, $\eta = 0$. Trace (A) of figure 4 represents the results obtained from this exercise. For low values of α, η_w is independent of α and for $\alpha > 0{\cdot}01$, η_w increases with α. This essentially shows that for the same sheath thickness a collisional sheath can handle more potential difference. Hence the electric fields are stronger in a collisional sheath.

To get the Child's law [13–15], which describes the collisionless sheath, α is set equal to zero and $\eta \gg 1$ limit is taken. The second limit allows us to neglect the contribution of the electrons in determining the potential profile of the sheath. Hence,

$$\eta' = u u' \tag{7}$$

$$\eta'' = u_0/u. \tag{8}$$

Equations (7) and (8) are exactly solvable and gives the dimensionless version of Child's law,

$$\eta \propto \xi^{4/3} \tag{9}$$

By using (9), the value of η_w is obtained, such that at $\xi = 0$, $\eta = 0$, satisfying the boundary conditions. This is shown in trace (B) of figure 4. The η_w obtained from the (7) and (8) are independent of α and for small values of α traces (A) and (B) nearly match. Hence for a collisionless ion sheath and for high electrode bias Child's law is a satisfactory description for the sheath.

As α denotes the degree of collisionality hence for a collision dominated sheath the term containing α will have more contribution in the momentum equation (eq. 5). The limits on α are presented later in this section where this argument holds good. Hence to get the collision dominated ion sheath the term uu' is dropped in (5). The limit $\eta \gg 1$ is also taken and hence the contribution of the electrons is neglected. The equations thus obtained are

$$\eta' = \alpha u^2 \tag{10}$$

$$\eta'' = u_0/u. \tag{11}$$

Equations (10) and (11) are exactly solvable and by using the above boundary conditions the solution is

$$\eta \propto \xi^{5/3}. \tag{12}$$

Again η_w is obtained for various α using (12), such that at $\xi = 0$, $\eta = 0$. This is shown in trace (C) of figure 4. As expected η_w has a strong dependence on α and for α ranging between 0·2 to 1·0 the numerical solutions of (5) and (6) and (12) match. Hence (9) and (10) are a good description for the entire sheath properties and can be used in place of the exact eqs (5) and (6) provided α lies between 0·2 and 1·0 and $\eta \gg 1{\cdot}0$. The limits also indicate the degree of collisionality required to define an ion sheath as collisional. Equation (12) when expressed in non dimensional parameters appears to be

$$J = A\phi^{3/2}/x^{5/2} \tag{13}$$

where J is the current density and $A = \varepsilon_0 (2e\lambda_i/M_i)^{1/2}\ (250/243)^{1/2}$.

Liberman [11] has proposed a collisional sheath model without specifying the degree of collisionality required for it to be valid. Though the dependences of J on ϕ and x are same in his model and our model but there is a difference between the constants by $(2/\pi)^{1/2}$. There [11] the mean ion velocity was obtained by carrying out a time averaging of the ion velocity over the distribution of mean free paths. This averaging was done because the ion motion was governed by the transport laws. In the present model the derivation starts with the fluid equations and the directed motion of ions in the sheath is a consequence of the electric field of the sheath.

3.2 *Derivation of dynamic collisional sheath thickness and the current*

To get the dynamic collisional ion sheath model eq. (13) is used in the quasistatic approximation. This is valid, provided certain assumptions that are made holds good. The assumptions are,

(a) the electron motion is inertialess and hence electrons respond instantaneously to the potential and are driven away
(b) the current required by the bias applied on the electrode at each instant of time is given by the penetration of the sheath plasma interface deeper in the plasma. This exposes more ions to respond to the potential
(c) the transit time of ions in the sheath is faster than the rate of sheath expansion
(d) the pulse time periods are larger than the ion plasma response time scales
(e) the ion motion in the sheath is collisional, with charge exchange being the dominant collision mechanism and hence the collision is characterized by the property of constant mean free path
(f) the quasistatic sheath expands with the sheath plasma interface having the same area as the electrode and also remains parallel to it at all times of evolution.

These assumptions are generally made in dealing with dynamic collisional plasma sheaths [1–3, 11, 16]. We do not put any restriction on the ion density inside the sheath as done by Vahedi *et al* [16]. In their collisional sheath model they have assumed that ion density remains constant inside the sheath which gives a parabolic potential profile inside the sheath. As indicated in (9) and (12), which describe the collisionless and the collisional sheaths, the potential profiles are not parabolic.

On the application of the bias the sheath edge moves with a speed $(\mathrm{d}x/\mathrm{d}t)$ giving a current $= en(\mathrm{d}x/\mathrm{d}t)$. The above assumptions permit us to write,

$$J = A\phi^{3/2}/x^{5/2} = en(\mathrm{d}x/\mathrm{d}t). \tag{14}$$

If the dependence of ϕ on time is known then (14) can be integrated to find out the properties of the dynamic sheath. As the interest is in estimating the current collected in the experiment, $\phi(t)$ should be the experimental pulse (figure 2). The properties of the pulse can be summarized as,

$$\frac{\phi}{\phi_0} = \begin{cases} t/t_r & 0 < t < t_r \\ 1 & t_r < t < t_r + t_p \\ \exp[(-t + t_r + t_p)/\tau] & t_r + t_p < t < t_r + t_p + t_f \end{cases} \tag{15}$$

where t_r, t_p and t_f denotes the rise time, flat top and fall time respectively. τ denotes the time constant during the falling part of the pulse. The current density can be calculated in each phase of the pulse.

3.2.1. For $0 < t < t_r$, $\dfrac{\phi}{\phi_0} = t/t_r$ hence (14) can be integrated with the boundary condition at $t = 0$, $x = 10\lambda_d$. As the electrode is initially floating (figure 3) it is justified in making this boundary condition. Hence,

$$x = [(7A/5en)(\phi_0/t_r)^{3/2} t^{5/2} + (10\lambda_d)^{7/2}]^{2/7}. \tag{16}$$

Equation (16) when substituted in (14) gives

$$J = \frac{A(\phi_0/t_r)^{3/2} t^{3/2}}{[(10\lambda_d)^{7/2} + (7A/5en)(\phi_0/t_r)^{3/2} t^{5/2}]^{5/7}} \tag{17}$$

and

$$x(t_r) = [(7A/5en)(\phi_0)^{3/2} t_r + (10\lambda_d)^{7/2}]^{2/7}. \tag{18}$$

Equation (17) indicates that in an expanding collisional plasma sheath at initial times the current density increases as $t^{3/2}$ whereas at later times it falls as $t^{4/7}$ though the bias applied can still increase linearly at time.

3.2.2. As $\phi/\phi_0 = 1$ for $t_r < t < t_r + t_p$ integration of (14) with the boundary condition at $t = t_r$, $x = x(t_r)$ (given by (18))

$$x = [(7A/2en)(\phi_0)^{3/2}(t - 3t_r/5) + (10\lambda_d)^{7/2}]^{2/7}. \tag{19}$$

The expression for J is,

$$J = \frac{A(\phi_0)^{3/2}}{[(10\lambda_d)^{7/2} + (7A/2en)(\phi_0)^{3/2}(t - 3t_r/5)]^{5/7}} \tag{20}$$

and

$$x(t_r + t_p) = [(7A/2en)(\phi_0)^{3/2}(t_p + 2t_r/5) + (10\lambda_d)^{7/2}]^{2/7}. \tag{21}$$

Though the bias does not change with time during this phase of the pulse the current density indicated by (20) goes on decreasing starting from its value given by $J(t_r)$.

3.2.3. In the third phase $\phi/\phi_0 = \exp[(-t + t_r + t_p)/\tau]$ for $t_r + t_p < t < t_r + t_p + t_f$ integration of (14) can be carried out with the boundary condition, at $t = t_r + t_p$, $x = x(t_r + t_p)$ (given by (21))

$$x = \left[(7A/en)(\phi_0)^{3/2} \left\{ \frac{\tau}{3} + \frac{t_p}{2} + \frac{t_r}{3} - \frac{\tau}{3}\left(\exp\left(\frac{-t + t_r + t_p}{\tau} \right) \right)^{3/2} \right\} + (10\lambda_d)^{7/2} \right]^{2/7}. \tag{22}$$

The expression for J is,

$$J = \frac{A(\phi_0)^{3/2}\left(\exp\left(\frac{-t + t_r + t_p}{\tau} \right) \right)^{3/2}}{\left[(10\lambda_d)^{7/2} + (7A/en)(\phi_0)^{3/2} \left\{ \frac{\tau}{3} + \frac{t_p}{2} + \frac{t_r}{3} - \frac{\tau}{3}\left(\exp\left(\frac{-t + t_r + t_p}{\tau} \right) \right)^{3/2} \right\} \right]^{5/7}} \tag{23}$$

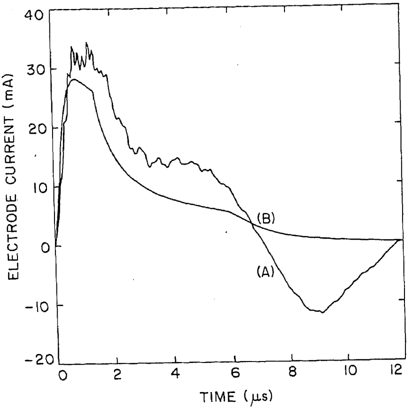

Figure 5. Comparison of the experimental [A] and the model current [B]. $n_i = 4{\cdot}04 \times 10^8\,\mathrm{cc}^{-1}$ and $\alpha = 0{\cdot}21$.

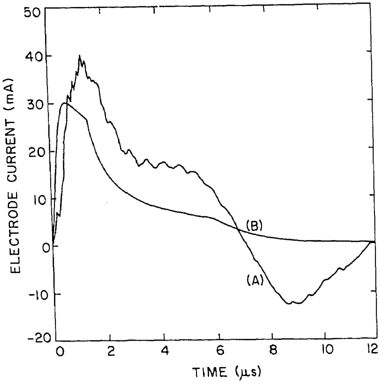

Figure 6. Comparison of the experimental [A] and the model current [B]. $n_i = 8{\cdot}1 \times 10^8\,\mathrm{cc}^{-1}$ and $\alpha = 0{\cdot}35$.

The current further reduces starting from its value at $J(t_p)$ and goes to zero at the end of the pulse.

Thus the expressions for current density and the sheath thickness at each instant of time is known. The calculated current density (eqs 17, 20, 23) is multiplied by the area of the electrode and compared with the measured current obtained from the experiment. The currents predicted by the model are shown in figure (5) (trace B) and figure (6) (trace B).

4. Results and discussion

The experimental conditions ensure that the plasma and the sheath is highly collisional $(0{\cdot}2 < \alpha < 1{\cdot}0)$ so that comparisons can be made between the experiment and the model. In both the figures (5) and (6), during the rising part (0 to $1{\cdot}4\,\mu$s) and in the flat top phase (1·4 to $6{\cdot}0\,\mu$s) of the applied pulse the agreement is good and the model indicates the general trend of the experimental current. In the falling part of the pulse (6·0 to $12{\cdot}0\,\mu$s) the experimental current becomes negative and the agreement with the model is also not satisfactory. The discrepancies during each of these phases of the applied voltage pulse are discussed below.

During the rise time and the flat top phase of the pulse, the current predicted by the model is less than the measured value. It is assumed in the model that the sheath plasma interface always expands having the same area as the disc electrode. This allows us to multiply the current densities obtained from eqs. (17), (20), (23) by the electrode area to get the total current. Experiments done by Malik *et al* [6] has proved that the sheath produced by a planar electrode expands in all directions and is not confined to expand only in one direction. Expansion in other directions will expose more ions to respond to the electrode potential and hence increase the current. The effect of secondary electrons emitted from the electrode by the bombardment of ions can also contribute to the increase in net current. Shamim *et al* [8] has measured the effect of electron emission from the electrode for high negative biases and has shown that the current from the secondary electron emission can be significant.

In the falling part of the pulse (6·0 to $12{\cdot}0\,\mu$s) the experimental current becomes negative and then goes to zero. A negative electrode current during the pulse is observed earlier [1]. The model does not predict the negative current rather the current predicted by the model goes on decreasing from its value at $6{\cdot}0\,\mu$s. The discrepancy during this period can be explained qualitatively as the effect of reduction of the net charge inside the sheath with time. This is happening because the sheath is contracting due to the effect of reduction of the bias. As $(\mathrm{d}Q/\mathrm{d}t)$ is negative, where Q is the charge, the current driven is negative. To quantify this effect one must have the idea of the sheath capacitance. Even during the rise time of the pulse as $(\mathrm{d}Q/\mathrm{d}t)$ is positive, a positive current can be driven. The details of this technique and its feasibility are discussed later. In a recent paper Wood *et al* [17] have shown that when the decay period of the pulse is much slower the current does not go negative. In the experiments performed by us and ref. [1] the decay period is much faster to bring the effect of $(\mathrm{d}Q/\mathrm{d}t)$.

In § 3·1 it is stated that the present collisional sheath model is valid for α ranging between 0·2 and 1·0. At this point we would like to discuss the experiments already carried out [1–3]. Though the approach used there is much similar to ours, i.e., equating the current demanded by the collisional sheath to the current generated by the sheath expansion, the value of $\alpha \ll 0{\cdot}2$. Hence their experiment is carried out in an intermediate range of degree of collisionality, and the sheath cannot be treated as either fully collisionless or fully collisional.

The validity of the limit on α is also checked in the present study. By keeping all the experimental conditions same but by lowering the pressure (10^{-4} torr) the electrode current is measured during the application of the pulse. Though the mean

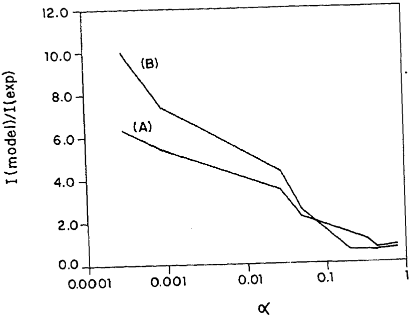

Figure 7. I(model)/I(exp) vs. α at (A) $t = 1{\cdot}4\,\mu$s and (B) $t = 3{\cdot}7\,\mu$s. The value I(model)/I(exp) is approaching unity for $\alpha > 0{\cdot}2$, indicating the validity of eqs (17), (20) and (23) for this degree of collisionality.

free paths are much larger than λ_d at this pressures still eqs (17), (20) and (23) are used to calculate the current. The previous calculations indicate that eqs (17), (20) and (23) are valid for $0{\cdot}2 < \alpha < 1{\cdot}0$. So for $\alpha < 0{\cdot}2$, the following equations is not a right description of the sheath dynamics. For lower pressures (10^{-4} torr), $\alpha \ll 0{\cdot}2$, the above equations are still used so as to indicate the range of applicability of the entire approach. At a given time, the ratio of the current predicted by the model (I_{model}) and measured current (I_{exp}) for various α is plotted in figure 7. Figure 7 indicates, that for small values of α the model is not a good description of sheath dynamics because the model predicts a current much larger than that measured in the experiment. But for $\alpha \geqslant 0{\cdot}2$, the agreement between the model and the experiment is good. Ideally for $\alpha \geqslant 0{\cdot}2$, ($I_{\text{model}}/I_{\text{exp}}$) should be unity. But it is less than unity because of the discrepancies already discussed earlier. Hence the limit on α discussed in § 3·1 is valid.

In the modeling of plasma source ion implantation and collisionless ion sheath dynamics, Wood [10] has proposed an alternate current calculation technique. The same technique can be extended for collisional ion sheath dynamics for better agreement in the experimental and model currents. The dynamic sheath plasma interface, which is at plasma potential, and the biased electrode can act as the two electrodes of a capacitor. As the interface moves in the plasma because of the current requirements of the target the entire phenomenon can be viewed as a change in net charge content in the sheath. Hence,

$$I = \mathrm{d}Q/\mathrm{d}t = C\mathrm{d}V/\mathrm{d}t + V\mathrm{d}C/\mathrm{d}t. \tag{24}$$

When the flow of ions is planar and satisfy Child's law (eq. 9) Bull [18] has shown that $C \approx 2\varepsilon_0 \times (\text{area})/x$, where x is the distance between the electrode and the sheath plasma interface and area denotes the area of the electrode. For a collisional ion sheath the value of sheath capacitance is yet to be found out.

Equation (24) thus gives the current for the dynamic sheath and it is possible to give a qualitative picture of the sheath dynamics at each phase of the pulse. During the rise time $(\mathrm{d}V/\mathrm{d}t)$ is positive but $(\mathrm{d}C/\mathrm{d}t)$ is negative as the sheath thickness is increasing. A competition between $(C\mathrm{d}V/\mathrm{d}t)$ and $(V\mathrm{d}C/\mathrm{d}t)$ exists, but as C is a secondary effect of sheath expansion, $(V\mathrm{d}C/\mathrm{d}t)$ will be less than $(C\mathrm{d}V/\mathrm{d}t)$ and the current will increase. In the flat top phase of the pulse $(\mathrm{d}V/\mathrm{d}t)$ is zero, but the sheath expands and hence the current reduces from its value at the end of the rise time of the pulse, and this can be given by $(V\mathrm{d}C/\mathrm{d}t)$. In the decay phase of the pulse, $(C\mathrm{d}V/\mathrm{d}t)$ is now negative but $(V\mathrm{d}C/\mathrm{d}t)$ is positive. As $(\mathrm{d}V/\mathrm{d}t)$ is larger during the initial part of the decay phase the current is driven negative from where it goes to zero as all time derivatives vanish. The difficulty in this entire technique is a right estimation of the dynamic capacitance when the sheath is collisional. Our ignorance of the value of the capacitance makes us unable to use this technique.

5. Conclusion

An experiment is performed by giving a pulsed negative bias on a disc electrode immersed in a collisional plasma. The pulse is characterized by a linear rise time followed by a flat top phase and then an exponential decay. A collisional sheath model is developed using the fluid equations and the limits on the degree of collisionality are found when this model is valid.

The model is further extended to study the dynamic evolution of a collisional ion sheath using the actual pulse shapes of the experiment. The effort is to explain the entire current profile. A good agreement is seen between the measured and the model current during the rise time and flat top phase of the pulse. In the falling part of the pulse the agreement is not satisfactory because of the exclusion of the role played by the negative rate of change of net charge in the sheath $(\mathrm{d}Q/\mathrm{d}t)$. The residual discrepancies can be due to expansion of the sheath in other dimensions, secondary electron emission from the electrode by ion bombardment. An alternate current calculation scheme based on the concept of an expanding capacitor is also discussed. Presently efforts are made to estimate the value of the capacitance in the collisional ion sheath so that the alternate current calculation scheme can be implemented.

It is necessary to have a brief discussion regarding the merits and shortcomings of the model. Firstly the model is valid for a very small range of α, from 0·2 to 1·0, as indicated in figure 4. It cannot be extrapolated to lower values of α, because the convective term (uu') begins to give its contribution in the ion momentum equation. This model is valid for one dimensional planar sheath expansion and that too without the contribution of the secondary emitted electrons. In an experiment the sheath expands in all the directions and secondary electrons are also emitted, and both the processes enhances the current. In spite of its shortcomings and restricted region of application, the model has one merit, it is closer to the measured current by a factor less than 10%. This is of great help is plasma processing, where a prior knowledge of the electrode current and the corresponding sheath dynamics, helps in designing the power supplies, in deciding the spacing between target electrodes, etc.

Acknowledgements

The authors would like to thank Prof. A Sen, Dr H Ramchandran and Dr R Singh for useful discussions and suggestions.

References

[1] S Qin, C Chan, N E McGruer, J Browning and K Warner, *IEEE Trans. Plasma Sci.* **19**, 1272 (1991)

[2] S Qin and C Chan, *IEEE Trans. Plasma Sci.* **20**, 569 (1992)

[3] S Qin, C Chan, J Browning and S Meassick, *J Appl. Phys.* **74**, 1548 (1993)

[4] J R Conrad, R A Dodd, F J Worzala and X Qiu, *Surface and Coatings Technology* **36**, 927 (1988)

[5] M Shamim, J T Scheuer and J R Conrad, *J. Appl. Phys.* **69**, 2904 (1991)

[6] S M Malik, R P Fetherson, K Sridharan and J R Conrad, *Plasma Sources Sci. Technol.* **2**, 81 (1983)

[7] J T Scheuer, M Shamim and J R Conrad, *J. Appl. Phys.* **67**, 1241 (1990)

[8] M M Shamim, J T Scheuer, R P Fetherson and J R Conrad, *J. Appl. Phys.* **70**, 4756 (1991)

[9] R A Stewart and M A Liberman, *J. Appl. Phys.* **70**, 3481 (1991)

[10] B P Wood, *J. Appl. Phys.* **73**, 4770 (1993)

[11] M A Liberman, *J. Appl. Phys.* **65**, 4186 (1989)

[12] F B A Frungel, in *High Speed Pulse Technology* edited by F B A Frungel (Academic Press, New York, 1965) Vol. 1, p. 234

[13] T E Sheridan and J Goree, *Phys. Fluids* **B3**, 2796 (1991)

[14] F F Chen, in *Introduction to Plasma Physics* edited by F F Chen (Plenum, New York, 1974) p. 248

[15] T E Sheridan and J A Goree, *IEEE Trans. Plasma Sci.* **17**, 884 (1989)

[16] V Vahedi, M A Liberman, M V Alves, J P Verboncoeur and C K Birdsall, *J. Appl. Phys.* **69**, 2008, (1991)

[17] B P Wood, I Hennins, R J Gribble, W A Reass, R J Faehl, M A Nastasi and D J Rej, *J. Vac. Sci. Technol.* **B12**, 870 (1994)

[18] C S Bull, *Proceedings of the Institution of Electrical Engineers* **B104**, 374 (1957)

PRAMANA
— journal of
physics

© Printed in India

Vol. 44, No. 1,
January 1995
pp. 67–76

Instrumentation for beam-foil spectroscopic studies in the UV-visible region

TAPAN NANDI, V NANAL, W A FERNANDES, C A DESAI, M B KURUP, K G PRASAD, P M R RAO* and S PADMANABHAN*
Tata Institute of Fundamental Research, Homi Bhabha Road, Bombay 400005, India
*Spectroscopy Division, Bhabha Atomic Research Centre, Bombay 400085, India

MS received 19 August 1994

Abstract. A facility for carrying out beam-foil spectroscopic studies in the UV and visible region using the 400 kV electrostatic ion accelerator at Tata Institute of Fundamental Research, Bombay is described.

Keywords. Beam-foil spectroscopy; mean lifetimes; relative excitation function; IR telemetry; ion accelerator.

PACS No. **32·70**

1. Introduction

The 400 kV positive ion accelerator [1] was recently re-installed at the Tata Institute of Fundamental Research with many modifications to improve its operation for various experiments like Beam-Foil Spectroscopy (BFS), Rutherford Back Scattering (RBS) and channeling, inner shell ionization, ion implantation, etc. Three beam lines have been installed to facilitate these measurements. The full operation of the accelerator is controlled by an infrared (IR) telemetry system designed and built indigenously. An inclined plate electrostatic deflector is used to direct the beam into any of the three beam lines. One of the beam lines is dedicated for BFS to study the properties of excited electronic states in atoms and ions [2]. In this paper we describe in detail the BFS set up in addition to the 400 kV accelerator and its control system.

In the BFS method, excited levels in neutral and ionized species are created by passing the energetic ion beam through a thin carbon foil. Electrons may be lost or excited during passage of ions through the foil, and additional electrons may be captured while the ions are emerging from the foil. After this electronic rearrangement the ion or atom is frequently left in a singly or multiply excited electronic configurations. Singly excited states may be low or high lying or Rydberg states while multiply excited states lie above the ionization limit. The latter can therefore autoionize. However, many of them are forbidden against autoionization and decay radiatively. Excited states decaying by the emission of photon can be detected using the technique of BFS which is a very useful method to gain insight into the properties of excited levels. The high lying, Rydberg and multiply excited states are not often populated in conventional photon sources. An added advantage is that BFS is suitable for measuring the lifetimes of these wide variety of states in neutral and ionized atoms in 10 ps to 100 ns range in a relatively simple way. This also enables one to measure quantum beats, Lamb shift, etc [2].

2. 400 kV ion accelerator

The schematic diagram of the 400 kV ion accelerator is shown in figure 1. A Neilsen type hot cathode penning ion source [3] is used. This ion source is capable of producing ions both from gaseous and solid materials. In the case of solid materials CCl_4 or Ar is used as a supporting gas. Ions extracted by the extraction electrode (0–30 kV) are focused by an Einzel lens and are then analyzed for isotopic purity by a 90° analyzing magnet, having rigidity of 4000 Gm, before the main acceleration. The maximum acceleration voltage of 400 kV is achieved using the Danfysik high frequency multidoubler type high voltage power supply. The ion source, ion extractor, Einzel lens, the mass analyzing magnet and associated electronics together with the turbomolecular pumping system operate at this terminal voltage. The required AC power to operate these components is provided by a motor-generator set, with the generator floating at the terminal voltage. The motor is coupled to the generator using an insulating PVC shaft.

The pumping system was designed to achieve vacuum better than 1×10^{-5} torr in the entire pre-acceleration region. Three beam lines were set up at 0°, $+12°$ and $-12°$ with respect to the initial beam direction. Using a pair of inclined (8°) electrostatic deflection plates [4] the accelerated beam could be switched to any one of these three lines. The inclined plate geometry was adopted to facilitate larger bending by using comparatively smaller voltages than that required in the case of parallel plates for the same incident beam condition. After acceleration the beam may be focused with the electrostatic quadrupole lens before entering the deflector.

The wireless telemetry system for the 400 kV accelerator is based on infra-red transmitter-receiver diode pair which are robust and readily available. Remote control operation using the infra-red link offers some advantages such as lower spurious radiation and less interference from multiple reflections. The IR telemetry system is

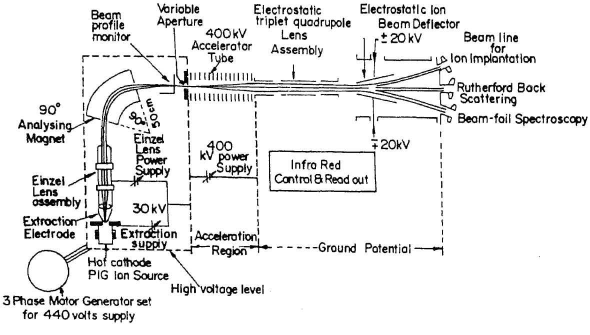
Beam profile monitor
Variable Aperture
400 kV Accelerator Tube
Electrostatic triplet quadrupole Lens Assembly
Electrostatic Ion Beam Deflector
± 20 kV
Beam line for Ion Implantation
Rutherford Back Scattering
Beam-foil Spectroscopy
∓ 20kV
90° Analysing Magnet
90°
50 cm
Einzel Lens Power Supply
400 kV power Supply
Infra Red Control & Read out
Einzel Lens assembly
30 kV
Extraction Electrode
Extraction supply
Acceleration Region
Ground Potential
Hot cathode PIG Ion Source
High voltage level
3 Phase Motor Generator set for 440 volts supply

Figure 1. A schematic diagram of the 400 kV heavy ion accelerator at TIFR. The ion source is kept at 15 kV above the dome potential. Hence its control and read out connections are isolated from the dome using fibre optic cables.

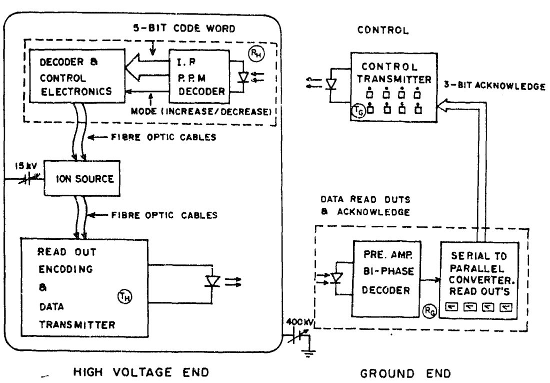
5-BIT CODE WORD
DECODER & CONTROL ELECTRONICS
I. R P.P.M DECODER
R_H
MODE (INCREASE/DECREASE)
FIBRE OPTIC CABLES
15 kV
ION SOURCE
FIBRE OPTIC CABLES
READ OUT ENCODING & DATA TRANSMITTER
T_H
CONTROL
CONTROL TRANSMITTER
T_G
3-BIT ACKNOWLEDGE
DATA READ OUTS & ACKNOWLEDGE
PRE. AMP. BI-PHASE DECODER
SERIAL TO PARALLEL CONVERTER. READ OUT'S
R_G
400 kV
HIGH VOLTAGE END
GROUND END

Figure 2. A schematic diagram of the infra-red telemetry system to control, monitor and optimize the operation of the 400 kV heavy ion accelerator at TIFR.

divided into two parts (figure 2) each consisting of a transmitter and a receiver. The control transmitter at the ground end (T_G) controls the parameters at the high voltage end. The transmitter T_H at high voltage end transmits the set values of parameters to the ground side which are read by the receiver R_G and are displayed on panel meters.

The control transmitter (T_G) operates different parameters through a matrix of switches. Each parameter has been assigned a code word which is transmitted using a Pulse Position Modulated (PPM) code. In PPM code, the time interval between the two pulses is different for '1', '0' and 'stop' bits. The relation between '1', '0', and 'stop' intervals in the transmitted pulse is set to the standard value of 2:3:6. Each code word is 5-bits in length and hence we can control 32 parameters. A carrier of 36 kHz is normally inserted in the 5 bit code word to distinguish between the noise and signal. This word is received at the high voltage end by a PIN photodiode (R_H) where PPM signal is amplified and decoded properly in order to control the particular parameter. The parameters controlled are: ion source filament current, gas pressure, source magnet current, anode voltage, extraction voltage, lens voltage and the analyzing magnet current. The transmitter at the high voltage end (T_H) transmits each parameter (channel) in digital form, having 8 or 12 bits depending on the resolution required. These parameter values are sent in a bi-phase format to eliminate interference from extraneous IR sources. All parameters are sent sequentially and serially along with the Sync word and acknowledge bits using time division multiplexing (TDM). The sync word locks the transmitter and receiver clocks to ensure proper decoding by the receiver. The receiver at ground end separates each channel and displays corresponding parameter on pre assigned meter. The acknowledge bits are decoded to illuminate the appropriate LED on the control panel to indicate the parameter that is being controlled.

3. The beam-foil chamber and spectrometer

The dedicated beam line made of stainless steel for the beam-foil spectroscopic studies consists of a pumping cross with a closed cycle cryopump, a continuously variable double slit collimator and an electrically insulated target chamber which also serves as a deep Faraday cup. The variable collimator (0–100 mm^2) consists of two diamond shaped openings of 1 cm × 1 cm made diametrically opposite to each other on a hollow cylinder of 40 mm diameter. The beam size can be varied by simply rotating this cylinder along its axis which is perpendicular to the beam axis. The beam-foil target chamber is basically a cross of 100 mm diameter tubes. A schematic diagram of the chamber along with the beam line is shown in figure 3. The cross has two 50 mm diameter asymmetric ports perpendicular to the beam axis. This asymmetry facilitates the foil traversal of 80 mm upstream along the beam path for lifetime measurements. One of these two ports has a quartz window to enable light emitted by the excited ions to be transmitted to the spectrometer. At the end of the chamber, there is a NaCl coated glass window which acts as a view port. Because of large scattering angle of ions at low energy [5], the scattered particles can hit the chamber walls easily and consequently the secondary electron suppression becomes very important in charge measurements. Therefore the entire target chamber is isolated from the rest of the beam line and is used as Faraday cup. At the entrance of the chamber there is a provision for electrostatic suppression of secondary electrons. The target holder is mounted from the top of the chamber using Wilson seal arrangement. This target ladder can hold up to ten foils at a time. Special care has been taken in designing the target ladder so that it does not block any light emitted by the excited ions as they emerge from the foil.

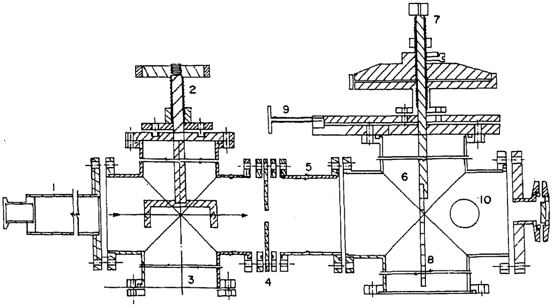

Figure 3. A schematic diagram of a dedicated beam line and the target chamber (not to the scale) for beam-foil spectroscopy experiment in the UV-visible range: (1) a drift tube (2) a variable (0–100 mm^2) collimator, (3) a pumping port for a closed cycle cryopump, (4) electron suppressor, (5) another drift tube as a part of the Faraday cup, (6) the target chamber cum Faraday cup, (7) target manipulator with 3-degrees of freedom, (8) the target ladder capable of holding eleven targets and also avoids shadowing due to the frame, (9) an arrangement for translational movement of the target holder along the beam direction, and (10) quartz window for the light detection.

The target ladder can be tilted to any angle with respect to the beam direction about the vertical axis. Its lateral movement in the vacuum is controlled by a guided screw of a fine pitch with a precision of 0·025 mm. This movement is measured by a vernier scale attached parallel to the beam axis on the top flange. The entire target chamber is evacuated by a cryopump to obtain hydrocarbon free vacuum of the order of 1×10^{-6} torr or better. This has helped greatly in reducing foil deterioration during the measurements. Carbon foils of thickness 4–5 μg/cm^2 were prepared by cracking ethylene gas under DC discharge [6].

Radiation emitted from the ions excited while passing through the foil is recorded in a direction perpendicular to the beam downstream from the foil. A quartz lens is used to focus, with unity magnification, the emitted radiation onto the entrance slit of a 0·45 m monochromator (Pacific precision instruments Co.) having a Czerny-Turner mount as shown in figure 4. This monochromator is equipped with a 1180 grooves/mm grating blazed at 3000 Å having a linear dispersion of 16 Å/mm. The widths of the entrance and exit slits of the monochromator were fixed at 200 μm. The entire optical system was aligned to achieve highest resolution and efficiency. The monochromator was calibrated with standard sources like mercury lamp and iron hollow cathode discharge tube which showed that the system could resolve spectral lines of less than 2 Å separation. The overall resolution of the spectrometer becomes slightly worse when we use the beam foil source. This is caused by the Doppler broadening due to the finite acceptance angle of the spectrometer and second order Doppler shift. The wavelength dispersed photons were detected by a thermo-electrically cooled photomultiplier operated in the single-photon counting mode. The background without the beam was usually about 0·5 count/sec. The relative efficiency of the spectrometer is measured using a mercury lamp and is shown in figure 5. A multichannel scalar (MCS) based on 8085 microprocessor (μP) [7] is used to record the spectrum. The signal from the photon detector is amplified and fed to a pulse height discriminator whose digital output is counted in a 4 stage binary counter. The

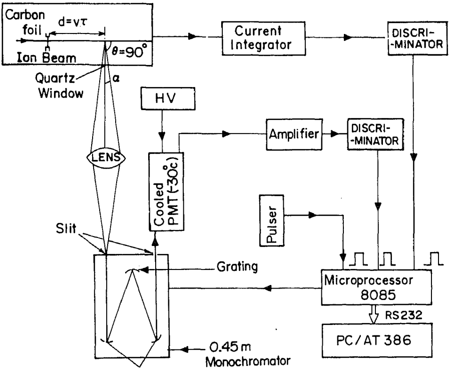

Figure 4. A block diagram of the data processing system for beam-foil spectroscopy experiment in the UV-visible range.

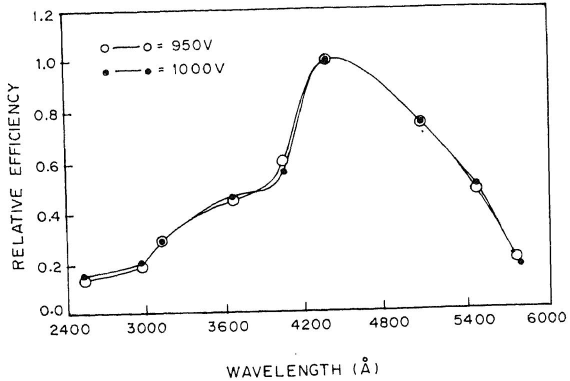

Figure 5. The relative efficiency curve for a spectrometer in the UV-visible range at two different high voltages applied to photo cathode of the photomultiplier tube.

wavelength setting of the monochromator is changed with the help of a built in stepper motor, which also is controlled by the microprocessor. The range of wavelength over which the spectrum is to be recorded, the step size ($\delta\lambda$) and number of normalizing pulses (from the current integrator) for which data is to be collected at each step are supplied as input parameters to the microprocessor. The μP generates a signal to move the motor which in turn changes the monochromator setting by the preset step size $\delta\lambda$. The μP then gives the signal to reset the counter and start the photon counting. The digital output of the current integrator is counted in a separate counter. When this count reaches the preset value, the photon counting is stopped and the reading is stored in the memory. Memory address is then incremented to the next value and the monochromator setting is changed. This process is continued till the final preset value of the wavelength range is reached. While data are being collected at a given setting, the recorded spectrum is displayed on the oscilloscope. The system has the facility for accepting inputs from two detectors. To take care of beam current instability, time taken for data collection at each wavelength is also recorded. This is done by counting pulses from a standard pulse generator and is used for proper background subtraction. The data are then transferred to a PC through RS232 serial link for further analysis.

4. Data collection and analysis

Two typical beam foil spectra one each of Na ions and Ar ions passing through carbon foil are shown in figure 6. The wavelength of the respective lines are indicated in the figure. Further, the charge state of the ion from which the spectral line originates is also shown against each line. It should be noted that lines from a number of ionic states are present in the beam foil spectra. Usually, the charge state of the de-exciting ion can be determined by measuring the excitation function, i.e. by observing the

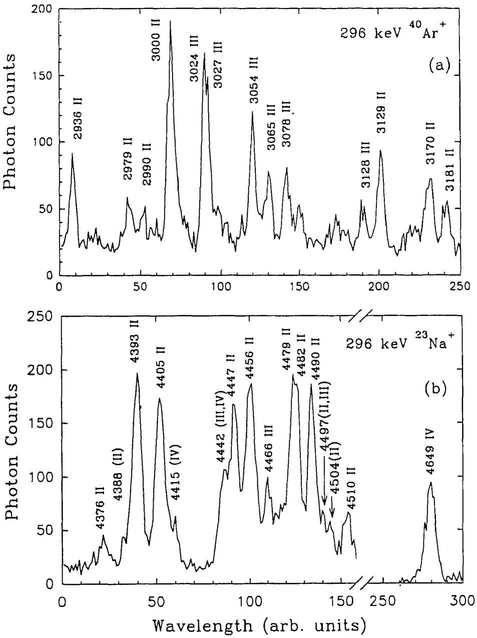

Figure 6. Beam-foil spectra of 296 keV (a) Ar^+ ions in the wave length range 2390–3190 Å/ and (b) Na^+ ions in the wave length range 4360–4660 Å/ and passing through a 5 μg/cm^2 carbon foil. The charge state corresponding to the parent ions from which the transitions take place is shown along side the wavelength.

intensity of the photons as a function of energy of the incident ions. In order to get the excitation function curves, the population N_i of level i, is calculated from the yield S_{ij} of the de-exciting optical transition (from level i to level j) of wavelength λ_{ij} in the usual way from the expression [8],

$$N_i = \frac{4\pi S_{ij} v}{\Omega K_{ij} A_{ij} I \Delta l} \tag{1}$$

where K_{ij} is the quantum efficiency of the detection system for wavelength λ_{ij}, Δl is the width of the observation region (which is kept constant) in the direction of the projectile, Ω is the solid-angle subtended at the monochromator by the effective optical source and I is the incident projectile flux. The velocity v of the projectile after emerging from the foil is estimated from the post foil energy, $E_{\text{postfoil}} = E_{\text{inc}} - E_{\text{loss}}$

(E_{loss} can be estimated from the program TRIM90 [9]), using the following non-relativistic expression

$$v = 0{\cdot}4397(E_{\text{postfoil}}(\text{keV})/M(\text{amu}))^{1/2} \times 10^8\,\text{cm/sec}. \tag{2}$$

The quantity A_{ij} is the transition probability for λ_{ij}. As knowledge of A_{ij} is lacking in many cases, only relative level populations,

$$P_i = S_{ij}v/I \tag{3}$$

have been estimated in our investigation. Further, for comparison, these P_i's are normalized at a certain incident ion energy. A typical relative excitation function curve along with the known relative charge state distribution [10] with incident ion energy is shown in figure 7. It may be seen from this figure that the normalized excitation behaviour closely follows the charge state distribution. This agreement is better for higher ionic states.

For the lifetime measurements the time of flight method is usually used. In this method the distance of the foil from the entrance slit of the spectrometer is varied and the respective photon counts are observed to record an intensity decay curve for extracting the mean lifetime. The data are recorded upto a length for which the

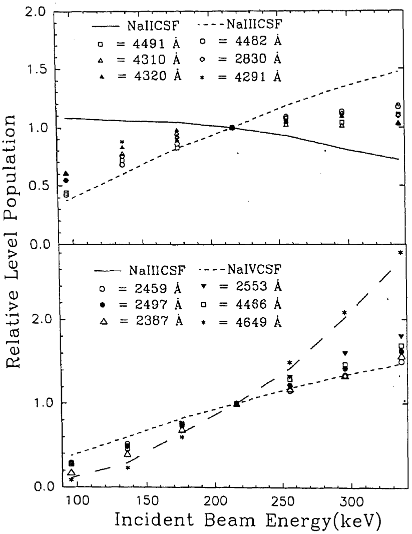

Figure 7. Relative excitation function curves observed for the various transitions from highly excited levels in Na II–IV. The overall uncertainty on each point is about 20%. CSF indicates the corresponding charge state fractions [10].

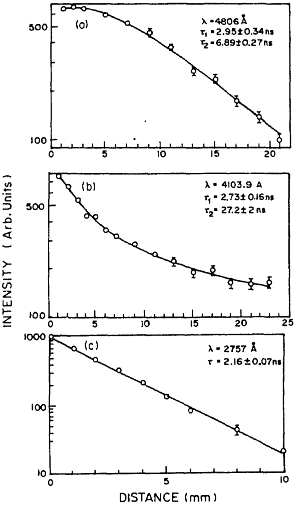

Figure 8. Decay curves for the measurement of lifetimes of (a) $4p^4P_{5/2}$ level in Ar II, (b) $5s^4P_{5/2}$ level in Ar II, (c) $4p^2P^0_{7/2}$ level in Ar IV. The cascading effects are clearly visible in (a) and (b), where τ_2 is the lifetime of the feeding level.

observed counts fall close to the background. The width of the beam-foil light viewed by the spectrometer, dx, should be very small compared to the decay length of a level $v\tau$. As mentioned earlier, this short observation window is obtained by using an adjustable slit at the focal point of a unity magnification optical system. Since in the beam-foil excitation, levels higher than the one that is of the interest can also be populated, the experimentally observed decay curve is usually a sum of several exponentials due to 'feeding in' and 'cascading effects'. However, in most of the cases one to three exponential components give a very good estimate of the primary lifetime. Usually different numerical methods are employed in order to fit a multiexponential function to the experimental decay curve. We have extracted lifetimes by fitting a multi-exponential function using the Levenbery-Marquardt method for non-linear least square fit which is a standard library routine in the CYBER computer at TIFR. Typical time of flight spectra with and without cascading effects are shown in figure 8.

Using this set-up detailed spectroscopic studies in systems like C, Na, Mg and Ar have been carried out [11–14] and many interesting results have been obtained.

5. Acknowledgements

The authors acknowledge Dr G Krishnamurthy for the valuable guidance and discussions while setting up the experimental facilities. One of us (TN) is highly grateful to Dr R G Pillay for his invaluable advice in developing the electrostatic ion beam deflector. Authors are thankful to Mr D C Ephraim for making carbon foils and Central Workshop staff for building all the vacuum components. The help from S S Chauhan at all stages of instrumentation is acknowledged.

References

[1] R P Sharma, *Phys. News* (India) 7, 110 (1976)
[2] I Martinson, *Rep. Prog. Phys.* **52**, 152 (1989)
[3] K O Neilsen, *Nucl. Instrum. Methods* **1**, 289 (1957)
[4] Tapan Nandi, M B Kurup and K G Prasad, *DAE Symp. in Nucl. Phys.* (India) **B36**, 400 (1993)
[5] H G Berry, *Rep. Prog. Phys.* **40**, 155 (1977)
[6] G Dollinger and P Maier-Komor, *Nucl. Instrum. Methods* **A282**, 223 (1989)
[7] Vandana Nanal, M B Kurup and K G Prasad, *DAE Symp. in Nucl. Phys.* (India) **B33**, 323 (1990)
[8] B Andresen, S B Jensen, P S Ramanujam and E Veje, *Phys. Scr.* **20**, 65 (1979)
[9] J F Ziegler and J P Biersack, *The stopping and range of ions in solids* (Pergamon Press, NY 1990)
[10] P Hvelplund, E Laegsgaard, J O Olsen and S E Harris, *Nucl. Instrum Methods* **90**, 272 (1970)
[11] Tapan Nandi, M B Kurup, K G Prasad and P M R Rao, *J. Phys.* **B27**, 1975 (1994)
[12] Tapan Nandi, M B Kurup, K G Prasad, P M R Rao, S Padmanabhan, G Krishnamurthy, and A P Misra, *J. Quant. Spectrosc. Radiat. Transfer* **49**, 389 (1993)
[13] Tapan Nandi, M B Kurup and K G Prasad, *Natl. Conf. on current trends in atomic and molecular physics* (India) CURTAMP **93**, 170 (1993)
[14] B N Rajashekhar, P M R Rao, S Padmanabhan, M Jagdeesh, M B Kurup and K G Prasad, *Natl. Conf. on current trends in atomic and molecular physics* (India) CURTAMP **93**, 172 (1993)

PRAMANA
— journal of
physics

© Printed in India

Vol. 44, No. 1,
January 1995
pp. L77–L83

Gap states in a doped Mott–Hubbard insulator

PRASENJIT SEN, SAURABH BASU and AVINASH SINGH
Department of Physics, Indian Institute of Technology, Kanpur 208 016, India

MS received 4 July 1994

Abstract. Static, non-magnetic impurities give rise to gap states in a doped Mott–Hubbard antiferromagnetic insulator. The spectral and spatial features of these gap states are discussed, and it is argued that these gap states are responsible for the observed local-moment behaviour in zinc-doped cuprates.

Keywords. Doped antiferromagnet; gap state; local moment.

PACS Nos 71·27; 71·55; 75·10; 75·20

1. Introduction

Doping of static, non-magnetic impurities like zinc, gallium, aluminium into the Cu–O plane of superconducting cuprates has recently been studied quite intensively, aimed partly at exploring the fundamental nature of the superconducting state. One of the very intriguing consequences of doping with these non-magnetic impurities is the observed presence of local moments in the Cu–O plane. This was inferred earlier from the Curie–Weiss behaviour of the magnetic susceptibility [1, 2], and has been recently confirmed in the Y-NMR linewidth studies of doped 1–2–3 systems, as seen in the progressively increasing linewidth of the NMR signal with decreasing temperature [3, 4]. The drastic reduction in T_c upon doping with static, non-magnetic impurities which replace Cu from the Cu–O plane is another remarkable effect and it is believed that the suppression in T_c is due to the magnetic pair-breaking effect. While some correlation between the suppression in T_c and the size of the local moment induced in the Cu–O plane has been found [5] quantitative attempts to ascribe the T_c-reduction to conventional magnetic pair-breaking mechanism range from a several-orders-of-magnitude discrepancy [6] to an order-of-magnitude agreement [4].

A Zn^{++} ion with its filled 3d shell replacing a Cu^{++} ion in $3d^9$ configuration eliminates a Cu spin producing a local spin deficiency in the CuO plane, and hence the local moment produced has been discussed in terms of a spin-hole. Such a view of the system as an antiferromagnet (AF) plus a spin-hole at the impurity site is, however, too simplistic in the context of the recent Y-NMR experiments in which the absolute local moment is probed, and which, in fact, seem to indicate the presence of appreciable local moment on Cu sites neighbouring the zinc dopant sites [4]. Obviously a detailed electronic picture of the doped antiferromagnet would be useful.

In this communication we initiate a study of electronic and magnetic properties of the Mott–Hubbard antiferromagnet doped with static, nonmagnetic impurities in terms of a Hubbard model representation for 3d holes. We model zinc-type dopants by high impurity potentials (V) on the dopant sites, to ensure the absence of any 3d hole density on these sites. Focussing on the electronic spectral properties, we find that an impurity produces, in addition to the impurity state at energy near V, a localized state within the *Hubbard gap*. For large V this gap state lies very close to one of the band edges (upper/lower band for positive/negative V), and has a wavefunction which is localized around the dopant site with appreciable amplitude on nearest-neighbour sites, and which falls-off as a power law at large distances. The electron occupying the localized gap state produces a moment in the Cu–O plane with a Curie-type contribution to the total magnetic susceptibility. Electrons in the Hubbard band and in the impurity states form compensated spin systems and therefore contribute (for $T \ll J$) an essentially temperature-independent term to the magnetic susceptibility.

The specific model we consider is a Hubbard model for 3d holes (with two orbitals per site), together with non-magnetic impurity-potential terms, on a square lattice. The results are trivially generalizable to any bipartite, hypercubical lattice in D dimensions. The Hamiltonian is

$$H = -t \sum_{\langle ij \rangle \sigma} (a^{\dagger}_{i\sigma} a_{j\sigma} + \text{h.c.}) + U \sum_{i} n_{i\uparrow} n_{i\downarrow} + V \sum_{I} a^{\dagger}_{I\sigma} a_{I\sigma} \tag{1}$$

where $a_{i\sigma}$ and $a^{\dagger}_{i\sigma}$ are the destruction and creation operators for 3d holes of spin σ at site i, V is the (high) impurity potential and the sum Σ_I is over all impurity sites. We consider a filling with one 3d hole for each Cu site remaining in the system, i.e. relative to the half-filled case for the undoped antiferromagnet with one 3d hole per Cu site, one 3d hole is removed for each zinc-type impurity replacing a Cu from the CuO plane. At this filling the system has no mobile holes and is an insulator.

In the undoped case the quantum antiferromagnetic state of the Mott–Hubbard insulator has been studied in detail within a Hartree-Fock-plus-fluctuations approach, and quantum corrections to sublattice magnetization, spin-wave amplitude and the ground-state energy have been evaluated in the strong coupling limit [7]. In fact a systematic procedure for computing quantum corrections has been developed in terms of an inverse-degeneracy expansion scheme which parallels the $1/S$-expansion for spin-S Quantum Heisenberg AF [8]. Thus a good framework exists for studying the effects of doped static impurities in the AF state.

It must be noted here that for the case of doped *mobile* holes in the antiferromagnet (AF), the Hartree-Fock (HF) approach has serious limitations. A self-consistent procedure results in the added hole being self-consistently trapped into a localized spin-bag state, thereby breaking the translational symmetry of the system. The situation is much simpler with static impurities which do in fact break the translational symmetry, and the HF procedure yields a qualitatively correct description of the ground state with AF order, and a good starting point about which quantum fluctuations in conjunction with impurity scattering can be studied.

We have used two different approaches to study the Hubbard model with doped static impurities within the HF approximation. In one scheme we start with the HF description of the undoped AF as the host, and then treat the impurity terms perturbatively within a Green's function formalism. For a single impurity the perturbation can be treated exactly in terms of the T-matrix formalism. This procedure is not fully self-consistent because density modifications introduced by the high impurity-potential terms are not treated self consistently. We therefore supplement this T-matrix analysis with a fully self-consistent numerical study by exact diagonalization of the

HF Hamiltonian on a square lattice with periodic boundary conditions. These results are summarized at the end and presented in more detail elsewhere [9].

We first discuss briefly results of the T-matrix analysis in the AF state. The HF approximation on the Hubbard model yields our unperturbed Hamiltonian,

$$\langle k|H_0^\sigma|k\rangle = \begin{bmatrix} -\sigma\Delta & \varepsilon_{\mathbf{k}} \\ \varepsilon_{\mathbf{k}} & \sigma\Delta \end{bmatrix}$$

in the two-sublattice basis, with quasiparticle energies $E_{\mathbf{k}\sigma\pm} = \pm\sqrt{\Delta^2+\varepsilon_{\mathbf{k}}^2} \equiv \pm E_{\mathbf{k}}$, and quasiparticle amplitudes $(a_{\mathbf{k}\sigma\pm}\ b_{\mathbf{k}\sigma\pm})$ describing the host system [7]. Here 2Δ is the Hubbard gap, $\varepsilon_{\mathbf{k}}$ the free-particle energy on the square lattice, and the quasiparticle amplitudes are given by, $a_{\mathbf{k}\sigma\pm}^2 = (1 \mp \sigma\Delta/E_{\mathbf{k}})/2$ and $b_{\mathbf{k}\sigma\pm}^2 = (1 \pm \sigma\Delta/E_{\mathbf{k}})/2$. The $\pm$ signs refer to states in the upper and lower Hubbard bands respectively. In terms of quasiparticle amplitudes and energies, the host Green's functions for H_0^σ are given by,

$$g^\sigma(\mathbf{k},\omega) = \left\langle \mathbf{k}\left|\frac{1}{\omega - H_0^\sigma(\mathbf{k})}\right|\mathbf{k}\right\rangle = \sum_s \begin{bmatrix} a_{\mathbf{k}\sigma s}^2 & a_{\mathbf{k}\sigma s}b_{\mathbf{k}\sigma s} \\ a_{\mathbf{k}\sigma s}b_{\mathbf{k}\sigma s} & b_{\mathbf{k}\sigma s}^2 \end{bmatrix} \frac{1}{\omega - E_{\mathbf{k}\sigma s} + is\eta} \tag{2}$$

here s refers to the two signs $+/-$ corresponding to the upper/lower Hubbard band. The Green's function for the single-impurity problem is now given in terms of the T-matrix, $T^\sigma(\omega) = V/(1 - Vg_{II}^\sigma(\omega))$ as

$$G_{ij}^\sigma(\omega) = g_{ij}^\sigma(\omega) + g_{iI}^\sigma(\omega)\, T^\sigma(\omega) g_{Ij}^\sigma(\omega). \tag{3}$$

Information regarding additional poles is contained in the T-matrix, and therefore a study of the local Green's function $g_{II}^\sigma(\omega)$ in the AF state is of the interest. While a detailed analysis of $G^\sigma(\omega)$ will be presented elsewhere [9], the main features are discussed below. If for concreteness we consider the impurity on an A-sublattice site, then using $a_{\mathbf{k}\sigma\oplus}^2 = b_{\mathbf{k}\sigma\ominus}^2$ and also $a_{\mathbf{k}\sigma\ominus}^2 - b_{\mathbf{k}\sigma\ominus}^2 = \sigma\Delta/E_{\mathbf{k}}$, we obtain,

$$g_{II}^\sigma(\omega) = \frac{1}{N}\sum_{\mathbf{k}} \frac{\omega - \sigma\Delta}{\omega^2 - E_{\mathbf{k}}^2}. \tag{4}$$

A plot of $g_{II}^\uparrow(\omega)$ vs ω is given in figure 1 and show logarithmic divergences at energies $\pm\sqrt{\Delta^2 + (4t)^2}$, a stronger divergence $(\omega+\Delta)^{-1/2}\ln(\omega+\Delta)$ as $\omega \to -\Delta$ from above, and a $\sqrt{\Delta - \omega}\ln(\Delta - \omega)$ dependence as $\omega \to \Delta$ from below. The intersection with $1/V$ yields the poles, and for large V we obtain a defect state at energy $V - \Delta$(V relative to the lower band at energy $-\Delta$), and another state inside the Hubbard gap close to the upper band edge. In semiconductor terminology, such gap states arising from defects are referred to as deep traps, and for large V and two similar bands, occur near the mid-gap position. To effect the asymptotic convergence of the trap energy to some fixed position near mid-gap as $V \to \infty$, the concept of pinning has been introduced – large differences in atomic energies influence the trap energies only weakly [10]. The energy separation $\eta \equiv \Delta - E_g$ of the gap state at energy E_g, from the lower edge of the upper Hubbard band is approximately given by $\sqrt{\eta}\ln\eta \sim 1/V$, so that η vanishes essentially as $(1/V)^2$ as $V \to \infty$. For ↓-spin there is only a defect state and no gap state for positive V. For negative V the gap state appears slightly above the band edge of lower Hubbard band, i.e. slightly above energy $-\Delta$.

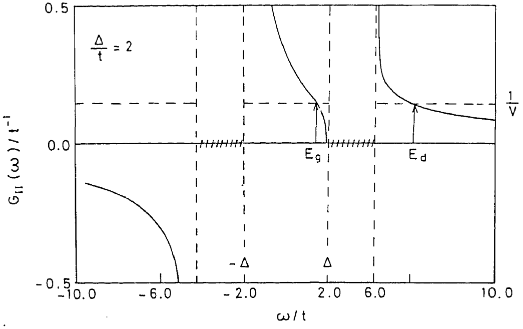

Figure 1. The local host Green's function, $g^{\uparrow}_{II}(\omega)$, in the antiferromagnetic state as a function of ω for regions excluding the two Hubbard bands (shown as hatched). Intersections with 1/V yield gap state (E_g) and the defect state (E_d).

Both the defect state and the gap state, lying as they do outside the AF band, are localized. The defect state is essentially site localized on the impurity sites in the strong coupling limit. The gap-state has amplitude mainly on the B-sublattice site in the strong coupling limit and for large V. In the $V \to \infty$ limit, the gap-state wavefunction goes as $\Sigma_{\mathbf{k}} \varepsilon_{\mathbf{k}}^{-1} e^{i\mathbf{k}.\mathbf{r}}$, which exhibits a power-law fall-off at large distances. From (3) the change in the Green's function, $\delta G_{ij}(\omega) = G_{ij}(\omega) - g_{ij}(\omega)$, due to impurity scattering can be written, for energies outside the band and very close to the gap-state energy, E_g, as:

$$\delta G_{ij}(\omega \sim E_g) = \frac{g_{iI}(E_g)\left[-\left.\frac{\partial g_{II}(\omega)}{\partial \omega}\right|_{\omega = E_g}\right]^{-1} g_{Ij}(E_g)}{\omega - E_g + i\eta} \tag{5}$$

where $g_{II}(\omega)$ has been Taylor-expanded near E_g, and we have used $1 - Vg_{II}(E_g) = 0$ which determines E_g. The above equation can be rewritten in the following form, yielding the gap-state Green's function in terms of $\phi^i_g \equiv g_{iI}(E_g)/\sqrt{-\partial g_{II}(\omega)/\partial\omega|_{E_g}}$, which gives the amplitudes for the gap state,

$$\delta G_{ij}(\omega \sim E_g) = \frac{\phi^i_g \phi^j_g}{\omega - E_g + i\eta}. \tag{6}$$

We now examine the nature of the gap-state wavefunction, $\phi_g(\mathbf{r})$ where $\mathbf{r} \equiv \mathbf{r}_i - \mathbf{r}_I$ is the relative positive vector. $\phi^{\uparrow}_g(\mathbf{r})$ is proportional to $g^{\uparrow}(\mathbf{r}, \omega = E_g)$ and, for site i belonging to the A-sublattice, is therefore given by,

$$\phi^{\uparrow}_g(\mathbf{r}) \sim \frac{1}{N} \sum_{\mathbf{k}} \frac{E_g - \Delta}{E_g^2 - E_{\mathbf{k}}^2} e^{i\mathbf{k}.\mathbf{r}} \tag{7}$$

In the large V limit, as $V \to \infty$, the gap-state wavefunction therefore has vanishingly small amplitudes on A-sublattice sites as $E_g \to \Delta$ in this limit. A similar analysis, with use of the identity $a_{\mathbf{k}\uparrow\ominus} b_{\mathbf{k}\uparrow\oplus} = \varepsilon_{\mathbf{k}}/2E_{\mathbf{k}}$, shows that on B-sublattice sites the gap-state wavefunction is given by,

$$\phi_g^{\uparrow}(\mathbf{r}) \sim \frac{1}{N} \sum_{\mathbf{k}} \frac{\varepsilon_{\mathbf{k}}}{E_g^2 - E_{\mathbf{k}}^2} e^{i\mathbf{k}.\mathbf{r}} \qquad (8)$$

Again, in the large V limit, as $E_g \to \Delta$, the gap-state wavefunction is given by $\phi_g(\mathbf{r}) \sim \Sigma_{\mathbf{k}} \varepsilon_{\mathbf{k}}^{-1} \exp(i\mathbf{k}.\mathbf{r})$. At large x and y distances, the long-wavelength modes contribute predominantly, and this yields a power-law fall-off, $\phi_g(\mathbf{r}) \sim 1/xy$.

We believe that these gap states which are occupied with electrons and localized around the impurity sites are responsible for the presence of local moments observed in these systems. For a zinc atom sitting on an A-sublattice site, the gap state is occupied by an $\uparrow$-spin electron. In terms of electrons, the dopant site is occupied by two electrons (empty of holes), and there are $(N-1)$ $\uparrow$-spin and $\downarrow$-spin electrons in the antiferromagnetic band states (in the upper Hubbard band). These electrons form compensated spin systems, and therefore should contribute an essentially temperature-independent (for $T \ll J$) magnetic susceptibility. The lone electron in the localized gap state behaves essentially like a free spin in the dynamical state when there is no barrier between the up and down spin states, and hence should have a Curie-type $1/T$ contribution.

Such a magnetic behaviour has been well established in zinc-doped cuprates in cases where local AF order is present [1,2], as has been the observation that the local moments responsible for the paramagnetic behaviour are present predominantly on Cu sites neighbouring the dopant site [4].

All these results regarding the defect and gap states obtained via the T-matrix approach as described above have been verified using a fully self-consistent numerical study of the AF system on a finite lattice. It becomes clear that the response of the host (AF) system to the insertion of the impurity is a higher-order correction. In this unrestricted Hartree-Fock approach the HF Hamiltonian with the impurity-potential term is diagonalized exactly on a finite lattice with periodic boundary conditions, and local spin densities evaluated to update the HF Hamiltonian, and the procedure is iterated till self-consistency is obtained. In this study density modifications caused by the high impurity potential are allowed and treated self-consistently. Detailed results of this study are presented elsewhere [9].

We now qualitatively discuss effects of additional doping with holes in the static-impurity-doped antiferromagnet. Each gap state produced by the static impurity can trap one added hole into the localized state, and an added hole going in the gap state will, at the HF level, remove the local-moment associated with the gap state. However, fluctuations – both thermal as well as quantum – will result in some spectral weight of electrons in the gap states, and hence the local moments will persist even with additional holes. With further addition of holes the situation is not very clear as the exact nature of the ground state of the Hubbard model away from half-filling is itself not unambiguously known at present. Long-range AF order is believed to be destroyed efficiently by hole doping, and the qualitative picture that is emerging is that the added holes from states with vanishingly small Fermi-liquid-type coherent weight and a predominantly incoherent spectral function. This qualitative picture is presented solely to suggest that the mobile holes in a doped Mott–Hubbard system do see the presence of local moments produced by gap states.

The situation is relatively simpler within the three-band picture of cuprates, with a predominantly oxygen-like band lying between the two predominantly copper-like Hubbard bands. The gap states in this case are still expected to be close to the upper Hubbard band. Added holes go in the oxygen-like band which is well below the upper Hubbard band, and therefore, the local moment formation due to the gap states is robust with respect to additional hole doping in this case – even at HF level.

Coming now to the dynamics of the local moments formed by the occupied gap states, it is clear that when long-range AF order exists, which is frozen in time the local-moment direction is also fixed, and the system should hence resemble a spin glass with frozen moments. With long-range AF order destroyed by the mobile holes, the local-moment direction fluctuates in time following the local staggered-magnetization direction, and therefore the local moment behaves, over times scales long compared to the dynamical time scale of the fluctuating local order, as a free spin. Therefore in the dynamical, spin-disordered state with fluctuating local order, the local moment associated with the gap state should yield a Curie-type susceptibility.

In conclusion, static, non-magnetic impurities have been shown to give rise to gap states in addition to defect states in a Mott–Hubbard antiferromagnet. The gap states are pinned at the band edges. The gap-state wavefunction falls-off as a power-law away from the dopant site. Electrons occupying gap states are argued to be responsible for the local-moment behaviour observed in systems such as zinc-doped cuprate antiferromagnets. The local-moment distribution is predominantly on sites neighbouring the dopant zinc sites, as has been seen in recent Y-NMR studies [4]. The local-moment associated with the gap states should also be present within the three-band Hubbard model of copper-oxides, even after doping with mobile holes. It should therefore be of interest to examine the scattering of carriers and of superconducting pairs off these local moments, and to see whether any enhancement in pair-breaking results from their extended size. Recent quantitative attempts to correlate the reduction in the superconducting transition temperature with impurity concentration within standard Abrikosov's pair-breaking theory have ranged from complete disagreement [6] to order-of-magnitude agreement [4]. An RPA-level study of spin-wave spectral properties is currently under progress. Self-energy corrections to the spin-wave propagator due to impurity scattering should be of interest for studying the magnetic dynamics in doped antiferromagnets due to thermal excitation. Such an analysis, with interlayer coupling and anisotropy effects appropriately included, will be useful for a quantitative understanding of the Néel-temperature variation of cuprate antiferromagnets with (zinc) doping concentration [11, 12].

Acknowledgement

Helpful conversations with V A Singh are gratefully acknowledged.

References

[1] C S Gee *et al*, *J. Superconductivity* **1**, 63 (1988)
[2] G Xiao, M Z Cieplak and C L Chien, *Phys. Rev.* **B42**, 240 (1990a)
[3] H Alloul, P Mendels, H Casalta, J F Marucco and J Arabski, *Phys. Rev. Lett.* **67**, 3140 (1991)

[4] A V Mahajan, H Alloul, G Collin and J F Marucco, *Phys. Rev. Lett.* **72**, 3100 (1994)
[5] G Xiao, M Z Cieplak, J Q Xiao and C L Chien, *Phys. Rev.* **B42**, 8752 (1990b)
[6] R E Walstedt, R F Bell, L F Schneemeyer, J V Waszczak, W W Warren Jr, R Dupree and A Gencten, *Phys. Rev.* **B48**, 10646 (1993)
[7] A Singh and Z Tešanovic, *Phys. Rev.* **B41**, 11457
[8] A Singh, *Phys. Rev.* **B43**, 3617 (1991)
[9] S Basu and A Singh, 1994 (to be published)
[10] H P Hjalmarsson, P Vogl, D J Wolford, J D Dow, *Phys. Rev. Lett.* **44**, 810 (1980)
[11] S W Cheong, A S Cooper, L W Rupp, B Batlogg, J D Thompson and Z Fisk, *Phys. Rev.* **B44**, 9739 (1991)
[12] B Keimer, A Aharony, A Auerbach, R J Birgeneau, A Cassanho, Y Endoh, R W Erwin, M A Kastner and G Shirane, *Phys. Rev.* **B45**, 7430 (1992)

RAMAN RESEARCH INSTITUTE
LIBRARY
BANGALORE-80.
7 APR 1995

PRAMANA
— journal of
physics

© Printed in India

Vol. 44, No. 2,
February 1995
pp. 85–108

A new computation scheme for triangular quantum billiards

PAOLO BELLOMO
School of Physics, Georgia Institute of Technology, Atlanta, Georgia, 30332-0430, USA

MS received 6 August 1994; revised 26 October 1994

Abstract. A new scheme for computing the eigenvalues and eigenstates of the Laplacian with Dirichlet boundary conditions on arbitrary triangular domains is presented. Its reliability is tested by comparing numerical results with analytical ones whenever possible. The computation of eigenvalues shows a good agreement with analytical results. The procedure is shown to give accurate results also in the case of eigenfunctions computation. Finally, the sensitivity of our scheme to the geometry of the domain is discussed and the algorithm is shown to detect small changes in the shape of the domain.

Keywords. Quantum billiards; spectral statistics; pseudointegrable systems, quantum chaos; eigenvalues computation.

PACS Nos 03·65; 05·45; 41·20

1. Introduction

In recent years the investigation of quantum eigenvalues–eigenstates of classically chaotic quantum systems has attracted much attention. Many (for an extensive set of references see [1]) have tried to identify quantum universalities that can be considered as fingerprints of classical chaos in the fully quantum regime. The numerical quantization of classically nonintegrable systems has been performed using diverse strategies and billiard quantization has become a common ground for computational studies in the field. In fact, classical billiards are capable of showing the whole panoply of dynamical properties: integrability, pseudointegrability, ergodicity (only) and chaos; and the restricted set of triangular billiards encompasses all the properties of the wider category of arbitrary convex polygonal billiards [2]. Billiard quantization has so far been carried out by many authors in many ways: Sinai billiard was quantized by Berry [3] by converting the problem into a band structure one; Bunimovich's stadium [4] was first solved by McDonald and McDonald and Kaufman [5], using the Green function method developed by Riddel [6, 7], and later tackled by Heller [8] who used a superposition of systematically oriented plane waves to represent the eigenfunctions of the laplacian. Cheon and Cohen [9] studied a pseudointegrable approximation to Sinai billiard by replacing the infinite walls of their billiard with a very large, but finite, potential barrier; Biswas and Jain [10] also employed Riddel's algorithm in the quantization of the $(\pi/3)$-rhombus billiard.

The present work describes the quantization of arbitrary triangular quantum billiards. The solution of such a problem is particularly interesting because of the paradigmatic nature of triangular billiards (they can exhibit all the properties including the "A-integrability" concept [11]). Moreover the analytical solutions for the few exactly integrable cases are known (equilateral triangle, half equilateral triangle, half square) and they provide a confidence test for numerical results. Surprisingly enough, in spite of the suitability of triangular billiards for the study of many interesting phenomena such as eigenvalue statistics [1], investigation of scars [8, 12] and the relationship between periodic orbits and quantization [13], to the best of our knowledge no systematic calculation of both their eigenvalues and eigenfunctions exists; the majority of numerical studies of quantum billiard spectra was so far dedicated to the investigation of classically chaotic examples (triangular billiards can be at most only ergodic). Finally, we want to point out that recent experiments in microwave resonators have put triangular quantum billiards within the realm of experimental nonlinear dynamics [14].

It is therefore our intent to give a very detailed account of our solution in the hope of stimulating systematic investigations both of the properties of the spectra of arbitrary triangular quantum billiards and, more specifically, of the characteristics of their eigenfunctions. A first application of the scheme is given in [12, 15]. The same scheme can be also used to solve the problem of a triangular billiard with some non-singular potential. Our numerical scheme is very easy to apply: it is simple and effective; it requires surprisingly small computation times and, as we show in the following paragraphs, it provides very accurate results for the billiard eigenfunctions.

2. Representation of the quantum billiard operator

By a rescaling of the physical constants, the quantum billiard problem can be reduced to the following equation and boundary conditions

$$\begin{aligned} &-\nabla^2\psi(x,y)=\lambda\psi(x,y),\\ &\mathbf{q}\in\partial\mathscr{D}\Rightarrow\psi(\mathbf{q})=0,\\ &\psi(\mathbf{q})\in\mathscr{L}^2(\mathscr{D}),\end{aligned}\tag{1}$$

where $\partial\mathscr{D}$ denotes the boundary of the domain considered. In this paper we refer to the "*quantum billiard operator*" (henceforth denoted QBO) as a shorthand for the operator of Eq. (1). We stress here that the QBO is not merely the laplacian, because the vanishing of the functions on the boundary of the billiard is required (*Dirichlet* boundary conditions). We will indicate the QBO as $-\nabla^2_{\partial\mathscr{D}}$.

The solution presented in this paper makes use of a matrix representation, properly truncated, of the QBO. By a judicious choice of the Hilbert space vectors employed in the construction of the matrix, we were able to take into account the proper boundary conditions (i.e. vanishing of the wave functions on the sides of the triangle) and therefore to construct a *faithful* representation of the QBO. The desired matrix elements are of the form

$$\mathscr{D}_{i,j}=\langle i|-\nabla^2_{\partial\mathscr{D}}|j\rangle,\tag{2}$$

where $|i\rangle$, $|j\rangle$ must be vectors belonging to some complete set of orthonormal functions, $\mathscr{L}^2$-integrable on the domain $\mathscr{D}$ and satisfying the boundary conditions (1). The Hamiltonian operator is linear and real, and the eigenfunctions can always be made real-valued; therefore in what follows we will neglect complex conjugation. The construction of the desired basis vectors is best illustrated in a two-step procedure. We begin by considering the eigenfunctions of the QBO on a unit square [16]

$$\psi^{\text{square}}_{m,n}(x,y)=2\sin(m\pi x)\sin(n\pi y),\tag{3}$$

with m and n being some arbitrary nonzero integers. By antisymmetrization with respect to a diagonal, one can form the eigenfunctions of the QBO on the half unit square domain, i.e. on a $((\pi/4), (\pi/4), (\pi/2))$-triangle, having its $(\pi/2)$ angle vertex sitting in the origin of the frame of reference [16]

$$\psi_{m,n}^{((\pi/4),(\pi/4),(\pi/2))}(x,y) = 2\{\sin(m\pi x)\sin(n\pi y) + (-1)^{m+n+1}\sin(n\pi x)\sin(m\pi y)\}. \tag{4}$$

Indices n and m must obey an additional constraint: $n \neq m$. We now consider the eigenfunctions of the QBO on a rectangle of side lengths a and b respectively [they are a generalization of (3)]

$$\psi_{m,n}^{\text{rectangle}}(x,y) = \frac{2}{\sqrt{ab}}\sin\left(\frac{m\pi x}{a}\right)\sin\left(\frac{n\pi y}{b}\right). \tag{5}$$

Next we apply the same antisymmetrization and we obtain the following set of functions

$$\phi_{m,n}(x,y) = \frac{2}{\sqrt{ab}}\left\{\sin\left(\frac{m\pi x}{a}\right)\sin\left(\frac{n\pi y}{b}\right) + (-1)^{m+n+1}\sin\left(\frac{n\pi x}{a}\right)\sin\left(\frac{m\pi y}{b}\right)\right\}. \tag{6}$$

Once again, $n \neq m$ is required. Clearly, the $\phi_{m,n}(x,y)$'s are not eigenfunctions of the QBO on the half rectangle, because $a \neq b$; nevertheless they constitute a complete set of orthonormal functions, as we are going to prove. Let us denote by $\mathscr{Q}_1$ the triangle defined by the diagonal of the rectangle and having its $(\pi/2)$ angle placed in the origin; by $\mathscr{Q}_2$ we denote the half unit square obtained from the former triangle upon a rescaling of the sides lengths $(x' = (x/a), y' = (y/b))$. We then consider the changes under such rescaling in the inner product of two functions (6)

$$\begin{aligned}&\iint_{\mathscr{Q}_1}\phi_{m,n}(x,y)\phi_{i,j}(x,y)\mathrm{d}x\mathrm{d}y\\ &\quad = \frac{1}{ab}\iint_{\mathscr{Q}_2}\psi_{m,n}^{((\pi/4),(\pi/4),(\pi/2))}(x',y')\psi_{i,j}^{((\pi/4),(\pi/4),(\pi/2))}(x',y')\frac{\partial(x,y)}{\partial(x',y')}\mathrm{d}x'\mathrm{d}y'.\end{aligned} \tag{7}$$

Since the Jacobian of the transformation is $J = (\partial(x,y)/\partial(x',y')) = ab$, it is easy to see that we are left with the inner product of two normalized eigenfunctions of the QBO on the half unit square. They are eigenfunctions of a hermitian operator and therefore they are orthonormal to each other; this proves that functions (6) are orthonormal to each other also. In order to prove the completeness of the set, we consider some arbitrary, $\mathscr{L}^2$-integrable function $f(x,y)$ that vanishes on $\partial\mathscr{Q}_1$. By the same coordinate transformation we obtain

$$\begin{aligned}&\iint_{\mathscr{Q}_1}\phi_{m,n}(x,y)f(x,y)\mathrm{d}x\mathrm{d}y\\ &\quad = \sqrt{ab}\iint_{\mathscr{Q}_2}\psi_{m,n}^{((\pi/4),(\pi/4),(\pi/2))}(x',y')f(ax',by')\mathrm{d}x'\mathrm{d}y'.\end{aligned} \tag{8}$$

If the left hand side of (8) vanishes for every pair (m, n), so does the right hand side; but the vanishing of the right hand side integral allows us to conclude that $f \equiv 0$, because the ψ's are a complete set for those functions like $f(ax, by)$ that vanish on $\partial\mathscr{Q}_2$. We conclude that the only function orthogonal to all the ϕ's is the null function, and this proves that the set is complete. In the next step we construct the basis set for the more general case of an arbitrary triangle.

Consider the following active transformation of the plane into itself

$$\begin{aligned} x' &= x + y\cdot\tan\gamma \\ y' &= y \end{aligned} \tag{9}$$

where $\gamma = (\pi/2) - \eta$ and η is the angle of the desired triangle with the vertex in the origin of the coordinate axes. Transformation (9) maps a rectangle into a parallelogram and therefore the half rectangle into an arbitrary triangle [see figure 1]. We now consider the functions

$$\begin{aligned} \chi_{m,n}(x, y) = \frac{2}{\sqrt{ab}} \Bigg\{ &\sin\left[\frac{m\pi(x - y\cdot\tan\gamma)}{a}\right] \sin\left(\frac{n\pi y}{b}\right) \\ &+ (-1)^{m+n+1} \sin\left[\frac{n\pi(x - y\cdot\tan\gamma)}{a}\right] \sin\left(\frac{m\pi y}{b}\right) \Bigg\}; \end{aligned} \tag{10}$$

which is the desired basis set. In fact, we only need to perform the inverse transformation of (9); any arbitrary triangle is mapped into some half rectangle which, in turn, can be mapped into a half unit square by rescaling the sidelengths. Clearly, the two transformations in sequence map the functions (10) into the eigenfunctions of the QBO on the half unit square. Orthonormality and completeness can then be proven by reducing every integral to an integration over the half unit square that involves eigenfunctions of the QBO on that domain (we still have $J = ab$). Moreover,

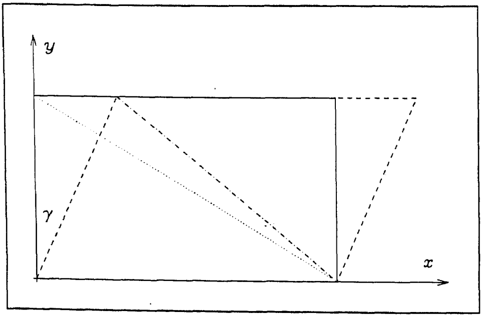

Figure 1. Under the affine transformation (9) a rectangle (solid line) is mapped into a parallelogram (dashed line); consequently its half is mapped into some triangle determined by the angle γ.

the mapping of the half unit square into an arbitrary triangle is linear and this guarantees that functions (10), being the image of eigenfunctions that vanish on the boundary of the half unit square, satisfy the Dirichlet boundary conditions.

We can now proceed to the construction of the matrix representation of the QBO (a detailed calculation of the matrix elements is reported in the appendix). In doing so some care must be taken about the ordering of the basis vectors, because functions (10) are labeled by a pair of indices rather than a single one. The most reasonable choice is to order the vectors according to the expectation value of the QBO

$$\langle -\nabla^2_{\partial\mathscr{D}} \rangle = \iint_{\mathscr{D}} \chi_{m,n}(x,y)(-\nabla^2_{\partial\mathscr{D}})\chi_{m,n}(x,y)\mathrm{d}x\mathrm{d}y. \tag{11}$$

The expectation value above represents the energy content of a given vector, namely how rapidly the corresponding wave function oscillates. It is therefore sensible to expect that low energy eigenstates, i.e. relatively slowly varying eigenfunctions, do not have large projections on high energy vectors, i.e. rapidly oscillating functions. From the considerations above we assume that some proper truncation of the matrix can still yield satisfactory results, at least for the first few lowest lying eigenstates. Of course, the sole justification for such an assumption is the good agreement between numerical and analytical results in those cases in which the latter are available. The outcome of such a comparison is described in the next section, where we consider the analytical solution of (1) in an equilateral triangle.

3. Reliability of the solution

In this last section we present the comparison between numerical and analytical results. Not surprisingly, an analytical solution is available solely for those quantum billiards which are classically integrable. In the class of triangular billiards this amounts to the equilateral triangle, the half equilateral triangle and the half square. We applied our scheme to the equilateral triangle and compared our results with the analytical ones.

The quantum billiard in an equilateral triangle was first solved by Lamé [17], who was interested in the vibrating membrane problem; a mathematically rigorous solution of the same problem was recently published by Pinsky [18]. The eigenvalues of the QBO on the equilateral triangle with side length l are given by

$$E_{m,n} = \frac{16\pi^2}{27l^2}(m^2 + n^2 - mn), \tag{12}$$

where n and m are integers satisfying the following conditions

$$\begin{aligned} &n + m = 3k \quad k = \text{integer} \\ &\quad m \neq 2n \\ &\quad n \neq 2m. \end{aligned} \tag{13}$$

The case in which both $m = 0$ and $n = 0$ must also be ruled out. The (unnormalized) eigenfunctions are given by

$$\psi^{((\pi/3),(\pi/3),(\pi/3))}_{m,n}(x,y) = \sum_{(m,n)} \pm \exp\left[\left(\frac{2\pi i}{3l}\right)\left(nx + \frac{(2m-n)y}{\sqrt{3}}\right)\right]. \tag{14}$$

Exactly six (m,n) pairs must be considered in (14) and the rule is

$$(m,n)\rightarrow(m,m-n)\rightarrow(-n,m-n)\rightarrow(-n,-m)\rightarrow(n-m,-m)\rightarrow(n-m,n); \tag{15}$$

each transition induces a change of sign. We considered a triangle of side length $l=\pi$. The first test concerns eigenvalues computation: results are summarized in figure 2, where we compare the first 925 numerical eigenvalues (this corresponds to a maximal magnitude of the De Broglie wave vector $|\boldsymbol{\kappa}|\sim 54$) with their analytical counterparts. In figure 2a we plot the logarithm in base 10 of the relative error versus $|\boldsymbol{\kappa}|$, while in figure 2b we report the mean value of the same, again versus $|\boldsymbol{\kappa}|$. Figure 2 shows good agreement with the analytical results, especially if one considers the small dimensions (2000 × 2000) of the matrix representing the QBO. Approximately half of the eigenvalues are an accurate approximation to the exact spectrum. In spite of the small dimensions of the matrix our results are very good up to a wavelength of the order of $\sim\frac{1}{25}$ of the side length. The eigenvalues considered in figure 2 were counted by taking degeneracy into account; this was done because when the method is applied to some asymmetric triangle there will be no degeneracy, and our counting

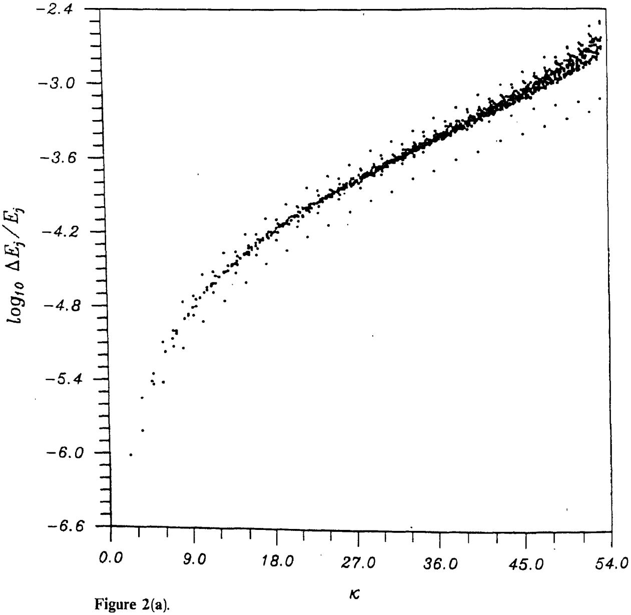

Figure 2(a).

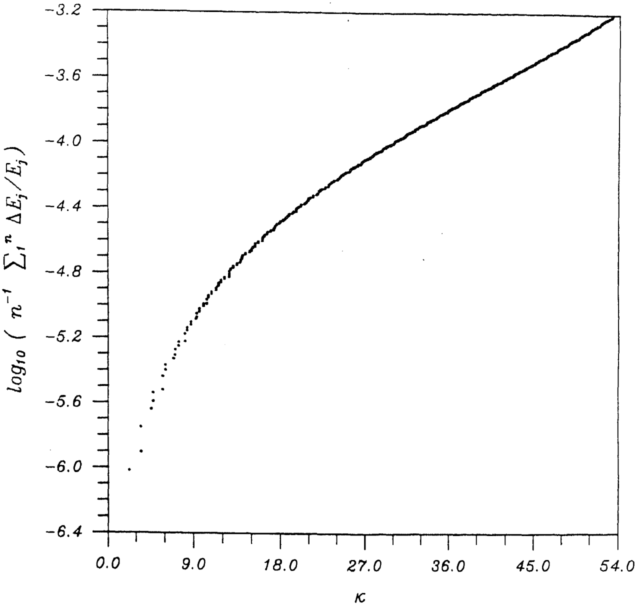

Figure 2(b).

Figure 2. Comparison between the numerical result and the analytical values for the spectrum of the equilateral triangle; (**a**) Logarithm (in base 10) of the relative error between the numerical eigenvalues and the exact ones vs. the magnitude of the wave vector $\boldsymbol{\kappa}$; (**b**) Logarithm (in base 10) of the average error between numerical eigenvalues and analytical ones vs. the magnitude of the wave vector $\boldsymbol{\kappa}$.

gives information about how many distinct eigenvalues can be computed, and their precision, in the case of some classically nonintegrable billiard. However, a moment's thought shows that such an estimate can hold only for triangles not too different from the equilateral one. Consider, for example, the half equilateral triangle: there, the same calculation, i.e. a matrix of the same dimensions, yields approximately half as many accurate eigenvalues, namely the energy levels of those equilateral triangle eigenstates which are odd under reflection about the height of the triangle. This is a consequence of Weyl's law for the integrated density of states $\mathcal{N}(E)$ which, including low energy corrections, reads [1]

$$\mathcal{N}(E) = \frac{A}{4\pi}E - \frac{L}{4\pi}\sqrt{E} + \Sigma c(\alpha_i) \tag{16}$$

with:

$$c(\alpha_i)=\frac{1}{2\pi}\left(\frac{\pi}{\alpha_i}-\frac{\alpha_i}{\pi}\right), \tag{17}$$

where L is the perimeter of the triangle and α_i is the ith internal angle. Weyl's law can be used as test for the results of any numerical calculation of billiard spectra. The equilateral triangle is a special billiard, therefore we performed Weyl's law test and verified the consistency of our scheme, also when applied to classically nonintegrable triangles. The results of the test are displayed in figures 3–4. Figure 3 refers to an irrational triangular billiard, with angles not very different from $(\pi/3)$: as expected the numerical staircase (solid line) fits well Weyl's law prediction (dashed line) up to ~ the 950th eigenvalue, namely the same range of precision as for the equilateral triangle. Figure 4a, instead, refers to a pseudointegrable billiard, a $((\pi/10), (3\pi/10), (6\pi/10))$ triangle: in it one sees that the loss of precision occurs much earlier in terms of

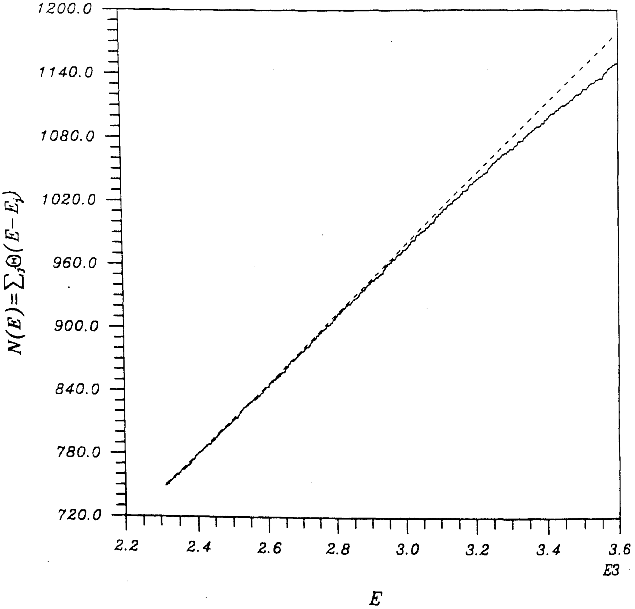

Figure 3. Analytical integrated density of states (dashed line) and numerical staircase (solid line) for an irrational billiard. The divergence between the two reflects the drop in the computational precision. For lower energies the two overlap and become indistinguishable on a coarse scale.

number of eigenvalues, but approximately in the same energy range as before. The range in which the calculation begins to lose precision is the one predicted by keeping the energy fixed and rescaling $\mathcal{N}(E)$ by the area of the billiard as required by Weyl's law; and the smaller number of accurate eigenvalues obtained in the pseudointegrable case is yet another example of the well-known difficulty in computing the spectra of narrow triangles [19]. For smaller energies than those presented in figures 3–4 the theoretical prediction and the numerical staircase overlap exactly. It is also interesting to observe that the onset of the divergence between the computed eigenvalues and the predictions of Weyl's law is very sharp, as it can be appreciated from figure 4b, where the relative deviation from the area rule for the same pseudointegrable triangle is plotted.

It is known that the Green function method allows a slightly better precision in the computation of the eigenvalues for a given matrix dimension, since one can concentrate all the computational power in the evaluation of a single eigenvalue. However, the method requires a scanning of the real axis which implies long computing times and the risk of missing some eigenvalues, and it cannot resolve degenerate eigenvalues. This is not the case for our scheme, which moreover requires surprisingly modest computing times (the matrix elements can be evaluated analytically; this

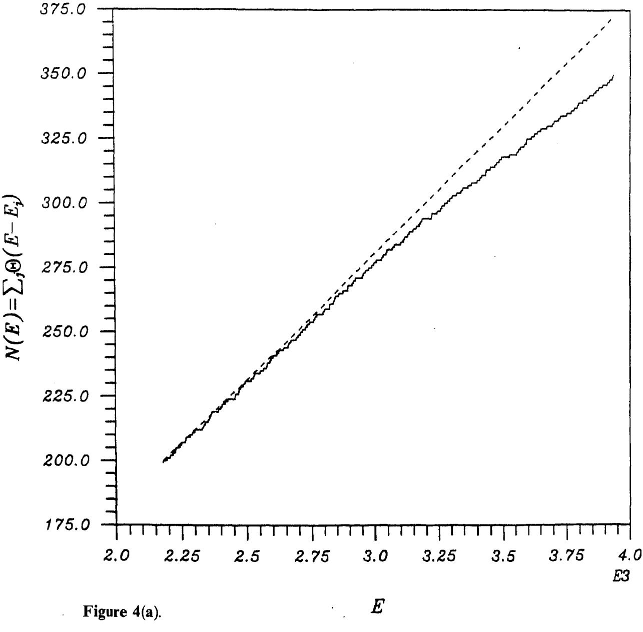

Figure 4(a).

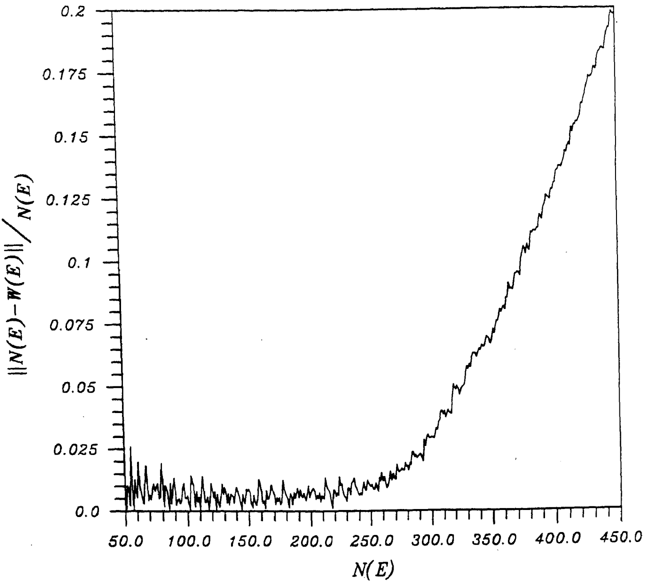

Figure 4(b).

Figure 4. Integrated density of states for a pseudointegrable $((\pi/10), (3\pi/10), (6\pi/10))$ triangle; (**a**) Analytical integrated density of states (dashed line) and numerical staircase (solid line). The divergence between the two occurs after fewer states than in figure 3, but approximately in the same energy range; (**b**) Absolute value of the relative difference between the numerical staircase and the predictions of Weyl's law (plus corrections): the sudden onset of an exponential divergence is apparent.

shortens the time needed for the computation of the matrix dramatically). However, the main feature of our solution is the very good precision in the computation of the eigenfunctions. This is illustrated next.

In figure 5 we plot the value of the correlation integrals between numerical and analytical eigenfunctions up to the 380th eigenstate

$$I(j) = \iint_{\mathscr{D}} \psi_j^{\text{analytical}}(x, y)\,\psi_j^{\text{numerical}}(x, y)\,\mathrm{d}x\,\mathrm{d}y. \tag{18}$$

From the form of Pinsky's [18] solution one can immediately deduce the existence of a double degeneracy due to the sine-cosine decomposition of the exponentials:

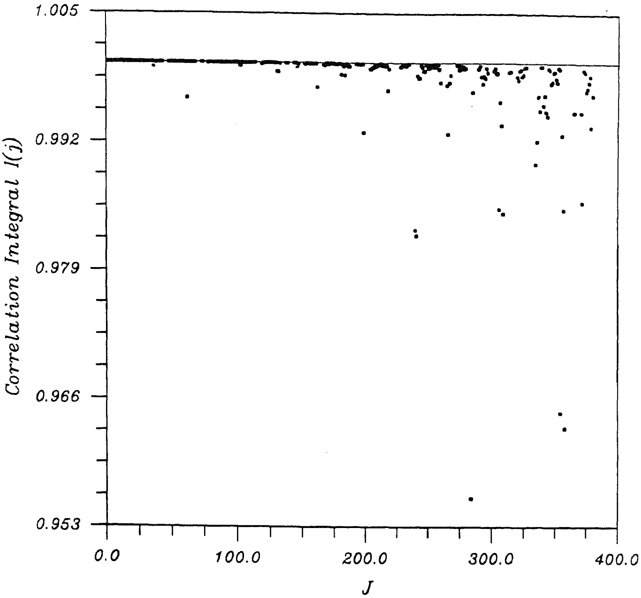

Figure 5. Correlation integrals between the first 380 normalized numerical eigenfunctions and their exact counterparts. The great accuracy of the computation is evident.

clearly, in (18) by $\psi_j^{\text{analytical}}$ we mean either sine or cosine (in the case $n = m$ there is no double degeneracy: the cosine solution vanishes identically). Figure 5 shows the high precision of our calculation. A more detailed account of it can be found in table 1, where the explicit values of $I(j)$ for the first 20 eigenfunctions are exhibited. Results of figure 5 and table 1 were evaluated semi-analytically: a numerically computed eigenfunction consists of a finite linear combination of the basis functions (10)

$$\psi_j^{\text{numerical}}(x, y) = \sum_{m,n} a_{m,n} \chi_{m,n}(x, y); \tag{19}$$

therefore integral (18) can be reduced to a summation of simpler terms

$$I(j) = \sum_{m,n} a_{m,n} \iint_{\mathscr{D}} \psi_j^{\text{analytical}}(x, y) \chi_{m,n}(x, y) \mathrm{d}x \mathrm{d}y. \tag{20}$$

Each integral in (20) can be evaluated analytically, making the computation of $I(j)$

Table 1. Results of the correlation integral between the first 20 numerical and analytical wavefunctions of the equilateral triangle.

Table 1.	Correlation integrals.
1	0·9999998808
2	0·9999998235
3	0·9999997616
4	0·9999998808
5	0·9999996424
6	0·9999996424
7	0·9999993443
8	0·9999997616
9	0·9999994040
10	0·9999988079
11	0·9999998212
12	0·9999996424
13	0·9999989867
14	0·9999988675
15	0·9999991655
16	0·9999990463
17	0·9999992251
18	0·9999993443
19	0·9999958873
20	0·9999994636

precise and the test reliable. The results of figure 5 are particularly interesting because they were obtained diagonalizing a very small (1000 × 1000) matrix, which required very short computing times. In figure 5 the correlation integral is not plotted for every possible eigenfunction, the reason being that in some cases, besides the already mentioned sine-cosine degeneracy, there happens to be some higher degeneracy, due to the possibility of producing the same eigenvalue with two [or more] distinct pairs of integers. In the case of doubly degenerate solutions the algorithm yields naturally the same basis for the eigenspace as Pinsky's [18], which makes the correlation integral meaningful. On the other hand, for more highly degenerate eigenvalues the numerical calculation selects a different eigenspace basis. For example, for fourfold degenerate eigenvalues, the sine-cosine distinction is still preserved, but some mixing occurs between the two sine [or cosine] solutions related to the two distinct pairs of integers. Clearly, in such a situation a superposition integral does not give any useful information about the precision of the numerical results; however, by inspecting contour plots of proper linear combination of Pinsky's [18] eigenfunction, it was possible to recognise the consistency of our numerical results.

For eigenfunction computation there is no test (like a comparison with Weyl's law predictions) to verify the consistency of the results in the case of nonintegrable billiards. However, in figure 6a we plot the components along the basis vectors for the normalized 250th state of the same irrational billiard considered before. They were obtained by diagonalizing a 1000 × 1000 matrix. It is apparent that such components become very small as higher energy basis vectors are considered. This ensures (at a reasonable degree of confidence: some large components along extremely energetic basis vectors might always exist) that our numerical calculation yields a very good approximation to the actual wave function. In figure 6b we plot the components for the 430th normalized eigenstate of the same billiard, which belongs to that range of the spectrum where the precision of the computation begins to drop (for the given dimension of the matrix). The interesting feature is the smallness of the first ~ 100 components, which implies that a representation of the QBO obtained by leaving out, say, the first 100 basis vectors and including 100 high energy functions (those ranging from the 1001st to the 1100th) would yield a better result. This observation suggests the possibility of scanning a large portion of the spectrum using a series of matrices centered on states of increasing energy. Such matrices would not be of fixed dimension (the increasing complexity of rapidly oscillating high energy eigenfunction would require a larger basis set) but they would still be relatively small. Note that, in a given application, not all the elements of expansion (19) need to be considered. In fact, once a threshold for the desired precision is fixed, all those coefficient in (19) that lead to contributions below that threshold can be dropped leading to some little computing time consuming expressoin for the eigenfunctions [which we actually did in many of our calculations].

Finally, we address the issue of the sensitivity of the scheme to change of the geometrical shape of the QBO domain. To this end, we first show in figure 7a one

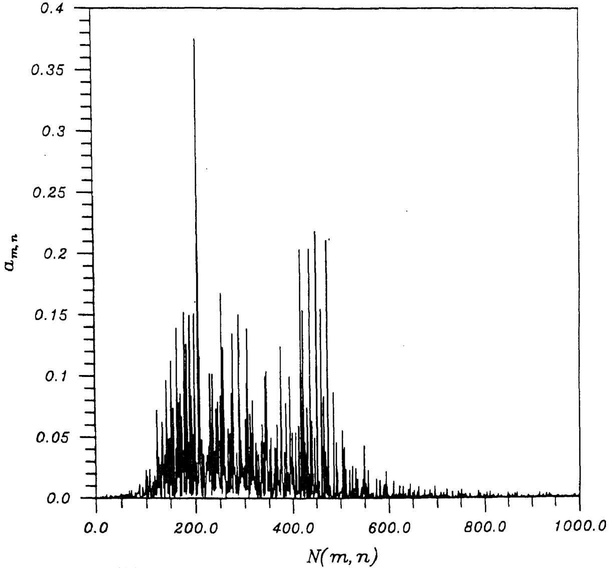

Figure 6(a).

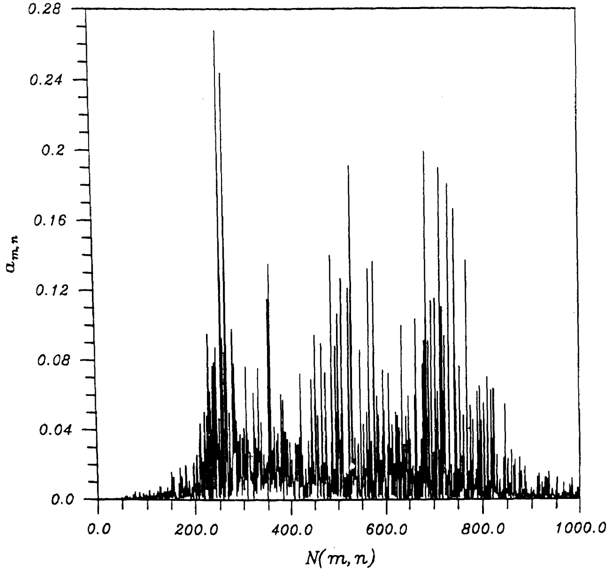

Figure 6(b).

Figure 6. Components of the eigenfunctions along the basis states; (**a**) 250th eigenstate: components become very small with increasing energy making the result very reliable; (**b**) 430th eigenstate: the projection on the lowest energy basis states is almost negligible, therefore a smaller matrix would still yield accurate results.

of the two first excited states (recall the double degeneracy) of the equilateral triangle, which was computed diagonalizing a 400 × 400 matrix. As expected a nodal line coincides with one of the bisectors of the triangle, specifically the one bisecting the angle the vertex of which sits at the origin of the frame of reference; in fact, we performed the computation placing the origin of the coordinates on the vertex which is labeled "α" in the figure. The relationship between the location of the nodal line and the position of the frame of reference is also shown in figure 7b, which refers to a calculation (again a 400 × 400 matrix) performed putting the origin of the coordinates on vertex "β". Next, we turned to the study of an isosceles triangle obtained by slightly stretching the height relative to the x-axis side of the equilateral triangle of figures 7a, 7b (a billiard which, to the best of our knowledge, nobody has ever investigated). For that eigenstate of the isosceles triangle that originates from the one of figures 7a and 7b, one expects from symmetry arguments that the nodal line lie along the longest height, independently of the location of the reference frame. We performed a calculation using a 400 × 400 matrix and placing the frame of

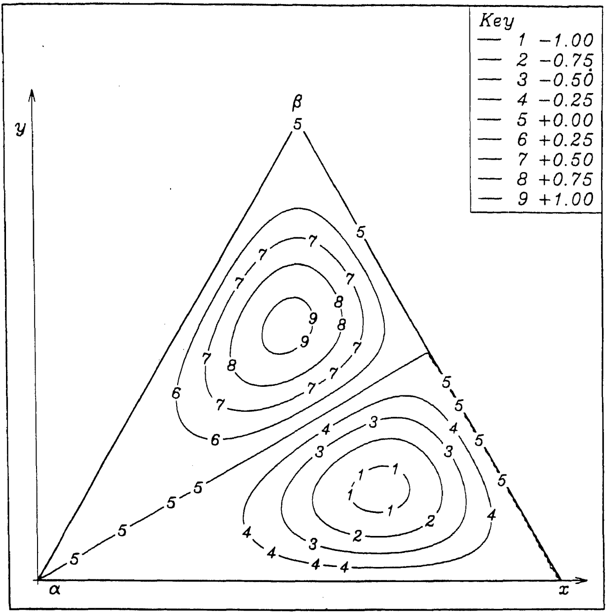

Figure 7(a).

reference on vertex "α", and we studied an isosceles triangle very close to the equilateral triangle, namely we stretched the height relative to the x-axis base only by 0·1%. The result displayed in figure 7c clearly indicates the capacity of the algorithm to detect the small change in the domain. However, because of the smallness of the distortion of the shape of the billiard, one finds eigenfunctions that are nicely symmetric (or antisymmetric) about the longest height of the triangle only up to a certain energy, because at higher energies the precision of the computation is not enough to resolve between states which originate from some pair of *degenerate* equilateral triangle eigenstates and which are either even or odd under reflection about the longest height. In fact, the algorithm yields eigenstates which are combinations of both types of eigenfunctions and therefore do not have definite parity. For the case at hand, namely a 400 × 400 matrix, we observed that all the eigenfunctions up to approximately the 50th eigenstate display the desired parity; at higher energies a transition regime takes place, where we find eigenfunctions with definite parity along with slightly distorted ones and with eigenfunctions with no parity at all (see figure 8). We also studied the same triangle using a larger matrix (600 × 600); in this case the transition regime starts approximately after the 80th eigenstate, suggesting an approximately linear scaling with the dimensions of the matrix. Unfortunately, the extensive calculations

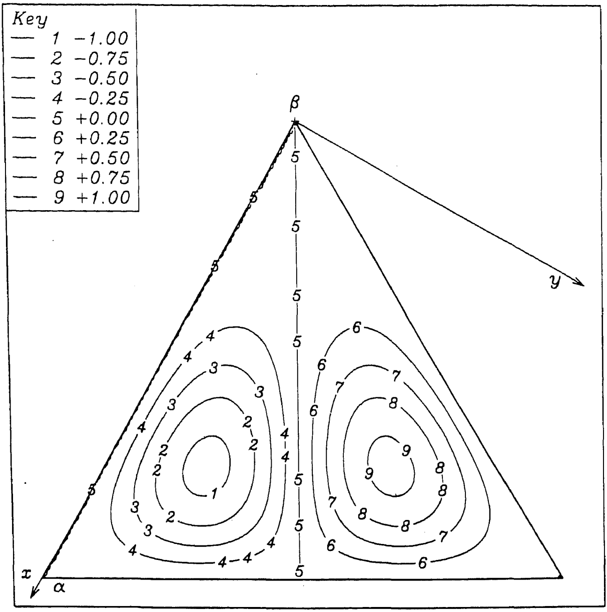

Figure 7(b).

necessary to determine the exact relationship between the dimensions of the matrix, and up to what state the eigenfunctions display well defined parity and also the size of the change in the domain, are beyond our computational reach. However, it should be noted that the problem of properly resolving quasi-degenerate states is very rare. It is well known that classically nonintegrable systems show level repulsion [1]: the energy levels of chaotic systems repel each other linearly (barring the case in which the time reversal symmetry in broken by some magnetic field), whereas some numerical evidence [15, 20] suggests that pseudointegrable systems do so according to a power law, with exponent ranging between 0·5 and 1. Therefore, degenerate or quasi-degenerate states, which are the cause of the problems encountered in the isosceles triangle, are very rare and in this case they are due to the special symmetry of the domain. Finally it can also be argued that not even the exact analytical eigenstates, because of their finite wavelength, would be able to detect very small changes in the domain of the billiard, if not in very special situations like the one at hand, which is a case of spontaneously broken symmetry.

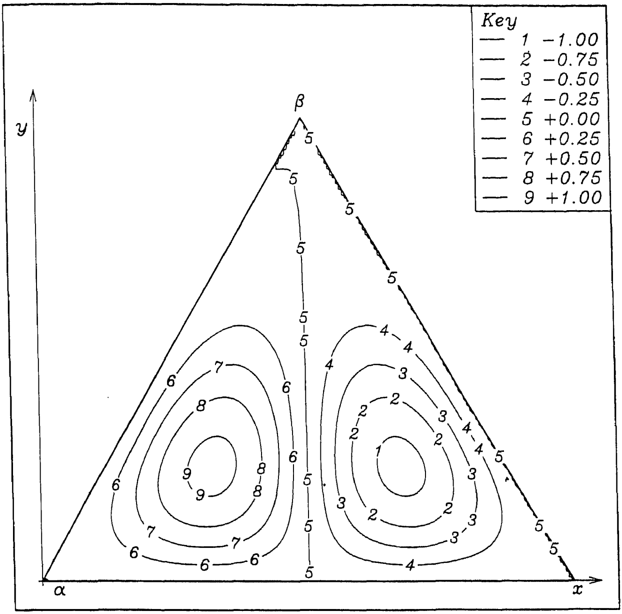

Figure 7(c).

Figure 7. Contour plot of one of the two 1st excited states (recall degeneracy) of the equilateral triangle and of an isosceles triangle; (**a**) Equilateral triangle: the calculation was performed putting the frame of reference in the lower left corner of the triangle; (**b**) Equilateral triangle: the computation was performed setting the frame of reference on the upper vertex of the triangle; (**c**) Isosceles triangle: 3rd normalized eigenstate (the removal of degeneracy energetically favors the other state of the degenerate pair); the triangle was obtained by slightly stretching the equilateral one along the height relative to the x-axis. The state was computed setting the frame of reference on the lower left corner. The result proves the capacity of the algorithm to detect small changes in the shape of the domain.

4. Conclusions

In this paper we have presented a comprehensive solution for the problem of the QBO in arbitrary triangular domains. We addressed this problem because due to its paradigmatic nature it is attracting increasing attention in the nonlinear dynamics community. Our solution requires short computing times and yields excellent results, particularly for the eigenfunctions. Moreover, it yields the eigenfunctions in a very

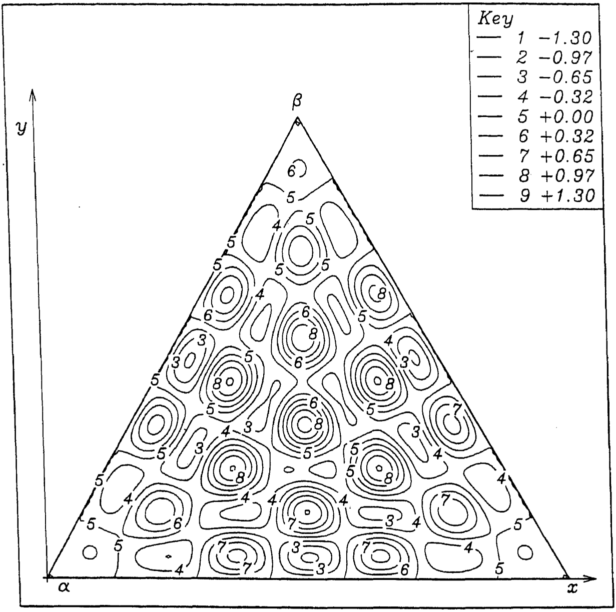

Figure 8(a).

tractable form, like (19), which allows "semi-analytical" calculations, like the one we performed in evaluating the integral (18). Such a feature offers precise, reliable and computationally economic studies of the most interesting properties of the eigenfunctions, such as investigations of the amplitude probability distribution and of the spatial correlation function and the construction of Path Correlation Functions [21] for triangular billiards. A first application of the method has led to the discovery of scars along ghosts of neutrally stable periodic orbits [12]. A more general application of the scheme and study of the statistical properties of the eigenfunctions will be presented in a forthcoming paper.

Also, the same basis set can be used with no modification to study the problem of triangular billiards in presence of some perturbing field, just by adding the matrix elements of the field to the matrix representing the laplacian; such a study would allow the study of the evolution of eigenvalues and eigenfunctions as the classical systems undergoes a transition to chaos and such studies are in progress in our group. Finally, with some small modifications the present procedure can be easily applied to the problem of quantum billiards in parallelograms: in fact, the functions obtainable simply by leaving out the antisymmetrization step are clearly a suitable Hilbert space basis for the parallelogram problem.

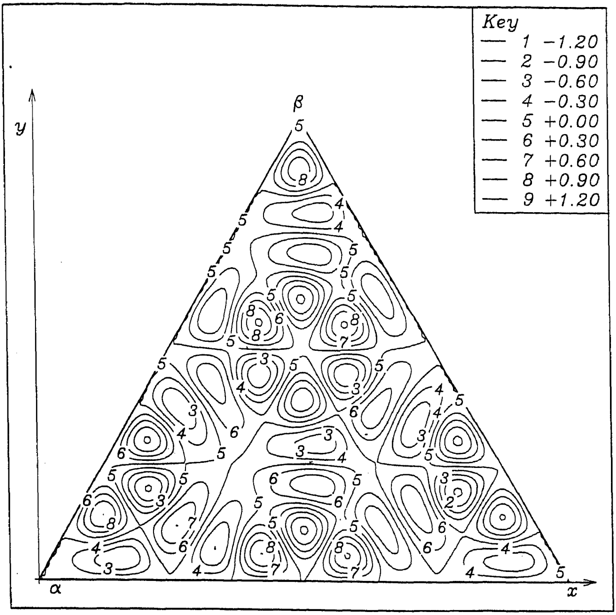

Figure 8(b).

Acknowledgements

The author wishes to thank S Bright for introducing him to Ga-tech computational facilities. He is also grateful to Prof. A Scotti who introduced him to the problem. Finally, thanks are due to Prof. T Uzer for a critical reading of the manuscript. This work was partially supported by the "Domenica Rea D'Onofrio" fellowship and by the National Science Foundation through a grant for the Institute for Theoretical Atomic and Molecular Physics at the Harvard-Smithsonian Astrophysical Observatory.

Appendix 1

Evaluation of the matrix elements

Here we give the explicit matrix elements for the QBO on an arbitrary triangular domain with base $B = a\pi$ and height $H = b\pi$: this is a larger triangle than the one

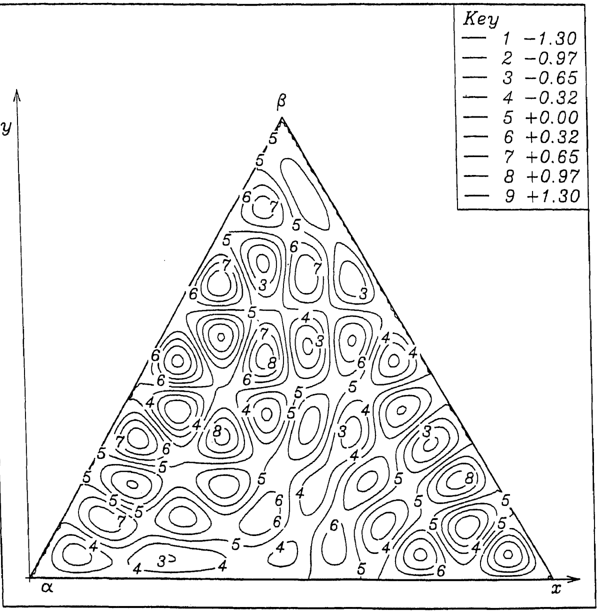

Figure 8(c).

Figure 8. Contour plots of some eigenfunctions of the isosceles triangle, computed with a 400 × 400 matrix, in the transition regime; (**a**) 57th eigenstate: the contours pattern is clearly symmetric with respect to the height of the triangle; (**b**) 59th eigenstate: the wave function shows some approximate symmetry, but is a little distorted; (**c**) 56th eigenstate: in this case every definite parity is lost and the wave function is not symmetric nor antisymmetric with respect to the height.

considered in the rest of the paper, but this simple rescaling of the sides allows us not to write a series of π's in the arguments of the basis functions keeping the notation a little less cumbersome. We will write Γ as a short for $\tan\gamma$ and we will also set $((1+\Gamma^2)/a^2)=(1/\alpha^2)$.

The matrix elements are

$$\mathscr{D}(m,n,j,k)=\frac{4}{\pi^2 ab}\iint_{\mathscr{T}} \mathrm{d}x\mathrm{d}y\left\{\sin\frac{m(x-\Gamma y)}{a}\sin\frac{ny}{b}\right.$$
$$\left.+(-1)^{m+n+1}\sin\frac{n(x-\Gamma y)}{a}\sin\frac{my}{b}\right\}$$

$$\times (-\nabla^2)\left\{\sin\frac{j(x-\Gamma y)}{a}\sin\frac{ky}{b}+(-1)^{j-k+1}\sin\frac{k(x-\Gamma y)}{a}\sin\frac{jy}{b}\right\}. \tag{A1}$$

We consider the following change of variables

$$x'=\frac{x-\Gamma y}{a} \qquad y'=\frac{y}{b} \tag{A2}$$

which induces a transformation of the laplacian

$$\nabla^2\to\nabla^{2'}=\frac{1}{a^2}\frac{\partial^2}{\partial x'^2}+\frac{1}{b^2}\frac{\partial^2}{\partial y'^2}+\frac{\Gamma^2}{a^2}\frac{\partial^2}{\partial x'^2}-\frac{2\Gamma}{ab}\frac{\partial^2}{\partial x'\partial y'}; \tag{A3}$$

and the matrix elements reduce to

$$\begin{aligned}\mathscr{D}(m,n,j,k)=\frac{4}{\pi^2}\int_0^\pi \mathrm{d}x\int_0^{\pi-x}\mathrm{d}y\{\sin mx\sin ny+(-1)^{m+n+1}\sin nx\sin my\}\\ \times\left\{\left[\left(\frac{j^2}{\alpha^2}+\frac{k^2}{b^2}\right)\sin jx\sin ky+(-1)^{j+k+1}\right.\right.\\ \left.\times\left(\frac{k^2}{\alpha^2}+\frac{j^2}{b^2}\right)\sin kx\sin jy\right]\\ \left.+\frac{2\Gamma}{ab}jk[\cos jx\cos ky+(-1)^{j+k+1}\cos kx\cos jy]\right\}.\end{aligned} \tag{A4}$$

We have two separate integrals, one involving sines only and the other involving cosines also

$$\mathscr{D}(m,n,j,k)=\frac{4}{\pi^2}[\mathscr{I}(m,n,j,k)+\mathscr{J}(m,n,j,k)]. \tag{A5}$$

We add the following null quantity to the sine only integral

$$(-1)^{j+k+1}\left(\frac{j^2}{\alpha^2}+\frac{k^2}{b^2}\right)\quad\{\sin kx\sin jy-\sin kx\sin jy\} \tag{A6}$$

and we obtain

$$\begin{aligned}\mathscr{I}=\left(\frac{j^2}{\alpha^2}+\frac{k^2}{b^2}\right)\int_0^\pi\mathrm{d}x\int_0^{\pi-x}\mathrm{d}y\,\{\sin mx\sin ny+(-1)^{m+n+1}\sin nx\sin my\}\\ \times\{\sin jx\sin ky+(-1)^{j+k+1}\sin kx\sin jy\}+(-1)^{j+k}\left[\frac{b^2-\alpha^2}{\alpha^2b^2}(j^2-k^2)\right]\\ \times\int_0^\pi\mathrm{d}x\int_0^{\pi-x}\mathrm{d}y\{\sin mx\sin ny+(-1)^{m+n+1}\sin nx\sin my\}\{\sin kx\sin jy\}.\end{aligned} \tag{A7}$$

We can separate also $\mathscr{I}$ in two integrals

$$\mathscr{I}(m,n,j,k)=\left(\frac{j^2}{\alpha^2}+\frac{k^2}{b^2}\right)\mathscr{I}_1(m,n,j,k)+\left[\frac{b^2-\alpha^2}{\alpha^2b^2}(j^2-k^2)\right]\mathscr{I}_2(m,n,j,k); \tag{A8}$$

the first one can be solved by using the orthonormality of the eigenfunctions of the QBO on the half square

$$\mathscr{I}_1(m,n,j,k)=\frac{\pi^2}{4}\delta_{m,j}\delta_{n,k}; \tag{A9}$$

whereas for the second one we set

$$\mathscr{I}_2(m,n,j,k)=\mathscr{I}_3(m,n,k,j)+(-1)^{m+n+1}\mathscr{I}_3(n,m,k,j) \tag{A10}$$

where

$$\begin{aligned}\mathscr{I}_3(l_1,l_2,l_3,l_4)&=\int_0^\pi \mathrm{d}x\int_0^{\pi-x}\mathrm{d}y\sin l_1x\sin l_2y\sin l_3x\sin l_4y\\&=\int_0^\pi \mathrm{d}x\int_0^{\pi-x}\mathrm{d}y\sin l_1x\sin l_3x\frac{1}{2}\{\cos[(l_2-l_4)y]\\&\qquad-\cos[(l_2+l_4)y]\},\end{aligned} \tag{A11}$$

and l_1, l_2, l_3, l_4 are integer indices which are equal to m,n,k,j in the first case and to n,m,k,j in the second; we also write

$$\mathscr{I}_3(l_1,l_2,l_3,l_4)=\mathscr{I}_4(l_1,l_2,l_3,l_4)-\mathscr{I}_4(l_1,l_2,l_3,-l_4), \tag{A12}$$

where

$$\mathscr{I}_4(l_1,l_2,l_3,l_4)=\frac{1}{2}\int_0^\pi \mathrm{d}x\sin l_1x\sin l_3x\int_0^{\pi-x}\mathrm{d}y\cos[(l_2-l_4)y]. \tag{A13}$$

The integral $\mathscr{I}_4$ is simple, but some care must be taken for the cases in which the arguments of the sinusoidal functions vanish. The result is

$$\mathscr{I}_4=\begin{cases}\dfrac{1}{4}\left\{\dfrac{\pi^2}{2}+\dfrac{1}{(l_1+l_3)^2}[(-1)^{l_1+l_3}-1]\right\} & \text{if } l_2-l_4=0 \text{ and } l_1-l_3=0;\\[2ex] \dfrac{1}{4}\left\{\dfrac{[(-1)^{l_1+l_3}-1]}{(l_1+l_3)^2}-\dfrac{[1-(-1)^{l_1-l_3}]}{(l_1-l_3)^2}\right\} & \text{if } l_2-l_4=0 \text{ and } l_1-l_3\neq 0;\\[2ex] \dfrac{-(-1)^{l_2-l_4}}{4(l_2-l_4)}\{\mathscr{I}_5[l_1,l_3,(l_2-l_4)]-\mathscr{I}_5[l_1,l_3,(l_4-l_2)]\} & \text{if } l_2-l_4\neq 0;\end{cases} \tag{A14}$$

and integral $\mathscr{I}_5[l_1,l_3,(l_2-l_4)]$ is defined as:

$$\mathscr{I}_5[l_1,l_3,(l_2-l_4)]=\int_0^\pi \mathrm{d}x\sin l_1x\cos\{[(l_3-(l_2-l_4)]x\}. \tag{A15}$$

Setting $l_5 = l_3 - (l_2 - l_4)$ we have

$$\mathscr{I}_5(l_1, l_5) = \begin{cases} \dfrac{1-(-1)^{l_1}}{l_1} & \text{if } l_5 = 0; \\ \dfrac{1-(-1)^{l_1 - l_5}}{2(l_1 - l_5)} & \text{if } l_5 \neq 0 \text{ and } l_5 + l_1 = 0; \\ \dfrac{1-(-1)^{l_1 + l_5}}{2(l_1 + l_5)} & \text{if } l_5 \neq 0 \text{ and } l_5 - l_1 = 0; \\ \dfrac{l_1[1-(-1)^{l_1 + l_5}]}{l_1^2 - l_5^2} & \text{if } l_5 \neq 0, \quad l_5 - l_1 \neq 0 \text{ and } l_5 - l_1 \neq 0; \end{cases} \tag{A16}$$

This result concludes the first part of the calculation.

We now turn to the calculation of the integral involving the cosines; we have

$$\begin{aligned} \mathscr{I}(m,n,j,k) = \frac{8\Gamma}{\pi^2 ab} jk \{ & \mathscr{I}_1(m,n,j,k) + (-1)^{m+n+1} \mathscr{I}_1(n,m,j,k) \\ & + (-1)^{j+k+1} \mathscr{I}_1(m,n,k,j) + (-1)^{m+n+j+k} \mathscr{I}_1(n,m,k,j) \}; \end{aligned} \tag{A17}$$

where

$$\begin{aligned} \mathscr{I}_1(l_1,l_2,l_3,l_4) &= \int_0^{\pi} \mathrm{d}x \int_0^{\pi - x} \mathrm{d}y \sin l_1 x \sin l_2 y \cos l_3 x \cos l_4 y \\ &= \frac{1}{4} \int_0^{\pi} \mathrm{d}x \{ \sin[(l_1 + l_3)x] + \sin[(l_1 - l_3)x] \} \\ &\quad \times \int_0^{\pi - x} \mathrm{d}y \{ \sin[(l_2 + l_4)y] + \sin[(l_2 - l_4)y] \}, \end{aligned} \tag{A18}$$

and also

$$\begin{aligned} \mathscr{I}_1(l_1,l_2,l_3,l_4) = \{ & \mathscr{I}_2(l_1,l_2,l_3,l_4) + \mathscr{I}_2(l_1,l_2,-l_3,l_4) \\ & + \mathscr{I}_2(l_1,l_2,l_3,-l_4) + \mathscr{I}_2(l_1,l_2,-l_3,-l_4) \}, \end{aligned} \tag{A19}$$

where $\mathscr{I}_2$ is defined as:

$$\mathscr{I}_2(l_1,l_2,l_3,l_4) = \frac{1}{4} \int_0^{\pi} \mathrm{d}x \sin[(l_1 + l_3)x] \int_0^{\pi - x} \mathrm{d}y \sin[(l_2 + l_4)y]. \tag{A20}$$

We finally set $l_{13} = l_1 + l_3$ and $l_{24} = l_2 + l_4$ and we obtain $\mathscr{I}_2$

$$\begin{cases} 0 & \text{if } l_{13} = 0 \text{ or } l_{24} = 0; \\ \dfrac{1}{4} \left\{ \dfrac{(-1)^{l_{24}}}{2 l_{24}} \left[\dfrac{(-1)^{l_{13} + l_{24}} - 1}{l_{13} + l_{24}} \right] + \dfrac{1 - (-1)^{l_{13}}}{l_{13} l_{24}} \right\} & \text{if } l_{13} - l_{24} = 0; \\ \dfrac{1}{4} \left\{ \dfrac{(-1)^{l_{24}}}{2 l_{24}} \left[\dfrac{(-1)^{l_{13} - l_{24}} - 1}{l_{13} - l_{24}} \right] + \dfrac{1 - (-1)^{l_{13}}}{l_{13} l_{24}} \right\} & \text{if } l_{13} + l_{24} = 0; \\ \dfrac{1}{4} \left\{ \dfrac{(-1)^{l_{24}}}{2 l_{24}} \left[\dfrac{(-1)^{l_{13} - l_{24}} - 1}{l_{13} - l_{24}} + \dfrac{(-1)^{l_{13} + l_{24}} - 1}{l_{13} + l_{24}} \right] + \dfrac{1 - (-1)^{l_{13}}}{l_{13} l_{24}} \right\} & \text{if } l_{13} + l_{24} \neq 0 \text{ and } l_{13} - l_{24} \neq 0; \end{cases} \tag{A21}$$

This completes the evaluation of the matrix elements.

References

[1] B Eckhardt, *Phys. Rep.* **163**, 205 (1988)
[2] I P Cornfeld, S V Fomin, Ya G Sinai, *Ergodic theory* (Springer Verlag, Heidelberg, 1980)
[3] M V Berry, *Ann. Phys.* (*NY*) **131**, 163 (1981)
[4] L A Bunimovich, *Commun. Math. Phys.* **65**, 295 (1979)
[5] S W McDonald and A N Kaufman, *Phys. Rev.* **A37**, 3067 (1988)
[6] R J Riddel Jr, *J. Comput. Phys.* **31**, 21 (1979)
[7] R J Riddel Jr, *J. Comput. Phys.* **31**, 42 (1979)
[8] E J Heller, in *Chaos and quantum physics*, NATO Les Houches Lecture Notes (1989)
[9] T Cheon and T D Cohen, *Phys. Rev. Lett.* **62**, 2769 (1989)
[10] D Biswas and S R Jain, *Phys. Rev.* **A42**, 3170 (1990)
[11] B Eckhardt, J Ford and F Vivaldi, *Physica* **D13**, 339 (1984)
[12] P Bellomo and T Uzer, *Phys. Rev.* **E50**, 1886 (1994)
[13] M C Gutzwiller, *Chaos in classical and quantum mechanics* (Springer Verlag, Heidelberg, 1990)
[14] H M Lauber, P Weidenhammer and D Dubbers, *Phys. Rev. Lett.* **72**, 1004 (1994)
[15] Paolo Bellomo, *Int. J. Bifurction and Chaos* (in press)
[16] R Courant and D Hilbert, *Methods of mathematical physics* (J. Wiley & Sons, New York, 1953) **vol. 1**
[17] M G Lamé, *Leçons sur la Theorie Mathematique de l' Elasticité des Corps Solides* (Bachelier, Paris, 1852)
[18] M A Pinsky, *SIAM J. Math. Anal.* **11**, 819 (1980)
[19] M V Berry and M Wilkinson, *Proc. R. Soc. London* **A356**, 15 (1984)
[20] A Shudo and Y Shimizu, *Phys. Rev.* **E47**, 54 (1993)
[21] M Shapiro and G Goelman, *Phys. Rev. Lett.* **53**, 1714 (1984)
[22] J Ford and M Ilg, *Phys. Rev.* **A45**, 6165 (1992)

PRAMANA
— journal of
physics

© Printed in India

Vol. 44, No. 2,
February 1995
pp. 109–119

On the accuracy of wavefunctions obtained by the Fourier grid Hamiltonian method

P DUTTA* and S P BHATTACHARYYA
Department of Physical Chemistry, Indian Association for the Cultivation of Science, Jadavpur, Calcutta 700 032, India
*Present address: S N Bose National Centre for Basic Sciences, DB-17, Sector I, Salt Lake, Calcutta 700 064, India

MS received 25 April 1994; revised 2 September 1994

Abstract. The quality of wavefunctions obtained by the Fourier grid Hamiltonian (FGH) method is analyzed. The criteria used for judging the quality are the extent to which virial, hypervirial and Hellmann-Feynman theorems are satisfied by the numerically computed FGH-wavefunction. The quality of the FGH-wavefunction is also examined from the point of view of local error in the wavefunction. It is shown that high quality wavefunctions can be obtained from the FGH recipe if the grid length (L) and grid spacings are chosen after properly examining the range of the potential and its nature.

Keywords. Fourier grid Hamiltonian (FGH); discrete variable representation; accurate quantum mechanical methods for bound states; accuracy of FGH wavefunction; Fourier transform methods.

PACS No. 3·65

1. Introduction

The Fourier transform method [1–2] has emerged as a very powerful tool in solving both time-dependent and time-independent quantum mechanical problems. The idea has been to use different representations to treat the kinetic and potential energy terms in evaluating the quantity $H\psi$ which is central to the time propagation, and use fast Fourier transform technique to move back and forth from one representation to the other. In a couple of recent papers, Marston and Balint-Kurti [3–4] have beautifully demonstrated that the matrix representation of the Hamiltonian ($\hat{H}$) in the vector space generated by the values of ψ and $H\psi$ on a grid of points in the coordinate space is extremely simple, requiring only the evaluation of the potential at the grid points and applications of forward and inverse Fourier transforms which analytically reduce to a finite sum over cosine functions. Once the H matrix is formed in this space, straightforward diagonalization of the Hamiltonian matrix (H matrix is symmetric in this representation as opposed to the unsymmetric H matrix encountered in the collocation method [5]), provides the bound state eigenvalues, the eigenvectors directly providing the amplitudes of the eigenfunctions of H on the grid points chosen. It may be noted that the Fourier grid Hamiltonian (FGH) method as Marston and Balint-Kurti calls it, is variational in the same sense as most other methods for calculating eigenvalues and eigenfunctions of Hamiltonian operator. In fact the FGH method is a special case of the socalled discrete variable representation (DVR) method extensively developed by Light *et al* [6–7], following the earlier work of Harris *et al* [8]. DVR has been shown to be related to the gaussian quadrature method by Dickinson and Certain [9]. Viewed from a variational point of view, the FGH method works with two crucial parameters, the grid length (L) and grid density (N/L). It is therefore important to understand how the choice of these parameters affect the accuracy of the FGH eigenfunctions and eigenvalues. Marston and Balint-Kurti [3] showed that the FGH-wavefunction for a Morse oscillator nicely coincides with the corresponding analytical solution at the grid points and that the convergence of eigenvalues with respect to the number of grid points is fast. The level of accuracy of FGH wavefunctions is of paramount importance since energy eigenvalues are always estimated one order better than the corresponding eigenfunctions. How does one check the accuracy of the computed eigenfunctions which directly affects values of other non-commuting observables? One obvious solution is to compare the FGH-wavefunction with the corresponding exact wavefunction, if known. But the FGH method is expected to be of value in cases where analytical solutions are not easily obtained or are unavailable. An alternative strategy therefore would be to check whether FGH wavefunctions obey certain theorems which the exact wavefunctions would satisfy; for example, we may think of virial and hypervirial theorems, Hellmann-Feynman theorem, Frost's local energy criterion, etc.

It may be noted in this context that the DVR is isomorphic with an approximate finite basis set representation in which some matrix elements of the Hamiltonian are determined by numerical quadrature over the DVR points. Light *et al* [6] have shown that in one dimensional problems DVR may be truncated just as in the finite basis set representation with comparable loss of accuracy in the eigenvalues. However, impact of truncation on the quality of the eigenfunctions and other non-commuting observables was not analyzed. The present paper focuses on this central question; how does the truncation affect the quality of the FGH wavefunctions? The yardstick for quality of ψ employed by us is conformability of FGH-wavefunction with certain theorems obeyed by exact wavefunctions. The analysis has special significance in the context of many dimensional extension of the FGH method [10] which leads to a rapid escalation of the dimensionality of the space in which the Hamiltonian has to be diagonalized. Alternatively, some mean-field approximations must be used. Truncation is thus inevitable in multidimensional problems. One must therefore know in advance the impact of truncation on the FGH-wavefunction at least in one-dimensional problems where the parameters of crucial importance as noted already, are the grid length and grid spacing. In what follows we attempt to achieve this objective.

2. Results and discussion

i) *FGH-wavefunction and virial theorem*

Although satisfaction of the virial theorem does not guarantee the exactness of the wave function, it is a necessary condition that accurate wavefunctions obey the virial theorem [11]. To investigate the extent to which the FGH-wavefunction conforms to this necessary condition we have solved the one-dimensional Schrödinger equation for i) harmonic and ii) quartic anharmonic oscillators by the FGH method. The wavefunctions thus obtained for different bound states have been used to calculate the expectation values required to compute the virial ratio. The νth eigenstate of the oscillator $|\psi_v\rangle$ obtained by FGH method is represented as follows:

$$|\psi_v\rangle = \sum_{i=1}^{N} \omega_i^v \Delta x |x_i\rangle \tag{1}$$

where, N is the number of grid points, ω_i^vs are the values of the vth bound state wavefunction at the grid points. The expectation value of a quantum mechanical operator A corresponding to the normalized state function $|\psi\rangle$ is

$$\langle A\rangle_\psi = \langle\psi|\hat{A}|\psi\rangle/\langle\psi|\psi\rangle = \sum_{ij}\omega_i^*\omega_j A_{ij}\Big/\sum_i|\omega_i|^2 \tag{2}$$

where

$$A_{ij} = \langle x_i|\hat{A}|x_j\rangle.$$

Virial theorem for a potential V which is homogeneous in coordinate x_i and of degree n leads to the equation

$$2\langle T\rangle = \langle\Sigma x_i \partial V/\partial x_i\rangle = n\langle V\rangle \tag{3}$$

where $\langle T\rangle$ and $\langle V\rangle$ are the expectation values corresponding to kinetic and potential energy operators, respectively. The virial equation for a harmonic oscillator potential $[V(x) = (1/2)kx^2]$ therefore takes the form

$$2\langle T\rangle_v = 2\langle V\rangle_v \quad \text{or} \quad \langle T\rangle_v/\langle V\rangle_v - 1 = 0. \tag{4}$$

For an anharmonic quartic potential $[V(x) = (1/2)kx^2 + \lambda x^4]$ the corresponding virial equation is as follows:

$$2\langle T\rangle = \langle x\partial V/\partial x\rangle = 2\langle V\rangle + 2\lambda\langle x^4\rangle \quad \text{i.e.}$$
$$\langle T\rangle_v = \langle V\rangle_v + \lambda\langle x^4\rangle_v. \tag{5}$$

Table 1. Required expectation values have been calculated using the FGH wavefunctions for the first few vibrational states of a harmonic and quartic oscillator to demonstrate that the FGH wavefunctions satisfy virial theorem.

	Harmonic oscillator*	Quartic oscillator#	
v	$[\langle T\rangle/\langle V\rangle - 1]_v$	$\langle T\rangle_v$	$[\langle V\rangle + \lambda\langle x^4\rangle]_v$
0	0·000 000 00	0·253 656 42	0·253 656 42
1	0·000 000 00	0·768 032 06	0·768 032 06
2	0·000 000 00	1·296 143 24	1·296 143 24
3	0·000 000 00	1·837 256 76	1·837 256 76
4	0·000 000 00	2·390 725 30	2·390 725 30
5	0·000 000 00	2·955 972 88	2·955 972 88
6	0·000 000 00	3·532 483 48	3·532 483 48
7	0·000 000 00	4·119 791 93	4·119 791 93
8	0·000 000 00	4·717 476 60	4·717 476 60

*see text, eq. (4) #see text, eq. (5)

The angular brackets denote expectation values of the operators in the FGH representation enclosed within [equation 2]. These expectation values [$\langle T\rangle$, $\langle V\rangle$ and $\langle x^4\rangle$] for different bound states have been calculated with the FGH-wavefunction obtained by solving the corresponding Schrödinger equation by the FGH method. The grid length ($L = 13$ a.u) and the number of grid points ($N = 69$) used in our calculations for both the cases were found to be adequate (the appropriate choices of these parameters are discussed in detail in § 3). The results corresponding to (4) and (5) [$\lambda = 0{\cdot}005$] are displayed in table 1 which confirm that the FGH-wavefunction fulfils the necessary condition of complying with the virial theorem when a sufficient number of grid points (N) are taken. The point to note is that N is not large at all. Since the representation used is discrete, scale-optimization and virial satisfaction need not be explored in the present context, as the effect of coordinate scaling can be effectively mimicked by making Δx small enough.

ii) *FGH-wavefunction and Hellmann–Feynman theorem*

The variational version of the Hellmann–Feynman (H–F) theorem [12] is often written as

$$\partial E/\partial \sigma = \langle \partial H/\partial \sigma\rangle \tag{6}$$

where, σ is a real parameter in the Hamiltonian (H) of the system under study. Here, we have dealt with three different types of one-dimensional oscillators.

a) *Harmonic oscillator*: The system of harmonic oscillator is represented by the Hamiltonian H which is a function of the force constant (k) of the oscillator as follows:

$$H(k) = T + (1/2)kx^2.$$

Differentiation of H with respect to k gives,

$$\langle \partial H/\partial k\rangle = (1/2)\langle x^2\rangle. \tag{7}$$

Since the analytical values of energy (E) as well as ($\partial E/\partial k$) as functions of k are available for the harmonic oscillator, one can measure what may be called the "deviation from the HF theorem" ($\delta_{\text{H-F}}$) by comparing the analytical $\partial E/\partial k$ value with that on the right hand side of (7) computed with the FGH-wavefunction for a specific vibrational state. The comparison is made in table 2 for a grid of 69 points. Compliance with HF theorem is easily noticeable.

b) *Quartic oscillator*: The Hamiltonian H representing the anharmonic quartic oscillator is of the form:

$$H(\lambda) = T + (1/2)x^2 + \lambda x^4. \tag{8}$$

Differentiating both sides of (8) with respect to λ we get

$$\langle \partial H/\partial \lambda\rangle = \langle x^4\rangle. \tag{9}$$

The quantity $\langle x^4\rangle$ in (9) has been calculated using the FGH wavefunctions for different bound states obtained by solving the Schrödinger equation for the quartic

Table 2. Results computed with the FGH wavefunctions have been reported to demonstrate the compatibility of the FGH wavefunctions with the Hellmann–Feynman theorem.

	Harmonic*	Quartic#		Morse&	
v	$\delta_{\mathrm{H\ F}}$	$\langle \partial H/\partial \lambda \rangle_v$	$\langle \partial E/\partial \lambda \rangle_v$	$\langle \partial H/\partial \beta \rangle_v$	$\langle \partial E/\partial \beta \rangle_v$
0	0·000 000 00	0·664 281	0·664 282	0·007 693	0·007 693
1	0·000 000 00	3·131 412	3·131 410	0·022 048	0·022 048
2	0·000 000 00	7·637 511	7·637 502	0·035 026	0·035 026
3	0·000 000 00	13·790 941	13·790 910	0·046 627	0·046 627
4	0·000 000 00	21·331 281	21·331 203	0·056 851	0·056 851

*see text, eq. (7) #see text, eq. (9) &see text, eqs (12, 13).

oscillator by the FGH method using $L = 13$ a.u. and $N = 69$. Since the analytical energy (E) and ($\partial E/\partial \lambda$) values are not available in this case, we have computed ($\partial E/\partial \lambda$), numerically. The close agreement between $\langle \partial H/\partial \lambda \rangle$ obtained from (9) and $\partial E/\partial \lambda$ (obtained numerically) as shown in table 2 again shows that the FGH wavefunctions are quite accurate if L and N are carefully chosen.

c) *Morse oscillator*: In the case of a Morse oscillator the Hamiltonian (H) is a function of the real parameter β as defined below:

$$\hat{H} = \hat{T} + D_e[1 - \exp\{-\beta(\hat{x} - x_{\mathrm{eq}})\}]^2. \tag{10}$$

The problem at hand is analytically solvable and the analytical energy eigenvalues are given by

$$E_v = \beta\sqrt{2D_e/\mu}(v + 0\cdot 5) - (\beta^2/2\mu)(v + 0\cdot 5)^2 \tag{11}$$

where, D_e is dissociation energy, μ is the reduced mass of the system and β is the non-linear parameter in the potential. Differentiating both sides of (10) with respect to β followed by quantum mechanical averaging over the state (ψ_v) [equation (2)] gives

$$\langle \partial H/\partial \beta \rangle_v = 2D_e \langle (x - x_{\mathrm{eq}})[1 - \exp\{-\beta(x - x_{\mathrm{eq}})\}][\exp\{-\beta(x - x_{\mathrm{eq}})\}] \rangle \tag{12}$$

Differentiation of (11) with respect to β on the other hand gives

$$(\partial E/\partial \beta)_v = [(v + 0\cdot 5)\sqrt{2D/\mu} - (\beta/\mu)(v + 0\cdot 5)^2] \tag{13}$$

The computed results displayed in table 2 are the quantities corresponding to (12) and (13) for the first few vibrational states ($v = 0 - 4$) and are just as the exact wavefunctions are supposed to give.

iii) *Hypervirial theorems and FGH eigenfunctions*

If $\hat{A}$ is a hermitian operator such that the set of trial function is invariant under the continuous family of unitary transformations $U(\alpha) = e^{i\alpha A}$ (α real parameter), then a

Table 3. Results computed with the FGH wavefunctions for the first few states of a Morse oscillator [see eq. (14)] have been reported to demonstrate the compatibility of the FGH wavefunctions with the diagonal hypervirial theorem.

v	$\langle e^{-\beta u}\rangle_v$	$\langle e^{-2\beta u}\rangle_v$
0	0·978 2011	0·978 2011
1	0·934 6037	0·934 6037
2	0·891 0072	0·891 0072
3	0·847 4115	0·847 4115
4	0·803 8113	0·803 8113
5	0·760 2138	0·760 2138
6	0·716 6163	0·716 6163
7	0·673 0188	0·673 0188

variationaly selected ψ will satisfy the condition

$$\langle\psi|[\hat{H},\hat{A}]|\psi\rangle = 0$$

for any state ψ. The condition has been known as the diagonal hypervirial theorem [13–14]. The condition is obviously obeyed by an exact wavefunction. For a Morse oscillator [$V(x)$], one can show [15] that the diagonal hypervirial theorem leads to the following relation:

$$\langle e^{-\beta u} - e^{-2\beta u}\rangle_v = 0$$

i.e.

$$\langle e^{-\beta u}\rangle_v = \langle e^{-2\beta u}\rangle_v \tag{14}$$

where the potential $V(x)$ is represented as follows:

$$V(x) = D[e^{-2\beta u} - 2e^{-\beta u}], \quad u = (x - x_{\mathrm{eq}}).$$

We have reported in table 3 the expectation values on the left and right hand side of (14) computed with FGH wavefunctions for the first few states of a Morse oscillator. A reasonable choice of grid ensures compatibility of FGH wavefunctions with the diagonal hypervirial theorem.

iv) *FGH-wavefunctions and local error*

As demonstrated in [3] and to be discussed further in § 3, the FGH method with adequate grid length (L) and number of grid points (N) can provide highly accurate value of global energy or energy eigenvalues (E)

$$E = \langle\psi|H|\psi\rangle/\langle\psi|\psi\rangle. \tag{15}$$

But one may ask whether the FGH wavefunctions are equally good from a local point of view. Needless to mention that an exact wavefunction is expected to satisfy

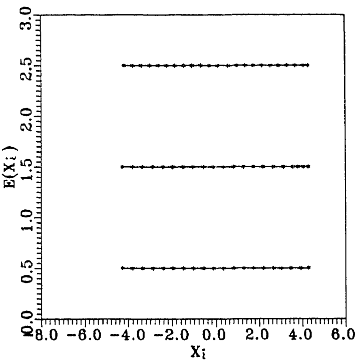

Figure 1. Energy values $E_v(x_i)$ (represented as $***$) at all the grid points $\{x_i\}$ obtained by the FGH method are the same and equal to the corresponding energy eigenvalue (denoted by solid line) [$v = 0, 1$ and 2].

certain local criteria as well [16]. The Schrödinger equation at a coordinate point (x_i) is

$$H\psi(x_i) = E(x_i)\psi(x_i),$$
$$E(x_i) = H\psi(x_i)/\psi(x_i). \tag{16}$$

In general, the local energy $E(x_i)$ in (16) is coordinate dependent for an approximate wavefunction while the exact wavefunction provides local energy values $(E(x_i))$ independent of x_i and equal to the global E of (15). As the eigenvectors obtained by FGH method directly gives the amplitudes or values of the wavefunction at the grid points, the question now turns out to be whether the $E(x_i)$ calculated (eq. 16) at each grid point (x_i) are the same and is equal to the value E in (15)?

To answer this question we have employed the FGH method for a harmonic oscillator and obtained both the energy eigenvalues (E_v) (eq. 15) and the wavefunctions $[\psi_v(x)]$. The $E_v(x_i)$ values at all the grid points $\{x_i\}$ have been calculated by invoking a suitable numerical differentiation scheme to compute the $H[\psi(x_i)]$ part in (16). The results, as is clear from figure 1 which displays the profiles of $E_v(x_i)$ for $v = 0, 1$ and 2 at the grid points $\{x_i\}$, answer the question in the affirmative.

3. Convergence properties

As far as the success of any numerical method for solving Schrödinger equation is concerned, the computational cost that the method involves is no less important than the accuracy of the energy eigenvalues provided by the method. As the method requires matrices of order $(N \times N)$ to be diagonalized, where N is the number of grid points, the convergence property of the method with respect to N plays a key role in its success. Another important parameter, the total length (L) of the grid also needs to be optimized to provide results of desired accuracy. In [3] Marston and Balint-

Kurti have used $L = 1{\cdot}5$ times the outer classical turning point of the highest bound state in the case of a Morse oscillator. We think that it would be worthwhile to have a closer look into the convergence properties of the method with respect to both L and N. In a way these two parameters together conform to what may be analogous to a measure of completeness of the basis set in a finite basis set representation. For the purpose at hand, we have done two sets of calculations for two types of exactly solvable potential (harmonic and Morse):

i) Keeping N fixed and sufficiently high ($N = 99$) the grid length (L) has been varied from a small value (7·5 a.u) to an appreciably high value for solving the Schrödinger equation by the FGH method.
ii) The same course of calculations have been done by varying the number of grid points (N) keeping L fixed at an adequately high value ($L = 13$ a.u).

To demonstrate the convergence properties, one obvious choice is to check the convergence of energy with respect to N or L or both. In addition to that one can enquire about the convergence of FGH-wavefunctions in the context of satisfaction of the virial and Hellmann–Feynman theorems. For this purpose, let us define three terms δ_{E}, δ_{VT} and $\delta_{\mathrm{H\text{-}F}}$. δ_{E} measures the deviation of computed energy obtained by using particular values of N and L, from the exact or converged energy, whichever is available, i.e.

$$\delta_{\mathrm{E}} = E(\text{computed}) - E(\text{exact or converged})$$

δ_{VT} stands for deviation from the virial theorem and $\delta_{\mathrm{H\text{-}F}}$ for deviation from the Hellmann–Feynman theorem. For harmonic potential they are measured by

$$\delta_{\mathrm{VT}} = \{\langle T\rangle/\langle V\rangle - 1\} \quad \text{and} \quad \delta_{\mathrm{H\text{-}F}} = \{\langle \partial H/\partial k\rangle - (1/2)\langle x^2\rangle\}. \tag{17}$$

Both δ_{VT} and $\delta_{\mathrm{H\text{-}F}}$ are zero for exact wavefunctions [eqs (4) and (7)]. In figure 2 the profiles of δ_{E}, δ_{VT} and δ_{HF} values for $\nu = 9$ have been displayed against L (grid length) while figure 3 shows the convergence of δ_{E}, δ_{VT} and δ_{HF} for different N values for $\nu = 9$. In each case, the convergence is near exponential so that highly accurate wavefunctions can be obtained at a low computational cost.

Now the question arises whether the *adequate* values of N and L are system (potential) and state dependent? If so, how sensitive are these values? To answer these questions we have done a series of calculations to see the convergence of energy of ground as well as of higher energy states of the quartic anharmonic oscillator (eq. 8) for different values of the coupling strength (λ varies from 0·01 to 5·0). Figure 4 displays the variation of *adequate* N i.e. the minimum N value required to get the converged energies (E_ν, $\nu = 0, 4, 9$) as a function of the coupling strength (λ) for a fixed value of $L = 13$. The variation of *adequate* L (using fixed and high value of $N = 99$) for three different states ($\nu = 0, 4$ and 9) as a function of λ is demonstrated in figure 5. Both the figures show that the variation in N or L is sharp initially but saturates quickly as λ increases. The convergence profiles for three different states are different but the trend of variation is the same in each case. It is to be noted that the difference in adequate N or L values for different states is not much which suggests that the method can be used for providing good wavefunctions even for higher states at reasonably low computational cost. However, for certain long range potentials with singularity at the origin (e.g. $-1/x$, $-1/x^2$, $-1/|x|$, etc.), our experience so far indicates that for an appropriately large length L, the energy eigenvalues do not show

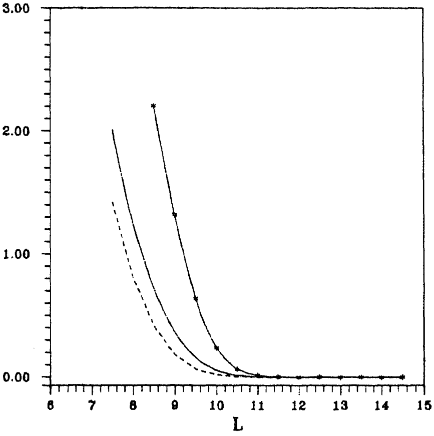

Figure 2. Profiles δ_{VT}(—— line), δ_{HF}(---- line) and δ_E(−∗−∗−∗−) for the 10th vibrational state ($v = 9$) of harmonic oscillator [see text, eq. 17] as a function of the grid length (L).

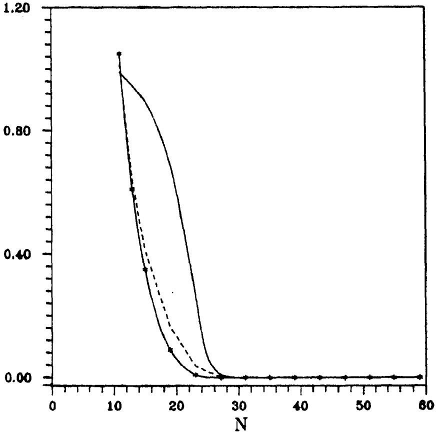

Figure 3. Convergence of δ_{VT}(—— line) and δ_{HF}(---- line) and δ_E(−∗−∗−∗−) for the 10th vibrational state ($v = 9$) of harmonic oscillator [see text, eq. 17] for different number of grid points (N) used.

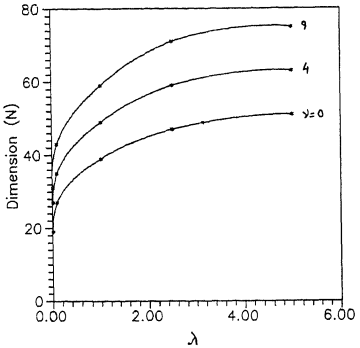

Figure 4. The variation of adequate N for $\nu = 0, 4, 9$ as a function of oscillator strength (λ) of a quartic anharmonic oscillator (see eq. 8), for $L = 13$ a.u.

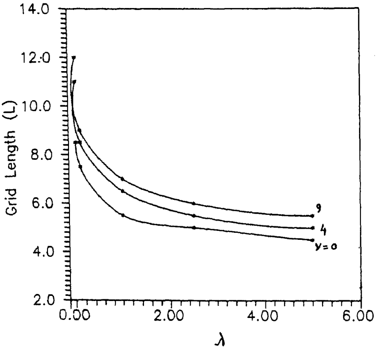

Figure 5. The variation of adequate L (using $N = 99$) for three different states ($\nu = 0, 4$ and 9) as a function of λ for the same system as in figure 4.

monotonic convergence with respect to the number of grid points (N) or grid density (L/N). For a given L, there appears to be an optimum grid density for which best eigenvalues are obtained. The reason for this non-monotonicity of the convergence is intimately related with the problem of representing a state on the discretized co-ordinate or momentum space. Further analysis is on the way at present.

4. Conclusion

The FGH method has been shown to provide very accurate wavefunction as well as energy eigenvalues. Both the local and global properties of FGH wavefunctions are generally satisfactory if sufficient number of grid points and an appropriate grid length are chosen. Convergence with respect to grid length (L) and number of points (N) is nearly exponential. In a many-dimensional application therefore, effective dimensionality of the problem can be kept within limits with suitable truncation along each axis. A detailed analysis of the accuracy of the wavefunctions for the many-dimensional cases will be reported in due course.

Acknowledgements

The authors are greatly indebted to the CSIR, Govt. of India, New Delhi for a research grant.

References

[1] R Kosloff and H Tal-Ezer, *Chem. Phys. Lett.* **127**, 223 (1986)
[2] R Kosloff, *J. Phys. Chem.* **92**, 2087 (1986)
[3] C C Marston and G G Balint-Kurti, *J. Chem. Phys.* **91**, 3571 (1989)
[4] G G Balint-Kurti, C L Ward and C C Marston, *Comput. Phys. Commun.* **67**, 285 (1991)
[5] W Yang and A C Peet, *J. Chem. Phys.* **92**, 522 and references cited therein (1990)
[6] J C Light, I P Hamilton and J V Lill, *J. Chem. Phys.* **82**, 223 (1986)
S E Choi and J C Light, *J. Chem. Phys.* **90**, 2593 (1984)
[7] Z Bacic, R M Whitnall, D Brown and J C Light, *Comput. Phys. Commun.* **51**, 35 (1988)
R M Whitnell and J C Light, *J. Chem. Phys.* **90**, 1774 (1989)
[8] D O Harris, G G Enyerholm and W D Gwinn, *J. Chem. Phys.* **43**, 1515 (1965)
[9] A S Dickinson and P R Certain, *J. Chem. Phys.* **49**, 4209 (1968)
[10] P Dutta, S Adhikary and S P Bhattacharya, *Chem. Phys. Lett.* **212**, 677 (1993)
[11] P O Lowdin, *J. Mol. Spectrosc.* **3**, 46 and references cited therein
[12] R P Feynman, *Phys. Rev.* **56**, 340
H Hellmann, in *Ein fuhruns in die Quantenchemie* (Dennticke, Leipzig, 1937) p 285
[13] S T Epstein, in *The variational methods in quantum chemistry*, (Academic Press, New York, 1974) p. 92
[14] J O Hirschfelder, *J. Chem. Phys.* **33**, 1462 (1960)
[15] J Morales, A Palma and L Sandoval, *Int. J. Quantum. Chem.* **29**, 211
[16] A A Frost, *J. Chem. Phys.* **25**, 1150 (1956)

[redacted]

PRAMANA
— journal of
physics

© Printed in India

Vol. 44, No. 2,
February 1995
pp. 121–131

Conversion of a chaotic attractor into a strange nonchaotic attractor in an one dimensional map and BVP oscillator

S RAJASEKAR
Department of Physics, Manonmaniam Sundaranar University, Tirunelveli 627 002, India

MS received 4 July 1994; revised 21 October 1994

Abstract. In this paper we investigate numerically the possibility of conversion of a chaotic attractor into a nonchaotic but strange attractor in both a discrete system (an one dimensional map) and in a continuous dynamical system – Bonhoeffer–van der Pol oscillator. In these systems we show suppression of chaotic property, namely, the sensitive dependence on initial states, by adding appropriate i) chaotic signal and ii) Gaussian white noise. The controlled orbit is found to be strange but nonchaotic with largest Lyapunov exponent negative and noninteger correlation dimension. Return map and power spectrum are also used to characterize the strange nonchaotic attractor.

Keywords. One dimensional map; Bonhoeffer-van der Pol oscillator; controlling of chaos; strange nonchaotic attractor.

PACS Nos 05·45; 42·50

1. Introduction

In recent years there has been increasing interest in the study of controlling of chaotic motion in both theoretical model equations and experimental systems [1–8]. There are also recent attempts to use chaos profitably, by synchronizing chaotic orbits [9–11]. The existing control methods are capable of converting a chaotic motion into a regular dynamics either by stabilizing an unstable periodic orbit embedded in the chaotic attractor [2, 4–7] or by creating a new periodic orbit [1, 3, 7, 8]. One of the motivations for controlling chaotic motion is its extreme sensitive dependence on initial conditions. In the chaotic regime two nearby trajectories diverge exponentially until they become completely uncorrelated and hence future prediction becomes inaccurate. It is thus important to investigate the possibility of suppression of sensitive dependence on initial conditions and maintaining strangeness of the attractor instead of stabilizing a periodic orbit.

In this paper we wish to make a detailed study of conversion of chaotic attractor into a strange nonchaotic attractor by adding appropriate i) chaotic signal and ii) Gaussian noise. We carry out our investigation in both a discrete system [12, 13]

$$x_{n+1} = x_n \exp(A(1 - x_n)), \quad x_n > 0 \tag{1}$$

and in a continuous dynamical system, the Bonhoeffer-van der Pol (BVP) oscillator [7]

$$\dot{x} = x - x^3/3 - y + f \cos t, \tag{2a}$$

$$\dot{y} = c(x + a - by). \tag{2b}$$

In (2) a, b, c are constant parameters and f is the amplitude of the external periodic force. Recently, Carroll and Pecora [14] studied the effect of added chaotic and noise signals in a Duffing oscillator circuit in a different context. They studied the effect of added signal on flipping of the state of the system between two coexisting periodic attractors. Stochastic resonance has been observed. In our present study we use chaotic and noise signals in the context of controlling of chaos.

Firstly, we consider the one dimensional map (1). We fix the parameter A in a chaotic regime. Then a chaotic solution is added to the system. The dynamics of the system is studied by varying the coupling parameter. The key observation is that strange nonchaotic attractor replaces actual chaotic attractor of the map for coupling parameter value greater than certain critical value. Lyapunov exponent, power spectrum, correlation dimension are used to characterize strange nonchaotic attractor. The effect of Gaussian noise has also been studied by varying the amplitude of the noise for a fixed value of mean and standard deviation. Strange nonchaotic attractor occurs for a range of amplitude of the noise signal. These results are presented in §2.

Secondly, we report our studies on the BVP equation (2) in §3. The parameters a, b, c and f are fixed in a chaotic region. Chaotic solution generated from the logistic map $x_{n+1} = 4x_n(1 - x_n)$ is added to the right hand side of (2a). Here again, chaotic attractor is destroyed and strange nonchaotic attractor is found to occur for a range of amplitude of the chaotic signal. Finally, §4 contains summary and conclusions.

2. Strange nonchaotic attractor in the map (1)

In this section we study the effect of chaotic solution and Gaussian white noise in the map (1). Map (1) is often used in theoretical studies of population growth with x_n as the population density at time n. First the dynamics of equation (1) is studied as a function of A. Bifurcation diagram 1a illustrate the period doubling route to chaos. The one dimensional Lyapunov exponent of the attractors of (1) is estimated using the relation

$$\lambda = \lim_{n \to \infty} (1/n) \sum_{i=1}^{n} \ln|f'(x_i)|, \tag{3a}$$

where

$$f'(x) = \exp(A(1 - x)) - Ax\exp(A(1 - x)). \tag{3b}$$

The variation of Lyapunov exponent against the parameter A is plotted in figure 1b. As expected λ is negative in the regular regime and is positive in the chaotic regime. Chaotic motion is found for $A = 3$. The Lyapunov exponent of this chaotic attractor is $\approx 0{\cdot}39$. Now, we investigate the effect of addition of chaotic signal to (1).

2.1 *Effect of chaotic signal*

The map with the addition of chaotic solution can be written as

$$x_{n+1} = x_n \exp(B(1 - x_n)) + Cy_n, \tag{4}$$

where y_n is the chaotic solution generated from the map (1). We fix B at 3. First we study the influence of chaotic solution generated with $A = 3$ from (1). Later, we show the effect of chaotic solution of (1) generated with different values of A.

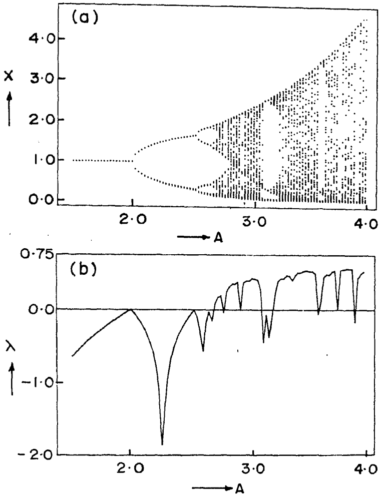

Figure 1. **a**) Bifurcation diagram showing period doubling route to chaos. **b**) Calculated Lyapunov exponent against the parameter A.

Figure 2 shows the estimated Lyapunov exponent as a function of the parameter C. From this figure we note that λ is positive for $C < C^* \approx 0{\cdot}075$ while it takes negative value for $C > C^*$. Lyapunov exponent with negative value implies that the solution is insensitive to small disturbance in the initial conditions. In other words, chaotic property is suppressed for $C > C^*$ and hence the attractor is nonchaotic. Figure 3 shows the attractor in x_n versus x_{n+1} plane for $C = 0{\cdot}1$. The Lyapunov exponent of the attractor is $-0{\cdot}12$. Further, we have estimated correlation dimension D_c of the controlled attractor. To calculate D_c we used the algorithm proposed by Grassberger and Proccacia [15]. Suppose $x_i (i = 1, 2, \ldots, N)$ represents the attractor points in the return map. We count the number of points within a ball of radius r centred at each x_i for a set of N points. The correlation function is defined by

$$C(r) = \lim_{N\to\infty} (1/N^2) \sum_i \sum_j H(r - |x_i - x_j|), \tag{5a}$$

where $H(\Theta) = 1$ for $\Theta > 0$ and $H(\Theta) = 0$ for $\Theta < 0$. Then , the correlation dimension is given by

$$D_c = \lim_{r\to 0} \ln C(r)/\ln(r). \tag{5b}$$

D_c is the slope in the $\ln C(r)$ versus $\ln(r)$ plot. The correlation dimension of the

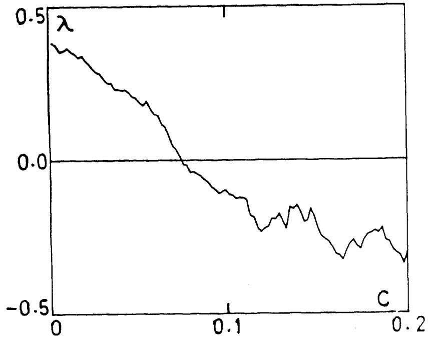

Figure 2. Estimated Lyapunov exponent versus the parameter C.

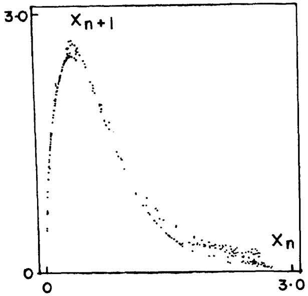

Figure 3. Strange nonchaotic attractor of equation (4) for $C = 0{\cdot}1$.

attractor shown in figure 3 is estimated as 0·82 where we have used $N = 10^4$. The attractor is thus strange. The negative Lyapunov exponent, noninteger dimension and return map (figure 3) imply that the controlled attractor is strange but nonchaotic. Strange nonchaotic attractor has been previously found to occur in numerical studies of many nonlinear systems and also in actual experiments [16–20].

The occurrence of strange nonchaotic attractor is further confirmed by power spectrum analysis. For a strange nonchaotic attractor the number of peaks $N(\sigma)$ in a power spectrum exceeding a threshold amplitude σ scale as [21]

$$N(\sigma) \propto \sigma^{-\alpha}, \quad 1 < \alpha < 2 \tag{6}$$

while for quasiperiodic attractor

$$N(\sigma) \propto \ln(1/\sigma). \tag{7}$$

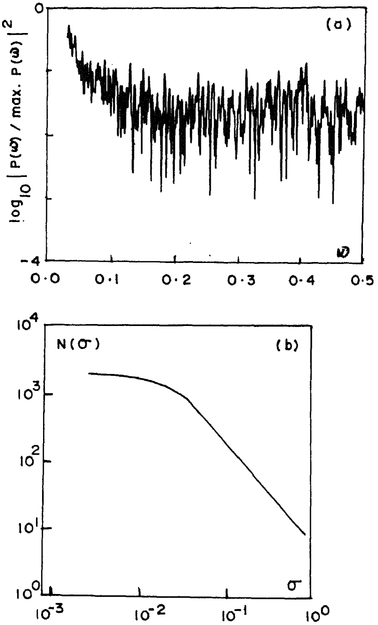

Figure 4. **a)** Power spectrum of the strange nonchaotic attractor (figure 3). **b)** The log–log plot of the threshold dependence of the number of peaks $N(\sigma)$ with the amplitude greater than the threshold σ.

Power spectrum of the attractor (figure 3) is obtained using fast Fourier transform with 4096 data points and is shown in figure 4a. The variation of $N(\sigma)$ against the threshold amplitude σ on log–log scale is plotted in figure 4b. The value of the scaling exponent α is estimated as 1·45. This is in agreement with the power-law scaling relation (6).

We have also used another measure, the invariant density which shows differences between the chaotic and strange nonchaotic attractors. We measured the densities $P(x)$ using 10^4 data points with the results shown in figure 5a for the uncontrolled chaotic orbit and figure 5b for the strange nonchaotic attractor. $P(x)$ is much more sharply defined for chaotic attractor than for the strange nonchaotic attractor. Moreover, the strange nonchaotic attractor displays a considerably smaller amplitude.

Strange nonchaotic attractor is found for C values for which $\lambda \leqslant 0$. Figure 6 shows the variation of correlation dimension as a function of the parameter C. Figures 2 and 6 clearly support the occurrence of strange nonchaotic attractor for $C > C^*$. In the map (4) the interaction between dynamic and stochastic (coupling term) forces gives

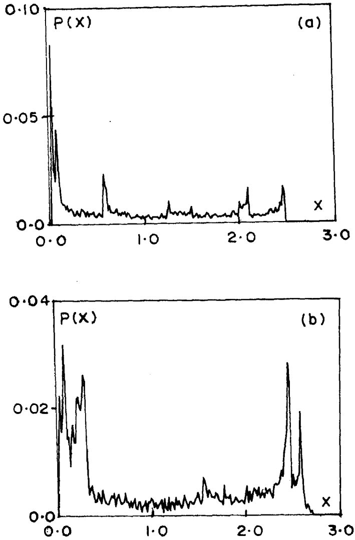

Figure 5. Calculated probability density of the **a**) uncontrolled chaotic attractor and **b**) strange nonchaotic attractor shown in figure 3.

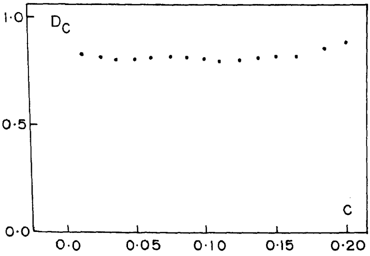

Figure 6. Variation of correlation dimension as a function of C.

rise to the strange nonchaotic attractor. The effect of various nonlinear coupling terms such as y^3, $\sin y$ and $\exp(y)$ has also been studied. The critical value C^* above which strange nonchaotic attractor occurs for the coupling terms y^3, $\sin y$ and $\exp(y)$ are found to be 0·0425, 0·168 and 0·0225 respectively. Further, we have carried out our analysis using the chaotic solution generated for various values of A. For C

values in the interval (0, 0·2) we estimated Lyapunov exponent of attractors of (4) and determined the value of C^* above which λ becomes negative. Table 1 gives the C^* value for different A values.

2.2 *Effect of Gaussian white noise*

In this subsection we study the effect of noise added to the chaotic solution of (1). The map (1) with external noise can be written as

$$x_{n+1} = x_n \exp(A(1 - x_n)) + D\eta(n), \tag{8}$$

where $\{\eta(n)\}$ are independent random numbers with mean m and standard deviation σ. We fix A at 3. We study the influence of noise by varying the amplitude D of the noise for $m = 0{\cdot}2$ and $\sigma = 0{\cdot}1$. We used the Box-Müller algorithm to generate Gaussian random variables from uniform random variables. Figure 7 shows the mean Lyapunov exponent obtained by averaging over 500 realisations of $\eta(n)$ as a function of D. For

Table 1. Estimated critical value C^* for different A values used to generate chaotic solution. The generated chaotic solution is added to equation (4).

A	C^*
2·8	0·051
2·9	0·067
3·0	0·075
3·1	0·064
3·3	0·101
3·4	0·086
3·5	0·090
3·7	0·187
3·8	0·158

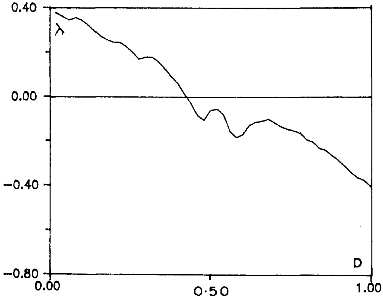

Figure 7. Estimated Lyapunov exponent versus the amplitude D.

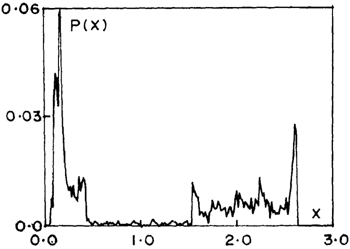

Figure 8. Calculated probability density function of the strange nonchaotic attractor with $D = 0{\cdot}6$.

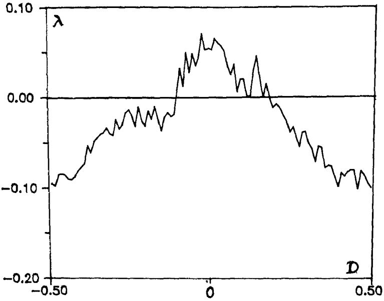

Figure 9. Maximal Lyapunov exponent as a function of D for the BVP oscillator.

$D < D^*$ the Lyapunov exponent is positive. In this case the long time motion is still chaotic. For $D > D^*$ the Lyapunov exponent is negative and the attractor is nonchaotic. We have estimated the probability density function $P(x)$ for $D = 0{\cdot}6$ and is plotted in figure 8. Here again we note that $P(x)$ is much more sharply defined for chaotic attractor (figure 5a) than for the strange nonchaotic attractor. Further, the height of the peaks are considerably smaller for strange nonchaotic attractor.

3. Strange nonchaotic attractor in BVP oscillator

The BVP oscillator with a chaotic signal added to the periodic driving force can be written as

$$\dot{x} = x - x^3/3 - y + f\cos t + Du, \tag{9a}$$

$$\dot{y} = c(x + a - by), \tag{9b}$$

where $u(t)$ is the chaotic solution generated from the logistic map

$$u_{n+1} = 4u_n(1 - u_n). \tag{10}$$

Iteration of map (10) lies in the interval (0, 1). The solution is then converted into the range $(-1, 1)$. D in (9a) is the amplitude of the chaotic solution added to the driving force. The parameters a, b, c are fixed at 0·7, 0·8 and 0·1 respectively. In the absence of $Du(t)$ period doubling phenomenon culminating in chaos is observed when f is

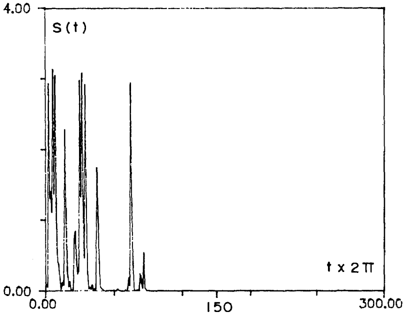

Figure 10. Calculated $S(t)$ versus t for $D = 0{\cdot}3$.

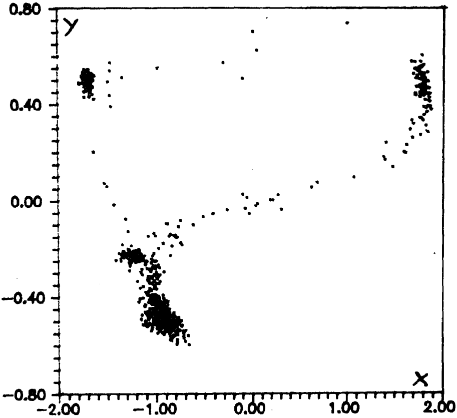

Figure 11. Strange nonchaotic attractor of the BVP equation (9) with $D = 0{\cdot}3$.

increased from small value. At $f = 0{\cdot}7182$ the system enters into a chaotic domain. We fix f at 0·74 for which a well developed chaotic motion is observed. Chaotic solution generated from the logistic map (10) is added to the system after every $(2\pi/50)$ time step. The long time behaviour of the system is analysed using Lyapunov exponent. Figure 9 shows the variation of the maximal Lyapunov exponent as a function of D. It is seen that for a range of D values λ is negative, that is, the motion is nonchaotic. We can illustrate the influence of added chaos signal more clearly by looking at the distance $S(t)$ between two orbits starting from two nearby initial conditions. The distance $S(t)$ between two trajectories starting from $X(0)$ and $X'(0)$ is given by

$$S(t) = \|X(t) - X'(t)\|.$$

For regular behaviour $S(t)$ will decay to zero in the limit $t \to \infty$. On the other hand, it will vary irregularly with time for chaotic motion. In figure 10 we report the calculated $S(t)$ for $D = 0{\cdot}3$. The $S(t)$ diminishes to zero after short-lived irregular variation. This clearly supports the loss of sensitive dependence on initial conditions. Figure 11 shows the Poincaré map of the attractor for $D = 0{\cdot}3$. The λ of the attractor is negative as seen from figure 9. From the negative value of the Lyapunov exponent and Poincaré map (figure 11) we conclude that the controlled attractor is strange nonchaotic. Strange nonchaotic attractor has been observed in the BVP equation when appropriate Gaussian white noise is added to the system instead of chaos [7].

4. Summary and conclusions

In this paper we have studied the effect of external chaotic signal and noise term in an one-dimensional map and BVP equation. To these systems chaos from deterministic dynamical systems is added. However, to the map (1) chaotic solution from the same system is added whereas chaotic signal from a different dynamical system is added to the BVP equation. When a chaotic solution is added to these systems strange nonchaotic attractor is found to replace the strange chaotic attractor for a range of coupling strength. Strange nonchaotic attractor is also observed when Gaussian noise is added instead of chaotic signal. Though the controlled orbit still appears complex, it is structurally stable and small errors in an initial conditions will not have strong effect on the long time prediction. Further, chaos is not always an unwanted phenomenon. It can be utilized for useful purposes. In such a case, conversion of a chaotic attractor to a strange nonchaotic attractor may provide much better predictability.

Acknowledgements

The author thanks Sudeshna Sinha for many useful suggestions and K P N Murthy for critical reading of the manuscript and stimulating discussion. The numerical calculations reported in this paper were done at the computer centre, Indira Gandhi centre for atomic research, Kalpakkam.

References

[1] B A Huberman and L Lumer, *IEEE Trans. Circuits Syst.* **37**, 547 (1990)
[2] E Ott, C Grebogi and J Yorke, *Phys. Rev. Lett.* **64**, 1196 (1990)
[3] R Lima and M Pettini, *Phys. Rev.* **A41**, 726 (1990)

[4] J Singer, Y Z Wang and H H Bau, *Phys. Rev. Lett.* **66**, 1123 (1991)
[5] K Pyragas, *Phys. Lett.* **A170**, 421 (1992)
[6] S Bielawaski, D Derozier and P Glorieux, *Phys. Rev.* **E49**, R971 (1994)
[7] S Rajasekar and M Lakshmanan, *Physica* **D67**, 282 (1993)
[8] S Rajasekar, *Pramana – J. Phys.* **41**, 295 (1993)
[9] L M Pecora and T L Carroll, *Phys. Rev. Lett.* **64**, 821 (1990)
[10] M de Sousa Vieira, A J Lichtenberg and M A Lieberman, *Int. J. Bifur. Chaos* **1**, 691 (1991)
[11] T Endo and L O Chua, *Int. J. Bifur. Chaos* **1**, 701 (1991)
[12] R M May, *Nature (London)* **261**, 459 (1976)
[13] J G Milton and J Belair, *Theor. Popul. Biol.* **37**, 273 (1990)
[14] T L Carroll and L M Pecora, *Phys. Rev. Lett.* **70**, 576 (1993)
[15] P Grassberger and I Proccacia, *Physica* **D13**, 34 (1984)
[16] M Ding, C Grebogi and E Ott, *Phys. Lett.* **A137**, 167 (1989)
[17] W Ditto *et al*, *Phys. Rev. Lett.* **65**, 533 (1990)
[18] J Heagy and W Ditto, *J. Nonlin. Sci.* **1**, 423 (1991)
[19] T Kapitaniak, E Ponce and J Wojewoda, *J. Phys.* **A23**, L383 (1990)
[20] T Kapitaniak and M S El Naschi, *Phys. Lett.* **A154**, 249 (1991)
[21] C Grebogi, E Ott, S Pelikan and J A Yorke, *Physica* **D13**, 261 (1984)

PRAMANA
— journal of
physics

© Printed in India

Vol. 44, No. 2,
February 1995
pp. 133–144

Wormholes in higher dimensions with Gauss–Bonnet terms

B C PAUL[†], A BEESHAM* and S MUKHERJEE[†]*
[†]Physics Department, North Bengal University, District Darjeeling, 734 430, India
*Department of Applied Mathematics, University of Zululand, Kwa-dlangezwa, South Africa

MS received 17 September 1994

Abstract. A class of wormhole solutions permitted in a theory with Gauss–Bonnet terms in the gravitational action in higher dimensions have been studied. The case of de-Sitter type instantons, with a compact inner space, are of particular interest here. Some of the configurations, when continued analytically to the Lorentzian metric lead to the standard inflationary universe. Some multiple-sphere configurations of the type studied by Myers have also been noted. The Euclidean action for the solutions has been calculated and the relevance of the solutions in the quantum creation of the universe has been considered.

Keywords. Wormholes; higher dimensional cosmology; Gauss-Bonnet terms; quantum cosmology.

PACS Nos 04·20; 04·60; 98·80

1. Introduction

Model building in higher dimensions was initiated by Kaluza and Klein (KK) [1] who tried to unify gravity with electromagnetic interaction by introducing an extra dimension. The approach has been revived and considerably generalized after realizing that many interesting theories of particle interactions need more than four dimensions for their formulation. It is considered essential to check if consistent cosmological solutions, which can accommodate these theories, are also allowed. Attempts have been made to build cosmological models [2] in higher dimensions which may undergo a spontaneous compactification leading to a product space $M^4 \times M^d$, with M^d describing the compact 'inner' space. The advent of superstrings [3] saw a spurt in model building activities in higher dimensions. Zweibach [4] suggested that the string corrections to Einstein action up to first order in the slope parameter α' and fourth power of momenta should be a term of the type α' (GB), where the Gauss-Bonnet term is given by $(\mathrm{GB}) = R_{ABCD}R^{ABCD} - 4R_{AB}R^{AB} + R^2$, with R_{ABCD}, R_{AB}, R denoting the Riemann tensor, Ricci tensor and Ricci scalar respectively. Some attempts [5, 6] have already been made to build cosmological models including the Gauss-Bonnet terms in the action. Bailin *et al* [6] found that the GB terms permit an approximate stable Friedmann solution with a slowly varying compact internal space which is unstable with the $R_{ABCD}R^{ABCD}$ term only. Lorentz-Petzold [7] obtained cosmological solutions with the GB terms in the presence of matter. A consistent scenario of the higher-dimensional early universe and its subsequent evolution into a 4-dimensional FRW stage remains to be fully developed. The problem is seen clearly in the standard KK models, in which the dilaton field in the effective 4-dimensional theory, has negative kinetic energy and an energy spectrum unbounded from below. With the Einstein-Hilbert action, one may conformally rescale the 4-dimensional metric which converts the dilaton into a self interacting scalar field, minimally coupled to gravity and the ground state becomes stable against its fluctuations. However, the method does not work if GB-terms are present. Thus, a theory with GB-terms with geometric fields (one or more inflatons) is an intrinsically unstable theory. However, we have discussed elsewhere [8] a cosmological model with an action in which R and the GB terms have opposite signs, contrary to what one obtains in the small slope expansion of string theory. However, with appropriate compactification, one can recover at a large time the usual Einstein equations [8]. The calculations showed the rich structure of the theories with quadratic curvature terms which may be useful in model building.

A related exercise is to consider quantum cosmology in higher dimensions. Here, a provision has to be made for considering possible topological fluctuations. In the Euclidean path-integral formulation of quantum cosmology, a special role is supposed to be played by wormholes, which are described often by instanton-like configurations. These are the solutions of the D-dimensional Euclidean field equations, connecting two given $(D-1)$ surfaces. It has been suggested by Baum [9], Hawking [10] and Coleman [11] that inclusion of these wormholes may provide a mechanism for the vanishing of cosmological constant. Although it is not clear if this mechanism is really self-consistent, it is nevertheless important to identify and understand explicitly wormhole solutions in as wide a class of theories as possible. Instanton solutions have been noted already in a number of higher-dimensional theories. Gonzalez-Diaz [12], in particular, has studied the solution to a six dimensional Einstein-Gauss- Bonnet theory in $R^1 \times M^5$ manifold and has obtained the Tolman-Hawking wormhole. The purpose of this paper is to study possible instanton configurations in a higher dimensional model $(D \geqslant 6)$ in which the action includes the Gauss-Bonnet terms viz. eq. (1). We will restrict to manifolds of the type $M^4 \times M^d$, where M^d is a compact space of dimension d. We intend to study the role of the GB terms in a simple situation in which the compact space is assumed to have a constant radius, smaller than the outer space scale factor. The effect of a space or time-dependent inflaton field will be taken up elsewhere.

2. Field equations

We consider an Euclidean action which includes a cosmological constant, the GB terms and a matter field term:

$$I_E = \int \sqrt{g}\, d^D x [C_0 + C_1 R + C_2 (\mathrm{GB}) + L_m], \tag{1}$$

where $A, B, \ldots$ are $D(=1+3+d)$ dimensional indices; C_0, C_1 and C_2 are dimensional constants. We consider the minisuperspace metric

$$\mathrm{d}s^2 = \mathrm{d}\tau^2 + a^2(\tau)\mathrm{d}\Omega_3^2 + b^2(\tau)\mathrm{d}\Omega_d^2, \tag{2}$$

with $\mathrm{d}\Omega_3^2 = \dfrac{\mathrm{d}r^2}{1-k_3 r^2} + r^2(\mathrm{d}\theta^2 + \sin^2\theta\,\mathrm{d}\phi^2)$ and $\mathrm{d}\Omega_d^2$ is its d-dimensional generalization. We shall choose $k_3 = k_d = 1$, and assume that the internal space is compact, $b = b_0$. The solutions are thus relevant for tunneling processes of a FRW universe with additional d compact dimensions.

The energy momentum tensor is written as

$$T_{AB} = [\rho, p g_{ij}, p' g_{mn}], \tag{3}$$

with $i, j = 1, 2, 3$ and $m, n = 4, \ldots, d$. The field equations for the metric (2) becomes $[\Lambda = C_0/2]$

$$-C_1\left[\frac{d(d-1)}{2}\frac{1}{b_0^2} - 3\left(\frac{\dot{a}^2}{a^2} - \frac{1}{a^2}\right)\right]$$

$$= \Lambda - \rho + C_2\left[\frac{d(d-1)(d-2)(d-3)}{2b_0^4} - \frac{6d(d-1)}{b_0^2}\left(\frac{\dot{a}^2}{a^2} - \frac{1}{a^2}\right)\right] \tag{4a}$$

$$-C_1\left[\frac{d(d-1)}{2b_0^2} - 2\frac{\ddot{a}}{a} - \left(\frac{\dot{a}^2}{a^2} - \frac{1}{a^2}\right)\right] = \Lambda + p$$

$$+ C_2\left[\frac{d(d-1)(d-2)(d-3)}{2b_0^4} - \frac{2d(d-1)}{b_0^2}\left(\frac{\dot{a}^2}{a^2} - \frac{1}{a^2}\right) - \frac{4d(d-1)}{b_0^2}\frac{\ddot{a}}{a}\right] \tag{4b}$$

$$-C_1\left[\frac{(d-1)(d-2)}{2b_0^2} - 3\left(\frac{\dot{a}^2}{a^2} - \frac{1}{a^2}\right) - 3\frac{\ddot{a}}{a}\right]$$

$$= \Lambda + p' + C_2\left[12\frac{\ddot{a}}{a}\left(\frac{\dot{a}^2}{a^2} - \frac{1}{a^2}\right) + \frac{(d-1)(d-2)(d-3)(d-4)}{2b_0^4}\right.$$

$$\left. - \frac{6(d-1)(d-2)}{b_0^2}\frac{\ddot{a}}{a} - \frac{6(d-1)(d-2)}{b_0^2}\left(\frac{\dot{a}^2}{a^2} - \frac{1}{a^2}\right)\right]. \tag{4c}$$

The conservation equation for ρ, p and p' is given by

$$\frac{\mathrm{d}}{\mathrm{d}\tau}[\Omega_3 \Omega_d \rho] + p\Omega_d \frac{\mathrm{d}\Omega_3}{\mathrm{d}\tau} + p'\Omega_3 \frac{\mathrm{d}\Omega_d}{\mathrm{d}\tau} = 0 \tag{5}$$

where $\Omega_3 = 2\pi^2 a^3$ and $\Omega_d = \dfrac{2\pi^{(d+1)/2}}{\Gamma((d+1)/2)} b_0^d$. The scalar curvature is given by

$$R = -6\left[\frac{\ddot{a}}{a} + \left(\frac{\dot{a}^2}{a^2} - \frac{1}{a^2}\right)\right] + \frac{d(d-1)}{b_0^2}. \tag{6}$$

The model considered above involves essentially a large number of parameters C_0, C_1, C_2, d, b_0^2. We would, therefore, look for relations among the parameters so that instanton solutions of the type discussed in our earlier paper [13] can be obtained. The approach followed here is to leave C_1 and C_2 undetermined (but $C_1 < 0$, $C_2 > 0$) and look for required values of C_0, b_0^2 and d (or constraints on their values) and also to determine the relevant equation of state for the matter part. A number of interesting solutions are given in the next section which may be useful in quantum cosmology.

3. Wormhole solutions

Solutions of the type

$$\dot{a}^2 = 1 - \mu a^2 - \sum_{n=1}^{N} \frac{\nu_n}{a^{2n}} \tag{7}$$

can now be obtained following the prescription of [13]. We consider three cases,

$N=0$, $N=1$ and $N=2$.

(A) *For* $N=0$:

We neglect the matter contribution and get a de Sitter instanton given by

$$a=\frac{1}{\sqrt{\mu}}\sin\sqrt{\mu}\tau \tag{8}$$

where μ is related to the D-dimensional cosmological constant, viz.

$$\Lambda=C_0/2=-3\mu C_1-\tfrac{1}{2}d(d-1)C_1b_0^{-2}-\tfrac{1}{2}d(d-1)(d-2)(d-3)C_2b_0^{-4}-6d(d-1)\mu C_2b_0^{-2} \tag{9}$$

Equation (4c) now gives a quadratic equation for μ, viz

$$A\mu^2+B\mu+C=0, \tag{10}$$

with

$$A=12C_2 \tag{11a}$$

$$B=3[C_1+2(d-1)(d-4)C_2b_0^{-2}] \tag{11b}$$

$$C=-(d-1)b_0^{-2}[C_1+2(d-2)(d-3)C_2b_0^{-2}] \tag{11c}$$

For an acceptable instanton solution, we should satisfy (9) and (10) simultaneously. For a given d, this relates Λ and μ with b_0^2. The relation can be described conveniently by dividing the range of b_0^2 values into several regions. The allowed values for Λ and μ can be determined by studying the discriminant of (10).

Region 1. When $B>0$ and $C<0$, we have $0<b_0^2\leqslant 2(d-1)(d-4)C_2/|C_1|$, this allowspositive as well as negative values for μ. For a given b_0^2, two values each of $\mu(\mu_+,\mu_-)$ and $\Lambda(\Lambda_+,\Lambda_-)$ are allowed. The positive root (μ_+) here corresponds to a negative Λ_+ and the negative root (μ_-) corresponds to a positive Λ_-. We have shown these results for $D=10$, 11 and 26 in figures 1–3. We note that when b_0^2 is small, both Λ_- and $|\Lambda_+|$ are very large. With an increase in b_0^2, μ_- increases and the corresponding Λ_- decreases. In the other branch, as b_0^2 increases, μ_+ decreases and the corresponding Λ_+ moves towards zero. Note that the solutions with $\mu>0$ are physically interesting.

Region 2. Here, $B<0$ and $C<0$. This corresponds to $2(d-1)(d-4)\,C_2/|C_1|<b_0^2<2(d-2)(d-3)C_2/|C_1|$ and also leads to $\mu>0$ and $\mu<0$. From figures 1, 2 and 3, it is observed that with an increase in b_0^2, Λ_- still decreases; the corresponding μ_- increases from the negative side. However, in the other branch, with an increase of b_0^2, Λ_+ eventually becomes positive.

A special case occurs when $C=0$, $B<0$, so that $b_0^2=2(d-2)(d-3)C_2/|C_1|$. This gives for $d>3$,

$$b_0^2=2(d-2)(d-3)C_2/|C_1| \quad\text{and}\quad \mu=b_0^{-2}. \tag{12}$$

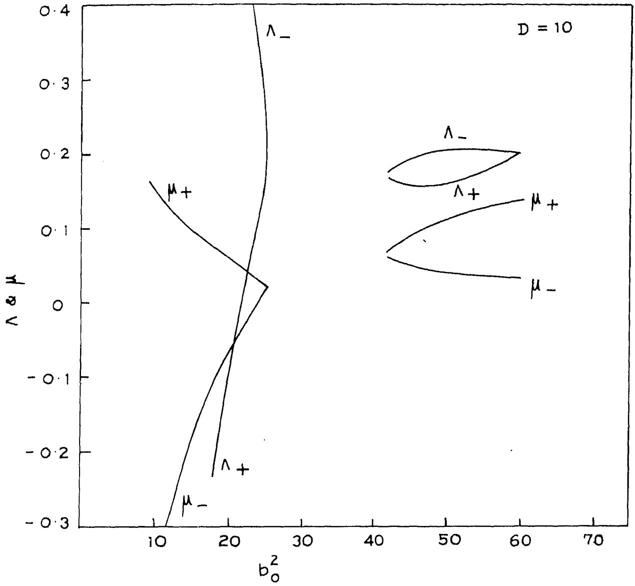

Figure 1. Permitted values of Λ and μ in units of C_1^2/C_2 and $|C_1|/C_2$ respectively for various b_0^2 (in units of $C_2/|C_1|$) for $D = 10$. Λ_+, Λ_- corresponds to μ_+, μ_- respectively.

The higher dimensional cosmological constant Λ, which permits the solution, may be written as

$$\Lambda = C_2 b_0^{-4}[(d^2 - 5d)[6 + \tfrac{1}{2}d(d-1)] + 36 - 3d(d-1)], \tag{13}$$

which shows that $\Lambda > 0$ only for $d \geqslant 6$. For $d = 6$, $b_0^2 = 24C_2/|C_1|$, and $\mu = b_0^{-2}$.

Region 3. For $C > 0$, $B^2 \geqslant 4AC$, we have $2(d-2)(d-3)C_2/|C_1| < b_0^2 \leqslant \frac{2}{3}[(3d-8)(d-1) - 4((d-1)(d-4))^{1/2}]C_2/|C_1|$. In this range μ_+, μ_- both are positive and they are equal $[= -(B/2A)]$ at the boundary $b_0^2 = \frac{2}{3}[(3d-8)(d-1) - 4((d-1)(d-4))^{1/2}]C_2/|C_1|$.

Region 4. For $B^2 < 4AC$, $C > 0$, we have $\alpha_- < b_0^2 < \alpha_+$ where $\alpha_- = \frac{2}{3}[(3d-8)(d-1) - 4((d-1)(d-4))^{1/2}]C_2/|C_1|$ and $\alpha_+ = \frac{2}{3}[(3d-8)(d-1) + 4((d-1)(d-4))^{1/2}]C_2/|C_1|$. The quadratic eq. (10) now leads to imaginary values for μ and Λ. Thus one

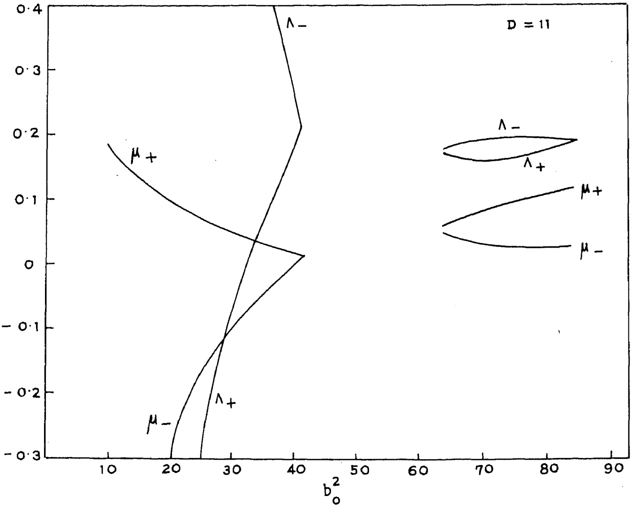

Figure 2. Permitted values of Λ and μ in units of C_1^2/C_2 and $|C_1|/C_2$ respectively for various b_0^2 (in units of $C_2/|C_1|$) for $D = 11$. Λ_+, Λ_- corresponds to μ_+, μ_- respectively.

cannot get an instanton solution for this range of values of b_0^2. In the context of this model, the region is a forbidden zone for instanton solutions.

Region 5. $B^2 - 4AC > 0$, $C \geqslant 0$, which gives $b_0^2 \geqslant \alpha_+$. However, we may put an upper bound on b_0^2, viz. $b_0^2 < 2d(d-1)C_2/|C_1|$ which follows from the condition that the 4-dimensional Newton's Gravitational constant $G_4 > 0$. In this range also, we have two branches of Λ, whose values (Λ_+, Λ_-), and the corresponding values of $\mu(\mu_+, \mu_-)$ are all positive. From figures 1–3 we see that with an increase of b_0^2, μ_- increases but the corresponding Λ_- first decreases, attains a minimum value and then increases. In the other branch, when μ_- decreases, Λ_- increases, attains a maximum and thereafter decreases. In both the cases, for $b_0^2 = 2d(d-1)C_2/|C_1|$, Λ_+ and Λ_- attain the same numerical value

$$\Lambda_+ = \Lambda_- = \frac{d^2 - 3d - 6}{8d(d-1)} \frac{C_1^2}{C_2}. \tag{14}$$

We note that for a given value of Λ, we have in general two different values of b_0^2 excepting for the following ranges of Λ (in units of C_1^2/C_2) values: (i) (0·155 − 0·170) and (0·170 − 0·205) for $d = 6$, (ii) (0·155 − 0·170) and (0·170 − 0·195) in $d = 7$ and (iii)

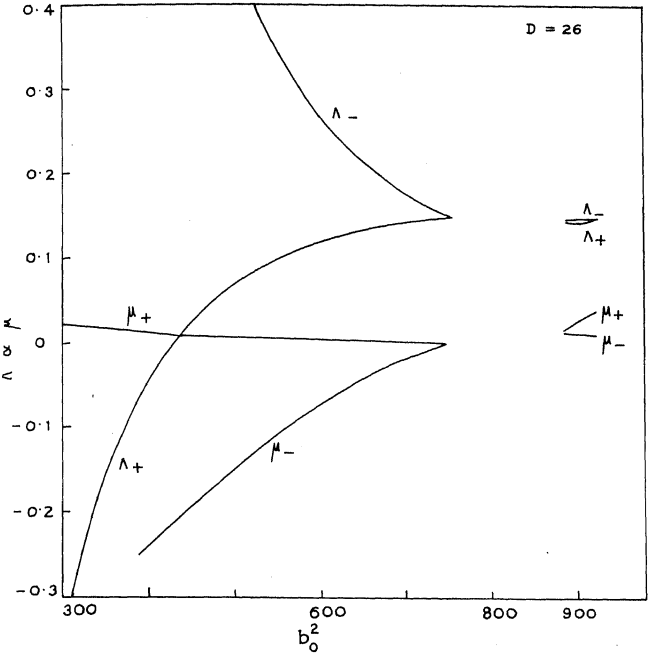

Figure 3. Permitted values of Λ and μ in units of C_1^2/C_2 and $|C_1|/C_2$ respectively for various b_0^2 (in units of $C_2/|C_1|$) for $D = 26$. Λ_+, Λ_- corresponds to μ_+, μ_- respectively.

$(0{\cdot}142 - 0{\cdot}145)$ and $(0{\cdot}146 - 0{\cdot}149)$ for $d = 22$. Within the ranges mentioned, three different values of b_0^2 are permitted. It may be noted that as the number of extra dimensions increases the widths of these ranges decrease. Also, for $\mu > 0$, the D-dimensional cosmological constant lies in the range

$$0 < \Lambda < \frac{d(d-1)}{8(d-2)(d-3)} \frac{C_1^2}{C_2},$$

whereas for $\mu < 0$, we have

$$\frac{d(d-1)}{8(d-2)(d-3)} \frac{C_1^2}{C_2} < \Lambda < \infty.$$

The case $\mu < 0$ does not give instanton configuration, but it may be useful in cosmological model building. We note that even with negative values of D-dimensional Λ, we can have a de Sitter type instanton with a small b_0^2.

The euclidean action for the de Sitter type solution (8) may be written as:

$$I_E^0 = \tfrac{8}{3}\pi^2[C_0 + 12\mu C_1 + d(d-1)b_0^{-2}C_1 + C_2(\mathrm{GB}_0)]\; V_d\mu^{-2} \tag{15}$$

where $\mathrm{GB}_0 = d(d-1)(d-2)(d-3)b_0^{-4} + 24\mu^2 + 24d(d-1)b_0^{-2}\mu$, and V_d is the volume of the extra space. The action is finite.

4. Wormhole solutions with higher N

We have found some approximate wormhole solutions with $N = 1$ and $N = 2$, by including a perfect fluid. These are given below:

(B) *For* $N = 1$

We assume that $b_0 < a$, neglect terms of order a^{-8} and obtain a solution

$$\dot{a}^2 = 1 - \mu a^2 - \frac{\nu_1}{a^2} \tag{16}$$

where ν_1 is given by

$$\nu_1 = \frac{\rho a^4}{3(C_1 + 2d(d-1)C_2 b_0^{-2})}$$

with

$$\rho = 3p \quad \text{and} \quad p' = 0(a^{-8}) \sim 0. \tag{17}$$

The instanton corresponding to (16) is

$$a = (2\mu)^{-1/2}[1 + \eta\cos\sqrt{\mu}\tau]^{1/2} \tag{18}$$

where $\eta = \sqrt{(1 - 4\mu\nu_1)}$.

This solution requires the same Λ as in (9) and the pressure $p' = 0$ implies the condition given in (10). Since (9) and (10) give the same parametric relations, the results regarding the behaviour of Λ and μ obtained for the de Sitter instantons will be valid in this case also. However, the action here is not finite, as we will see in the next section.

An interesting case is obtained by putting $\mu = 0$, viz.

$$\dot{a}^2 = 1 - \frac{\nu_1}{a^2}. \tag{19}$$

This gives $b_0^2 = 2(d-2)(d-3)C_2/|C_1|$ and $\Lambda = \dfrac{d(d-1)C_1^2}{8(d-2)(d-3)C_2}$. The instanton corresponding to (19) is described by

$$a^2 = \tau^2 + \nu_1 \tag{20}$$

so that $a \sim \tau$, as $\tau \to \infty$. This when continued to Lorentzian metric gives an asymptotic flat space.

C. For $N = 2$

We find a few interesting solutions of the type

$$\dot{a}^2 = 1 - \mu a^2 - \frac{\nu_2}{a^4} \tag{21}$$

for specific values of b_0^2. The first solution corresponds to the stiff matter equation of state in 4-dimensions:

$$\rho = p = 3\left(C_1 + \frac{2d(d-1)}{b_0^2} C_2 \right) \frac{\nu_2}{a^6} \tag{22}$$

$\Lambda = C_0/2 = \dfrac{(d^2 + 2d - 9)C_1^2}{8d(d-2)C_2}$ and $p' = 0$ when terms of order a^{-12} are neglected. The solution requires $b_0^2 = 2d(d-2)C_2/|C_1|$ and $\mu = \dfrac{1}{4d}\dfrac{|C_1|}{C_2}$. This is similar to the instanton solution obtained by Lee [14] for a complex scalar field in Einstein gravity in 4-dimensions.

Lastly, we note that for $D = 6$ i.e., with $d = 2$, and $C_1 = 0$, eq. (21) reduces to a simple form:

$$\dot{a}^2 = 1 - \nu_2 a^{-4} \tag{23}$$

with

$$\rho = p = 12 C_2 \nu_2 b_0^{-2} a^{-6}, p' = 0. \tag{24}$$

The wormhole corresponding to eq. (23) is similar to that obtained by Giddings and Strominger [16] in 4-dimensions in the presence of an antisymmetric tensor field $B_{\mu\nu}$.

Another solution is obtained for

$$\rho = p = p' \tag{25}$$

with

$$b_0 = (2d(d-2)C_2/|C_1|)^{1/2},$$

$$\mu = \frac{(d-1)|C_1|}{2d(d-2)C_2}, \tag{26}$$

$$\Lambda = \frac{C_0}{2} = \frac{d^3 - 19d + 18}{8d(d-2)^2}\frac{C_1^2}{C_2} \tag{27}$$

This type of wormhole configuration was noted by Myers [15] in higher dimensions without the GB term.

5. Action for wormholes with $N = 1, 2$

The wormholes discussed above involve coordinate singularities. There is, however, no curvature singularity and one has to consider a regular extension of the metric beyond the extremal surfaces $a = a_{\min}$ and $a = a_{\max}$. One may follow Halliwell and Myers [17] and consider sewing together a sequence of Euclidean manifolds of the type (7). A multitude of tunneling processes can be described by these configurations, although the calculations have technical difficulties excepting for $2+1$ dimensions [17]. The actions of the Euclidean solutions (16) and (21) covered within the coordinate patch $a_{\min}$ to $a_{\max}$ can be determined analytically. For the solution (16), the Euclidean action is given by:

$$I_E^1 = 2\pi^2 V_d A\mu^{-1/2}\left[((1+\eta)/(18\mu))^{1/2}\left[\frac{2}{\mu}E\left(\frac{\pi}{2},q\right)+\frac{2v_1}{1+\eta}F\left(\frac{\pi}{2},q\right)\right]\right]$$

$$+2\pi^2 V_d\left(C_1+\frac{2d(d-1)}{b_0^2}C_2\right)v_1(2/(1+\eta))^{1/2}F\left(\frac{\pi}{2},q\right) \tag{28}$$

where $F(E)$ are the elliptic integrals of first (second) kind,

$$\eta = (1-4\mu v_1)^{1/2}$$

$$q = (2\eta/(1+\eta))^{1/2}, \quad v_1 > 0,$$

$A = 0$ when $\mu = 0$ and

$$= d(d-1)b_0^{-2}[C_1+(d-2)(d-3)C_2 b_0^{-2}] - \frac{12d(d-1)C_1}{(d-2)(d-3)b_0^2}$$

$$+\frac{d^4-6d^3-13d^2+66d-48}{4(d-2)^2(d-3)^2}\frac{C_1^2}{C_2} \quad \text{where} \quad \mu \neq 0 \tag{29}$$

The Euclidean action corresponding to the wormhole given by (21) is

$$I_E^2 = \frac{4\pi^2 AV_d}{3\mu^{3/2}}\left[\frac{2\gamma}{(\alpha-\gamma)^{1/2}}F\left(\frac{\pi}{2},\psi\right)+2\frac{\alpha}{\beta}(\alpha-\gamma)^{1/2}E\left(\frac{\pi}{2},\psi\right)\right]+\frac{\pi^2 BV_d}{(\mu)^{1/2}}\left[\frac{2}{\alpha\gamma(\alpha-\gamma)}\right.$$

$$\left.(\gamma-\beta)\Pi\left(\frac{\pi}{2},\frac{\gamma}{\beta}\psi^2,\psi\right)+\beta F\left(\frac{\pi}{2},\psi\right)\right] \tag{30}$$

where F, E, Π are the elliptic integrals of first, second and third kinds respectively, $\psi = \left[\frac{\alpha-\beta}{\alpha-\gamma}\right]^{1/2}$, and A and B are given below for the equation of states (22) and (25):

(i) for $\rho = p$ and $p' = 0$:

$$A = \frac{3(d-1)C_1^2}{d^2(d-2)C_2}, \quad B = \frac{3(3d-4)}{d^2(d-2)^2}C_1 v_2. \tag{31}$$

When $D = 6$, $C_1 = 0$ ($\mu = 0$), the Euclidean action is given by

$$I_E^2 = 6\pi^3 C_2 v_2 V_d/b_0^2. \tag{32}$$

The action is finite:

(ii) for $\rho = p = p'$:

$$A = \frac{9d^2-15d+6}{d^2(d-2)^2}\frac{C_1}{C_2}, \quad B = \frac{3(5d-4)}{d(d-2)}C_1 v_2, \tag{33}$$

we note also that $\nu_2 > 0$ and α, β and γ are the roots of the polynomial

$$-x^3 + \mu^{-1}x^2 + \nu_2\mu^{-1} = 0, \quad (x = a^2)$$

and $\alpha > \beta > 0 > \gamma$.

6. Discussion

We have presented above a number of wormhole solutions in a theory based on an action which includes the Gauss-Bonnet combination of quadratic terms in curvatures. The model is different from what one gets from the string theory in the small slope limit, as we have chosen C_1 and C_2 with opposite signs. The resulting theory has some striking features. If one tries to build a quantum cosmological model starting from this classical action, in dimensions $D = 4 + d$, the instanton-like configurations mentioned above will be relevant. Of particular interest in this connection are de-Sitter type instanton configurations. The model makes some definite predictions for the cosmological tunneling probabilities. We note that the action for the de-Sitter instantons increases rapidly as b_0^2 increases from zero up to $b_0^2 = \frac{2}{3}[(d-1)(3d-8) - 4((d-1)(d-4))^{1/2}]C_2/|C_1|$. Obviously the universe is unlikely to nucleate with $b_0^2 \leqslant \frac{2}{3}[(d-1)(3d-8) - 4((d-1)(d-4))^{1/2}]C_2/|C_1|$. Again for the range of values, $\frac{2}{3}[(d-1)(3d-8) - 4((d-1)(d-4))^{1/2}]C_2/|C_1| < b_0^2 < \frac{2}{3}[(d-1)(3d-8) + 4((d-1)(\mathrm{d}-4))^{1/2}]C_2/|C_1|$, there is no instanton. A tunneling mechanism is, therefore, more likely in region 5. While the probability for cosmic tunneling may or may not be testable by any experiment now, there is one prediction which in principle can be tested. If the universe is actually higher dimensional, with d extra dimensions of radius b_0, this model predicts that b_0^2 cannot have a value lying between $\frac{2}{3}[(d-1)(3d-8) - 4((d-1)(d-4))^{1/2}]C_2/|C_1|$ and $\frac{2}{3}[(d-1)(3d-8) + 4((d-1)(d-4))^{1/2}]C_2/|C_1|$. This of course, presupposes that the nucleation is described by a de-Sitter instanton. The Myers-type wormholes mentioned above have infinite action and a possible application of these solutions to quantum cosmology is still uncertain.

Acknowledgements

One of the authors (SM) would like to thank Inter-University Centre for Astronomy and Astrophysics, Pune and the University of Zululand, South Africa for hospitality during the period of this work. SM and AB also acknowledge financial support from FRD (South Africa).

References

[1] T Kaluza, *Sitz. Preuss. Acad. Wiss* **F1**, 966 (1921)
O Klein, *Z. Phys.* **37**, 895 (1926)
[2] P G O Freund and M A Rubin, *Phys. Lett.* **B97**, 233 (1980)
M J Duff, B E W Nilsson and C N Pope, *Nucl. Phys.* **B233**, 433 (1984)
J Schwarz, *Nucl. Phys.* **B226**, 269 (1983)
E Cremmer and J Scherk, *Nucl. Phys.* **B108**, 409 (1976)
S Randjbardaemi, A Salam and J Strathdee, *Phys. Lett.* **B124**, 349 (1983); *Nucl. Phys.* **B214**, 491 (1983)
P S Howe and P C West, *Nucl. Phys.* **B238**, 181 (1984)

[3] M B Green and J H Schwarz, *Phys. Lett.* **B149**, 117 (1984); **B151**, 21 (1985)
[4] B Zweiebach, in *Anomalies, geometry and topology* edited by W A Bardeen and A White (Singapore, World Scientific, 1985); *Phys. Lett.* **B156**, 314 (1985)
[5] Q Shafi and C Wetterich, *Nucl. Phys.* **B289**, 787 (1987)
C Wetterich, *Phys. Lett.* **B113**, 377 (1982)
F S Accetta, M Gleiser, R Holman and E W Kolb, *Nucl. Phys.* **B276**, 501 (1986)
[6] D Bailin and A Love, *Phys. Lett.* **B163**, 135 (1985)
D Bailin, A Love and D Wong, *Phys. Lett.* **B165**, 270 (1985)
[7] D Lorentz-Petzold, *Prog. Theor. Phys.* **78**, 969 (1987); *Mod. Phys. Lett.* **A3**, 827 (1988)
[8] B C Paul and S Mukherjee, *Phys. Rev.* **D42**, 2595 (1990)
[9] E Baum, *Phys. Lett.* **B133**, 185 (1983)
[10] S W Hawking, *Phys. Lett.* **B134**, 403 (1984)
[11] S Coleman, *Nucl. Phys.* **B310**, 643 (1988)
[12] P Gonzalez-Diaz, *Phys. Lett.* **B247**, 251 (1990)
[13] S Mukherjee, B C Paul, N Dadhich and A Kshirsagar, *Phys. Rev.* **D45**, 2772 (1992)
[14] K Lee, *Phys. Rev. Lett.* **61**, 263 (1988)
[15] R C Myers, *Nucl. Phys.* **B323**, 225 (1989)
[16] S Giddings and A Strominger, *Nucl. Phys.* **B306**, 890 (1988); **B307**, 854 (1988)
[17] J J Halliwell and R C Myers, *Phys. Rev.* **D40**, 4011 (1989)

PRAMANA
— journal of
physics

© Printed in India

Vol. 44, No. 2,
February 1995
pp. 145–152

Magnetic moments of decuplet baryons in an independent particle potential model

N BARIK, P DAS* and A R PANDA*
P. G. Department of Physics, Utkal University Bhubaneswar, 751 004, India
*Department of Physics, Kendrapara College, Kendrapara 754 211, India

MS received 18 July 1994

Abstract. Magnetic moments of decuplet baryons have been calculated in a relativistic independent quark model with a phenomenological potential in equally mixed scalar-vector harmonic form. Such a model has been succeessful in describing wide ranging hadronic phenomena in mesonic and baryonic sectors. Using the solutions of the constituent quark orbitals with the model parameters taken from its earlier applications, the magnetic moments of decuplet baryons Δ^{++} and Ω^- have been obtained which are in good agreement with the available experimental data. However, the agreement is found to be much better when the magnetic moment ratios such as $\mu_{\Delta^{++}}/\mu_p$ and $\mu_{\Omega^-}/\mu_\Lambda$ are considered. Model predictions for the magnetic moments of other decuplet baryons together with the charge radii have also been calculated which may be verified in future experiments.

Keywords. Magnetic moments; decuplet baryons; independent quark; potential model.

PACS Nos **12·40; 13·40; 14·20**

1. Introduction

Recently in two experimental measurements such as the pion-bremstrahlung analysis [1] and the E756 collaboration [2], the magnetic moments of Δ^{++} and Ω^- have been reported. Study of magnetic moments of the decuplet baryons is important so far as their structure is concerned. The above-mentioned experimental measurements [1, 2] in fact have generated a fresh interest in their investigation resulting in several publications on different theoretical models [3–6]. In one such recent work [3], it has also been claimed that it is a challenge for every hadronic model to get consistent values for the magnetic moments of Δ^{++} and Ω^-.

However, magnetic moment of hadrons being a low energy attribute cannot be studied from the first principle applications of quantum chromodynamics (QCD) [7], despite its being the correct theory for hadrons. One resorts to phenomenological models of hadrons incorporating the basic ingredients of QCD. Thus, we investigate here the magnetic moments of decuplet baryons in a phenomenological potential model of relativistic and independent quarks, where the binding between the confined quarks is described by a potential having an equal admixture of vector and scalar parts of the form [8]

$$U(r) = (1/2)(1 + \gamma^0)\, V(r), \tag{1.1}$$

with a harmonic form for $V(r)$ as

$$V(r) = ar^2 + V_0; \quad a > 0. \tag{1.2}$$

With such a potential, the Dirac equation derivable from a zeroth order quark-Lagrangian-density

$$\mathscr{L}_q^0(r) = (-i/2)\bar{q}(r)\gamma^\mu \overleftrightarrow{\partial}_\mu q(r) - \bar{q}(r)[m_q + U(r)]q(r) \tag{1.3}$$

becomes solvable to yield the static quark orbital solutions for positive frequency as [8]

$$\psi_\xi(\mathbf{r}) = \begin{pmatrix} ig_\xi(r)/r) \\ (\boldsymbol{\sigma}\cdot\hat{r})f_\xi(r)/r) \end{pmatrix} U_\xi(\hat{r}); \tag{1.4}$$

where $\xi = (l, j, m)$ represents the set of Dirac quantum numbers specifying the corresponding confined eigen modes and $U_\xi(\hat{r})$ represents the spin angular wave function described as

$$U_{l,j,m}(\hat{r}) = \sum_{m_l, m_s} \langle l, m_l \tfrac{1}{2} m_s | j, m\rangle \, Y_l^{m_l}(\hat{r}), \tag{1.5}$$

with

$$E'_q = (E_q - V_0/2), m'_q = (m_q + V_0/2), \lambda_q = (E'_q + m'_q) = (E_q + m_q),$$

$$r_{0q} = (a\lambda_q)^{-1/4} \tag{1.6}$$

one obtains the solutions to the reduced radial equations for $f_\xi(r)$ and $g_\xi(r)$ leading to the bound state conditions for the independent quarks as [8]

$$(\lambda_q/a)^{1/2}(E'_q - m'_q) = (4n + 2l - 1), \tag{1.7}$$

which in turn gives the zeroth order binding energy for quarks inside the hadron for different eigen modes.

However, in the present calculation to estimate the magnetic moments of the decuplet baryons in their ground states, one requires only the lowest eigen modes in the positive frequency sector which when explicitly written become

$$\psi_{1S1/2}(\mathbf{r}) = \frac{1}{\sqrt{4\pi}} \begin{pmatrix} ig_q(r)/r \\ (\boldsymbol{\sigma}\cdot\hat{r})f_q(r)/r \end{pmatrix} \chi_\uparrow. \tag{1.8}$$

with the spinors as

$$\chi_\uparrow = \begin{pmatrix} 1 \\ 0 \end{pmatrix} \text{ and } \chi_\downarrow = \begin{pmatrix} 0 \\ 1 \end{pmatrix}. \tag{1.9}$$

Further, the reduced radial parts in the upper and the lower components of the solution for a particular flavor q when evaluated become

$$g_q(r) = N_q(r/r_{0q})\exp(-r^2/2r_{0q}^2)$$

and

$$f_q(r) = -\frac{N_q}{\lambda_q r_{0q}}(r/r_{0q})^2 \exp(-r^2/2r_{0q}^2) \tag{1.10}$$

with the normalization constant calculated as

$$N_q = \left[\frac{8\lambda_q}{\sqrt{\pi}r_{0q}} \cdot \frac{1}{(3E'_q + m'_q)}\right]^{1/2}. \tag{1.11}$$

In its earlier applications, the present model with chiral symmetry restoration has been proved to be a simple and successful alternative to the cloudy bag model (CBM). It has also been successful in explaining the leptonic decays of light neutral vector mesons [9] and radiative transitions between vector and pseudoscalar mesons [10] as well as in estimating the pseudoscalar decay constants [11] and the top quark mass from the weak mixing between B_d^0 and $\bar{B}_d^0$ mesons [12]. Most recently, it has also been able to estimate correctly the electromagnetic polarizabilities of proton [13]. This model was also used earlier to study several low energy phenomena in baryonic sector such as mass spectrum [14], weak electric form factors [15] and magnetic moments [16] of octet baryons as well as their charge radii and electromagnetic form factors [8]. Also in the light meson sector, the model was applied successfully to estimate $(q\bar{q})$ pion mass in consistency with that of PCAC-pion [17] and $(\varrho - \pi)$ as well as $(\varrho - \omega)$ mass splittings [18]. In view of these successes of the model in explaining varieties of hadronic phenomena, we apply it here to estimate the magnetic moments of decuplet baryons to see if it can meet the challenge described in ref. [3].

We organize the present article as follows. In § 2, we estimate the magnetic moments of decuplet baryons. In § 3, we discuss our results and compare them with other model calculations and experimental results.

2. Magnetic moments of decuplet baryons

The magnetic moment vector $\boldsymbol{\mu}_q$ of a confined quark inside the baryon core is expressed in terms of the electromagnetic current in a conventional manner as

$$\boldsymbol{\mu}_q = (1/2)\int \mathrm{d}\mathbf{r}(\mathbf{r} \times \mathbf{J}_{\rm em}), \tag{2.1}$$

where the current $\mathbf{J}_{\rm em}$ when expressed in terms of confined quark wave functions of the present potential model becomes,

$$\mathbf{J}_{\rm cm} = e\, e_q \bar{\psi}_q(\mathbf{r}) \boldsymbol{\gamma} \psi_q(\mathbf{r})$$

which when substituted in the expression (2.1) yields

$$\boldsymbol{\mu}_q = (1/2) e\, e_q \int \mathrm{d}\mathbf{r}\, \psi_q^{\dagger}(\mathbf{r})(\mathbf{r} \times \boldsymbol{\alpha})\psi_q(\mathbf{r}) \tag{2.2}$$

where e and e_q are the magnitudes of proton charge and the electric charge of quark (in units of proton charge) respectively. However, with the conventional identification of $(\boldsymbol{\mu}_q)_z$ to be the magnetic moment of the quark, we obtain

$$\mu_q = (1/2) e\, e_q \int \mathrm{d}\mathbf{r}\, \psi_q^{\dagger}(\mathbf{r})(\mathbf{r} \times \boldsymbol{\alpha})_z \psi_q(\mathbf{r}), \tag{2.3}$$

where $\psi_q(\mathbf{r})$ is the ground state wave function of quarks. Thus, using eqs (1.8)–(1.11) the expression for the magnetic moment of quark of flavor q becomes

$$\mu_q = \frac{4 M_P e_q}{(3E'_q + m'_q)}\, nm. \tag{2.4}$$

with M_P as the mass of the proton. Next, with the usual assumptions of quark addivitity, the quark core contribution towards the magnetic moments of the decuplet baryons can be obtained from the defining relation described as

$$\mu_B^0 = \left\langle B_{3/2} \left| \sum_q \mu_q \sigma_{qz} \right| B_{3/2} \right\rangle \tag{2.5}$$

with μ_q's as the individual quark magnetic moments as described in (2.4). However, a consideration of the normalized decuplet baryon state along with their appropriate spin, flavor and isospin configurations yields (2.5) to

$$\mu_B^0 = \sum_q \mu_q, \tag{2.6}$$

which results effectively to the fact that the magnetic moment of a decuplet baryon as the sum of their respective individual quark magnetic moments, as expected. Thus, with (2.4), it yields to an explicit expression for the magnetic moment of a baryon in the decuplet as

$$\mu_B^0 = 4M_P \sum_q \frac{e_q}{(3E_q' + m_q')}. \tag{2.7}$$

However, we may note here that the estimation of the magnetic moment in (2.7) considers only the independent motion of the quarks inside the baryon core and such a consideration does not lead to a state of definite total momentum as it should represent the physical state of the baryon. Hence, appropriate correction due to the centre-of-mass-motion must be taken into consideration. In doing so we would follow the same prescription as adopted in ref. [8] so as to obtain the centre-of-mass-motion corrected expression for the magnetic moment of a decuplet baryon as

$$\mu_B = \left[2\mu_B^0 + \frac{Q_B}{3}\left(\frac{M_P}{M_B}\right)(1 - \delta_B^2)/(1 + \delta_B^2) \right]. \tag{2.8}$$

Here the quantity δ_B^2 in terms of which the centre-of-mass-motion correction is effected is defined in accordance with ref. [8] as,

$$\delta_B^2 = \langle M_B^2 / E_B^2 \rangle = [1 - \langle \mathbf{P}_B^2 \rangle / E_B^2] \tag{2.9}$$

with the centre-of-mass momentum $\mathbf{P}_B$ obtained through the expression

$$\langle \mathbf{P}_B^2 \rangle = \sum_q \langle p_q^2 \rangle = \sum_q \frac{(11E_q' + m_q')(E_q'^2 - m_q'^2)}{6(3E_q' + m_q')}. \tag{2.10}$$

We must note here that M_B and Q_B in (2.8) are respectively the observed mass and the charge (in units of proton charge) of the baryons. The total energy of the baryon E_B is obtained through the relativistic mass energy relation as $(\langle \mathbf{P}_B^2 \rangle + M_B^2)^{1/2}$.

One can also estimate the charge radii of the decuplet baryons within the framework of the present potential model at the quark core level, from its defining relation as

$$\langle \mathbf{r}^2 \rangle_B = \left\langle B_{3/2} \left| \sum_q e_q \langle \mathbf{r}_q^2 \rangle \right| B_{3/2} \right\rangle \tag{2.11}$$

which with the normalised decuplet baryon state $|B_{3/2}\rangle$ and the reduced orbital solutions of the model becomes

$$\langle \mathbf{r}^2\rangle_B^0 = \frac{3}{2}\sum_q e_q \frac{(11\,E'_q + m'_q)}{(3\,E'_q + m'_q)(E'^2_q - m'^2_q)}. \tag{2.12}$$

Again, with the prescription of ref. [8], the centre-of-mass-motion corrected expression for the charge radius of a baryon in the decuplet becomes

$$\langle \mathbf{r}^2\rangle'_B = 3[\langle \mathbf{r}^2\rangle_B^0 - Q_B\langle \mathbf{R}^2\rangle]/(2+\delta_B^2) \tag{2.13}$$

where $\langle \mathbf{R}^2\rangle$ is the mean square centre-of-mass radius and the expression for it in terms of the model parameters is written as

$$\langle \mathbf{R}^2\rangle = \frac{3}{2E_B^2}\sum_q E_q^2 \frac{(11\,E'_q + m'_q)}{(3\,E'_q + m'_q)(E'^2_q - m'^2_q)}. \tag{2.14}$$

3. Results and discussion

We now estimate the magnetic moments of decuplet baryons using the expression obtained in the earlier section. We must point out here that there exists only a couple of data points in this sector corresponding to the magnetic moments measured for Δ^{++} and Ω^- and a satisfactory reproduction of these two measured quantities in the present model with as many as five parameters (such as a, V_0, m_u, m_d and m_s) may not appear to be a big achievement for the model. Therefore instead of searching afresh the appropriate values for the model parameters to fit the measured magnetic moments of Δ^{++} and Ω^-, we prefer to take the same set of parameters with which the model in its earlier applications has successfully described wide ranging phenomena in the mesonic and baryonic sectors [8–17]. In that case we would be having effectively no free parameters in the present calculation which on reproducing the measured magnetic moments of Δ^{++} and Ω^- to a reasonable extent can add to the credibility of the model. Hence, we take the model parameters such as the flavor independent potential parameters and the quark masses from the earlier applications of the model [8–17] as

$$(a, V_0) = (0{\cdot}017166\,\mathrm{GeV}^3, -0{\cdot}1375\,\mathrm{GeV})$$

and

$$m'_u = m'_d = 0{\cdot}01\ \mathrm{GeV}; m'_s = 0{\cdot}247\,\mathrm{GeV}. \tag{3.1}$$

Then the binding energies of the quarks in their lowest eigen mode; which are relevant to the present calculation and are derivable from the solution of the bound state condition in (1.7), become

$$E'_u = E'_d = 0{\cdot}54\,\mathrm{GeV};\quad E'_s = 0{\cdot}65975\,\mathrm{GeV}. \tag{3.2}$$

Thus with these parameters and expressions (2.7) and (2.8) of the earlier section, we estimate the uncorrected and the corrected magnetic moments for all the decuplet baryons and report them in table 1, where we observe a reasonable agreement with the available experimental data [1, 2]. In fact for Δ^{++}; the centre-of-mass-motion corrected estimation is a little higher than the corresponding measured value.

Table 1. Estimated centre-of-mass-motion uncorrected and corrected magnetic moments (in nm) of decuplet baryons in the present investigation compared with the experiment and other theoretical estimations.

	Present investigation			Ref. [3]	Ref. [4]	Ref. [5]	Ref. [6]	Ref. [19]	Expt. [1,2]
μ_B	uncorr.	δ_B^2	corr.						
$\mu_{\Delta^{++}}$	4·60	0·797	5·18	4·76	4·53	6·54	6·09	5·56	4·52 ± 0·50
$\mu_{\Delta^{+}}$	2·30	0·797	2·59	2·38	2·09	—	3·05	2·73	—
$\mu_{\Delta^{0}}$	0·00	0·797	0·00	0·00	− 0·36	—	0·00	− 0·09	—
$\mu_{\Delta^{-}}$	− 2·30	0·797	− 2·59	− 2·38	− 2·80	—	− 3·05	− 2·92	—
$\mu_{\Sigma^{*+}}$	2·51	0·813	2·79	1·82	2·55	—	3·16	3·09	—
$\mu_{\Sigma^{*0}}$	0·20	0·813	0·23	− 0·27	− 0·02	—	0·33	0·27	—
$\mu_{\Sigma^{*-}}$	− 2·10	0·813	− 2·34	− 2·36	− 2·60	—	− 2·50	− 2·56	—
$\mu_{\Xi^{*0}}$	0·41	0·827	0·45	− 0·60	0·40	—	0·58	0·63	—
$\mu_{\Xi^{*-}}$	− 1·89	0·827	− 2·09	− 2·41	− 2·31	—	− 2·08	− 2·20	—
μ_{Ω}	− 1·68	0·839	− 1·85	− 2·35	− 1·98	− 2·52	− 1·73	− 1·83	− 1·94 ± 0·22

Table 2. Estimated ratios of the centre-of-mass-motion uncorrected and corrected magnetic moments $\mu_{\Delta^{++}}/\mu_p$ and $\mu_{\Omega^-}/\mu_\Lambda$ in the present model compared with the experiment and theoretical estimations.

Magnetic moment	Present investigation uncorr.	Present investigation corr.	Ref. [3]	Ref. [4]	Ref. [5]	Ref. [6]	Ref. [19]	Expt. [1,2]
$\mu_{\Delta^{++}}$	4·60	5·18	4·76	4·53	6·54	6·09	5·56	4·52 ± 0·50
$\mu_{\Delta^{++}}/\mu_p$	2·0	1·90	1·69	1·98	2·34	2·18	2·00	1·62 ± 0·18
μ_{Ω^-}	− 1·68	− 1·85	− 2·35	− 1·98	− 2·52	− 1·73	− 1·84	− 1·94 ± 0·22
$\mu_{\Omega^-}/\mu_\Lambda$	3·0	3·09	3·41	3·73	4·13	3·60	3·00	3·16 ± 0·28

Table 3. Estimated centre-of-mass-motion uncorrected and corrected charge radii $\langle \mathbf{r}^2 \rangle_B^{1/2}$ (in fm) of decuplet baryons in the present potential model.

Baryon B	Charge radius uncorrected	corrected
Δ^{++}	1·209	1·02
Δ^{+}	0·855	0·723
Δ^{0}	0·0	0·0
Δ^{-}	− 0·855	− 0·723
Σ^{*+}	0·894	0·788
Σ^{*-}	− 0·814	− 0·689
Σ^{*0}	0·262	0·276
Ξ^{*0}	0·370	0·381
Ξ^{*-}	− 0·770	− 0·651
Ω^{-}	− 0·725	− 0·608

However, when we compare the estimated ratios of the magnetic moments such as $\mu_{\Delta^{++}}/\mu_p$ and $\mu_{\Omega^-}/\mu_\Lambda$ with the corresponding experimental quantities [1, 2] as presented in table 2, the agreement seems much better. In tables 1 and 2 we also provide a comparison of our results with the estimations of some other models such as NQM [19], Skyrme model [4], CBM [5], lattice simulation [6] and light-front relativistic quark model [3]. We find that the present estimation is more or less comparable with the predictions of ref. [4, 19]. We must add here that we have ignored in this calculation any further additional contributions due to possible residual effects of the virtual pion and kaon cloud surrounding the bare quark core in a physical baryon as conceived in a chiral potential model. We believe that such additional contributions would be quite small only to the extent of fine tuning of model estimations.

Finally we estimate the charge radii for different decuplet baryons, both uncorrected and corrected ones using (2.12) and (2.13) respectively of the earlier section and present the results in table 3. However, since no experimental data in this regard are available, our results stand as model predictions and may be verified in future experiments.

Thus, the present potential model, even at the valency quark core level explains reasonably the experimentally measured magnetic moments and predicts the unobserved ones which may be verified in future experiments. It does so in a much simplified and tractable manner due to the ansatz for the potential as an admixture of equal scalar and vector parts in harmonic form. Nevertheless, we feel the accurate results from the succeeding experiments, expected to be obtained in near future, can further constrain different theoretical models [20].

Acknowledgements

The authors would like to thank K C Roy, A Nath and R K Sahoo for discussion.

References

[1] A Bosshard *et al*, *Phys. Rev.* **D44**, 1962 (1991)
[2] H T Deihl *et al*, *Phys. Rev. Lett.* **67**, 804 (1991)

[3] F Schlumpf, *Phys. Rev.* **D48**, 4478 (1993)
[4] J H Kim, C H Lee and H K Lee, *Nucl. Phys.* **A501**, 835 (1989)
[5] M I Krivoruchenko, *Yad. Fiz.* **45**, 169 1(987); *Sov. J. Nucl. Phys.* **45**, 109 (1987)
[6] D B Leinweber, T Draper and R M Woloshyn, *Phys. Rev.* **D46**, 3067 (1993)
[7] W Marciano and H Pagels, *Phys. Rep.* **C36**, 137 (1978)
[8] N Barik, B K Dash and M Das, *Phys. Rev.* **D31**, 1652 (1985); **D32**, 1725 (1985)
[9] N Barik, P C Dash and A R Panda, *Phys. Rev.* **D47**, 1001 (1993)
[10] N Barik, P C Dash and A R Panda, *Phys. Rev.* **46**, 3586 (1992)
[11] N Barik and P C Dash, *Phys. Rev.* **D47**, 2788 (1993)
[12] N Barik, P Das, A R Panda and K C Roy, *Phys. Rev.* **D48**, 3271 (1993)
[13] N Barik, B K Dash, P Das and A R Panda (submitted for publication)
[14] N Barik, and B K Dash, *Phys. Rev.* **33**, 1925 (1986)
[15] N Barik, B K Dash and M Das, *Phys. Rev.* **D31**, 1652 (1985)
[16] N Barik and B K Dash, *Phys. Rev.* **D34**, 2803 (1986)
[17] N Barik, B K Dash and P C Dash, *Pramana – J. Phys.* **29**, 543 (1987)
[18] B E Palladino and P Leal Ferreira, IFT Sao Paul Report No. IFT/P-38/88 (unpublished)
[19] Particle Data Group, *Phys. Rev.* **D50**, 1172 (1994) and references therein
[20] F Schlumpf, *Phys. Rev.* **D48**, 4478 (1993)
G Rameika, Fermilab Report, 1993 (unpublished)

PRAMANA
— journal of
physics

© Printed in India

Vol. 44, No. 2,
February 1995
pp. 153–166

A new approach for heavy ion fusion spin distribution

S V S SASTRY, A K MOHANTY and S K KATARIA
Nuclear Physics Division, Bhabha Atomic Research Centre, Bombay 400 085, India

MS received 16 June 1994; revised 3 October 1994

Abstract. The method of optical model analysis of generalized elastic scattering angular distributions (GESA) has been applied to heavy ion scattering to derive fusion spin distributions. This method is used to reproduce the coupled channel fusion spin distributions. When applied to experimental data, particularly to the fissile systems like $^{16}O + ^{232}Th$, the method gives large mean square spin values in agreement with "anomalous" values derived from experimental fission fragment anisotropies.

Keywords. Generalized elastic scattering; optical potentials; reduced reaction cross-section; fusion spin; coupled channel calculations.

PACS Nos 25·70; 24·10

1. Introduction

The study of heavy ion reactions at low energies has created much excitement in recent years due to rich interplay between the dynamics of the reactions and the nuclear structure of the participating nuclei. Measurements on many aspects of the colliding nuclei, such as elastic, inelastic, transfer and fusion reactions have shown that these processes are correlated and attempts are being made to develop a theoretical model which will take them all into account. The common feature of all these descriptions is the realisation of importance of the couplings among different channels, either implicitly through optical models or explicitly through the coupled channels (CC) method. These couplings result in significant multi-step contributions to various reaction channels in addition to the direct one-step amplitudes that are generally evaluated by methods such as the DWBA, barrier penetration models, optical model etc. In reality, the solution of a large set of coupled channel equations is difficult and hence several approximations are made, besides limiting the number of channels that are important for a particular reaction. These approximations give rise to serious discrepancies between the theory and the experimental measurements. In fusion reaction, many models fail to explain the fusion partial wave cross-section [1] even though they account for the total fusion cross-section. Therefore, to test any theory of heavy ion reactions, it is important to understand the reaction mechanism for each partial wave and also its contribution to different reaction channels. In this context, experimental measurement of partial wave cross-sections for different reaction channels is highly desirable. In this paper, we investigate the method of obtaining partial wave cross-section for fusion channel by fitting generalized elastic scattering angular distribution (GESA). The GESA is defined as the sum of strictly elastic and appropriate non-elastic channels and the corresponding reaction cross-section is called reduced reaction cross-section [2]. Usually, the simplest of the measurements, the elastic scattering is analysed to obtain the reaction cross-section and by measuring it properly one can ensure that the total reaction cross-section contains contribution from all possible reaction channels. If angular distribution for any non-elastic channel is available, one can define a GESA by adding it to the strictly elastic angular distribution. Oeschler *et al* [2] showed that for heavy ion collisions, the reduced reaction cross-section and its partial wave distribution obtained by fitting the GESA are consistent with the total reaction cross-section for the remaining channels that are not added to the generalized elastic channel. In heavy ion scattering, the elastic channel often contains the contributions from the low lying Coulomb excitations and in [2], emphasis was put on the question whether the analysis of the sum of Coulomb excited inelastic states and elastic scattering (GESA) gives a consistent value of the reduced reaction cross-section as the flux going into the remaining channels. It was also observed that one should use an optical model fit to the GESA in order to obtain the appropriate potential for coupled channel calculations. This is in contrast to the fact that the strictly elastic scattering some times may turn out difficult to fit due to the long range Coulomb excitations. We have applied this method to obtain the partial wave cross-section for fusion channel by fitting GESA. The fusion partial wave cross-sections obtained this way contain all the effects of channel couplings. However one needs the angular distributions of all the non-fusion reaction channels. In fusion reaction, particularly for fissile targets, direct measurement of fusion partial wave cross-section based on γ-ray multiplicity measurements is difficult. Usually, indirect methods are adopted to obtain mean square spin from the studies of fission fragment anisotropies which are model dependent and many times have turned out to be anomalous. The present method is useful to obtain fusion cross-section as the reduced reaction cross-section by fitting GESA which contains all the reaction channels other than fusion.

2. The method

The total scattering amplitude which involves phase shifts δ_l and σ_l due to nuclear and Coulomb potentials is given by

$$\begin{aligned} f(x) &= \frac{1}{2ik}\sum_l (2l+1)[(e^{2i\sigma_l}-1)+e^{2i\sigma_l}(e^{2i\delta_l}-1)]p_l(x), \\ &= f_C(x)+f_n(x). \end{aligned} \tag{1}$$

Applying optical theorem to the amplitude $f(x)$, it can be shown that [2],

$$(4\pi/k)\,\mathrm{Im}[f_n(x=1)] = \sigma_{\mathrm{R}} + 2\pi\int[\sigma_{\mathrm{el}}(x)-\sigma_{\mathrm{Ruth}}(x)]\,\mathrm{d}x, \tag{2}$$

where the total elastic and Rutherford cross-sections are given by

$$\sigma_{\mathrm{el}} = 2\pi\int|f(x)|^2\mathrm{d}x \quad \text{and} \quad \sigma_{\mathrm{Ruth}} = 2\pi\int|f_c(x)|^2\mathrm{d}x$$

In presence of strong Coulomb field as in heavy ion scattering, the contribution of the left hand side of (2) is very small in comparison to the total reaction cross-section σ_{R} and by setting it to zero, it is possible to write the total reaction cross-section as the difference of Rutherford and elastic angular distributions provided the limit of integration is taken properly (for details see ref. [2] and references therein)

$$\sigma_{\mathrm{R}} = \lim_{\varepsilon \to 0} 2\pi \int_{\varepsilon}^{\pi} [\sigma_{\mathrm{Ruth}}(\theta) - \sigma_{\mathrm{el}}(\theta)] \sin\theta \, \mathrm{d}\theta. \tag{3}$$

The above equality justifies the use of generalized elastic scattering to obtain the reduced reaction cross-section. Let (V, W) be the set of real and imaginary optical potentials that fits the strictly elastic scattering and σ_{R} the corresponding reaction cross-section. For simplicity, if we assume that there are only two reaction channels; fusion and inelastic, then σ_{R} will be the sum of σ_f and σ_{inel}. Now the GESA can be obtained by adding this inelastic angular distribution to the strictly elastic channel. Let V' and W' be another set of optical potentials that fits the GESA. The corresponding reduced reaction cross-section σ'_{R} is given by

$$\begin{aligned} \sigma'_{\mathrm{R}} &= 2\pi \int \{\sigma_{\mathrm{Ruth}}(\theta) - \sigma_{\mathrm{GES}}(\theta)\} \sin\theta \, \mathrm{d}\theta, \\ &= 2\pi \int \{\sigma_{\mathrm{Ruth}}(\theta) - [\sigma_{\mathrm{el}}(\theta) + \sigma_{\mathrm{inel}}(\theta)]\} \sin\theta \, \mathrm{d}\theta. \end{aligned}$$

The reduced reaction cross-section σ'_{R} will now be less than σ_{R} and using (3), it can be shown that

$$\sigma_{\mathrm{R}} - \sigma'_{\mathrm{R}} = 2\pi \int \sigma_{\mathrm{inel}}(\theta) \sin\theta \, \mathrm{d}\theta = \sigma_{\mathrm{inel}}. \tag{4}$$

Therefore, we can identify, σ'_{R} as the fusion cross-section and (V', W') as the corresponding optical potential for fusion. It will be in general different from bare potentials and will contain long range polarization contribution. Therefore, the reaction partial wave distribution obtained with this set of optical potentials will correspond to the fusion partial wave distribution. Now the difference of the two reaction partial wave distributions obtained with two sets of potentials (V, W) and (V', W') will give the partial wave distribution for inelastic channel. In a simple situation, where we have only elastic and inelastic angular distributions, we define the GESA as $\mathrm{d}\sigma_{\mathrm{el}}/\mathrm{d}\Omega + \mathrm{d}\sigma_{\mathrm{inel}}/\mathrm{d}\Omega$. By fitting optical model to GESA, we are trying to find the nuclear part of the scattering amplitude f_l, (absorbing all multiplicative factors) that satisfies the equation given by,

$$\left| f_c(x) + \sum_l f_l'^{\mathrm{el}} p_l(x) \right|^2 = \left| f_c(x) + \sum_l f_l^{\mathrm{el}} p_l(x) \right|^2 + \sum_m \left| \sum_{ll'} f_{ll'm} p_{l'm}(x) \right|^2 .$$

The f'_l values derived in this manner correspond to the pseudo-optical potentials (V', W') as mentioned above.

The above discussion is based on the assumption that, one can neglect the term on the LHS of (2) in comparison to the reaction cross-section. This term as a function of angular momentum is highly oscillatory, but the total sum i.e. $(4\pi/k)\mathrm{Im} f_n(x=1)$ extends to large l values in heavy ion scattering and is quite small in the presence of a strong coulomb field. In this paper we studied systems for which $Z_T Z_P \geqslant 450$ and the above sum is less than 0·1% of the total reaction cross-section and therefore it

Table 1. Im $[f_n(x=1)]$ compared to σ_R as a test for validity of GESA method in heavy ion case.

System	E_{lab}(MeV)	σ_R(mb)	$4\pi/k\,\text{Im}[f_n(x=1)]$
$^{16}O + ^{28}Si$	40	995	118
	50	1122	158
	60	1302	-336
	70	1419	460
$^{16}O + ^{208}Pb$	78	88·9	$0{\cdot}704 \times 10^{-4}$
	86	472	$-0{\cdot}222 \times 10^{-4}$
	90	673	$0{\cdot}808 \times 10^{-4}$
	98	1024	$-0{\cdot}118 \times 10^{-1}$
	110	1449	0·302

can be neglected. Table 1 gives an estimate of this quantity compared with the total reaction cross-section at different energies for a light ion case ($^{16}O + ^{28}Si$) and a heavy ion case ($^{16}O + ^{208}Pb$).

3. Results and discussion

First we test the validity of the GESA method for obtaining fusion *l*-distribution for a simple two channel case. The coupled channel calculations for $^{32}S + ^{130}Te$ system have been carried out with rotational coupling to the 2^+ state of ^{130}Te with a *Q* value of 100 KeV. The coupling parameters are taken from ref. [2]. The coupled channel (CC) code ECIS [3] has been used to generate elastic and inelastic angular distributions and also the *l*-distributions for both reaction, inelastic and fusion channels. The GESA is generated by adding these elastic and inelastic angular distributions. The CC fusion *l*-distribution is compared with the reduced reaction *l*-distribution obtained from the optical model analysis of GESA using the optical code SNOOPY [4]. As shown in ref. [2], it might be difficult to reproduce the reaction *l*-distribution for strictly elastic scattering using optical model, as one is trying to fit an angular distribution resulting from long ranged absorption due to Coulomb excitations with a short ranged imaginary potential. On the other hand, such problems are less serious in the case of GESA.

Figure 1(a) shows the angular distributions at two typical bombarding energies (much below, and around the Coulomb barrier). The corresponding partial wave distributions are shown in figure 1(b). As seen from figure 1(b), the CC fusion *l*-distribution is in good agreement with the reduced reaction *l*-distribution.

We have carried out this analysis for this case over a wide range of energies (108 MeV to 139·5 MeV), from much below to much above the Coulomb barrier and found this method satisfactory (figure 1c). The corresponding mean square spin of fusion is shown in figure 1(d). The good agreement between GESA estimates and CC results in figures 1(c, d) over wide energy region show the usefulness of the present method.

In the following, we study the sensitivity of GESA parameters on fusion spin distributions as different sets of parameters can be used to get the same quality of fit to GESA. This test is carried out at 128 MeV for different sets of optical model parameters (OMP) that reproduce the GESA of ECIS within 10% error, figure 2(a)

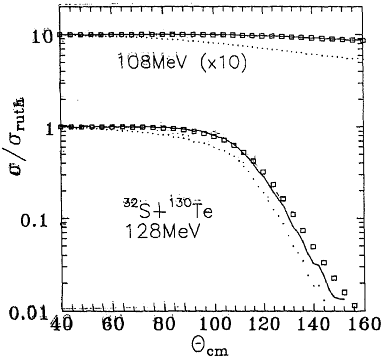

Figure 1a. $\sigma/\sigma_{\mathrm{Ruth}}$ vs θ_{cm} for strictly elastic scattering (dotted curve) and GESA (solid curve) for $^{32}S + {}^{130}Te$ system at $E_{\mathrm{lab}} = 108$ and 128 MeV obtained from ECIS. The open squares represent the optical model fits to GESA.

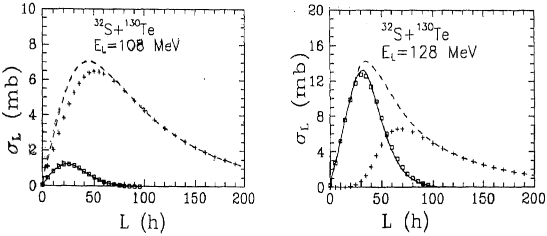

Figure 1b. σ_l vs l for $^{32}S + {}^{130}Te$ system at $E_{\mathrm{lab}} = 108$ MeV and 128 MeV. The dashed, solid curves and plus symbols represent l-distribution for total reaction, fusion and 2^+ inelastic state obtained from ECIS. The open squares are the fusion l-distribution obtained from the optical model fit to GESA.

shows OM fits to GESA with different sets of OM parameters as listed in table 2. Figure 2(b) shows the corresponding l-distributions. It can be concluded from figures 2(a, b) that fusion spin distribution is not very sensitive to optical parameters as long as they give acceptable fit to GESA. It is also interesting to note that though the OM parameter sets (see table 2) are different, the imaginary parts have same strength at strong absorption radius (R_s) as shown in figure 3(b), and real part has same strength at barrier radius (R_b) as seen in figure 3(a). Together, they determine the absorption of flux into the fusion channel. These features are very similar to those of OM potentials derived from strictly elastic scattering data.

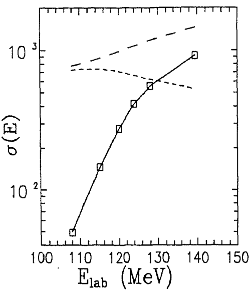

Figure 1c. Cross-sections for different reaction channels vs lab energy obtained from ECIS. The long and short dashes represent the CC results for total reaction and the inelastic channel. The CC fusion is shown by solid curve, obtained as the difference of long and short dashed curves. The squares represent the results of the GESA method.

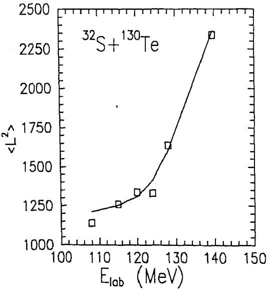

Figure 1d. Fusion $\langle L^2 \rangle$ versus lab energy with symbols as in figure 1c.

Table 2. Five sets of OMP which fit GESA data as shown in figure 2.

SET	V_0	r_0	a_0	W_0	r_i	a_i	χ^2/N	σ	$\langle L^2 \rangle$
A	100	1·217	0·5	100	1·24	0·52	3·619	544	1415
B	100	1·217	0·5	70	1·22	·59	2·045	562	1510
C	100	1·217	0·5	50	1·17	0·705	3·457	570	1658
D	100	1·217	0·5	30	1·21	0·705	4·581	558	1638
E	50	1·180	0·8	30	1·21	0·705	2·289	589	1652

^{32}S + ^{130}Te at $E_{\rm lab} = 128{\cdot}0$ MeV; $r_c = 1{\cdot}250$ fm, $N = 71$ and 10% error on data taken for calculating χ^2/N. σ_F(ECIS) = 555·8 mb and $\langle L^2 \rangle_F$(ECIS) = 1607 $\hbar^2$

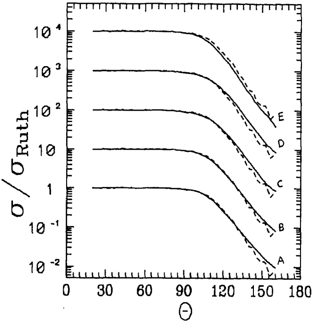

Figure 2a. Optical model fits (solid lines) to GESA obtained from ECIS (dashed lines) for the OMP sets listed in table 2.

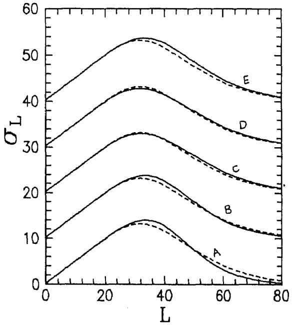

Figure 2b. The reduced reaction spin distribution corresponding to figure 2a.

In the above discussion only two reaction channels were considered, however, this method can be generalised even if more channels are present. In order to verify this, we carried out CC calculations for the $^{16}O + ^{152}Sm$ system at 72 MeV lab energy including the 2^+ and 4^+ states of Sm. The coupling parameters are taken from [5] which fit the experimental angular distributions for 2^+ and 4^+ inelastic states. In this case the GESA is the sum of elastic, 2^+ and 4^+ inelastic states. As before, the CC l-distribution for fusion is obtained as the difference of the l-distributions for total reaction and total inelastic channels obtained from the ECIS. Figure 4 shows that the reduced reaction l-distribution obtained from SNOOPY and the CC fusion l-distribution are in good agreement.

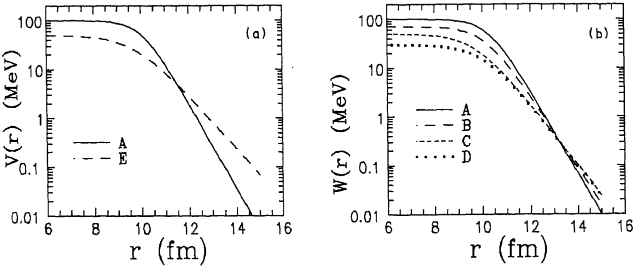

Figure 3a, b. Real part (3a) and Imaginary part (3b) of OMP of table 2 as a function of radial separation showing the agreement of imaginary strengths at strong absorption radius.

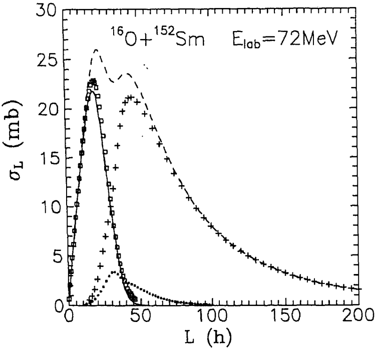

Figure 4. Same as figure 1(b), but for $^{16}O + ^{152}Sm$ system at $E_{lab} = 72$ MeV. The dashed, solid, plus symbols and the dotted curves represent the l-distributions for total reaction, fusion, 2^+, 4^+ inelastic states. The squares are the fusion l-distribution obtained from the optical model fit to GESA.

The reduced reaction of the model calculations for above cases of $^{32}S + ^{130}Te$ and $^{16}O + ^{152}Sm$ has been identified with fusion channel, since the model space consists of elastic, inelastic channels only. In heavy ion reactions, several inelastic as well as transfer channels contribute significantly to reaction and therefore the results of these cases cannot be compared with experimental fusion data. Thus, the accuracy of the method to obtain fusion depends on the relative contribution of the left out channels.

In general, for heavy ion reactions, single step as well as multi-step particle transfers following the inelastic excitations contribute significantly to the total reaction cross-section. Therefore, to verify the validity of the present method for fusion partial wave distribution in the presence of particle transfer, the coupled channels results for $^{16}O + ^{208}Pb$ system at 80 MeV have been analysed using the present method. The Coupled channel calculations were carried out using the code FRESCO [6]. The potentials and coupling parameters are taken from [6]. As before, the fusion l-distribution can be obtained using an optical model fit to the GESA, generated by adding the FRESCO angular distributions for elastic, inelastic and transfer channels. In this case the reduced reaction can be identified with true fusion since the coupling scheme includes all channels that contribute significantly to reaction.

Figure 5(a) shows the CC angular distributions for the strictly elastic channel and the GESA. Figure 5(b) shows the l-distributions for the total and reduced reaction cross-sections obtained by fitting the strictly elastic scattering and the GESA. The difference between the total and the reduced reaction (fusion) l-distributions gives the

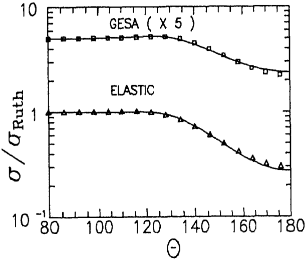

Figure 5a. $\sigma/\sigma_{\text{Ruth}}$ versus θ_{cm} for strictly elastic scattering (lower solid curve) and GESA (upper solid curve) obtained from FRESCO for $^{16}O + ^{208}Pb$ system at $E_{\text{lab}} = 80$ MeV. The optical model fits are shown by triangles (elastic) and squares (GESA).

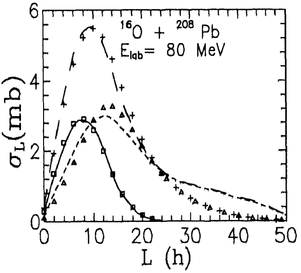

Figure 5b. σ_l versus l for $^{16}O + ^{208}Pb$ system at $E_l = 80$ MeV. The long dashed, continuous and the dashed lines represent the reaction, fusion and the transfer cross-sections obtained from FRESCO. The corresponding results from optical model fits to GESA are shown by plus symbols, squares and triangles (see text).

l-distributions for the inelastic plus transfer channels. However, for this system, the inelastic cross-section at this energy is negligible and the reaction comprises of mainly transfer and fusion channels. The coupled channel l-distributions for reaction, fusion and transfer channels are also shown for comparison. It can be seen that the reduced reaction l-distribution reproduces well the coupled channel fusion l-distribution. However, the reaction l-distribution obtained fitting strictly elastic scattering, does not agree well with the coupled channel reaction at higher l values. As a result, the transfer of l-distribution obtained from the optical model fit does not agree well with the coupled channels results for higher l values. In case of fusion, the coupled channel contribution to fusion from the non-elastic processes comes mostly from the low l values (see cc fusion l-distribution in figure 5(b)). Therefore, the GESA can be used to obtain the fusion l-distributions. On the basis of these studies, one can conclude that the present method is able to reproduce the fusion l-distribution derived from coupled channels calculations reliably.

This method has been applied to the experimental angular distributions of $^{16}O + ^{208}Pb$ system at 90 MeV, and to $^{16}O + ^{232}Th$ system at several energies for which complete measurements on elastic, inelastic and transfer channels are available [7–10]. The $\langle L^2 \rangle$ values experimentally determined from fission angular distributions for these systems, turn out to be anomalously large [8, 10]. The CC calculations for fusion also underpredict the $\langle L^2 \rangle$ values [11], showing the importance of higher order coupling processes leading to fusion.

In case of $^{16}O + ^{208}Pb$ system at 90 MeV due to large errors in the experimental data, the inelastic and transfer angular distributions are smoothed by a polynomial fit before being used to generate GESA in two ways. Initially, the total inelastic angular distribution is added to elastic data (case-I) and then both inelastic and transfer angular distributions are added to elastic data (case-II). The optical model reduced reaction l-distributions corresponding to these cases are shown in figure 6(a). The l-distribution for inelastic channels can be obtained as the difference of l-distribution for the total reaction and l-distribution for case-I. Similarly, the transfer l-distribution can be obtained as the difference of l-distribution for case-II and that

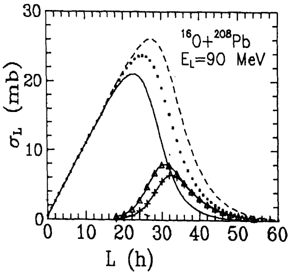

Figure 6a. σ_l versus l for $^{16}O + ^{208}Pb$ system at $E_l = 90$ MeV. The dashed, dotted, solid lines represent l-distributions for the three cases explained in the text. The plus symbols and the triangles represent total inelastic and transfer l-distributions respectively.

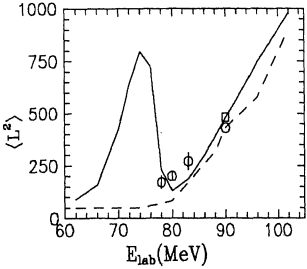

Figure 6b. Fusion mean square spin versus energy obtained by different methods. The results of FRESCO and BPM calculations are shown by solid and dashed curves. The result of GESA method obtained at 90 MeV is shown by square symbol. The experimental data are shown by circles.

for case-I. The reduced reaction l-distribution of case-II can be identified as true fusion l-distribution because the GESA for this case includes both inelastic and transfer channels. At 90 MeV, total reaction cross-section is about 670 mb and the total angle integrated cross-sections for inelastic and transfer are 92 ± 20 mb and 109 ± 5 mb. Therefore, fusion cross-section obtained by eliminating these non-elastic channels (with total cross-section of 201 ± 25 mb) from total reaction, is expected to be 469 ± 25 mb. The optical model fit to GESA of case-II predicts reduced reaction cross-section of 454 mb and average and the mean square l values are $20{\cdot}2\,\hbar$ and $481\,\hbar^2$. The experimental fusion cross-section is 450 ± 25 mb and mean square l value is $433\,\hbar^2$. The corresponding values from coupled channel calculations [6] are 466 mb, $20{\cdot}6\,\hbar$ and $488\,\hbar^2$ and from barrier penetration model (BPM as defined in [6]) are 448 mb, $19{\cdot}5\,\hbar$ and $433\,\hbar^2$. Thus, we have shown that the fusion cross-section and the l-distribution obtained from GESA method are consistent with the results of coupled channel method and the experimental measurements. At very high energy these values are more or less independent of the choice of any particular model as the transmission probability for fusion is nearly unity. As seen from figure 4, the inelastic l-distribution has a long tail due to the long range Coulomb excitations and such a behaviour is also expected in figure 6(a). This discrepency arises due to the fact that the optical model fit is not able to predict the large l behaviour of total reaction. Figure 6(b) shows the fusion mean square spin versus energy obtained by different methods. It is seen from the figure that the present method agrees well with the other methods. The fusion mean square spin from CRC method is observed to increase with decreasing energy and results in a peaking behaviour at deep sub-barrier energies. However, the exhaustive experimental data are not available at such deep sub-barrier energies and this aspect is under further study.

Figure 7(a) shows, for $^{16}O + ^{232}Th$ system, the reaction cross-section, fusion cross-sections at five bombarding energies obtained by this method and also the experimental fusion data. In order to obtain fusion, only available transfer angular distributions are added to the elastic channel, as the experimental elastic data already contains the contribution from the low lying excited states. The figure also shows the fusion obtained from Wong's model [12] (with deformation parameter $\beta_2 = 0{\cdot}22$,

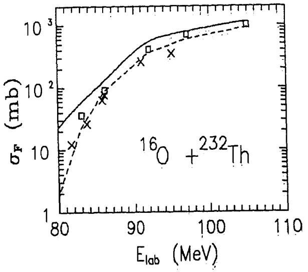

Figure 7a. Fusion and reaction cross-section versus energy for $^{16}O + {}^{232}Th$ system. The reaction cross-section is shown by solid curve. The fusion cross-sections obtained by GESA method at five bombarding energies is shown by squares (interpolated by long dashes in figure 7(b)) and the experimental fusion data are shown by crosses. The dashed curve represents the fusion obtained from Wong's model.

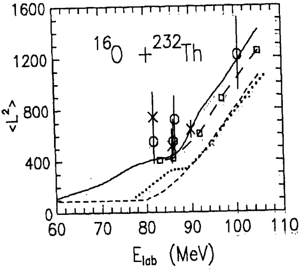

Figure 7b. Mean square spin values versus energy for different cases shown in figure 7(a). The crosses and circles with error bars are the experimental $\langle L^2 \rangle$ data. The dotted curve is the CC calculations [11].

$V_0 = 79{\cdot}7$ MeV, $\hbar\omega = 4{\cdot}96$ MeV and $R_0 = 12{\cdot}3$ fm). Figure 7(b) shows the corresponding mean square spin values for different cases shown in figure 7(a). As seen in figure 7(b), the mean square values obtained for fusion are much higher than Wong's model prediction as well as the CC calculations. At high energy, the Wong's model and CC calculations give same $\langle l^2 \rangle$ for fusion, which is less compared to the present method. This discrepancy with the present method at high energy is expected as we have not added all the transfer channels to the GESA and the reduced reaction cross-sections so obtained are also much higher than the experimental fusion cross-section (see figure 7(a)). For example, at $E_{\text{lab}} = 105$ MeV, the quasielastic reaction cross-section is about 1124 mb ($\langle L^2 \rangle = 1413\,\hbar^2$). By adding available transfer angular distributions for a few channels with total angle integrated cross-section of 120 mb, we get the reduced reaction cross-section about 1005 mb ($\langle L^2 \rangle = 1249\,\hbar^2$). However, at this energy, the total measured transfer cross-section is around 220 mb and fusion cross-section is about 914 mb. Therefore, if we include all transfer channels (i.e. contribution of another 100 mb more), it is possible to get the reduced reaction cross-section which will be quite close to the experimental fusion cross-section. The corresponding $\langle L^2 \rangle$ value will also agree with Wong or CC results.

Figures 8(a, b) show the l-distributions for different reaction channels at 105 and 83 MeV for the case of $^{16}O + ^{232}Th$. The dashed curve corresponds to the l-distribution obtained fitting quasi elastic data and the solid line for GESA data. At above barrier energy of 105 MeV the transfer l-distribution shows localisation in the L space around $L \simeq 50\,\hbar$. However, it is interesting to note that at 83 MeV the l-distribution for different reaction channels are very much similar to each other and does not show any localisation in L space. Therefore, if we include more transfer

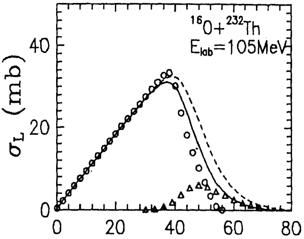

Figure 8a. σ_l versus l for $^{16}O + ^{232}Th$ system at 105 MeV. The dashed and the solid curves represent the l-distribution for reaction (without inelastic) and fusion obtained from optical model fits to GESA. The difference between the solid and dashed curves is shown by triangles, which represent the l-distribution for transfer channel. The circles are obtained from the Wong model fit to fusion excitation function.

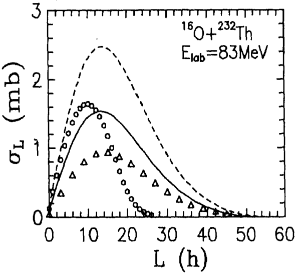

Figure 8b. Same as figure 8(a), but for $E_{lab} = 83$ MeV.

channels to get reduced reaction cross-section same as fusion cross-section, the shape of the l-distribution will not change. This is also evident from figure 7(b) where $\langle L^2 \rangle$ versus energy shows a plateau at energies around the Coulomb barrier and the values for the fusion and the reaction become the same. In other words, transfer reactions compete with the fusion process at all l values. As a result, the fusion $\langle L^2 \rangle$ values increase and approach that of reaction $\langle L^2 \rangle$ values at near barrier energies. The $\langle L^2 \rangle$ values obtained by the present method are in agreement with experimental data.

Summary

It is shown that the GESA method can be used to obtain the fusion spin distributions from the experimental, elastic and non-elastic angular distributions. The validity of this method has been verified in the presence of couplings to inelastic as well as transfer channels. When applied to fissile systems, the method gives large mean square spin, in agreement with the measured "anomalous" values. Further, the analysis shows that the fusion competes with transfer processes for all partial waves at low energy, whereas at high energy, the transfer exhibits localisation in l-space. These results are model independent as one uses only the experimental angular distributions for appropriate reaction channels.

Acknowledgements

We are thankful to Dr S S Kapoor for his keen interest in this work; Dr P Singh, Dr S Kailas, Dr K V Bhagwat and Prof. C V K Baba for several useful discussions during the course of this study. We are thankful to Dr I J Thompson for the FRESCO code.

References

[1] R Vandenbosch, *Annu. Rev. Nucl. Part. Phys.* **42**, 447 (1992)
[2] H Oeschler, H L Harney, D L Hillis and K S Sim, *Nucl. Phys.* **A325**, 463 (1979)
[3] J Raynal, *Phys. Rev.* **C23**, 2571 (1981)
[4] SNOOPY Computer program by P Schwandt, Indiana University, Cyclotron centre report (1988)
[5] R G Stokstad and E E Gross, *Phys. Rev.* **C23**, 281 (1981)
[6] I J Thompson, M A Nagarajan, J S Lilley and M J Smithson *Nucl. Phys.* **A505**, 84 (1989)
[7] F Videbaek, R B Goldstein, L Grodzins and S G Steadman, *Phys. Rev.* **C15**, 954 (1977)
[8] T Murakami, C C Sahm, R Vandenbosch, D D Leach, A Ray and M J Murphy, *Phys. Rev.* **C34**, 1353 (1986)
[9] J S Karp, S G Steadman, S B Gazes, R Ledoux and F Videbaek, *Phys. Rev.* **C25**, 1838 (1982)
[10] J P Lestone, J R Leigh, J O Newton and J X Wei, *Nucl. Phys.* **A509**, 178 (1990)
[11] H Esbensen and S Landwone, *Nucl. Phys.* **A467**, 136 (1987)
[12] C Y Wong, *Phys. Rev. Lett.* **31**, 766 (1973)

PRAMANA
— journal of
physics

© Printed in India

Vol. 44, No. 2,
February 1995
pp. 167–176

Momentum- and energy-dependence of J/ψ suppression in relativistic heavy ion collisions

R S KAUSHAL and S K KARN
Department of Physics and Astrophysics, University of Delhi, Delhi 110007, India

MS received 29 August 1994; revised 24 November 1994

Abstract. With a view to understand the available data on the momentum- and energy-dependences of the J/ψ suppression, we compute the suppression rate within the framework of a hydrodynamical evolution model for the quark-gluon plasma (QGP) formation. We make use of an ansatz for the temperature profile function which accounts not only for the space and time evolutions of QGP but also for the possiblity of a mixed phase in the boundary region of the deconfined phase. While the predictions are made for the longitudinal momentum- and energy-dependences of the suppression rate, a satisfactory agreement with the available data is found for its dependences on the transverse momentum and the transverse energy.

Keywords. Quark-gluon plasma; suppression rate; energy- and momentum-dependence.

PACS Nos 12·38; 25·70

1. Introduction

It is believed that heavy ion collision experiments at ultra-relativistic energies ($\geqslant 200$ GeV/nucleon) can offer [1, 2] the conditions well-suited for the formation of a deconfined state of quarks and gluons (called quark-gluon plasma (QGP)). Theoretically, the J/ψ suppression in these experiments has been argued [3] as one of the important signals for the QGP formation in the laboratory. In fact, J/ψ resonances produced in these collisions are not able to come out in the presence of QGP mainly due to the screening effect.

No doubt the mechanism responsible for the formation of QGP in the laboratory can throw light on the theories [2] of early Universe, but the situation regarding the understanding of J/ψ suppression still seems to be fluid in both experiment and theory. Not only the data [4, 5] on p_T-dependence clearly show large error bars throughout but also the data on E_T-dependence show the errors of the same magnitude at least for small values of E_T. In spite of this fact several [6–11] theoretical attempts have been made to understand this anomalous phenomenon. Unfortunately, none of the calculations has been able to reproduce both the pieces of available data, namely p_T (transverse momentum)- and E_T (transverse energy)-dependences of the suppression rate at the same time.

In the present work, we attempt to understand both pieces of data simultaneously within the framework of the hydrodynamical evolution model for the QGP formation. For this purpose an exponential-type temperature profile function is used which not only accounts for the time and space evolutions of QGP in the transverse and longitudinal directions, but also for the possibility of mixed phase in the boundary-region of the deconfined phase. In the next section, we briefly outline various theoretical works carried out in the recent past on the understanding of J/ψ suppression. In § 3, we compute the suppression rate within the framework of the present model. The calculated survival probability is then compared with experiments and with other theoretical results in § 4. Finally, the results are discussed and summarized in § 5.

2. Various theoretical approaches

The formation and subsequent evolution of baryonless QGP in the relativistic heavy ion collision experiment is fairly well described [12] within the framework of the Björken hydrodynamical model and in terms of thermodynamical variables like temperature (T), energy density (ε), entropy density (s), etc. In fact one calculates the survival probability (S) which is related [8] to the probability of disintegration (P) by [13]

$$P = 1 - S = 1 - \exp(-T). \tag{1}$$

Ftacnik *et al* [8] have considered the J/ψ suppression mainly due to J/ψ- and χ-disintegration in collisions with other hadrons in a dense hadronic gas formed in the collision. Karsch and Petronzio [7] (KP), on the other hand, study the E_T- and nuclear size-dependences of J/ψ suppression within the framework of the hydrodynamical model. They assume that QGP is formed in a finite volume and for a short time. While reasonably good results are obtained by both KP and Ftacnik *et al* for the E_T-dependence of S, the results for the p_T-dependence somehow do not turn out to be that good.

Recently, Gazdzicki and Mrowczynski [9] have tried to understand both strangeness enhancement and J/ψ suppression in terms of a common model for the nuclear interactions at high energies. However, the computed E_T-dependence of S shows a completely different behaviour at large E_T as compared to that of KP and Ftacnick *et al.* More recently, Gupta and Satz [11] have obtained a fairly good fit for the E_T dependence of S by accounting for the effects arising from the modification of the structure functions in nuclei and by considering the parton scattering in nuclear matter.

As far as the parametrization of thermodynamical variables for the purposes of calculating the suppression rate is concerned it has been done differently by different authors. For example, (i) Blaizot and Ollitrault [6] parametrize the entropy density by using the form

$$s(t_0, r) = s_0(1 - r^2/R^2)^{a'},$$

where R is the projectile radius and a', a free parameter. The predictions made on the basis of this model however could not be compared with experiments as the data were not available at that time (ii) Karsch and Petronzio [7] used the form for the temperature function,

$$T(r) = T(0)(1 - r^2/R^2)^{b/3},$$

where the parameter b is fixed as 1/3 (iii) Recently, Gupta and Satz [11] and earlier

Karsch and Satz [10] have used the energy density in the form

$$\varepsilon(r) = \varepsilon_0(1 - r^2/R^2)^{2/3},$$

and they have shown the possibility of a bump structure around 2 GeV/fm^3 in the energy dependence of S.

It may be noted that in all the above works the dependence of s, T or of ε on r is considered to be of the same power-type function, namely $(1 - r^2/R^2)^a$. This form, no doubt, is well-suited for the description of a collision of a large and a small nucleus, but somehow characterizes the sharp-boundaries for the deconfined phase and as such do not leave any scope for the description of a mixed phase in the peripheral region of the deconfined volume. On the other hand, in a realistic situation while the space-evolution of the deconfined region cannot be as steep as described by the above functional forms of s, T or ε, one should also account for the temporal evolution of QGP. For these regions we resort to choose an exponential fall for the temperature profile function not only in the transverse but also in the longitudinal direction. Also, we account for the time-dependence of T in accordance with the scaling law [12, 14].

In all works, except [9], the dependence of S on p_T is sought in a nontransparent manner in spite of the fact that $\mathbf{p}_T$ is the conjugate momentum of the coordinate $\mathbf{r}$ defined in the transverse plane of the cylindrical interaction-volume. Further, the computed results show a sensitive dependence on the critical plasma size, R_c, or, in other words, on the time period during which the QGP survives. In a way this latter type dependence of R_c again is the manifestation of the functional form chosen for the parametrization.

3. Present model

In this section, we consider the hydrodynamical evolution model for QGP in both space and time. We use [15, 16] the concept of temperature density normalized to unity over the plasma volume. Further the survival probability, S, will be computed separately as the functions of p_L, E_L, p_T and E_T. However, the experimental results are available only as a function of p_T or E_T.

For cylindrical symmetry, the temperature function, in general, can be written as [17]

$$T(\mathbf{r}, t) = T_0\, T(r) f(z, t), \tag{2}$$

where various functions are chosen as

$$T(r) = \exp(-br/R); \quad f(z, t) = \exp(-\eta z)t^{-1/3}, \tag{3}$$

where the parameter η is the measure of the steepness of the fall of temperature along z-direction. Further as mentioned earlier the t-dependence of T is set in accordance with the scaling law and overall normalization constant T_0 can be determined from [18]

$$\iint T(\mathbf{r}, t)\mathrm{d}^3 r\,\mathrm{d}t = 1. \tag{4}$$

as

$$T_0 = (\alpha^2\eta/6\pi)[(t_f^{2/3} - t_i^{2/3})\sinh(\eta l/2)\{1 - (1 + \alpha R_c)\exp(-\alpha R_c)\}]^{-1}, \tag{5}$$

where $\alpha = b/R$, and R is the radius of the projectile nucleus. Note that the form of $T(\mathbf{r}, t)$ in (2) clearly accounts for the fall of temperature with both space and time variables. The cylindrical plasma volume can be characterized by the critical radius R_c, the length l of the region with the origin at $z = 0$. The critical temperature, T_c equal to $T(R_c)$, is also related to the QGP life time t_f through [12] $T_i^3 t_i = T_c^3 t_f$.

After using the expression for T_0 from (5) the Fourier transforms of (2) with respect to z- and r-variables respectively lead to the p_L- and p_T-dependences of T as

$$|T(p_L)| = \frac{\eta}{\sinh(\eta l/2)(\eta^2 + p_L^2)^{1/2}} [\sinh^2(\eta l/2)\cdot\cos^2(p_L \cdot l/2) + \cosh^2(\eta l/2)\cdot\sin^2(p_L \cdot l/2)]^{1/2}, \tag{6}$$

$$|T(p_T)| = \frac{\alpha^2}{(\exp(\alpha R_c) - 1 - \alpha R_c)(\alpha^2 + p_T^2)} [R_c^2(\alpha^2 + p_T^2) + 2\alpha R_c + 2\exp(\alpha R_c)\cdot\{\cosh(\alpha R_c) - (1 + \alpha R_c)\cos(p_T R_c) - p_T R_c \sin(p_T R_c)\}]^{1/2}. \tag{7}$$

It may be mentioned that in obtaining (7) we have assumed that $i\mathbf{p}_T \cdot \mathbf{r} = ip_T r\cos\varphi \simeq ip_T r$, i.e. $\varphi = 0$. In Appendix we outline a method to estimate the corrections arising due to this assumption. This assumption seems to be reasonable for the order of energies involved in the problem. Thus, S as a function of p_L or p_T can be studied using (1).

To obtain E_T-dependence of S we now use the expression for the energy density $\varepsilon(r)$ as

$$\varepsilon(\mathbf{r}, t) = (\alpha_s \pi^2/15)\, T^4(\mathbf{r}, t) \tag{8}$$

where [7] $\alpha_s = N^2 - 1 + (7/4)Nn_f = 18{\cdot}5$. In fact, for $SU(N)$, $N = 3$ and n_f (the number of quark flavours) is taken to be 2. Further, in view of (4) the relation (8) should also involve a dimensional constant which may be useful for determining the absolute values of the transverse energy. However, in the present work, we restrict ourselves to the computation of the ratio $E/E_{\max}$, in which such a constant will cancel out. Thus in the same spirit as (2), the form of $\varepsilon(\mathbf{r}, t)$ is taken to be

$$\varepsilon(\mathbf{r}, t) = \varepsilon_0 \exp(-4\alpha r)\exp(-4\eta z)t^{-4/3}, \tag{9}$$

where $\varepsilon_0 (= (\alpha_s \pi^2/15)\, T_0^4)$ is now treated as a new normalization constant and determined from

$$\iint \varepsilon(\mathbf{r}, t)\mathrm{d}^3 r \mathrm{d}t = 1, \tag{10}$$

as

$$\varepsilon_0 = (16\alpha^2\eta/3\pi)[(t_f^{-1/3} - t_i^{-1/3})\sinh(2\eta l)\{1 - (1 + 4\alpha R_c)\exp(-4\alpha R_c)\}]^{-1}. \tag{11}$$

As before, the Fourier transforms of $\varepsilon(\mathbf{r}, t)$ with respect to z- and r-variables give rise to

$$\varepsilon(p_L) = \frac{4\eta}{\sinh(2\eta l)(16\eta^2 + p_L^2)^{1/2}} [\sinh^2(2\eta l)\cos^2(p_L \cdot l/2) + \cosh^2(2\eta l)\sin^2(p_L \cdot l/2)]^{1/2}, \tag{12}$$

and

$$\varepsilon(p_{\mathrm{T}}) = \frac{16\alpha^2}{\{\exp(4\alpha R_{\mathrm{c}}) - (1 + 4\alpha R_{\mathrm{c}})\}(16\alpha^2 + p_{\mathrm{T}}^2)}\,[R_{\mathrm{c}}^2(16\alpha^2 + p_{\mathrm{T}}^2) + 8\alpha R_{\mathrm{c}} + 2\exp(4\alpha R_{\mathrm{c}})\cdot\{\cosh(4\alpha R_{\mathrm{c}}) - (1 + 4\alpha R_{\mathrm{c}})\cos(p_{\mathrm{T}} R_{\mathrm{c}}) - p_{\mathrm{T}} R_{\mathrm{c}} \sin(p_{\mathrm{T}} R_{\mathrm{c}})\}]^{1/2}, \tag{13}$$

respectively. Once again, here $\varphi \approx 0$ is assumed for the angular integral in obtaining (13). It can be seen that for both $\varepsilon(p_{\mathrm{L}})$ and $\varepsilon(p_{\mathrm{T}})$ the maximum occurs at $p_{\mathrm{L}} = 0$ and $p_{\mathrm{T}} = 0$, respectively. Therefore, for comparison with experiments, we compute $X_1 = \varepsilon_{\mathrm{L}}/\varepsilon_{\mathrm{Lmax}}$ and $X_2 = \varepsilon_{\mathrm{T}}/\varepsilon_{\mathrm{Tmax}}$, where $\varepsilon_{\mathrm{L}} = \varepsilon(p_{\mathrm{L}})$; $\varepsilon_{\mathrm{Lmax}} = \varepsilon_{\mathrm{L}}(p_{\mathrm{L}} = 0)$; $\varepsilon_{\mathrm{T}} = \varepsilon(p_{\mathrm{T}})$ and $\varepsilon_{\mathrm{Tmax}} = \varepsilon(p_{\mathrm{T}} = 0)$. Further note that the expression for total energy (E), $E = \pi R^2 l\varepsilon$, is used throughout this work. Other simplifying points used in the computation of S as a function of X_1 and X_2, will be mentioned in the next section.

4. Comparison of results

The predictions made on the basis of the model discussed in § 3, are compared here with the results of NA38 experiments [4, 5] and also with the work of other authors for the oxygen-uranium (O–U) central collisions at 200 GeV/nucleon.

The predicted results for S as a function of p_{L} and X_1 are shown in figures (1) and (2), respectively for [7] $l = 2$ fm and for two values of the parameter η, namely $\eta = 0{\cdot}9\ \mathrm{fm}^{-1}$ (solid curve) and $\eta = 1{\cdot}1\ \mathrm{fm}^{-1}$ (dashed curve). In general, it can be seen that the J/ψ suppression decreases with p_{L} and increases with X_1. However, for comparison of either of these predictions, neither the experimental results are available nor these quantities are calculated earlier to the best of our knowledge except for some discussions mainly of qualitative nature (see, for example, [10], [15] and [19]). No doubt there are indications [19] of similar longitudinal and transverse momentum distributions of O–U events in NA38 experiments but somehow the suppression rate either as a function of p_{L} or as a function of X_1 has not been extracted from these data so far.

The calculated results for S as a function of p_{L} and X_2 are shown (solid curves) in

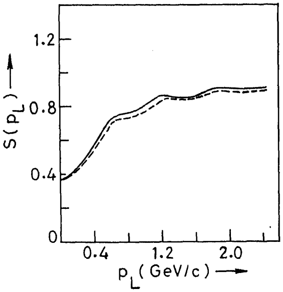

Figure 1. Survival probability as a function of p_{L}: solid and dashed curves correspond to two values of η, namely $\eta = 0{\cdot}9\ \mathrm{fm}^{-1}$ and $\eta = 1{\cdot}1\ \mathrm{fm}^{-1}$ respectively.

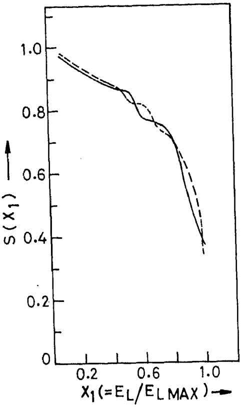

Figure 2. Survival probability as a function of $X_1(=E_L/E_{L\max})$. For the explanation of solid and dashed curve, see the caption for figure 1.

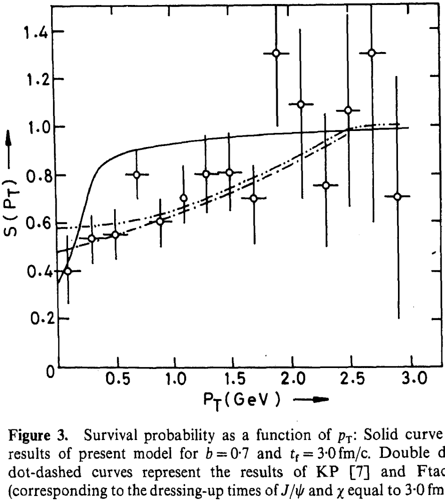

Figure 3. Survival probability as a function of p_T: Solid curve represents the results of present model for $b=0{\cdot}7$ and $t_f=3{\cdot}0\,\mathrm{fm/c}$. Double dot-dashed and dot-dashed curves represent the results of KP [7] and Ftacnik *et al* [8] (corresponding to the dressing-up times of J/ψ and χ equal to 3·0 fm/c) respectively. Experimental points are from Baglin *et al* [4].

figures 3 and 4 respectively for $b = 0{\cdot}7$ along with the experimental [4, 5] points and the theoretical results of other authors for the sake of comparison. From figure 3 it can be seen that our results show a stronger suppression and a faster saturation with p_T as compared to that of KP [7] (double dot-dashed curve) and of Ftacnik *et al* [8] (dot-dashed curve). In view of large error bars in the data for p_T-dependence it is however difficult to draw any definite conclusion at this stage regarding the merit of a theoretical model.

In figure 4, we compare our results for S vs X_2 not only with the experiments [5] but also with the results obtained in [6] (as cited in [8]), [7], [11], [9]. No doubt this piece of data is more stable as compared to that of S vs. p_T (cf. figure 3), however the large experimental errors at low E_T in this case have forced to normalize almost all theoretical calculations with experiments. For example, KP, Ftacnik *et al* and GS

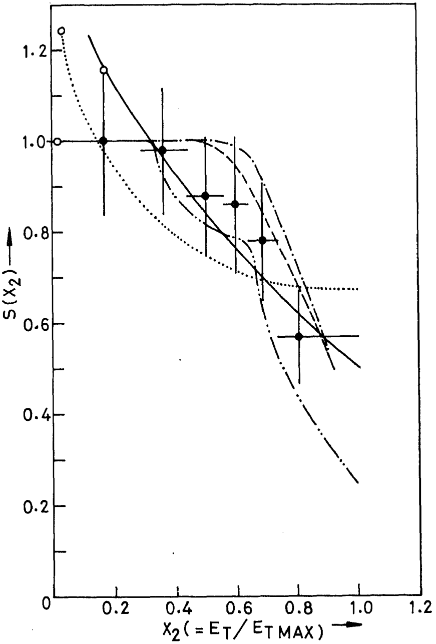

Figure 4. Survival probability as a function of $X_2 (= E_T/E_{T\max})$. Solid curve represents the results of present model for $b = 0{\cdot}7$ and $t_f = 3{\cdot}0$ fm/c. Dashed and dot-dashed curves are the results of KP [7] and Blaizot and Ollitrault [6] (as cited in [8]), respectively. Dotted and double dot-dashed curves represent the results of [9] and [11] respectively. Experimental points are from Baglin *et al* [5].

normalize their results at $S = 1$ (open circle) whereas GM normalize somewhere at $S = 1{\cdot}25$. We have also normalized our results at $S = 1{\cdot}16$, i.e. at the point which corresponds to the maximum error in S for the first data point.

As far as the overall trend of the calculated results is concerned, the results of [6] and [7] show somewhat fast suppression of J/ψ whereas those of [11], [9] and ours show some sort of saturation for large E_T. In fact, the results of [9] have the tendency to attain a constant value of S with E_T (something like $S = 0{\cdot}68$), those of [11] and ours show somewhat faster suppression of J/ψ for large E_T. However, this latter suppression is not as prominent as shown by the results of [7] and [6]. In a way our results show a balancing trend not only with experiments but also with other theoretical results. It may be mentioned that the data used in [11] are those from Pappilon's work [20] which is free from horizontal error bars whereas we have taken the experimental results from [5] and normalized them for unity at $E_{T_{\max}} = 70\,\text{GeV}$. Further for transcribing the theoretical results of [9] and [11] for the comparison in figure 4 we have normalized their results also for $\varepsilon_T/\varepsilon_{T\max} = 1$.

Regarding the computation of S as a function of X_1, it is noticed that the expression for X_1 (cf. eq. (12)) attains a much simpler form of the type $p_L = 4\eta(1 - X_1^2)^{1/2}/X_1$, as the square of the sine and cosine hyperbolic functions in (12) becomes large and almost equal for the values of l and η used in the calculations. Similarly, for S vs. X_2 (cf. figure 4) we first compute X_2 as a function of p_T from (13) and for these same values of p_T we compute $|T(p_T)|$ from (7) and subsequently obtain S from (1).

5. Discussion and Summary

Within the framework of the Björken hydrodynamical model we have tried to understand the space- and time-evolution of QGP by considering an exponential fall of the temperature in both longitudinal and transverse directions. The tail of this fall is expected to account for the possibility of a mixed phase in the peripheral region of QGP volume. In view of the agreement of the present results (cf. figures (3) and (4)) with experiments it may be emphasized that such a possibility cannot be ruled out. Perhaps it requires further fine-tuning of the data.

The predictions are made for the J/ψ suppression as a function of p_L and E_L (cf. figures 1 and 2). The presently available data [19] for the longitudinal momentum distribution however are not sufficient for a meaningful comparison of these predicted results. It may be mentioned that further experimental work from the point of view of extracting the information on this aspect is desirable. In fact, the studies of both p_L and p_T-dependences of S will be helpful in a complete understanding of this phenomenon of J/ψ suppression.

Finally, we discuss the role of dressing-up time of QGP in these calculations. In fact, such a dependence mainly arises through the computation of R_c (cr. $T_c = T(R_c)$). The results for S vs p_L and S vs. X_1 are found to be independent of such a parameter. While our results presented in figures 3 and 4 correspond to $t_f = 3\,\text{fm/c}$, the results for $S(X_2)$ vs. X_2 are found to be more sensitive than those for $S(p_T)$ vs. p_T with respect to the value of t_f. As a matter of fact similar observations are also made in earlier [6, 8] calculations. To some extent the normalization of the theoretical results with experiments can be attributed to this unknown parameter.

Acknowledgements

The authors are greatly benefited from the discussions with Professor H Satz at CERN and they wish to express their gratitude to him. Authors also wish to thank Dr S K Gupta of BARC (Bombay) for bringing the work of R A Salmeron to their notice. Thanks are also due to Dr Y K Mathur for several helpful discussions. RSK acknowledges the award of UGC Research Scientist Scheme during the course of this work.

Appendix

Here, we outline a method for computing the corrections arising from the angular integral in (7) and (13). For the exponential radial function this integral appears in the form

$$I_{r\varphi} = \int_0^{R_c} \exp(-\alpha r) r \, \mathrm{d}r \int_0^{2\pi} \exp(i p_{\mathrm{T}} r \cos\varphi) \mathrm{d}\varphi.$$

For small φ, one can however use $\cos\varphi \approx 1 - \varphi^2/2$ and obtain the corrections arising from the φ^2-term in terms of error functions. Alternatively, one can use the formula involving the Bessel function as

$$\int_0^{2\pi} \exp(i p_{\mathrm{T}} r \cos\varphi) \mathrm{d}\varphi = 2\pi J_0(p_{\mathrm{T}} r)$$

with

$$J_0(z) = \sum_{k=0}^{\infty} \frac{(-1)^k z^{2k}}{2^{2k}(k!)^2},$$

and obtain directly $|T(p_{\mathrm{T}})|$ as

$$|T(p_{\mathrm{T}})| = \left| 1 + \sum_{k=1}^{\infty} \frac{(-1)^k p_{\mathrm{T}}^{2k}}{2^{2k}(k!)^2} \cdot \left(\frac{M_k}{M_0} \right) \right|,$$

where

$$M_k = -[\alpha R_c + 2k + 1] \frac{R_c^{2k}}{\alpha^2} \exp(-\alpha R_c) + \frac{2k(2k+1)}{\alpha^2} M_{k-1},$$

with

$$M_0 = -(R_c/\alpha)\exp(-\alpha R_c) + \alpha^{-2}(1 - \exp(-\alpha R_c)).$$

A similar result can be derived for $\varepsilon(p_{\mathrm{T}})$ as well.

References

[1] L Van Hove, *Phys. Lett.* **B118**, 138 (1982); CERN Preprint No. TH-5069/88 (June)
[2] L McLerran, *Rev. Mod. Phys.* **58**, 1021 (1986)
[3] T Matsui and H Satz, *Phys. Lett.* **B178**, 416 (1986)
[4] C Baglin *et al*, *Phys. Lett.* **B262**, 362 (1991)
C Baglin *et al*, *Phys. Lett.* **B251**, 465 (1990)
[5] C Baglin *et al*, *Phys. Lett.* **B255**, 459 (1991)
[6] J P Blaizot and J Y Ollitrault, *Phys. Lett.* **B199** 499 (1987)

[7] F Karsch and R Petronzio, *Phys. Lett.* **B212**, 255 (1988); F Karsch and R Petronzio, *Z. Phys.* **C37**, 627 (1988)
[8] J Ftacnik, P Lichard, N Pisutova and J Pisut, *Z. Phys.* **C42**, 139 (1989)
[9] M Gazdzicki and S Mrowczynski, *Z. Phys.* **C49**, 569 (1991)
[10] F Karsch and H Satz, *Z. Phys.* **C51**, 209 (1991); P V Ruuskanen and H Satz, *Z. Phys.* **C37**, 623 (1988)
[11] S Gupta and H Satz, *Phys. Lett.* **B383**, 439 (1992)
[12] J D Bjorken, *Phys. Rev.* **D27**, 140 (1983)
[13] Here T is dimensionless. See § 3
[14] G Baym, B L Friman, J P Blaizot, M Soyeur and W Czyz, *Nucl. Phys.* **A407**, 541 (1983)
[15] S K Karn and R S Kaushal, *Proc. Nucl. Phys. Symp.* (Bombay) **B35**, 378 (1992)
[16] F Cooper, G Frye and E Schonberg, *Phys. Rev.* **D11**, 192 (1975)
[17] Note that the angular function ϕ, given by $\phi(\varphi) = \cos m\varphi/\sqrt{2\pi}$, is dropped all through out as it contributes only for $m = 0$ in the present normalization of $T(\mathbf{r}, t)$. Also, this will not affect the latter calculations as we shall be computing the ratio $\varepsilon/\varepsilon_{\max}$, only.
[18] It may be mentioned that the normalization of $T(\mathbf{r}, t)$ to unity in eq. (4) ensures the dimensionless character of $|T(p_L)|$ and $|T(p_T)|$ (cf. eqs. (6) and (7)) and subsequently that of S in eq. (1).
[19] See, for example, the data cited in R A Salmeron, "The suppression of the J/ψ in high energy nucleus–nucleus collisions: Experimental data and Models", Invited talk at 24th Recontres de Moriond, Les Arcs, France, 12–18 March, 1989; R A Salmeron, in "Quark-Gluon Plasma" edited by B Sinha *et al* (Springer Verlag, 1990) p. 44
[20] S Papillon, *Dependance en impulsion de la production du J/ψ dans les interactions* p–U, ^{16}O–U et ^{32}S–U a 200 GeV/c *par nucléon*. These, Universite de Paris-Sud, Orsay IPNO-T, 91-03, March 1991

PRAMANA
— journal of
physics

© Printed in India

Vol. 44, No. 2,
February 1995
pp. 177–182

Deep inelastic collisions of $^{32}S + ^{27}Al$ reaction at 130 MeV bombarding energy

R K CHOUDHURY, D M NADKARNI, V S AMBEKAR, B V DINESH,
A SAXENA, M S SAMANT*, D C BISWAS and L M PANT
Nuclear Physics Division, Bhabha Atomic Research Centre, Bombay 400 085, India
* Present address: Tata Institute of Fundamental Research, Bombay 400 005, India

MS received 10 October 1994

Abstract. The $^{32}S + ^{27}Al$ reaction was studied to investigate the deep inelastic collisions at a bombarding energy of 130 MeV which is well above the Coulomb barrier. The energy distributions of the binary decay products of $6 \leqslant Z \leqslant 10$ were determined using a large area position sensitive ionization chamber. The average kinetic energies of the reaction products indicate that the exit shapes correspond to highly stretched scission configurations in the deep-inelastic processes.

Keywords. $^{32}S + ^{27}Al$ reaction; deep inelastic scattering; kinetic energy of reaction products.

PACS No. 25·70

In recent years, there have been a number of experimental investigations to study the dynamical aspects of heavy ion collisions leading to fusion and deep inelastic processes. At energies around the Coulomb barrier, compound nucleus formation following fusion is the main reaction mechanism of heavy ion reactions. At higher energies, other processes such as incomplete fusion and deep inelastic reactions begin to become important. The compound nuclei, formed at large excitation energies ($E^* \approx 50$–100 MeV), deexcite predominantly by fission or by particle and gamma emission. The characteristics of various decay modes can be studied to derive information on the reaction mechanism and the structure of the compound nuclei produced in heavy ion collision processes [1–5]. There has been a lot of interest to study the binary fission like decay, particle and gamma decay of light compound nuclei. A number of measurements have been carried out for ^{59}Cu compound nucleus [6–8] produced in $^{32}S + ^{27}Al$ reactions. These studies have shown that at large angular momenta the compound nucleus may possess large spin induced deformation, connected with the dynamical effects in the shape relaxation during the formation of the compound nucleus. Since deep-inelastic collisions also correspond to events involving large damping of the kinetic energy and angular momentum, it would be of interest to study the features of this reaction for the above system. With this aim, we have measured, in the present work, the yields and the energy and angular distributions of various products emitted around the grazing angle in $^{32}S + ^{27}Al$ reaction at a bombarding energy of 130 MeV. The data were analysed to determine the average kinetic energies of the products. Assuming the products to arise from binary division of the composite system, it is found that the kinetic energies can be explained by invoking highly stretched configurations in the deep inelastic exit channels.

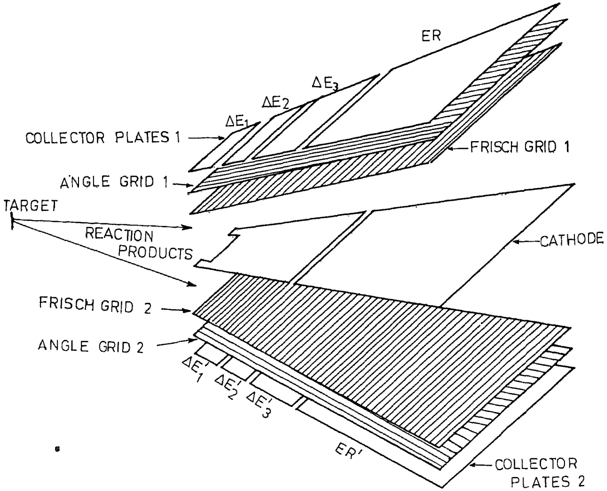

Figure 1. Schematic diagram of large area position sensitive ionization chamber (LIC).

The experiment was carried out using the ^{32}S beam from the 14UD BARC–TIFR Pelletron Accelerator at Bombay. A 300 μg/cm^2 self-supporting target of ^{27}Al was used and the reaction products were measured using a large area position sensitive ionization chamber (LIC) mounted at a mean angle of 54°, and having an angular coverage of $\pm 11°$. Figure 1 shows a schematic diagram of the ionization chamber. A surface barrier detector was mounted at 25° to monitor the elastically scattered particles. The LIC detector has an active gas length of 1·2 m, with four anode sections to measure the differential energy loss for identification and energy measurement of the products emitted in the reaction. The angle is measured from the Θ-grid pulses using the delay line readout technique. The details of the ionization chamber and its performance have been described elsewhere [9]. Only the top half of the ionization chamber was used in the present experiment to detect the reaction products emitted in the reaction. The chamber was filled with P-10 gas at a pressure of 70 mbar so as to stop all products of $Z > 6$ inside the active gas length. The gas was flowed continuously to maintain long term stability in the chamber operation. The signals from the anodes and Θ-grid were recorded for each event. The energy calibration of the anode sections was done by measuring in a separate experiment the elastically scattered events in ^{32}S + ^{197}Au reaction at different bombarding energies. The energy loss of the scattered ^{32}S ions in different anode sections was calculated from the energy loss tables and the pulse heights were normalized to these values for energy calibration. The accuracy in the measurement of energy was estimated to be about 1% by the present technique. The angle calibration was achieved from the dips in the position spectrum due to the shadows caused by the support structure in the window frame. Products of different charge could be identified from the correlation in the $\Delta E - E$ plots between the pulses of different anode sections of the ionization chamber. A typical plot between the pulse heights of 3rd and 4th anode sections is shown in figure 2, where it is seen that the lines for different product charges (circled numbers) are well separated. The energy distribution of different Z fragments is shown in figure 3. The energy spectra are seen to be broad and Gaussian like, suggestive of

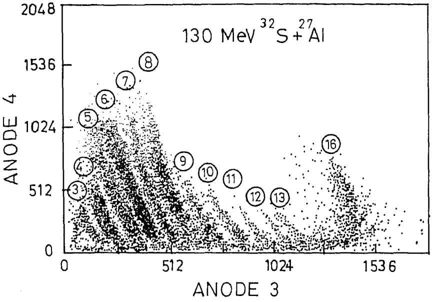

Figure 2. A typical particle identification spectrum with LIC.

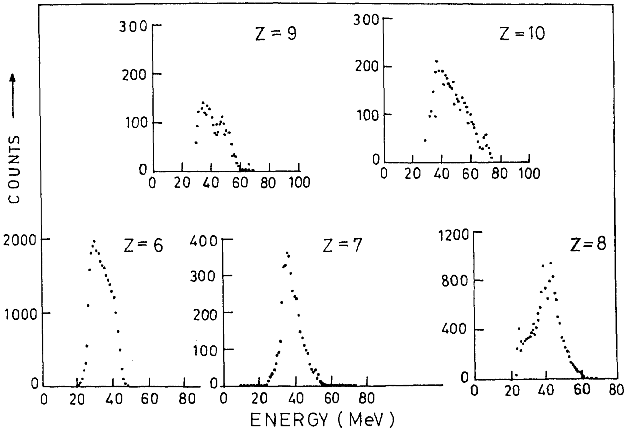

Figure 3. Energy distribution of fragments of $6 \leqslant Z \leqslant 10$.

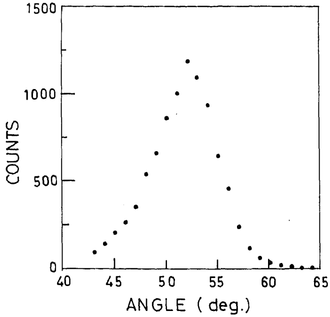

Figure 4. Typical angular distribution for $Z = 6$ products.

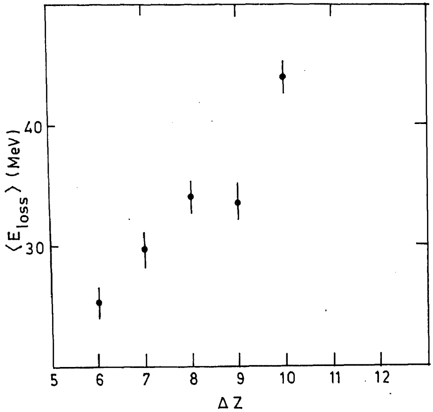

Figure 5. Variation of average energy loss with charge transfer from projectile nucleus.

a fully relaxed reaction mechanism such as deep inelastic or fission process giving rise to such events.

The angular distributions are seen to peak around 50 to 52°. The grazing angle for the reaction is given by

$$\Theta_g = 2\sin^{-1}(1/\varepsilon_g),$$

where $\varepsilon_g = r_g/a_0 - 1$, $a_0 = Z_P Z_T e^2/2E$, $r_g = r_B - \delta$.

In the above, Z_p, Z_T are the projectile, and target charges and E is the c.m. bombarding energy, r_B is the Coulomb barrier radius and $\delta \approx 0{\cdot}75$ fm. Θ_g was calculated to be about 49° for the $^{32}S + ^{27}Al$ reaction at 130 MeV. The angular distributions of the outgoing products are seen to be peaked at angles around the grazing angle, which establishes the peripheral nature of reaction contributing to the observed products. A typical angular distribution for $Z = 6$ products is shown in figure 4. Assuming two-body kinematics, the average kinetic energy loss $\langle E_{\text{loss}} \rangle$ could be derived from the measured energy spectra for different reaction channels. Figure 5 shows the variation of $\langle E_{\text{loss}} \rangle$ with the amount of the charge transfer (ΔZ) from the projectile nucleus. It is seen that with increasing charge or mass transfer during the collision, there is higher kinetic energy loss from the system.

Another way to examine the energetics of the reaction is to study the average kinetic energy with the product charge as shown in figure 6. This can be compared with the Coulomb energy of the dinuclear complex at the point of separation. The dashed line in figure 6 corresponds to the Coulomb energy of the product pair assuming them to be two touching spheres. It is seen that the observed kinetic energies are much lower than those calculated for the touching sphere configuration. The centre-to-centre distance, R_D for different charge pairs, are calculated by the liquid drop expression given by Myers and Swiatecki [10] lies in the range of 6·6 to 6·8 fm. The average kinetic energies are well reproduced using the values of R_D to be 9·4 fm, which would correspond to a deformed shape of the interacting nuclei at the time of separation. It is interesting to note that the grazing radial distance of the reaction is also at $r_B \approx 9{\cdot}4$ fm, which matches with the separation distance required to explain

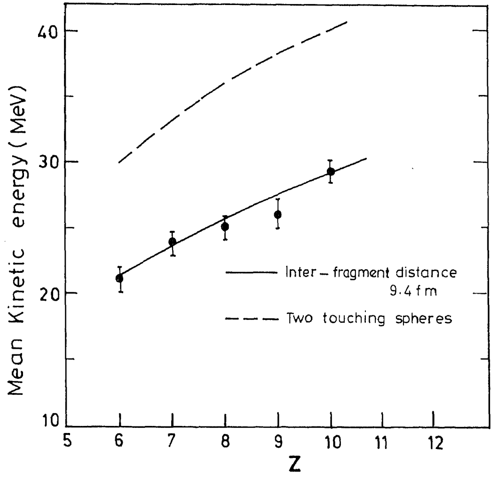

Figure 6. Variation of average kinetic energy with the charge of ejectile fragments.

the observed kinetic energies. One may therefore, conclude that in the $^{32}S + ^{27}Al$ reaction, at the grazing radial distance the kinetic energy is completely damped, and large mass/charge transfers take place leading to fully relaxed deep-inelastic processes. The grazing angular momentum for this system is calculated to be of the order of $40\hbar$. The exit shapes for the deep inelastic reactions correspond to highly stretched scission configurations of the dinuclear complex. The present results are complementary to the earlier observations of large spin induced deformations [6, 8] of the compound system formed in the $^{32}S + ^{27}Al$ reaction at similar bombarding energies.

References

[1] K Grotowski, Z Majka, R Planeta, M Szczodrak, Y Chan, G Guarino, L G Moretto, D J Morrissey, L G Sobotka, R G Stokstad, I Tserruya, S Wald and G J Wozniak, *Phys. Rev.* **C30**, 1214 (1984).

[2] C Beck, B Djerroud, B Heusch, R Dayras, R M Freeman, F Haas, A Hachem, J P Wieleczko and M Youlal, *Z. Phys.* **A334**, 521 (1989)

[3] R Planeta, P Belery, J Brzychczyk, P Cohilis, Y El Masri, Gh Gregoire, K Grotowski, Z Majka, S Micek, M Szczodrak, A Wieloch and J Albinski, *Phys. Rev.* **C34**, 512 (1986)

[4] S J Sanders, D J Kovar, B B Back, C Beck, B K Dichter, D Henderson, R V F Janssens, J G Keller, S Kauffman, T F Wang, B Wilkins and F Videback, *Phys. Rev. Lett.* **59**, 2856 (1987)

[5] D Shapira, *Phys. Rev. Lett.* **61**, 2153 (1988)

[6] R K Choudhury, P L Gonthier, K Hagel, M N Namboodiri, J B Natowitz, L Adler, S Simon, S Kniffen and G Berkowitz, *Phys. Lett.* **B143**, 74 (1984)

[7] B Fornal, G Viesti, G Nebbia, G Prete J B Natowitz, *Phys. Rev.* **C40**, 664 (1989)

[8] B Fornal, F Gramegna, G Prete, R Burch, G D'Erasmo, E M Fiore, L Fiore, A Pantaleo, V Paticchio, G Viesti, P Blasi, N Gelli, F Lucarelli, M Anghinolfi, P Corvisiero, M Taiuti, A Zucchiatti, P F Bortignon, J Ruiz, G Nebbia, M Gonin and J B Natowitz, *Phys. Lett.* **B255**, 325 (1991)

[9] S R S Murthy, *DAE Symposium on nuclear physics* **A30**, 348 (1987)

[10] W D Myers and W J Swiatecki, *Ann. Phys.* **84**, 160 (1974)

PRAMANA
— journal of
physics

© Printed in India

Vol. 44, No. 2,
February 1995
pp. 183–200

Trinucleon system with Reid soft core potential by hyperspherical harmonics expansion method

SATADAL BHATTACHARYYA and TAPAN KUMAR DAS*
Department of Physics, Burdwan University, Burdwan 713 104, India
* Department of Physics, Calcutta University, 92 APC Road, Calcutta 700 009, India

MS received 6 June 1994; revised 15 October 1994

Abstract. The hyperspherical harmonics expansion method has been used to solve the trinucleon system where the nucleons interact through Reid soft core potential. The binding energy of triton, both for extreme adiabatic approximation and uncoupled adiabatic approximation, and the *S*-state, *S'*-state and *D*-state probabilities are calculated and compared with the results by the Faddeev method.

Keywords. Nuclear structure; few body system; hyperspherical harmonics expansion method; Reid soft core potential.

PACS Nos 21·40; 21·10

1. Introduction

Since the development of the hyperspherical harmonics expansion (HHE) method [1–5] in the early seventies, it has been applied profitably for the determination of the bound state properties of a few nucleon systems [1–6] as well as light atomic and molecular systems [8]. In this method, the wave-function is expanded in an infinite series of generalized partial waves and the Schrödinger equation gives rise to an infinite set of coupled differential equations (CDE). Although the size of the expansion basis can be reduced by the introduction of the optimal subset [5], the sum over the hyperangular momentum quantum number (K) must be truncated in order to get a finite set of CDE, to be numerically tractable. Convergence of the expansion is slow, unless the potential is very soft. The usual criterion for the truncation of the expansion basis with respect to K is the attainment of convergence in binding energy (BE) up to a predetermined limit. This however does not guarantee an attainment of convergence in the asymptotic part of the wave-function and thus the wave-function (particularly the asymptotic part of it) is less reliable than the BE.

The HHE method is also not easily adoptable when the interaction potential is dependent on the state of the interacting particles, as in realistic nucleon nucleon (NN) potentials. This is the reason why the HHE method has so far been applied to nuclear problems with simple *S*-projected, relatively soft potentials only. Moreover such potentials are usually chosen to be a sum of Gaussians or exponentials, which although are convenient for a fast convergence, but still do not have the necessary one pion exchange tail. Hence the asymptotic part of the wave-function as determined by the asymptotic normalization constants, is not reliable [7] and cannot be compared with calculations by other methods or with experimental numbers. Nevertheless the

HHE method is interesting since it deals directly with the wave-functions and hence provides a clear physical picture.

The other and perhaps the most frequently used essentially exact technique to solve the three body problem is the Faddeev equation method [9]. In this approach, for a given partition of the three body system, the angular momentum quantum numbers of the interacting pair and those of the spectator particle specify the characteristics of each channel, for which Faddeev equations are written separately. This approach is particularly suited to realistic NN potentials. On the other hand inclusion of a long range interaction like the Coulomb potential, involving a large number of partial waves, is inconvenient in traditional momentum space Faddeev calculations. However, this problem does not arise in coordinate space Faddeev calculation, for which sophisticated numerical techniques have been developed [12]. One of the most commonly employed realistic NN potentials is the Reid soft core [10] (RSC) potential, which depends on the spin (s), isospin (t) and total angular momentum (j) of the interacting pair and thus the Faddeev equation method is suitable to deal with such an interaction. On the other hand, the calculation of matrix elements of this potential necessary for the HHE method becomes extremely complicated. For this reason, while there is an abundance of Faddeev calculation with the RSC potential [11–13], no attempt has so far been made to find the complete solution of the trinucleon system by the HHE method with this potential, although several works have been reported with simple potentials [1–6].

As has already been mentioned, the reliability of the asymptotic wave-function obtained by the HHE method has not been established. On the other hand, the asymptotic wave-function strongly depends on the correctness of the asymptotic part of the NN interaction chosen. To throw light on the convergence and correct behaviour of the asymptotic wave-function obtained by HHE method, it is necessary to solve the trinucleon system by this method with a realistic potential, having appropriate asymptotic behaviour. We have chosen the RSC potential for this purpose, for which Faddeev results are available for comparison. As a first step towards this goal, we have calculated in the present work the binding energy of triton using RSC potential by the HHE method. Mukhtarova [14] performed accurate HHE calculations with some of the realistic NN potentials like GPT [15], SSC [16], TRS [17] potentials etc, but RSC was not used by her. To the best of our knowledge, this is the first calculation of the trinucleon system by the HHE method using RSC potential. Adiabatic approximation has been used to approximately decouple the resulting equations. Convergence behaviour of the binding energy in the extreme and uncoupled adiabatic approximation (EAA and UAA respectively) have been studied. For the best computer facility available, we have been able to retain up to a maximum K value of 15 for each symmetry component, which gives the EAA and UAA binding energy to within about 1·3%. Following a theorem on the convergence of hyperspherical harmonics expansion by Schneider [18], a semiempirical extrapolation formula has been obtained for the missing binding energy. These results together with the probabilities of S, S' and D states have been compared with the earlier calculation by Faddeev method.

This paper is organized as follows. Section 2 contains a brief review of the HHE theory and its adoption to the RSC potential. In § 3, we present the results obtained and discuss the convergence behaviour. Conclusions have been drawn in § 4. Appendix A is provided for the coupling matrix elements. For clarity of our discussion the various components of the RSC potential are presented in Appendix B.

2. The theory

This section is divided into two subsections: in the first the coupled differential equations (CDE) are set up for realistic potentials and in the second the coupling matrices for the RSC potential are developed.

A. Coupled differential equations

The relative motion of trinucleon system is described in terms of the Jacobi coordinates

$$\mathbf{x} = \mathbf{r}_2 - \mathbf{r}_1$$
$$\mathbf{y} = 2/\sqrt{3}\,[\mathbf{r}_3 - (\mathbf{r}_1 + \mathbf{r}_2)/2], \tag{1}$$

where $\mathbf{r}_i$ is the position of the ith nucleon. The hyperradius r, defined through

$$r^2 = x^2 + y^2, \tag{2}$$

is invariant under exchange of any pair of nucleons and three dimensional rotations. The hyperangular set $\{\Omega\}$ describing the five other space degrees of freedom is constituted by four spherical polar angles $\hat{x}(\theta_x, \phi_x)$ and $\hat{y}(\theta_y, \phi_y)$ giving the orientations of $\mathbf{x}$ and $\mathbf{y}$ and one hyperspherical angle ϕ defined in terms of relative lengths of x and y by

$$\tan\phi = y/x, \quad 0 \leqslant \phi \leqslant \pi/2. \tag{3}$$

The wave-function is expanded in a complete orthonormal set of hyperspherical harmonics [5] as

$$\psi_{JM^J}^{TM_T}(r,\Omega) = \sum_{K,\varepsilon,T,S} n(\varepsilon) r^{-5/2} U_{2K+L}^{\varepsilon,T,S}(r)[{}^{\varepsilon}B_{2K+L}(\Omega) \otimes \Gamma_{TS}(\varepsilon^*)]_J^{M_J} \tag{4}$$

where T, S and L correspond to total isospin, spin and orbital angular momentum respectively and $\mathbf{J} = \mathbf{L} + \mathbf{S}$ is the total angular momentum; ε specifies the symmetry of the spatial part of the wave-function under exchange of particles, which can be the totally-symmetric S, mixed symmetry S'^{+}, S'^{-} and D^{+}, D^{-} states; the + or − signs correspond to symmetry or antisymmetry under the exchange of (12) pair of particles. The spectroscopic notations S and D correspond to $L = 0$ and $L = 2$ respectively, L being the total angular momentum. The factor $n(\varepsilon)$ is defined as

$$\begin{aligned} n(\varepsilon) &= 1 \text{ for } S \text{ state} \\ &= 1/\sqrt{2} \text{ for } S'^{+}, D^{+} \text{ and } D^{-} \text{ states} \\ &= -1/\sqrt{2} \text{ for } S'^{-} \text{ state.} \end{aligned}$$

$\Gamma_{TS}(\varepsilon^*)$ is the isospin-spin state of three nucleon system with total isospin T and total spin S and having a symmetry conjugate to ε, such that $[{}^{\varepsilon}B_{2K+L}(\Omega) \otimes \Gamma_{TS}(\varepsilon^*)]_J^{M_J}$ is totally antisymmetric. It is given by

$$\Gamma_{TS}(\varepsilon^*) = \sum_{s,t} b_s^t(\varepsilon^*)|(s\,1/2)SM_S\rangle|(t\,1/2)\,TM_T\rangle, \tag{5}$$

where s and t represent spin and isospin of the interacting pair and $b_s^t(\varepsilon^*)$ are coefficients determined by the symmetry requirement. An element of the appropriate optimal subset of hyperspherical harmonics is ${}^{\varepsilon}B_{2K+L}(r)$ (its explicit form is given in ref. [5]) and $[{}^{\varepsilon}B_{2K+L}\otimes\Gamma_{TS}(\varepsilon^*)]_J^{M_J}$ represents coupling of $\mathbf{L}$ and $\mathbf{S}$ to a total angular momentum J with z-component M_J (for the trinucleon $J=1/2$). The RSC potential depends on the angular momentum (j_1), spin(s) and isospin (t) of the interacting pair and the j_1 value $(\mathbf{j}_1=\mathbf{l}_1+\mathbf{s})$ is restricted to $j_1\leqslant 2$ (Appendix B). Thus it is convenient to express the spin-isospin hyperangular part of the wave-function, in $(j-j)$ coupling scheme:

$$\begin{aligned}
&[{}^{\varepsilon}B_{2K+L}\otimes\Gamma_{TS}(\varepsilon^*)]_J^{M_J}\\
&\quad={}^{\varepsilon}N_{2K+L}\sum_{\substack{s,t\\ [l_1],[l_2]}} b_s^t(\varepsilon^*)|(t\,1/2)\,TM_T\rangle[(2l_1+1)(2l_2+1)/(2L+1)]^{1/2}\\
&\qquad\langle l_1 l_2 0 0|\,L0\rangle\,{}^{\varepsilon}F^{l_2,l_1}_{2K+L}(\varphi)\\
&\quad{}^{(2)}P^{l_2,l_1}_{2K+L}(\phi)\sum_{[j_1][j_2]}\begin{bmatrix} l_1 & l_2 & L\\ s & 1/2 & S\\ j_1 & j_2 & J\end{bmatrix}|(l_1 s)j_1,(l_2\,1/2)j_2;JM_J\rangle
\end{aligned}\tag{6}$$

where $[j_1]$, $[l_1]$, etc represent restricted values as required from RSC potential. The normalization constant ${}^{\varepsilon}N_{2K+L}$ is given by

$${}^{\varepsilon}N_{2K}^{-2}=\sum_{[l_1]}(2l_1+1)|{}^{\varepsilon}F^{l_1,l_1}_{2K+L}(\varphi)|^2\times 0{\cdot}5\times\left[1+\sum_{[j_1][j_2]}\begin{bmatrix} l_1 & l_2 & 0\\ 1 & 1/2 & 1/2\\ j_1 & j_2 & 1/2\end{bmatrix}^2\right],\tag{7}$$

for the S and S' states and

$$\begin{aligned}
{}^{\varepsilon}N_{2K+2}^{-2}&=\sum_{[l_1][l_2]}(2l_1+1)(2l_2+1)\begin{pmatrix}2 & l_1 & l_2\\ 0 & 0 & 0\end{pmatrix}^2|{}^{\varepsilon}F^{l_2,l_1}_{2K+L}(\varphi)|^2\\
&\quad\times\sum_{[j_1][j_2]}\begin{bmatrix} l_1 & l_2 & 2\\ 1 & 1/2 & 3/2\\ j_1 & j_2 & 1/2\end{bmatrix}^2
\end{aligned}\tag{8}$$

for the D state. The quantity ${}^{\varepsilon}F^{l_2,l_1}_{2K+L}(\varphi)$ is given by

$${}^{\varepsilon}F^{l_2,l_1}_{2K+L}(\varphi)=\sum_{\varepsilon}{}^{(2)}P^{l_2,l_1}_{2K+L}(\phi)\tag{9}$$

where ${}^{(2)}P^{l_2,l_1}_{2K+L}(\phi)$ is a hyperspherical function and Σ_ε acts on a function $f(\varphi)$ as:

$$\sum_{0}f(\varphi)=1/3[f(0)+f(2\pi/3)+f(-2\pi/3)],\tag{10a}$$

$$\sum_{+}f(\varphi)=1/3[2f(0)-f(2\pi/3)-f(-2\pi/3)],\tag{10b}$$

$$\sum_{-}f(\varphi)=1/\sqrt{3}[f(-2\pi/3)-f(2\pi/3)].\tag{10c}$$

Substitution of (4) in the Schrödinger equation and projection on a particular hyperspherical harmonics leads to a system of coupled differential equations

$$\left[-\frac{h^2}{m}\left[\frac{\mathrm{d}^2}{\mathrm{d}r^2}-\frac{(2K+L+2)^2-1/4}{r^2}\right]-E\right]u^{\varepsilon TS}_{2K+L}(r)$$

$$+\sum_{K'\varepsilon'T'S'L'} C^{K\varepsilon TSL}_{K'\varepsilon'T'S'L'}(r)\,u^{\varepsilon'T'S'}_{2K'+L'}(r)=0, \tag{11}$$

where m is the nucleon mass, K represents the hyperangular momentum quantum number and $C^{K\varepsilon TSL}_{K'\varepsilon'T'S'L'}(r)$ is the coupling matrix elements explained in the next subsection.

B. *Coupling of the interaction*

The coupling matrix in (10) is given by

$$C^{K\varepsilon TSL}_{K'\varepsilon'T'S'L'}(r)=\pounds[{}^{\varepsilon}B_{2K+L}\otimes\Gamma_{TS}(\varepsilon^*)]^{MJ}_{J}\left|\sum_{i>j}V(r_{ij})\right|[{}^{\varepsilon'}B_{2K'+L}\otimes\Gamma_{T'S'}(\varepsilon'^*)]^{MJ\circ}_{J} \tag{12}$$

where $V(r_{ij})$ is the interaction potential of the (ij) pair. Detailed expressions for the coupling matrices for all possible combinations of RSC potential are already calculated [19]. The coupling between two states through central, **L·S** or tensor part can be obtained by using

$$\begin{aligned}\langle(l_1 s)j_1,(l_2\,1/2)j_2;JM_J|\,&V_c+V_{LS}\mathbf{L}\cdot\mathbf{S}+V_TS_{12}|(l'_1 s')j'_1,(l'_2\,1/2)j'_2;JM_J\rangle\\ &=\delta_{l_2l'_2}\delta_{j_2j'_2}[\delta_{l_1l'_1}\delta_{j_1j'_1}\delta_{ss'}\{V_C(r_{ij})+1/2\{j_1(j_1+1)-l_1(l_1+1)-s(s+1)\}^{1/2}\\ &\times V_{LS}(r_{ij})\}+\delta_{ss'}\delta_{j_1,j'_1}\langle(l_1 s)j_1|S_{12}|(l'_1 s)j_1\rangle V_T(r_{ij})]\end{aligned} \tag{13}$$

where $V_C(r_{ij})$, $V_{LS}(r_{ij})$ and $V_T(r_{ij})$ represent the radial dependences of central, **L·S** and tensor components of RSC potential (Appendix B). The matrix elements of the tensor operator S_{12} can be found in standard texts [20].

The possible component of RSC giving rise to coupling between (SS), $(S'S)$, $(S'S')$, (DS), (DS') and (DD) are given in table 1. Complete expressions for matrix elements of these blocks are given in Appendix A.

A typical term in the matrix element (12) contains (see Appendix A) an integral of the interaction potential and two ${}^{(2)}P^{l_2,l_1}_{L}$ functions [5], $\langle{}^{(2)}P^{l_2,l_1}_{2K+L}|\,V(r\cos\phi)|{}^{(2)}P^{l_2,l'_2}_{2K'+L}\rangle$, (note that $r_{12}=x=r\cos\phi$). Expressing the ${}^{(2)}P^{l_2,l_1}_{L}$ function in terms of Jacobi polynomials, this can be seen to be proportional to

$$I_{nn'}(r)=\int_{-1}^{1}P^{(\alpha,\beta)}_{n}(x)\,V(r_{12})P^{(\alpha',\beta')}_{n'}(x)(1-x)^{\gamma}(1+x)^{\delta}\mathrm{d}x \tag{14}$$

where $P^{(\alpha,\beta)}_{n}$ is a Jacobi polynomial and $\alpha=l_1+1/2$, $\beta=l_2+1/2$, $\gamma=(\alpha+\alpha')/2$, $\delta=(\beta+\beta')/2$; n,n' are determined from $2K+L=2n+l_1+l_2$ and $r_{12}=r((1+x)/2)^{1/2}$.

Since each of the element of the potential matrix contains contributions from several terms of the RSC potential (table 1 and Appendix A), a larger number of integrals of the type (14) are to be evaluated for each hyperradial mesh point. This would require an enormous computer time. The situation becomes more critical due

Table 1. Classification of different couplings.

Couplings	Components of RSC potential involved
SS	$V_C(^1S_0)$, $V_{C,LS}(^3S_1 - {}^3D_1)$, $V_C(^3D_2)$, $V_C(^1D_2)$
$S'S$	$V_C(^1S_0)$, $V_{C,LS}(^3S_1 - {}^3D_1)$, $V_C(^3D_2)$, $V_C(^1D_2)$
$S'S'$	$V_C(^1S_0)$, $V_{C,LS}(^3S_1 - {}^3D_1)$, $V_C(^3D_2)$, $V_C(^1D_2)$, $V_C(^1P_1)$, $V_C(^3P_0)$, $V_C(^3P_1)$, $V_{C,LS}(^3P_2 - {}^3F_2)$
DS	$V_T(^3S_1 - {}^3D_1)$
DS'	$V_T(^3S_1 - {}^3D_1)$, $V_T(^3P_2 - {}^3F_2)$
DD	$V_{C,LS,T}(^3S_1 - {}^3D_1)$, $V_C(^3D_2)$, $V_C(^3P_0)$, $V_C(^3P_1)$, $V_{C,LS,T}(^3P_2 - {}^3F_2)$

V_C, V_{LS} and V_T correspond to the central, LS and tensor component of the RSC potential.

to a large number of zeros of the integrand in the interval $[-1, 1]$ for large K, K' and so the numerical evaluation of the integral becomes tricky, requiring too large computer time for a specified precision. Instead, we evaluate the integral in (14) by expanding $V\{r[(1+x)/2]^{1/2}\}$ (whose typical form is as in (15)) in the complete set $\{P_{n''}^{(1/2,\,1/2)}(x)\}$

$$V(r(1+x)/2)^{1/2} = V_0 \frac{\exp\{-\mu r[(1+x)/2]^{1/2}\}}{(1+x)^{\rho/2}} = \sum_{n''=0}^{\infty} a_{n''}(r) P_{n''}^{(1,2,\,1/2)}(x) \tag{15}$$

where the potential multipoles $a_{n''}$ is given by

$$a_{n''}(r) = (1/h_{n''}^{1/2,\,1/2}) \int_{-1}^{1} V(r((1+x)/2)^{1/2}) P_{n''}^{(1/2,\,1/2)}(x)(1-x^2)^{1/2}\,\mathrm{d}x, \tag{16}$$

$h_{n''}^{1/2,\,1/2}$ being the norm of Jacobi polynomial $P_{n''}^{(1/2,\,1/2)}$. Substitution of (15) in (14) gives

$$I_{nn'}(r) = \sum_{n''=0}^{\infty} a_{n''}(r) \langle n | n'' | n' \rangle \tag{17}$$

where the geometrical structure coefficients (GSC)

$$\langle n | n'' | n' \rangle = \int_{-1}^{1} P_n^{(\alpha,\beta)}(x) P_{n''}^{(1/2,\,1/2)}(x) P_{n'}^{(\alpha',\beta')}(x)(1-x)^{\gamma}(1+x)^{\delta}\,\mathrm{d}x \tag{18}$$

is independent of the interaction potential as well as the hyperradius r. However eq. (17) is not advantageous unless the sum over n'' can be restricted. Since $P_n^{(\alpha,\beta)}$ is a polynomial of degree n in x, one can see from (18), by isolating one Jacobi polynomial together with its appropriate weight function and expressing the remaining part of the integrand as a polynomial and using the orthogonality property of Jacobi polynomials that $\langle n|n''|n'\rangle = 0$ unless n'' satisfies $n_{\min} \leqslant n'' \leqslant n_{\max}$. Then (17) can be rewritten as

$$I_{nn'}(r) = \sum_{n''=n_{\min}}^{n_{\max}} a_{n''}(r)\langle n|n''|n'\rangle. \tag{19}$$

The GSC can itself be evaluated [21] by using the completeness property of Jacobi polynomials and solving a set of linear inhomogeneous equations (LIE). Note that the GSC need to be calculated once only and stored, to be used for each mesh point, resulting in an efficient and fast numerical procedure.

The above procedure will always work, except for the case when after isolating one Jacobi polynomial together with its weight function in the integrand of (18), the remaining part is not a polynomial. Such a situation can occur only for the tensor part of $({}^3S_1 - {}^3D_1)$ and $({}^3P_2 - {}^3F_2)$ interaction components. In this case one can include a factor of $(1-x)^{-1/2}$ with the potential function $V(r((1+x)/2)^{1/2})$, so as to make (19) valid once again. Although this extra factor introduces a singularity in $a_{n''}(r)$ (see (15) and (16)), it has been shown by us [22], that the principal value of this modified potential multipole exists for the cases under consideration and a numerical calculation produces sufficiently accurate results.

3. Results and discussion

The ground state of the trinucleon has dominant contributions from the totally symmetric $L=0$ state (S), mixed symmetry $L=0$ (S') and mixed symmetry $L=2$ (D) states only. The only other possibility, a P-state, has negligible probability and has been disregarded. With a maximum $K(=K_{\max})$ values of 15 for each of S, S', and D states, one has to solve a system of 46 coupled differential equations (CDE). Numerical algorithm for solving such a large number of CDE (for example, by renormalized Numerov method [23]) is very slow and not sufficiently stable. For this reason we have adopted the adiabatic approximation scheme [24] to solve the system of CDE. Due to the strong short range repulsion of the RSC potential, the convergence in binding energy (BE) with respect to inclusion of higher partial waves, is not expected to be sufficiently fast.

We have taken 300 uniform mesh points (of interval size 0·05 fm) for the hyperradial variable (r). For each mesh point the coupling potential matrix is calculated. As explained in the previous section, an appropriate multipolar expansion of each component of the RSC potential is made and the corresponding geometrical structure coefficients (GSC) are calculated by the LIE method [21] and stored (outside the r-loop). Then for each r-mesh point, all the potential multipoles are calculated and using the stored GSC, the potential matrix is computed. The diagonal hypercentrifugal part is added to this and then the matrix is diagonalized to obtain the lowest eigen potential ($w_0(r)$). All calculations have been done in double precision on an EISA 486 personal computer. In table 2a we demonstrate the convergence behaviour of $w_0(r)$ for a few selected values of r and for various values of K. It can be seen from this table, that the convergence of $w_0(r)$ is fairly rapid for small values of r, while it is quite slow for large values of r. Since a major part of BE comes from near the minimum of $w_0(r)$, convergence in BE is faster than the asymptotic wave-function. This is clearly seen in table 2b where calculated BE for various r_∞ (upper cut off in r) and for a few selected

Table 2a. Convergence of minimum eigenvalue ($-w_0(r)$) for various values of r.

	r (in fermi)						
K	1·8	2·15	2·55	3·05	4·05	7·55	10·05
8	23·344	35·639	30·550	22·494	12·695	0·479	—
9	23·459	35·880	30·865	22·739	13·091	1·201	− 0·444
10	23·505	36·028	31·118	22·957	13·138	1·913	− 0·189
11	23·525	36·087	31·258	23·189	13·247	2·739	0·162
12	23·535	36·109	31·335	23·331	13·384	3·456	0·560
13	23·536	36·116	31·368	23·425	13·497	4·018	1·000
14	23·538	36·119	31·383	23·479	13·624	4·532	1·544
15	23·539	36·122	31·390	23·505	13·718	4·617	2·095

Table 2b. BE in MeV in extreme adiabatic approximation for a few K with various r_∞.

	r (in fm)			
K	9·0	11·0	12·0	13·0
7	5·5478	5·5409	5·5401	5·5401
11	7·4581	7·4616	7·4612	7·4610
13	7·7812	7·7959	7·7963	7·7961
15	8·0113	8·0174	8·0178	8·0180

K values have been presented. A choice of 15 fm for r_∞ appears to be sufficient for reliability up to third decimal place. Figure 1 shows the behaviour of $w_0(r)$ as a function of r for $K_{\max} = 15$. Using this $w_0(r)$ and the corresponding eigenvectors, approximately decoupled differential equations are obtained by the extreme and uncoupled adiabatic approximations [24] (EAA and UAA respectively). The decoupled equations have been solved by the Runge–Kutta method. Calculated BE by EAA ($-E_{\mathrm{EAA}}$) and UAA ($-E_{\mathrm{UAA}}$) together with incremental changes, have been presented in table 3. Convergence to 1·3% in both E_{EAA} and E_{UAA} have been achieved with $K_{\max} = 15$ for each of S, S' and D states.

Calculated probabilities of S, S' and D states (P_S, $P_{S'}$ and P_D respectively) for various K values are shown in table 4. From this it is seen that P_D increases gradually (mostly at the cost of P_S) as K increases, indicating that the tensor coupling terms, having strong r dependence in short separation region, contribute significantly to higher partial waves, thereby enriching the D state. In figures 2 and 3 calculated hyperradial partial waves are plotted for various K values for S and D states. Since the computer time and memory requirements increase rapidy with increase of $K_{\max}$ values, we restricted our calculations to $K_{\max} \leqslant 15$. However using the convergence theorems proved by Schneider [18], it is possible to estimate the converged energy by calculating the missing energy from a knowledge of the observed convergence trend for various K values. It was shown by Schneider that when the two-body potential is a sum of Yukawa terms, the convergence must be at least as fast as λ^{-4},

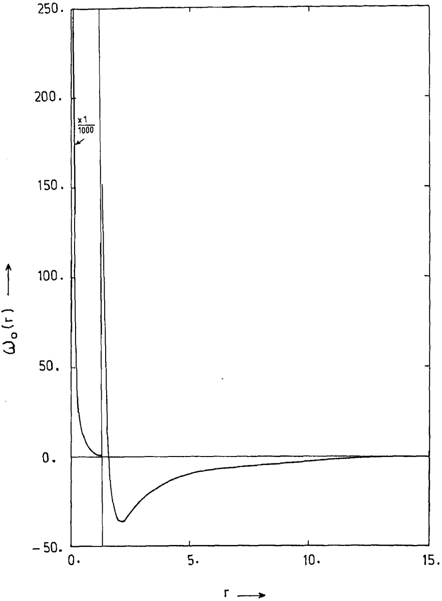

Figure 1. Lowest eigen potential, $\omega_0(r)$ as a function of r for $K_{\max} = 15$.

where $\lambda = (K(K+4))^{1/2}$. Following Ballot *et al* [25] we define $\Delta E_K = |E(K+3) - E(K)|$ and assume

$$\Delta E_K = C(K+x)^{-4}, \tag{20}$$

where C and x are constants to be determined empirically. In table 5a, ΔE_K has been presented for $K = 3n$ (n is integer), which shows that the value of C in (20) is approximately constant. We least square fitted all calculated ΔE_K to the relation (20) to obtain C (24·272 and 24·266 for EAA and UAA respectively) and x (4·241 and 4·461 for EAA and UAA respectively). Using this, the estimated values of E_{EAA} and E_{UAA} for $K > 15$ are presented in table 5b, which shows the convergence is well established. Finally using (20) for $K \geqslant K_M$, where K_M is sufficiently large, we can estimate the converged energy as

$$E_\infty = E(K_M) + \sum_{n=0}^{\infty} \Delta E(K_M + 3n). \tag{21}$$

Table 3. BE of triton in MeV with extreme adiabatic approximation ($-E_{\mathrm{EAA}}$) and uncoupled adiabatic approximation ($-E_{\mathrm{UAA}}$).

K	$-E_{\mathrm{EAA}}$	$-\Delta E_{\mathrm{EAA}}$	$-E_{\mathrm{UAA}}$	$-\Delta E_{\mathrm{UAA}}$
5	2·928		2·204	
		1·742		1·582
6	4·670		3·786	
		0·870		0·781
7	5·540		4·567	
		0·830		0·771
8	6·370		5·338	
		0·515		0·476
9	6·885		5·814	
		0·292		0·276
10	7·177		6·090	
		0·283		0·269
11	7·460		6·359	
		0·207		0·192
12	7·667		6·551	
		0·129		0·123
13	7·796		6·674	
		0·124		0·119
14	7·920		6·793	
		0·098		0·089
15	8·018		6·882	

Table 4. Values of P_S, $P_{S'}$ and P_D.

K	$P_S\%$	$P_{S'}\%$	$P_D\%$
5	91·44	0·73	7·83
6	90·32	1·01	8·67
7	89·80	1·13	9·07
8	89·20	1·16	9·64
9	88·70	1·21	10·09
10	88·30	1·26	10·44
11	88·00	1·24	10·76
12	87·69	1·25	11·06
13	87·65	1·21	11·14
14	87·69	1·18	11·13
15	87·67	1·16	11·17

For sufficiently large K_M, one can replace the sum by an integral to get

$$\begin{aligned} E_\infty &= E(K_M) + C\int_0^\infty \frac{\mathrm{d}n}{(K_M + x + 3n)^4}, \\ &= E(K_M) + C\frac{1}{9(K_M + x)^3}. \end{aligned} \tag{22}$$

Using (20) to evaluate $E(K_M)$ for $K_M = 45$ and then using (22) we obtain the convergent energies $-E_{\mathrm{EAA}} = 8{\cdot}492$ MeV and $-E_{\mathrm{UAA}} = 7{\cdot}339$ MeV. There are the upper and

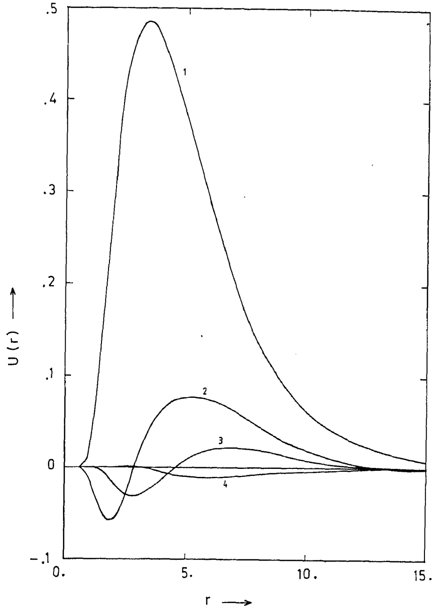

Figure 2. *S* state partial waves $U(r)$ for $K = 0$, 2, 4 and 10 (curve marked 1, 2, 3 and 4 respectively).

lower bounds of the exact binding energy [26], the latter being close to the UAA value. In table 6, we quote the results of careful Faddeev calculations [13] up to 34 channels. The UAA binding energy attained in the present calculation compares favourably with the 34 channel Faddeev result. From table 6, it is seen that P_D increases with increase in the number of channels, a trend similar to the HHE calculation with increasing partial waves, although the HHE value is larger than the Faddeev result.

4. Conclusion

In the first calculation of triton ground state with RSC potential by HHE method, the results obtained for the binding energy and the *S*, *S′* and *D* state probabilities compare favourably with those calculated by 34 channel Faddeev calculation. The *D* state probability calculated by HHE method is somewhat larger than that calculated by Faddeev method. The exact BE, which is larger than the UAA value, is also likely to

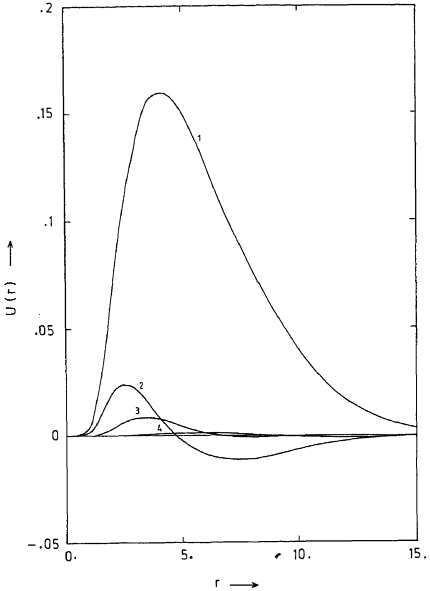

Figure 3. D state partial waves $U(r)$ for $K = 0$, 2, 4 and 10 (curve marked 1, 2, 3 and 4 respectively).

Table 5a. Value of C (in eq. (20)) from the least square fit.

	EAA			UAA		
K	$-E(K)$	$-\Delta E_K$	$C \times 10^{-3}$	$-E(K)$	$-\Delta E_K$	$C \times 10^{-3}$
6	4·67		24·362	3·786		24·291
		2·215			2·028	
9	6·885		24·036	5·814		24·201
		0·782			0·737	
12	7·667		24·419	6·551		24·305
		0·351			0·331	
15	8·018		24·272	6·882		24·266

be larger than 7·346 MeV obtained by 34 channel Faddeev calculation. These are probably related, since a higher D state probability produces larger S–D coupling and enhances the binding energy. However a conclusive remark can be made only after exact HHE calculation (without resorting to adiabatic approximations) is performed.

Table 5b. Extrapolated energy in MeV using relations (20) and (21).

K	EAA $-E(K)$	$-\Delta E_K$	UAA $-E(K)$	$-\Delta E_K$
18	8·195		7·051	
		0·099		0·095
21	8·294		7·146	
		0·060		0·058
24	8·354		7·204	
		0·038		0·037
27	8·392		7·241	
		0·026		0·025
30	8·418		7·266	
		0·017		0·017
33	8·435		7·283	
		0·013		0·012
36	8·448		7·295	
		0·009		0·009
39	8·457		7·304	
		0·007		0·007
42	8·464		7·311	
		0·005		0·005
45	8·469		7·316	

Table 6. Results of trinucleon Faddeev calculation for RSC potential.

Channel	BE	P_S	$P_{S'}$	P_D
3	6·384	90·08	1·91	8·01
5	7·023	88·91	1·67	9·34
9	7·210	88·88	1·60	9·43
18	7·231	89·04	1·46	9·42
26	7·342	89·01	1·41	9·50
34	7·346	89·02	1·40	9·50

Thus the present work fills in the gap left so far and provides the much needed check of the HHE method for a complete reliable calculation of the trinucleon system. Although the actual numerical calculations become prohibitively large for the inclusion of a large number of partial waves, the convergence theorems for hyperspherical harmonics expansion appear to be well obeyed and hence convergent binding energy can be extracted from the results with a finite number of partial waves. Although the number of channels in the Faddeev method is not directly related to the number of partial waves in the HHE method, the general convergence trends appear to be similar. The HHE provides more direct, physical insight since physical wave functions are obtained simultaneously.

Acknowledgements

The work has been financed by the University Grants Commission, India through a Departmental Special Assistance grant to the Physics Department of the University of Calcutta. One of us (SB) acknowledges receipt of a senior research fellowship from the University of Burdwan, India.

Appendix A

1. *Coupling matrix for (SS) block*

$$\begin{aligned}\langle S,K|\,V(r_{12})|S,K'\rangle &= {}^{(0)}N_{2K}\,{}^{(0)}N_{2K'}\big[{}^{(0)}F^{0,0}_{2K}\,{}^{(0)}F^{0,0}_{2K'}\times\\
&\langle{}^{(2)}P^{0,0}_{2K}|0{\cdot}5\{V({}^1S_0)+V_c({}^3S_1-{}^3D_1)\}|{}^{(2)}P^{0,0}_{2K'}\rangle\\
&+{}^{(0)}F^{2,2}_{2K}\,{}^{(0)}F^{2,2}_{2K'}\langle{}^{(2)}P^{2,2}_{2K}|0{\cdot}5(V_c({}^3S_1-{}^3D_1)-3V_{LS}({}^3S_1-{}^3D_1))\\
&+2{\cdot}5V({}^1D_2)+(5/6)\,V({}^3D_2)|{}^{(2)}P^{2,2}_{2K'}\rangle\big]\end{aligned}\tag{A1}$$

2. *Coupling matrix for (S′S) block*

$$\begin{aligned}\langle S',K|\,V(r_{12})|S,K'\rangle &= {}^{(+)}N_{2K}\,{}^{(0)}N_{2K'}\big[{}^{(+)}F^{0,0}_{2K}\,{}^{(0)}F^{0,0}_{2K'}\times\\
&\langle{}^{(2)}P^{0,0}_{2K}|(1/2\sqrt{2})(V({}^1S_0)-V_c({}^3S_1-{}^3D_1))|{}^{(2)}P^{0,0}_{2K'}\rangle\\
&+{}^{(+)}F^{2,2}_{2K}\,{}^{(0)}F^{2,2}_{2K'}\langle{}^{(2)}P^{2,2}_{2K}|(1/2\sqrt{2})\{(3V_{LS}({}^3S_1-{}^3D_1)-V_c({}^3S_1-{}^3D_1))\\
&+5V({}^1D_2)-5/3\;V({}^3D_2)\}|{}^{(2)}P^{2,2}_{2K'}\rangle\big]\end{aligned}\tag{A2}$$

3. *Coupling matrix for (S′S′)* block

$$\begin{aligned}\langle S',K|\,V(r_{12})|S',K'\rangle &= {}^{(+)}N_{2K}\,{}^{(+)}N_{2K'}\big[{}^{(+)}F^{0,0}_{2K}\,{}^{(+)}F^{0,0}_{2K'}\times\\
&\langle{}^{(2)}P^{0,0}_{2K}|(1/4)(V({}^1S_0)+V_c({}^3S_1-{}^3D_1))|{}^{(2)}P^{0,0}_{2K'}\rangle\\
&+{}^{(+)}F^{2,2}_{2K}\,{}^{(+)}F^{2,2}_{2K'}\langle{}^{(2)}P^{2,2}_{2K}|(1/4)\{(V_c({}^3S_1-{}^3D_1)-3V_{LS}({}^3S_1-{}^3D_1))\\
&+5V({}^1D_2)+5/3V({}^3D_2)\}|{}^{(2)}P^{2,2}_{2K'}\rangle\big]\\
&+{}^{(-)}N_{2K}\,{}^{(-)}N_{2K'}\big[{}^{(-)}F^{1,1}_{2K}\,{}^{(-)}F^{1,1}_{2K'}\times\langle{}^{(2)}P^{1,1}_{2K}|(1/12)\{(V({}^3P_0)+3V({}^3P_1)\\
&+9V({}^1P_1)+5(V_c({}^3P_2-{}^3F_2)+V_{LS}({}^3P_2-{}^3F_2))\}|{}^{(2)}P^{1,1}_{2K'}\rangle\\
&+{}^{(-)}F^{3,3}_{2K}\,{}^{(-)}F^{3,3}_{2K'}\langle{}^{(2)}P^{3,3}_{2K}|(1/12)5(V_c({}^3P_2-{}^3F_2)\\
&-4V_{LS}({}^3P_2-{}^3F_2))|{}^{(2)}P^{3,3}_{2K'}\rangle\big]\end{aligned}\tag{A3}$$

4. *Coupling matrix for (D, S)* block

$$\begin{aligned}\langle D^+,K|\,V(r_{12})|S,K'\rangle &= {}^{(D+)}N_{2K+2}\,{}^{(0)}N_{2K'}\big[{}^{(D+)}F^{2,2}_{2K+2}\,{}^{(0)}F^{2,2}_{2K'}\times\\
&\langle{}^{(2)}P^{2,2}_{2K+2}|(-1/\sqrt{2})\,V_T({}^3S_1-{}^3D_1)|{}^{(2)}P^{2,2}_{2K'}\rangle\\
&-{}^{(D+)}F^{0,2}_{2K+2}\,{}^{(0)}F^{0,0}_{2K'}\langle{}^{(2)}P^{0,2}_{2K+2}|\sqrt{2}V_T({}^3S_1-{}^3D_1)|{}^{(2)}P^{0,0}_{2K'}\rangle\\
&-{}^{(D+)}F^{2,0}_{2K+2}\,{}^{(0)}F^{2,2}_{2K'}\langle{}^{(2)}P^{2,0}_{2K+2}|\sqrt{2}V_T({}^3S_1-{}^3D_1)|{}^{(2)}P^{2,2}_{2K'}\rangle\big]\end{aligned}\tag{A4}$$

5. *Coupling matrix for (D, S') block*

$$\begin{aligned}
\langle D,K|V(r_{12})|S',K'\rangle &= {}^{(D+)}N_{2K+2}\,{}^{(+)}N_{2K'}[{}^{(D+)}F^{2,2}_{2K+2}\,{}^{(+)}F^{2,2}_{2K'}\times\\
&\langle{}^{(2)}P^{2,2}_{2K+2}|0{\cdot}5V_T({}^3S_1-{}^3D_1)|{}^{(2)}\mathrm{P}^{2,2}_{2K'}\rangle\\
&+{}^{(D+)}F^{0,2}_{2K+2}\,{}^{(+)}F^{0,0}_{2K'}\langle{}^{(2)}P^{0,2}_{2K+2}|V_T({}^3S_1-{}^3D_1)|{}^{(2)}P^{0,0}_{2K'}\rangle\\
&+{}^{(D+)}F^{2,0}_{2K+2}\,{}^{(+)}F^{2,2}_{2K'}\langle{}^{(2)}P^{2,0}_{2K+2}|V_T({}^3S_1-{}^3D_1)|{}^{(2)}P^{2,2}_{2K'}\rangle]\\
&+{}^{(D-)}N_{2K+2}\,{}^{(-)}N_{2K'}[{}^{(D-)}F^{1,1}_{2K+2}\,{}^{(-)}F^{1,1}_{2K'}\times\\
&\langle{}^{(2)}P^{1,1}_{2K+2}|(-1/30)\,V_T({}^3P_2-{}^3F_2)|{}^{(2)}P^{1,1}_{2K'}\rangle\\
&-{}^{(D-)}F^{3,1}_{2K+2}\,{}^{(-)}F^{3,3}_{2K'}\langle{}^{(2)}P^{3,1}_{2K+2}|(9/5)\,V_T({}^3P_2-{}^3F_2)|{}^{(2)}P^{3,3}_{2K'}\rangle\\
&-{}^{(D-)}F^{1,3}_{2K+2}\,{}^{(-)}F^{1,1}_{2K'}\langle{}^{(2)}P^{1,3}_{2K+2}|(9/5)\,V_T({}^3P_2-{}^3F_2)|{}^{(2)}P^{1,1}_{2K'}\rangle\\
&-{}^{(D-)}F^{3,3}_{2K+2}\,{}^{(-)}F^{3,3}_{2K'}\langle{}^{(2)}P^{3,3}_{2K+2}|(8/15)\,V_T({}^3P_2-{}^3F_2)|{}^{(2)}\mathrm{P}^{3,3}_{2K'}\rangle]
\end{aligned}\tag{A5}$$

6. *Coupling matrix for (D, D) block*

$$\begin{aligned}
\langle D,K|V(r_{12})|D,K'\rangle &= {}^{(D+)}N_{2K+2}\,{}^{(D+)}N_{2K'+2}[{}^{(D+)}F^{2,2}_{2K+2}\,{}^{(D+)}F^{2,2}_{2K'+2}\times\\
&\langle{}^{(2)}P^{2,2}_{2K+2}|(1/4)\{(V_c({}^3S_1-{}^3D_1)-3V_{LS}({}^3S_1-{}^3D_1))\\
&-2V_T({}^3S_1-{}^3D_1)+5/3V({}^3D_2)\}|{}^{(2)}P^{2,2}_{2K'+2}\rangle\\
&+{}^{(D+)}F^{2,0}_{2K+2}\,{}^{(D+)}F^{2,0}_{2K'+2}\langle{}^{(2)}P^{2,0}_{2K+2}|0{\cdot}5V_c({}^3S_1-{}^3D_1)|{}^{(2)}P^{2,0}_{2K'+2}\rangle\\
&-{}^{(D+)}F^{2,0}_{2K+2}\,{}^{(D+)}F^{2,2}_{2K'+2}\langle{}^{(2)}P^{2,0}_{2K+2}|V_T({}^3S_1-{}^3D_1)|{}^{(2)}P^{2,2}_{2K'+2}\rangle\\
&-{}^{(D+)}F^{2,2}_{2K+2}\,{}^{(D+)}F^{2,0}_{2K'+2}\langle{}^{(2)}P^{2,2}_{2K+2}|V_T({}^3S_1-{}^3D_1)|{}^{(2)}P^{2,0}_{2K'+2}\rangle\\
&+{}^{(D+)}F^{0,2}_{2K+2}\,{}^{(D+)}F^{0,2}_{2K'+2}\langle{}^{(2)}P^{0,2}_{2K+2}|(1/2)\times\\
&\{V_c({}^3S_1-{}^3D_1)-3V_{LS}({}^3S_1-{}^3D_1)-2V_T({}^3S_1-{}^3D_1)\}|{}^{(2)}P^{0,2}_{2K'+2}\rangle]\\
&+{}^{(D-)}N_{2K+2}\,{}^{(D-)}N_{2K'}[{}^{(D-)}F^{1,1}_{2K+2}\,{}^{(D-)}F^{1,1}_{2K'}\times\\
&\langle{}^{(2)}P^{1,1}_{2K+2}|\{1/3V({}^3P_0)+1/4V({}^3P_1)-1/150V_T({}^3P_2-{}^3F_2)\\
&+1/60(V_c({}^3P_2-{}^3F_2)+V_{LS}({}^3P_2-{}^3F_2))\}|{}^{(2)}P^{1,1}_{2K'+2}\rangle\\
&+{}^{(D-)}F^{3,1}_{K+2}\,{}^{(D-)}F^{3,1}_{2K'}\langle{}^{(2)}P^{3,1}_{2K+2}|\{-9/25V_T({}^3P_2-{}^3F_2)\\
&+0{\cdot}9(V_c({}^3P_2-{}^3F_2)+V_{LS}({}^3P_2-{}^3F_2))\}|{}^{(2)}P^{3,1}_{2K'+2}\rangle\\
&+{}^{(D-)}F^{1,3}_{K+2}\,{}^{(D-)}F^{1,3}_{2K'+2}\langle{}^{(2)}P^{1,3}_{2K+2}|\{-1{\cdot}44V_T({}^3P_2-{}^3F_2)\\
&+0{\cdot}9(V_c({}^3P_2-{}^3F_2)-4V_{LS}({}^3P_2-{}^3F_2))\}|{}^{(2)}P^{1,3}_{2K'+2}\rangle\\
&-{}^{(D-)}F^{1,1}_{K+2}\,{}^{(D-)}F^{1,3}_{2K'+2}\langle{}^{(2)}P^{1,1}_{2K+2}|9/25V_T({}^3P_2-{}^3F_2)|{}^{(2)}P^{1,3}_{2K'+2}\rangle\\
&-{}^{(D-)}F^{3,1}_{K+2}\,{}^{(D-)}F^{3,3}_{2K'+2}\langle{}^{(2)}P^{3,1}_{2K+2}|1{\cdot}44V_T({}^3P_2-{}^3F_2)|{}^{(2)}P^{3,3}_{2K'+2}\rangle\\
&-{}^{(D-)}F^{1,3}_{K+2}\,{}^{(D-)}F^{1,1}_{2K'+2}\langle{}^{(2)}P^{1,3}_{2K+2}|9/25V_T({}^3P_2-{}^3F_2)|{}^{(2)}P^{1,1}_{2K'+2}\rangle\\
&-{}^{(D-)}F^{3,3}_{K+2}\,{}^{(D-)}F^{3,1}_{2K'+2}\langle{}^{(2)}P^{3,3}_{2K+2}|1{\cdot}44V_T({}^3P_2-{}^3F_2)|{}^{(2)}P^{3,1}_{2K'+2}\rangle\\
&+{}^{(D-)}F^{3,3}_{K+2}\,{}^{(D-)}F^{3,3}_{2K'+2}\langle{}^{(2)}P^{3,3}_{2K+2}|(-32/75)\,V_T({}^3P_2-{}^3F_2)\\
&+4/15(V_c({}^3P_2-{}^3F_2)-4V_{LS}({}^3P_2-{}^3F_2))|{}^{(2)}P^{3,3}_{2K'+2}\rangle]
\end{aligned}\tag{A6}$$

The numerical factors arise from angular momentum coupling coefficients.

Appendix B

The various components of the RSC potential in MEV (corresponding to isospin $(t) = 1$) are given in eqs (B.1) through (B.5), where $h = 10{\cdot}463$ MeV and $x = \mu r$ with $\mu = 0{\cdot}7F^{-1}$ and r is the distance between the interacting two nucleons.

1. *Singlet even components*

$$V(^1S_0) = -h\frac{\exp(-x)}{x} - 1650{\cdot}6\frac{\exp(-4x)}{x} + 6484{\cdot}2\frac{\exp(-7x)}{x} \tag{B1}$$

$$V(^1D_2) = -h\frac{\exp(-x)}{x} - 12{\cdot}322\frac{\exp(-2x)}{x} - 1112{\cdot}6\frac{\exp(-4x)}{x} + 6484{\cdot}2\frac{\exp(-7x)}{x} \tag{B2}$$

2. *Triplet odd components*

$$V(^3P_0) = -h\left[\left(1+\frac{4}{x}+\frac{4}{x^2}\right)\exp(-x) - \left(\frac{16}{x}+\frac{4}{x^2}\right)\exp(-4x)\right]\Big/ x + 27{\cdot}133\frac{\exp(-2x)}{x} - 790{\cdot}74\frac{\exp(-4x)}{x} + 20662\frac{\exp(-7x)}{x} \tag{B3}$$

$$V(^3P_1) = h\left[\left(1+\frac{2}{x}+\frac{2}{x^2}\right)\exp(-x) - \left(\frac{8}{x}+\frac{2}{x^2}\right)\exp(-4x)\right]\Big/ x - 135{\cdot}25\frac{\exp(-2x)}{x} + 472{\cdot}81\frac{\exp(-3x)}{x} \tag{B4}$$

$$V(^3P_2 - {^3F_2}) = V_C + V_T S_{12} + V_{LS}\mathbf{L}\cdot\mathbf{S} \tag{B5}$$

where,

$$V_C = \frac{h}{3}\frac{\exp(-x)}{x} - 933{\cdot}48\frac{\exp(-4x)}{x} + 4152{\cdot}1\frac{\exp(-6x)}{x}$$

$$V_T = h\left[\left(1/3+\frac{1}{x}+\frac{1}{x^2}\right)\exp(-x) - \left(\frac{4}{x}+\frac{1}{x^2}\right)\exp(-4x)\right]\Big/ x - 34{\cdot}925\frac{\exp(-3x)}{x}$$

$$V_{LS} = -2074{\cdot}1\frac{\exp(-6x)}{x}.$$

The components of the RSC potentials in MeV corresponding to isospin zero are presented in eq. B6 through B8.

3. *Singlet odd components*

$$V(^1P_1) = 3h\frac{\exp(-x)}{x} - 634{\cdot}39\frac{\exp(-2x)}{x} + 2163{\cdot}4\frac{\exp(-3x)}{x} \tag{B6}$$

4. *Triplet even components*

$$V(^3D_2) = -3h\left[\left(1+\frac{2}{x}+\frac{2}{x^2}\right)\exp(-x) - \left(\frac{8}{x}+\frac{2}{x^2}\right)\exp(-4x)\right]\Big/ x - 220{\cdot}12\frac{\exp(-2x)}{x} + 871{\cdot}0\frac{\exp(-3x)}{x} \tag{B7}$$

$$V(^3S_1 - {}^3D_1) = V_C + V_T S_{12} + V_{LS}\mathbf{L}\cdot\mathbf{S} \tag{B8}$$

where

$$V_C = -h\frac{\exp(-x)}{x} + 105{\cdot}468\frac{\exp(-2x)}{x} - 3187{\cdot}8\frac{\exp(-4x)}{x} + 9924{\cdot}3\frac{\exp(-6x)}{x}$$

$$V_T = -h\left[\left(1+\frac{3}{x}+\frac{3}{x^2}\right)\exp(-x) - \left(\frac{12}{x}+\frac{3}{x^2}\right)\exp(-4x)\right]\Big/ x + 351{\cdot}77\frac{\exp(-4x)}{x} - 1673{\cdot}5\frac{\exp(-6x)}{x}$$

$$V_{LS} = 708{\cdot}91\frac{\exp(-4x)}{x} - 2713{\cdot}1\frac{\exp(-6x)}{x}$$

V_C, V_{LS} and V_T represent central, spin-orbit and tensor term of the RSC potential respectively. S_{12} is the usual tensor operator.

References

[1] Y A Simonov, in *Proceedings of the International Symposium on the Present Status and Novel Developments in the Nuclear Many body Problems*, Rome, 1972, edited by F Calogera and C Ciofi degli Atti (Editrice Compsitori, Bologna, 1974), p. 527

[2] J Bruinsma, R V Wageningen and J L Visschers, in *Few particle problems in Nuclear interaction* edited by I Slaus (North-Holland, Amsterdam, 1973) p. 368

[3] V F Demin and Y E Pokrovsky, *Phys. Lett.* **B47**, 394 (1973)

[4] G Erens, J L Visschers and R V Wageningen, *Ann. Phys.* **67**, 461 (1971)

[5] J L Ballot and M Fabre de la Ripelle, *Ann. Phys.* (*N.Y.*) **127**, 62 (1980)

[6] T K Das, H T Coelho and M Fabre de la Ripelle, *Phys. Rev.* **C26**, 2288 (1982)
T K Das and H T Coelho, *Phys. Rev.* **C26**, 697 (1982)
T B De and T K Das, *Phys. Rev.* **C36**, 402 (1987)

[7] A K Ghosh and T K Das, *Phys. Rev.* **C42**, 1249 (1990)

[8] V B Mandelzweig, *Nucl. Phys.* **A508** 63c (1990)

[9] L D Faddeev, *Zh. Eksp. Teor. Fiz.* **39**, 1459 (1960)
L D Faddeev, *Sov. Phys. JETP* **12**, 1014 (1961)

[10] R Reid, *Ann. Phys.* (*NY*) **50**, 411 (1968)

[11] G L Payne, J L Friar, B F Gibson and I R Afnan, *Phys. Rev.* **C22**, 823 (1980)
C Hajduk and P U Sauer, *Nucl. Phys.* **A369**, 321 (1981)
J L Friar, B F Gibson and G L Payne, *Phys. Rev.* **C37**, 2869 (1988)

[12] T Sasakawa and T Sawada, *Phys. Rev.* **C20**, 1954 (1979)
G L Payne, J L Friar and B F Gibson, *Phys. Rev.* **C22**, 832 (1980)
T Sasakawa, H Okuno and T Sawada, *Phys. Rev.* **C23**, 905 (1981)
S Ishikawa, T Sasakawa, T Sawada and T Ueda, *Phys. Rev. Lett.* **53**, 1877 (1984)
[13] C R Chen, G L Payne, J L Friar and B F Gibson, *Phys. Rev.* **C31**, 2266 (1985)
[14] M I Mukhtarova, *Sov. J. Nucl. Phys.* **49** 208 (1989)
[15] D Gogny, P Pires and R de Tourreil, *Phys. Lett.* **B32**, 591 (1970)
[16] R de Tourreil and D W I Sprung, *Nucl. Phys.* **A201**, 193 (1973)
[17] R de Tourreil, B Rouben and D W I Sprung, *Nucl. Phys.* **A242**, 445 (1975)
J Côte, *et al Nucl. Phys.* **A273**, 269 (1976)
[18] T R Schneider, *Phys. Lett.* **B40**, 439 (1972)
[19] T K Das and S Bhattacharyya, *Pramana – J. Phys.* **40**, 189 (1993)
[20] M K Pal, *Theory of Nuclear Structure*, Affliated East-West Press Pvt Ltd, New Delhi (1982) p. 30
[21] T K Das and T B De, *Pramana – J. Phys.* **28**, 645 (1987)
T B De and T K Das, *Phys. Rev.* **C36**, 402 (1987)
[22] S Bhattacharyya and T K Das, *J. Comput. Phys.* (*NY*) **114**, 308 (1994)
[23] B R Johnson, *J. Chem. Phys.* **69**, 4678 (1978)
[24] T K Das, H T Coelho and M Fabre de la Ripelle, *Phys. Rev.* **C26**, 2281 (1982)
[25] J L Ballot, M Beiner and M Fabre de la Ripelle, in *Present status and novel developments in the nuclear many body problems*, edited by F Calogera and C Ciofi degli Atti, (Rome 1972) p. 565
[26] J L Ballot, M Fabre de la Ripelle and J S Levinger, *Phys. Rev.* **C26**, 2301 (1982)

RAMAN RESEARCH INSTITUTE LIBRARY BANGALORE-80
2 MAY 1995

PRAMANA
— journal of
physics
© Printed in India
Vol. 44, No. 3,
March 1995
pp. 201–209

Phonons and fractons in sol-gel alumina: Raman study

ANUSHREE ROY and AJAY K SOOD*
Department of Physics, Indian Institute of Science, Bangalore 560012, India
*Also at Jawaharlal Nehru Centre for Advanced Scientific Research, Jakkur Campus, Bangalore 560064, India

MS received 11 November 1994

Abstract. We report Raman scattering from the boehmite, γ-, δ- and α-phases of the alumina gel. Samples are characterized by transmission and scanning electron microscopy, X-ray diffraction and density measurements. The main Raman line in the boehmite phase is red-shifted as well as asymmetrically broadened with respect to that in the crystalline boehmite, signifying the nanocrystalline nature of the gel. Raman signatures are absent in the γ- and δ-phases due to the disorder in cation vacancies. We also show that low frequency Raman scattering from the boehmite phase resembles that from a fractal network, characterized in terms of fraction dimension $\tilde{d}$. Taking Hausdorff dimension D of the boehmite gel to be 2·5 (or 3·0), the value of $\tilde{d}$ is $1{\cdot}33 \pm 0{\cdot}02$ (or $1{\cdot}44 \pm 0{\cdot}02$), which is close to the theoretically predicted value of 4/3.

Keywords. Al-gel; boehmite; disordered material; fractals; phonons; fractons.

PACS Nos **64·60; 78·30; 63·50**

1. Introduction

In recent years there has been a considerable interest in static and dynamic properties of random systems, such as gels and glassy networks. The sol-gel route of preparation of porous transparent alumina gel (Al-gel) was first established by Yoldas [1]. It is a three-step process: (i) hydrolysis and condensation of aluminium alkoxide in excess water to form AlO(OH) precipitate (ii) peptization of the hydroxide to clear the sol and (iii) concentration of the sol by slow evaporation of the solvent resulting in gel formation. It has been shown [2] that the morphology and structure of aluminium hydroxide gels prepared from aluminium-sec-butoxide under acidic conditions depend crucially on temperature. The gels formed by the peptization of the sol with an acid above 50°C termed as high temperature gels, show presence of nanocrystalline platelets. On the other hand, whenever all the chemical processing is performed at room temperature, the structure of the gel is termed as 'super amorphous' as studied by X-ray diffraction. In this paper we will discuss the structure and vibrational properties of the high temperature alumina hydrogel, boehmite γ-AlO(OH), and its other phases formed by the transformation sequence

$$\gamma\text{-AlO(OH)} \rightarrow \gamma\text{-Al}_2\text{O}_3 \rightarrow \delta\text{-Al}_2\text{O}_3 \rightarrow \alpha\text{-Al}_2\text{O}_3.$$

The structure of crystalline boehmite is orthorhombic [3, 4] with two AlO(OH) units per primitive unit cell. The structure consists of extended layers perpendicular to the b-axis [4]. Each layer has two planes of aluminium atoms and four planes of oxygen atoms. Each aluminium atom is bonded with six oxygen atoms in a distorted octahedron. The oxygen atoms present in the inner planes are each bonded with four aluminium atoms in a highly distorted tetrahedron. The outer plane oxygen atoms are each bonded to only two aluminium atoms. The intralayer interactions between atoms are through covalent and ionic bonding, whereas hydrogen bonding is present between the layers. A transformation from boehmite to the dehydroxylated alumina γ-phase, γ-Al_2O_3, occurs at ~ 400°C when water is expelled from boehmite resulting in collapse of the layers and the cubic structure is formed as a result of rearrangement of the oxygen atoms. The γ-Al_2O_3 has a defect spinel structure (A_2BO_4) in which A^{3+} ions are octahedrally coordinated to O^{2-} ions, while B^{2+} ions have tetrahedral coordination to the anions [5]. The oxygen atoms are in an almost perfect cubic close-packing with metal atoms lying in the holes of the packing. In γ-Al_2O_3 structure, the cation vacancies are assumed to be disordered among the octahedral and tetrahedral sites with the probability of the occupation of the vacancies in the tetrahedral sites being more by a factor of 2/3 than in the octahedral sites. The γ-Al_2O_3 to δ-Al_2O_3 phase transformation occurs at ~ 800°C. In δ-Al_2O_3 the vacancies are ordered on octahedral sites, giving it a spinel superstructure [6]. The transformation of δ-Al_2O_3 to α-Al_2O_3 phase occurs at ~ 1200°C. The structure of α-Al_2O_3 is rhombohedral and belongs to a space group D_{3d}^6 with two molecular Al_2O_3 per unit cell [7]. In α-Al_2O_3 the aluminium atoms are coordinated with two layers of oxygen atoms in distorted octahedra [8].

The high temperature boehmite gel is composed of nanocrystalline platelets with an average size of ~ 60 Å [1] and a narrow size distribution, which are somewhat ordered like in a smectic array [6]. The gel is highly porous (porosity ~ 60–70%) [1]. The dehydration of the boehmite to γ-Al_2O_3, δ-Al_2O_3 and α-Al_2O_3 represents topotactic deformation of the network (i.e. the crystal structures are accomplished without any change in crystalline morphology) and is accompanied by changes in the morphology of the porosity [9]. Wilson and Stacey [9] showed that the microstructure characteristic of γ-Al_2O_3 consists of a system of fine lamellar pores which are perpendicular to the planes of the boehmite platelets. Their orientation and spacing are quite regular with some evidence of extensive cross-linking. The pores take a planar hexagonal shape. In δ-Al_2O_3, the pores have the same morphology as in γ-Al_2O_3 but merged into larger hexagonal planar pores of several hundred angstroms. The average pore size increases with further heat treatment. In α-Al_2O_3, monocrystals with wormy texture [6] entrapping a high proportion of pores can be seen. Thus in spite of topotactic transformation, each stage of the transformation sequence has a characteristic microstructure due to the variations in the pores morphology.

Motivated by the above observations on wide variation of microstructure of different phases of Al-gel, we have studied the vibrational properties of such structures (characterized using X-ray diffraction) by Raman scattering. While this work had been almost completed, we learnt of a recent paper on Raman studies of the nanocrystalline boehmite phase of the Al-gel [4]. In this paper, we present results on the Raman scattering from the phonons in the different phases of the Al-gel and compare them with the known results in the literature. We have also studied, for the first time, the low frequency (20–300 cm^{-1}) Raman intensity which is known to give information about the dynamics of the fractal network—for example that of the silica gel [10] and the porous silicon [11]. It has been shown that the fracton dimension $\tilde{d}$ which characterizes vibration density of states of the fractal network, $g(\omega) \sim \omega^{(\tilde{d}-1)}$, can be determined from the Raman intensity in the low frequency range. Our experimental results do suggest that dynamics of the boehmite phase of the Al-gel has characteristics that of a fractal network below a certain length scale.

Section 2 gives the experimental details and the results along with their discussion are given in § 3.

2. Experimental

Hydrolysis of aluminium isopropoxide $Al(OC_3H_7)_3$ was performed in excess deionized water under vigorous stirring for 15–20 min at 80°C. For peptization, 12N hydrochloric acid was added as catalyst into the slurry kept at 90°C for about 25 min. The alkoxide to water to acid molar ratio was kept at 1:100:0·3 having pH of the solution ~ 3. The sol-gel transition occurs by slow evaporation of the solvent at room temperature for at least 48 h. The boehmite hydrogel was transformed to the other phases by heating it in air for fixed temperatures ranging from 125°C to 1200°C [12]. The transition temperature, T_γ, for γ-phase was 400°C and that for δ-phase, T_δ, was 800°C. The α-Al_2O_3 was formed by heating δ-phase at 1200°C for 10 h (T_α). In summary, the dehydration sequence of Al-gel is as follows:

$$\gamma\text{-AlO(OH)} \xrightarrow[400^\circ\text{C for 2 h}]{T_\gamma} \gamma\text{-Al}_2\text{O}_3 \xrightarrow[800^\circ\text{C for 4 h}]{T_\delta} \delta\text{Al}_2\text{O}_3 \xrightarrow[1200^\circ\text{C for 10 h}]{T_\alpha} \alpha\text{-Al}_2\text{O}_3.$$

X-ray diffraction of the powdered samples is obtained at room temperature using Philip's diffractometer, model PW 1050/70 equipped with a vertical goniometer and CuK_α radiation (wavelength $\lambda = 1{\cdot}514$ Å). The scanning and transmission electron microscopy are performed using Cambridge S360 and JEOL 2000CX instruments, respectively. The electron micrographs of the different phases are similar to the reported results [6, 9]. The density of the boehmite gel measured was 2·38 g/cc. Comparing this with the density of 3·01 g/cc for the crystalline boehmite indicates a porosity of 20% in the gel with respect to the crystalline boehmite. The densities of the γ-, δ- and α-phases are 3·19, 3·45 and 3·87 g/cc, respectively. The Raman spectra are recorded at room-temperature using Dilor X-Y spectrometer equipped with a liquid nitrogen cooled CCD detector and 5145 Å radiation from an argon ion laser (power $\sim$ 100 mW).

3. Results and Discussion

3.1 *X-ray diffraction*

X-ray diffraction patterns of the four different phases of Al-gel are shown in figure 1. The observed value of diffraction angles (2θ) for all the phases matches quite well with the reported data [13]. Analysis of X-ray diffraction patterns confirms the nanocrystalline structure of the boehmite gel. The peak assignment for the boehmite phase can be given with respect to the orthorhombic structures of its corresponding crystalline phase [3, 14]. The large linewidth is due to the finite size of the crystallites in the gel. The crystallite size, L, can be calculated from the full width at half maxima (FWHM), Γ (expressed in radians), of the X-ray diffraction peak using Scherrer's equation [15]

$$\Gamma = \frac{0{\cdot}94\lambda}{L\cos\theta}, \tag{1}$$

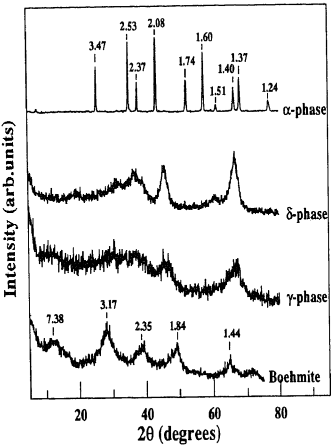

Figure 1. X-ray diffraction pattern for the different phases of alumina gel.

where θ is the diffraction peak position. Taking the diffractometer resolution function (DRF) to be Gaussian and the diffraction line to be Lorentzian, the linewidth correction for the X-ray instrumental broadening can be taken into account by using the empirical expression [16]

$$\eta = \eta_e - (1/\eta_e)^{\beta}, \tag{2}$$

where $\beta = 1 - 0{\cdot}1107/\eta_e$. The η_e is the ratio of observed FWHM (Γ_e) and the FWHM (Γ_d) of the DRF. The η is the ratio of the true FWHM (Γ) of the diffraction line and Γ_d. Γ_d is equal to 0·53° for our instrument. For the diffraction peak at $2\theta = 28°$ of the boehmite gel, $\Gamma_e = 1{\cdot}73°$ which gives $\Gamma = 1{\cdot}56°$ and hence the crystallite size can be estimated from (1) to be 55 Å. For γ- and δ-phases of alumina, the diffraction lines are much broader. These broad X-ray lines can arise due to considerable disorder as expected from their structure containing cation vacancies [5]. The α-Al_2O_3 phase shows sharp X-ray diffraction lines which confirms the high crystalline order of this phase and the values of the lattice spacings agree with that of the corundum structure [17]. The results of indexing for the boehmite and the α-Al_2O_3 have been summarized in tables 1 and 2, respectively.

3.2 *Raman spectra: Phonons*

Raman spectra of different phases of the Al-gel are shown in figure 2. We shall analyse the spectra in the context of their crystalline counterparts. The Al-O optical vibrational modes in crystalline boehmite can be classified according to the irreducible

Table 1. Reported d-values of the crystalline boehmite ($d_{x-\text{boehmite}}$) for some (hkl) values and d-values obtained from the powder diffraction pattern of boehmite gel (d_{gel}).

(hkl)	$d_{x-\text{boehmite}}$	d_{gel}
071	1·49	1·44
160	1·78	1·84
111	2·29	2·45
040	3·05	3·17

Table 2. Reported d-values of the corundum (d_{corundum}) and d-values as obtained from powder diffraction pattern of α-Al_2O_3 phase of the alumina gel ($d_{\alpha-Al_2O_3}$). The relative intensity of each diffraction line of corundum also has been listed with its corresponding (hkl) value.

hkl	Intensity	d_{corundum}	$d_{\alpha-Al_2O_3}$
012	75	3·48	3·47
104	90	2·55	2·53
110	40	2·38	2·37
113	100	2·09	2·08
024	45	1·74	1·74
116	80	1·60	1·60
018	8	1·51	1·51
124	30	1·40	1·40
030	50	1·37	1·37
1·0·10	16	1·24	1·24

representations of space group D_{2h}^{17} [18]

$$\Gamma_{\text{Al}-\text{O}} = 3A_{1g}^{R} + 3B_{1g}^{R} + 3B_{2g}^{R} + 2B_{1u} + 2B_{2u} + 2B_{2u},$$

in which only A_{1g}, B_{1g} and B_{2g} modes are Raman active. The observed Raman peak positions in crystalline boehmite are 676, 497 and 369 cm^{-1} for the A_{1g} modes (which are the most intense); 639, 272 and 232 cm^{-1} for the B_{1g} modes and 454, 343 and 260 cm^{-1} for B_{2g} modes. Raman spectra of the boehmite gel shows only the intense A_{1g} modes [figure 2]. The inset of figure 2 shows the expanded plot of the 359 cm^{-1} mode to bring out the asymmetric and broad lineshape with a shift in peak position towards the lower energy as compared to that of the crystalline boehmite. Such a broadening, asymmetry and peak shift (of ~ 10 cm^{-1}) of the Raman mode compared to that of the bulk crystalline boehmite can be attributed to the effect of phonon confinement as observed in the nanostructure of semiconductors [19–21]. In nanocrystallites, phonon can no longer be described by a plane wave but rather by a wave packet whose spatial dimensions are comparable to the crystallite size. This introduces a spread in the wavevector (proportional to the inverse of the particle size) as expected from the uncertainty principle. Since the optic phonon dispersion curves

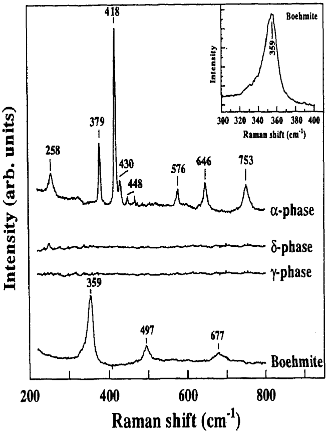

Figure 2. Raman spectra of the different phases of alumina gel.

of the bulk crystal usually bend towards lower frequency for nonzero wavevectors, an integration of the Lorentzian lineshape over the wavevector gives rise to a shift and an asymmetry of the Raman lines towards lower frequency side [19]. A quantitative analysis of the $359\,\mathrm{cm}^{-1}$ line shape (shown in the inset) in terms of the phonon confinement model will require the average dispersion curve of the crystalline boehmite, which is not yet available.

As shown in figure 2, Raman lines are absent in γ- and δ-phases. This interesting result can be understood as follows. Among all the vibrational modes for a regular spinel structure A_2BO_4, to which γ- and δ-phases are related, the only *Raman active vibrations* are the internal modes of *tetrahedral* BO_4 groups, whereas octahedral group vibrations are Raman inactive. In γ- and δ-phases cation vacancies are preferentially situated on the tetrahedral sites and the number of tetrahedrally coordinated Al^{3+} ions is a minor fraction compared to that of the octahedrally coordinated Al^{3+} ion. This can explain the absence of Raman lines in the γ- and δ-phases [22].

The irreducible representations for the optical modes in the α-Al_2O_3 crystal of space group D^6_{3d} are

$$2A^R_{1g} + 5E^R_g + 2A_{1u} + 3A_{2g} + 2A_{2u} + 2E_u.$$

Among all these modes, only seven vibrations $2A_{1g} + 5E_g$ are Raman active. The Raman peaks in α-phase occur at 379, 418, 430, 448, 576, 646 and $753\,\mathrm{cm}^{-1}$. These are the same as in the corundum phase [23], where the modes at 418 and $646\,\mathrm{cm}^{-1}$ correspond to the A_{1g} symmetry and modes at 379, 430, 448, 576 and $753\,\mathrm{cm}^{-1}$ belong to the E_g symmetry. The origin of the peak at $258\,\mathrm{cm}^{-1}$ is not clear at present.

3.3 *Fractons*

The vibrational modes in a disordered system can be localized in contrast to the propagating phonon states in crystalline materials. This localization can be a consequence of scattering (analogous to Anderson localization) or it can be geometric in origin as on a fractal network. For the latter, it has been shown that the vibrational density of states changes from the Debye form to a power law, $g(\omega) \sim \omega^{(\tilde{d}-1)}$ where $\tilde{d}$ is called the fracton dimension. These fracton modes can show up in low frequency Raman scattering experiments where the scattered intensity $I(\omega)$ by fraction modes obey the equation [10, 24]

$$\frac{I(\omega)\omega}{[n(\omega)+1]} \propto \omega^{\nu}, \tag{3}$$

where

$$\nu = \frac{\tilde{d}(2d_{\phi} + \mathrm{D})}{\mathrm{D}} - 1. \tag{4}$$

Here $[n(\omega)+1]$ is the usual Bose–Einstein factor, d_{ϕ} is the geometrical exponent describing the localization of the fractons in real space and D is the fractal Hausdorff dimension. The fractons are spatially localized for $\tilde{d} < 2$. Experimental determination of ν yields the fracton dimension $\tilde{d}$ of the fractal structure for a given value of D and d_{ϕ}. It has been demonstrated that the low frequency Raman scattering in the silica gel having a fractal morphology does obey (3). Figure 3 shows our data for the Raman scattering from the silica gel. From log-log plot of $I(\omega)\omega/[n(\omega)+1]$ vs ω, the slope ν obtained from the least square fit is $1{\cdot}35 \pm 0{\cdot}03$ [figure 3] which is very close to 1·39 reported before [10]. Taking $\mathrm{D} = 2{\cdot}5$ (or 3·0) and $d_{\phi} = 1$ the value of $\tilde{d}$ comes to be equal to $1{\cdot}31 \pm 0{\cdot}02$ (or $1{\cdot}41 \pm 0{\cdot}02$).

Motivated by the results on the silica gel, we have carried out Raman measurements from $\omega > 20\,\mathrm{cm}^{-1}$ on the clear platelet samples of the boehmite, γ- and δ- phases. Inset of figure 3 shows the log $I(\omega)\omega/[n(\omega)+1]$ vs log ω for HV polarization for different phases of Al-gel in the spectral range of $50\,\mathrm{cm}^{-1}$ to $200\,\mathrm{cm}^{-1}$. It is clear from the inset of figure 3, that only the plot for the boehmite phase of Al-gel can be fitted by a straight line, obeying (3). In figure 3 we show log $I(\omega)\omega/[n(\omega)+1]$ vs log ω plot for the boehmite gel both in HV and VV polarization. The depolarization ratio is 0·7. The least square fit to the experimental data has been shown by bold straight lines to yield $\nu = 1{\cdot}41 \pm 0{\cdot}03$ for HV and $\nu = 1{\cdot}46 \pm 0{\cdot}03$ for VV polarization. So far, there is no small angle X-ray or neutron scattering measurements of the boehmite gel to give the fractal dimension D. We can take D to be 2·5 as in silica gel [10]. It can be seen from (4) that the value of $\tilde{d}$ is not very sensitive to the value of D. Using (4), and taking $\nu = 1{\cdot}41$, $d_{\phi} = 1$ (same as in silica gel) and $\mathrm{D} = 2{\cdot}5$, we get the fracton dimension, $\tilde{d}$, of boehmite phase to be equal to $1{\cdot}33 \pm 0{\cdot}02$. This measured value of $\tilde{d}$ is surprisingly close [25] to the theoretical prediction of 4/3. The experimental coefficient $\nu = 1{\cdot}41$ fits the experimental data for frequencies higher than $\omega_{\min} \sim 50\,\mathrm{cm}^{-1}$. This means the fractal regime is effective at length scales [24] shorter than $L_f \sim v_{\mathrm{sound}}/c\ \omega_{\min}$, where v_{sound} is the speed of acoustic phonon in the medium and c is the speed of light. Taking $v_{\mathrm{sound}} = 10 \times 10^5$ cm/s for alumina gel and $\omega_{\min} = 50\,\mathrm{cm}^{-1}$, L_f calculated is 70 Å.

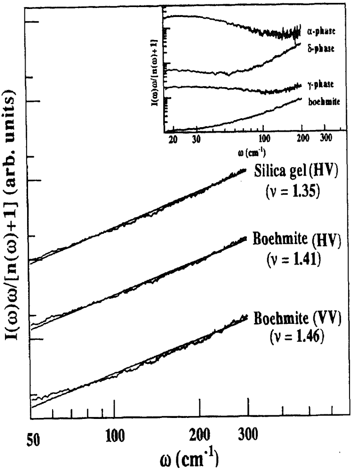

Figure 3. Log-log plot of $I(\omega)\omega/[n(\omega)+1]$ vs ω for ω between 50 and 200 cm^{-1} for the silica gel and the boehmite phase of the alumina gel. For the boehmite phase the plots for both polarization VV and HV are shown. The slope ν (eq. 3) has been marked for each case. Inset shows the plot for the different phases of the alumina gel.

4. Conclusions

We see that in spite of topotactic transformation of the Al-gel, each of its phases has different vibrational characteristics and different microstructure due to the variation in morphology of porosity. The main Raman line in the boehmite gel phase is red shifted and asymmetrically broadened with respect to the corresponding line in the crystalline boehmite, indicating the nanocrystalline nature of the gel. The absence of Raman lines in the γ- and δ-phases is attributed to preferential occupation of the octahedral sites in the spinel structure by Al^{3+} ions. Our low frequency Raman data suggest that the pore morphology in the boehmite alumina gel can be best characterized in terms of fractals below a certain length scale of ~ 70 Å. It would be very interesting to carry out small angle neutron and X-ray scattering measurements to measure the fractal Hausdorff dimension D.

Acknowledgements

One of the authors (AKS) thanks the Department of Science and Technology for financial assistance and Mrs Saraswati Venkataraman for introducing him to Al-gel in 1987 at Kalpakkam. He also thanks Dr V Haisler of the Russian Academy of Sciences, Novosibirsk, where some of the preliminary Raman spectra were recorded in

1987. Both the authors thank Mr K N Krishna for recording the X-ray diffraction patterns, Dr A R Raju for scanning electron microscopy work and Dr G N Subanna for transmission electron microscopy experiments.

References

[1] B E Yoldas, *Am. Ceram. Soc. Bull.* **54**, 286 (1975)
[2] A C Pierre and D R Uhlmann, *J. Non-Cryst. Solids* **82**, 271 (1986)
[3] C E Corbato, R T Tettenhorst and G G Christoph, *Clays clay Miner* **33**, 71 (1985)
[4] C J Doss and R Zallen, *Phys. Rev.* **B48**, 15626 (1993)
[5] M I Baraton and P Quintard, *J. Mol. Struct.* **79**, 337 (1982)
[6] X Yang, A C Pierre and D R Uhlmann, *J. Non-Cryst. Solids* **100**, 371 (1988)
[7] R W G Wyckoff, *Crystal structures* (Interscience Publishers, Inc., New York, 1948) vol 2
[8] S Geschind and S J P Remeika, *Phys. Rev.* **122**, 757 (1961)
[9] S J Wilson and M H Stacey, *J. Colloid, Interface Sci.* **82**, 507 (1981)
[10] A Boukenter, B Champagnon, E Duval, J Dumas, J F Quinson and J Serughetti, *Phys. Rev. Lett.* **57**, 2391 (1986)
[11] A Roy and A K Sood, *Solid State Commun.* **93**, 995 (1995)
[12] V Saraswati, G V N Rao and G V Rama Rao, *J. Mater. Sci.* **22**, 2529 (1987)
[13] B C Lippens and J H de Boer, *Acta Crystallogr.* **17**, 1312 (1964)
[14] G G Christoph, C E Corbato, D A Hofmann and R T Tettenhorst, *Clays Clay Miner.* **27**, 81 (1979)
[15] B E Warren, *X-ray diffraction* (Addison-Wesley, Reading, MA, 1969) pp. 253 and 258
H P Klug and L E Alexander, *X-ray diffraction procedures for polycrystalline and amorphous materials* (Wiley, New York, 1973) pp. 687 and 635
[16] A K Arora and V Umadevi, *Appl. Spectrosc.* **36**, 424 (1982)
[17] Powder diffraction file (International Centre for Diffraction Data, 1990) 10–173
[18] A B Kiss, G Keresztury and L Farkas, *Spectrochim. Acta* **A36**, 653 (1980)
[19] I H Campbell and P M Fauchet, *Solid State Commun.* **58**, 739 (1986)
[20] P M Fauchet and I H Campbell, *Critical review in solid state and materials sciences* **14**, S79 (1988)
[21] Anushree Roy, K Jayaram and A K Sood, *Solid State Commun.* **89**, 229 (1994)
[22] G Mariotto, E Cazzanelli, G Carturan, R Di Maggio and P Scardi, *J. Solid State Chem.* **86**, 263 (1990)
[23] S P S Porto and R S Krishnan, *J. Chem. Phys.* **17**, 1009 (1967)
[24] S Alexander and R Orbach, *J. Phys. Lett. (Paris)* **43**, L625 (1982)
[25] S Alexander, C Laermans, R Orbach and H M Rosenberg, *Phys. Rev.* **B28**, 4615 (1983)

[redacted]

PRAMANA
— journal of
physics

© Printed in India

Vol. 44, No. 3,
March 1995
pp. 211–217

Thermally stimulated luminescence and electron paramagnetic resonance studies on uranium doped $K_2Ca_2(SO_4)_3$

T K SESHAGIRI, V NATARAJAN and M D SASTRY
Radiochemistry Division, Bhabha Atomic Research Centre, Trombay, Bombay 400085, India

MS received 5 July 1994; revised 3 November 1994

Abstract. Thermally stimulated luminescence (TSL) studies of gamma-irradiated uranium-doped $K_2Ca_2(SO_4)_3$ revealed two glow peaks around 400 K and 435 K. Electron paramagnetic resonance (EPR) studies carried out on these samples have shown the formation of the radical ions SO_4^-, SO_3^-, SO_2^- and O_3^-. From the study of the thermal stabilities of these radical ions, it was found that the thermal destruction of SO_2^- and SO_4^- radical ions are associated with the glow peaks observed around 400 K and 435 K respectively. Uranate ion was identified as the luminescent centre for the observed TSL glow. The trap depth values for the glow peaks have been determined from TSL data.

Keywords. Thermally stimulated luminescence; electron paramagnetic resonance.

PACS Nos 61·80; 78·60; 76·30

1. Introduction

The luminescence properties of rare earth doped mixed sulphate compounds such as $K_2Ca_2(SO_4)_3$, $K_3Na_2(SO_4)_2$, $K_2Mg_2(SO_4)_3$ and $Rb_2Mg_2(SO_4)_3$ have been attracting the attention in the recent years [1–5]. In particular, the thermoluminescence properties of the mixed sulphate compound, $K_2Ca_2(SO_4)_3$ in undoped form as well as with Eu dopant have been investigated in detail with respect to their possible use in dosimetry of ionizing radiations [1, 2]. The thermally stimulated electron transfer processes in a number of actinide doped alkaline earth sulphate matrices have been investigated in our laboratory [6–12]. In these investigations, thermally stimulated luminescence and electron paramagnetic resonance techniques were used to get a complete understanding of the radiation induced defects and their thermally stimulated relaxation back to the virgin state of the phosphor. These investigations are an essential part of an integrated understanding of the optical properties of the phosphor doped with radioactive impurities. In the present paper, the results of TSL and EPR studies conducted on the uranium-doped mixed sulphate compound, $K_2Ca_2(SO_4)_3$ with a view to identifying the radiation induced electron/hole traps, their thermal stabilities and their role in the thermally stimulated luminescence are described. This compound contains two types of cations: monovalent (K^+) and divalent (Ca^{2+}). This affects the radical ions stabilized at SO_4^{2-} site and therefore should contrast with those features observed in alkaline earth sulphates.

2. Experimental

Analar grade K_2SO_4 was dissolved in distilled water. To this, uranium (0·1% by weight) was added in the form of uranyl nitrate and the water was boiled off. The resultant mixture was thoroughly mixed, ground with analar grade $CaSO_4$ in the molar ratio 1:2 and then heated at 1273 K for 24 h. The X-ray diffraction pattern of the sample agreed well with that reported in the literature [13]. The EPR spectra of the samples were recorded using a Bruker ESP-300 spectrometer at X-band frequency. A variable temperature accessory was used for EPR temperature variation experiments. A gamma chamber with ^{60}Co source was used for irradiation.

3. Results and discussion

The TSL glow curve of the samples gamma irradiated at room temperature (dose = 4 KGy) showed the presence of a prominent glow peak at 400 K with a shoulder

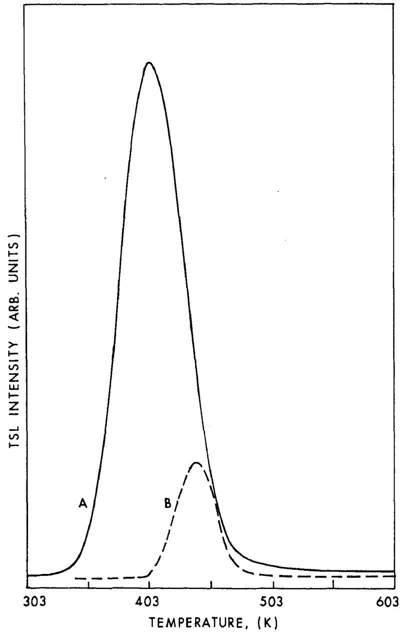

Figure 1. (A) TSL glow curve of gamma irradiated $K_2Ca_2(SO_4)_3$ in the 300–600 K range (dose = 4 kGy); (B) TSL glow curve of the gamma irradiated sample recorded after annealing at 400 K for 1 min.

Table 1.

TSL peak temp.* (K)	Trap depth(eV) DHR	IR	Frequency factor (s^{-1})
400	1·02 ± 0·08	0·94 ± 0·09	$1{\cdot}1 \times 10^{12}$
435	0·80 ± 0·06	0·90 ± 0·08	$1{\cdot}2 \times 10^{9}$

*-heating rate, $\beta = 2{\cdot}5\,\mathrm{K\,s^{-1}}$
DHR-different heating rate, IR -initial rise method.

around 435 K for a heating rate of 2·5 K/sec (figure 1). The dose dependence study of the composite TSL glow peak showed that the intensity saturates after a dose of 3 kGy. The relative intensity of the glow peaks did not change with dose. The trap depth for 400 and 435 K peaks were determined from different heating rates method and initial rise methods [14] and are given in table 1. Thermal bleaching at 400 K was employed to get correct value of $T_{\max}$ for the second peak. The spectral studies of the TSL glow peaks carried out using narrow band interference filters revealed emission around 569, 583 and 598 nm characteristic of UO_6^{6-} ion [10]. The absence of strong green emission around 510 and 535 nm [15] in the TSL glow clearly suggested the absence of emission from UO_2^{2+}. Further, in our earlier studies (10), UO_2^{2+} emission was observed only in uranium-doped $CaSO_4$ samples annealed at 870 K, whereas samples annealed at 1120 K showed emission due to UO_6^{6-} ions.

The unirradiated sample did not show the presence of any paramagnetic species prior to irradiation. The EPR spectrum of gamma irradiated samples recorded at room temperature showed signals due to SO_4^- ($g_\perp = 2{\cdot}007$ and $g_\parallel = 2{\cdot}033$), SO_3^- ($g_{\mathrm{iso}} = 2{\cdot}0032$), O_3^- ($g = 2{\cdot}0105$) and SO_2^- ($g_1 = 2{\cdot}0008$, $g_2 \simeq 2{\cdot}004$, $g_3 = 2{\cdot}0085$). The spectrum is shown in figure 2. In the work on alkaline earth sulphates doped with actinides [6–12], irradiation at room temperature did not yield SO_2^-. On the other hand, reports exist on the radiation induced formation of SO_2^- in alkali sulphates [16, 17]. Therefore it is possible that the formation of SO_2^- is due to the presence of K^+ ions. The formation of SO_2^- ion is expected to yield concomitant paramagnetic O_2^- ions. The g values of O_2^- are highly matrix dependent ($g_\parallel$ in the range 2·02 to 2·4 and $g_\perp$ in the range 1·95 to 2·005 [18]. A parallel feature around $g = 2{\cdot}0225$ indicated in figure 2 is tentatively assigned to O_2^- ion. No EPR signals due to UO_2^+ was observed either at 77 K or at room temperature in gamma irradiated samples below 12·5 kG, the highest magnetic field used by us.

The thermal stabilities of the radical ions were studied from the temperature dependence of the EPR spectra of irradiated sample (figures 3 and 4). The radical ion, SO_2^- was found to disappear around 400 K, whereas SO_4^- ion was found to get destroyed around 440 K. The line assigned to O_2^- ion also disappeared along with SO_2^- ion around 400 K. The other radical ions, SO_3^- and O_3^- were found to be stable up to 600 K though with reduced intensities of their EPR signals. The EPR spectra of the gamma irradiated sample heated up to 600 K and cooled to room temperature, contained some unresolved weak lines around $g \simeq 2{\cdot}0$ in addition to stronger signals from SO_3^- and O_3^- ions. These lines seem to arise fron the interaction of ^{39}K ($I = 3/2$)

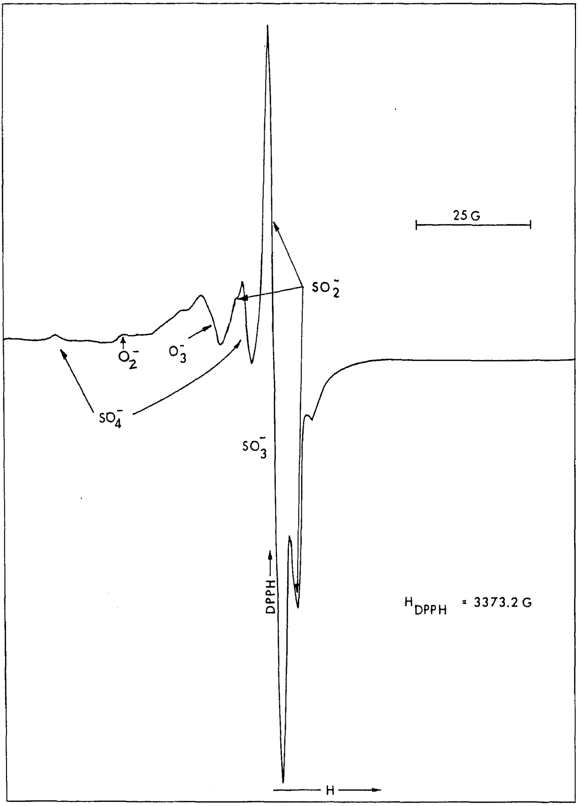

Figure 2. EPR spectra of gamma irradiated $K_2Ca_2(SO_4)_3$ recorded at 300 K (dose = 4 kGy).

with some unidentified radical. In the earlier studies [16, 19] on gamma irradiated alkali sulphates, centres attributed to alkali hyperfine interaction with sulphoxy radical ions have been reported.

The probable mechanisms for the observed glow peaks are as follows:

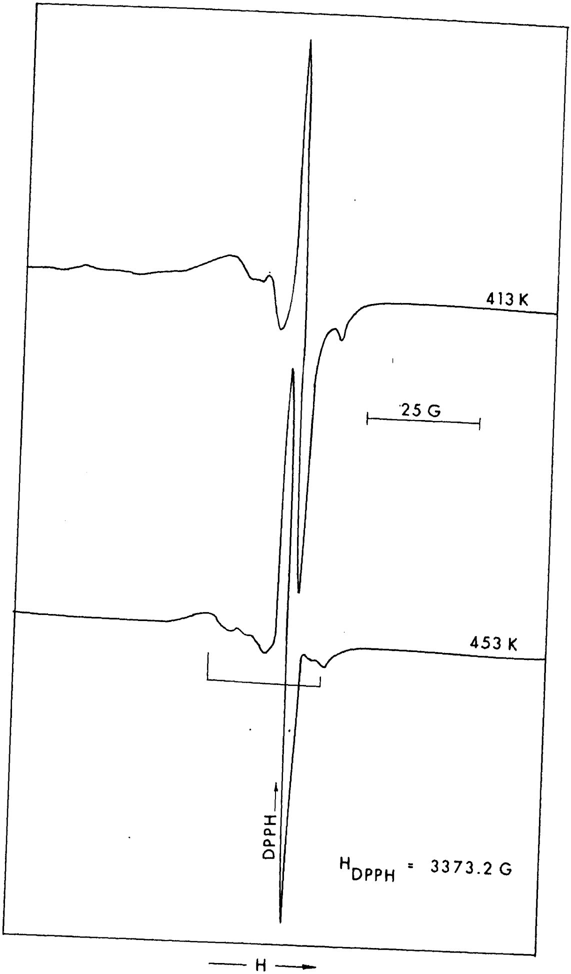

Figure 3. EPR spectra of gamma irradiated sample recorded at 413 K and at 453 K (dose = 4 KGy). The region marked contains three sets of unresolved hyperfine structure due to the nearest neighbour $^{39}K^+$ ($I = 3/2$) on an unidentified radical.

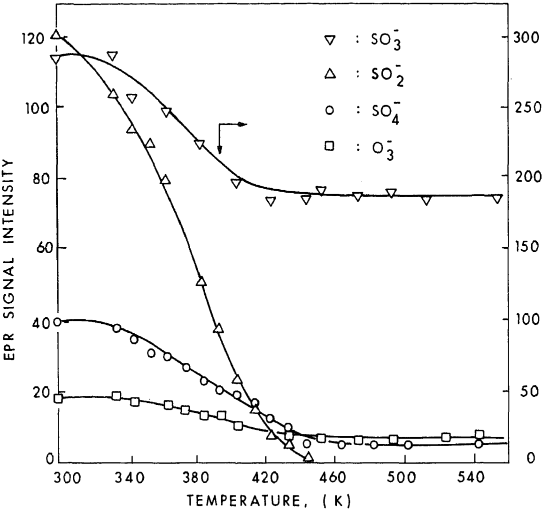

Figure 4. Thermal stabilities of the different radical ions in the 300–600 K range as seen by the intensity of their EPR signals.

On gamma irradiation,

$$SO_4^{2-} \rightarrow SO_4^- + e$$

$$SO_4^{2-} \rightarrow SO_2^- + O_2^-$$

$$UO_6^{6-} + e \rightarrow UO_6^{7-}$$

On heating to 435 K,

$$SO_4^- \rightarrow SO_4^{2-} + \text{hole}$$

$$UO_6^{7-} + \text{hole} \rightarrow UO_6^{6-*}$$

$$UO_6^{6-*} \rightsquigarrow UO_6^{6-} + h\nu^-$$

As shown earlier, spectral studies of the TSL glow suggest that hexavalent uranium centre, UO_6^{6-} acts as the emission centre. On heating to 435 K, the hole released from SO_4^- recombines at UO_6^{7-} site giving UO_6^{6-} emission. The radical ion, SO_2^- ion gets destroyed around 400 K suggesting its possible role in the peak observed around this temperature.

The TSL and EPR investigations of various actinide ions (UO_2^{2+}, ^{237}Np, ^{239}Pu, 241Am) doped $CaSO_4$ and $SrSO_4$ have been reported from our laboratory (6–12). The prominent glow peak around 425–435 K observed in these systems was found to coincide with the temperature at which the EPR signal of SO_4^- radical ion disappears. The average trap depth value for 'hole' detrapping at sulphate site in various actinide doped $CaSO_4/SrSO_4$ lattice was of the order of 0·8 to 0·9 eV (11). The trap depth value (average = 0·85 eV) obtained for the peak at 435 K (table 1) in the present investigation is in agreement with the value reported by us earlier. Thus it can be inferred that this trap depth value is independent of the dopant and also the cations in all the sulphate lattices investigated. This value corresponds to a thermally induced change transfer between SO_4^{2-} and adjacent SO_4^-. This remains mobile until it meets a rexombination/defect centre. In contrast to SO_4^- centre, which was observed in all the sulphates we have studied, SO_2^- is observed only in this system. There are no reported trap depth values for this centre in literature. So it is not possible to arrive at any general understanding of the matrix dependence of SO_2^- stability.

4. Conclusion

As in the case of actinide doped alkaline earth sulphates, the thermal destruction of SO_4^- ion and the associated hole transfer to the dopant ion (UO_6^{7-}) are found to be responsible for the glow peak observed around 435 K. SO_2^- radical ion was observed in this matrix on room temperature irradiation in contrast to $CaSO_4/SrSO_4$ matrices. The thermal destruction of this ion seems to be associated with the first glow peak observed around 400 K.

References

[1] P D Sahare, S V Moharil and B D Bhasin, *J. Phys.* **D22**, 971 (1989)
[2] P D Sahare and S V Moharil, *J. Phys.* **D23**, 567 (1990)
[3] M Ohta, S Asami and M Sakaguchi, *Denki Kagaku* **60**, 643 (1992)
[4] M Ohta, M Sakaguchi and M Sato, *Denki Kagaku* **60**, 881 (1993)
[5] M Ohta, M Sakaguchi and M Sato, *Nippon Kagaku Kaishi* **5**, 635 (1993)
[6] A G I Dalvi, M D Sastry, T K Seshagiri and B D Joshi, *J. Phys.* **C17**, 5865 (1984)
[7] T K Seshagiri, A G I Dalvi and M D Sastry, *J. Phys.* **C21**, 5891 (1988)
[8] V Natarajan, A G I Dalvi and M D Sastry, *J. Phys.* **C21**, 5913 (1988)
[9] Mithlesh Kumar, A G I Dalvi and M D Sastry, *J. Phys.* **C21**, 5923 (1988)
[10] T K Seshagiri, V Natarajan, A G I Dalvi and M D Sastry, *Pramana- J. Phys.* **33**, 685 (1989)
[11] T K Seshagiri, V Natarajan and M D Sastry *Nucl. Tracks, Radiat. Meas.* **21**, 271 (1993)
[12] M D Sastry and A G I Dalvi, in *Hand book on the physics and chemistry of actinides* edited by A J Freeman and C Keller (Elsevier Science Publishers, Amsterdam, 1991), ch. 8, p. 411
[13] H E Swanson, M C Morris and E H Evans, *Natl. Bur. Stand. (U.S.), Monogr.* **25** 7, 39 (1969)
[14] P Kivits and H J L Hagebeuk, *J. Lumin.* **15**, 1 (1977)
[15] N K Porwal, M D Sastry, S V Godbole and A G Page, *Mol. Phys.* **72** 295 (1991)
[16] N Hariharan and J Sobhanadri, *Mol. Phys.* **17**, 507 (1969)
[17] J Kamali and G N Walton, *Radiat. Eff.* **84**, 171 (1985)
[18] M D Sastry, in *Spectroscopic methods in heterogeneous catalysis*, edited by N M Gupta, V B Kartha and R A Rajadhyaksha (Tata McGraw-Hill Publishing Co., New Delhi, 1991), p. 221
[19] K Aiki and K Hukuda, *J. Phys. Soc. Jpn.* **22**, 663 (1967)

PRAMANA
— journal of
physics

© Printed in India

Vol. 44, No. 3,
March 1995
pp. 219–224

Structural, spectroscopic and dielectric properties of KVO_3

N K MISRA, R N P CHOUDHARY* and K L YADAV*
Department of Physics, P.K.H.N. College, Howrah 711 410, India
*Department of Physics, Indian Institute of Technology, Kharagpur 721 302, India

MS received 24 June 1994; revised 3 December 1994

Abstract. Polycrystalline samples of KVO_3, a member of the pyroxene structural family have been synthesised with high-temperature solid-state reaction technique. Preliminary structural and spectroscopic and detailed dielectric properties have been studied in different conditions. No dielectric anomaly or hysteresis loop has been observed in a wide temperature range (30°C to 450°C). Basic structural and spectroscopic (IR and Raman) studies suggest that at room temperature, KVO_3 is centrosymmetric as reported earlier. This and other observations do not support the recent report of ferroelectric phase transition in the compound.

Keywords. X-ray diffraction analysis; Raman and IR spectra; dielectric constant; ferroelectric phase transition.

PACS Nos 77·00; 77·80

1. Introduction

Potassium metavandate KVO_3 is a member of pyroxene structural family with a general formula AMO_3 (A = mono or divalent cations and M = Si, Ge, V or P) which has a wide structural flexibility, distortion, variant and interesting properties [1–6]. For example metavandates (AVO_3) with small alkali cations like Li^+ and Na^+, have monoclinic or clivo pyroxene centrosymmetric structures (space group *C* 2/*c*) and with larger ions like K^+, Rb^+, Cs^+ orthorhombic centrosymmetric (space group Pbcm; D_{2h}^{11}) structures [7]. These centrosymmetric structures at room temperature have been supported by others [8–9] from their spectroscopic (IR and Raman) studies. However, recently ferroelectric phase transition and other related properties in some vandates have been reported [10–12] which is contradictory to all the above previous studies. Further, if reported crystal structures are correct, ferroelectric properties should not be observed. Therefore, it was felt necessary to reinvestigate the structural, dielectric, spectroscopic and thermal properties of AMO_3 family to solve the above contradictory report. In this paper, we report our preliminary structural and spectroscopic, and detailed dielectric properties of the titled compounds.

2. Experimental

Polycrystalline samples of potassium vandate were prepared from K_2CO_3 (99·9% pure) and V_2O_5 (99·99% M/s Sigma Ltd.) by high-temperature solid-state reaction technique. Before weighing, these compounds were dried to remove their moisture contents. The oxides were mixed in a suitable stoichiometry in an agate mortar. After thorough mixing in ball milling, the mixture was calcined at 750°C for 20 h. The calcined material was again mixed to make fine powder of the sample. Finally, powders were cold pressed into pellets at a pressure of about 5×10^6 kg/m^2. These pellets were sintered in a platinum crucible at 500°C for 20 h and then quenched to room temperature (25°C).

At room temperature X-ray diffractogram of the pellet sample were recorded by Rigaku (Miniflex, Japan) X-ray powder diffractometer with CuK$_\alpha$ radiation ($\lambda = 1{\cdot}5418$ Å) in the 2θ range of $10 \leqslant 2\theta \leqslant 35°$ (θ = Bragg angle). The surface morphology, grain shape microstructure and final compositional ratio were studied by the help of 'CAMSCAN' scanning electron microscope (SEM) equipped with energy dispersive X-ray microanalysis (EDX) system.

Measurements of dielectric constant (K) and loss ($\tan \delta$) were carried out by GR-1620 capacitance measuring assembly as a function of temperature (room temperature to 450°C).

Infrared spectra were recorded using KBr pellet in a wide range of wave numbers (200 cm^{-1} to 4000 cm^{-1}) using a Perkin Elmer 598 spectrometer. The Raman spectra were recorded in the frequency range 20 to 4000 cm^{-1} with laser Raman spectrometer (Cary Model 82) consisting of Ar-ion laser and double grating monochromator with photon counting detector. The Raman spectrum was excited with the 541·3 nm line at a power of 200 mW.

3. Results and discussion

The sharp single X-ray profiles of all the reflections of the compound suggest the formation of single phase compound. Using d-values of all the reflection peaks, cell parameters of KVO$_3$ have been determined and refined by least-squares method which were consistent with those of the reported values. These are: $a = 5{\cdot}176$ (1) Å, $b = 10{\cdot}794(1)$ Å and $c = 5{\cdot}780(1)$ Å (estimated errors in parentheses). The calculated d spacing (from refined cell parameters and indexed reflections) are in very good agreement with those observed experimentally (table 1) which suggests the correctness of cell configuration and structures.

Table 1. Comparison of observed and calculated 'd' values (Å) (estimated error 10^{-4} Å) of some reflections of KVO$_3$ at room temperature

hkl	d_{obs}	d_{cal}	I/I_0
020	5·4049	5·3970	23
100	5·1852	5·1760	100
021	3·9171	3·9125	9
120	3·7385	3·7357	26
111	3·6187	3·6060	3
121	3·1210	3·1211	75
002	2·8488	2·9400	23
040	2·6983	2·6985	20
131	2·6212	2·6210	14
200	2·5887	2·5880	94

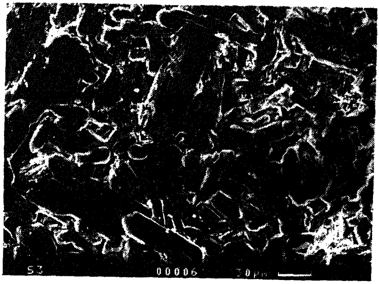

Figure 1. Scanning electron micrographs of KVO$_3$ sintered pellet.

Table 2. Raman and infrared active modes in the KVO$_3$.

Raman		Infrared	
of Raman active mode	Assignment	of I.R. active mode	Assignment
947 940 930 920	$\nu_s(VO_2)$	962 940 923	$\nu_s(VO_2)$
910 637	$\nu_{as}(VO_2)$	892 862	$\nu_{as}(VO_2)$
		680	ν_{as}(V–O–V)
525 497	Combination of ν_s(V–O–V) and ν_{as}(V–O–V)	498	Combination of ν_s(V–O–V) and ν_{as}(V–O–V)

In figure 1 the SEM photograph of KVO$_3$ indicate that particles are not spherical. Elemental analysis from EDX recording has shown that the chemical formula of the prepared compound is very close to that of KVO$_3$.

Detailed and careful spectroscopic analysis of (IR. and Raman) of KVO$_3$ at room temperature has confirmed the reported centrosymmetric group PbCm (D_{2h}^{11}) and configuration of pyroxene structure. In this structure there are two chains per unit cell running parallel to *c*-axis. These chains are held together by *K*-ions. The site symmetry of the chains in the unit cell is C_{2v}. The backbone consists of V$_2$O$_2$, the line group of which is D_{2h}. Details of the correlation scheme and assignments of the band have been discussed elsewhere [2, 3] which are in good agreement with our observed spectral data.

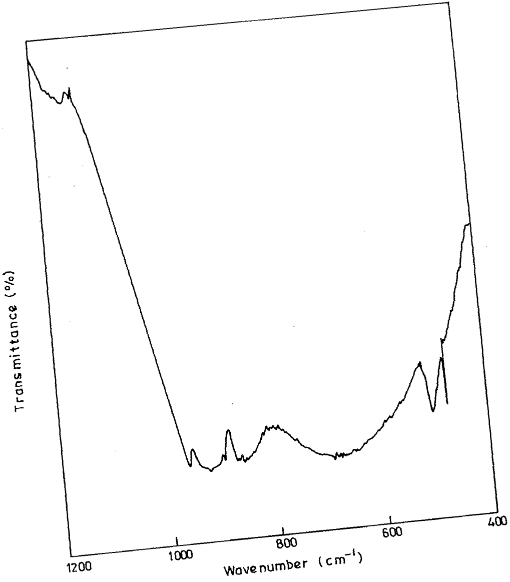

Figure 2. Infrared spectra of KVO_3 at room temperature.

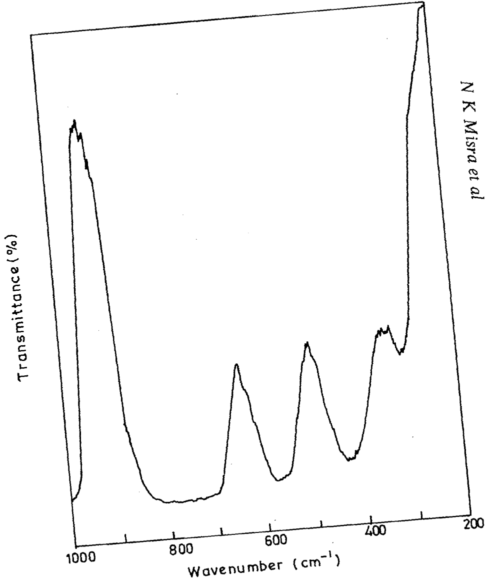

Figure 3. Raman spectra of KVO_3 at room temperature.

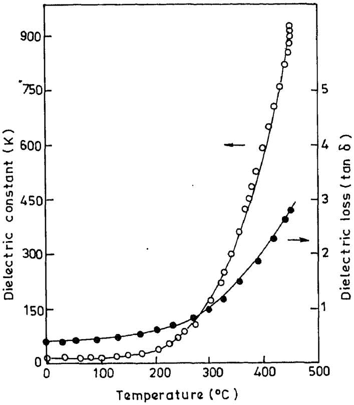

Figure 4. Temperature dependence of dielectric constant and dielectric loss of KVO_3.

As shown in table 2 and figures 2 and 3 there are eight Raman and seven IR bands up to wave number $500\,cm^{-1}$ of which the coupling of C_{2v} with unit cell yield 4 Raman and 3 IR peaks. Others are originated from V_2O_6 chain.

Figure 4 shows the variation of K and tan δ of KVO_3 with temperature at a frequency of 10 kHz. The room temperature K was 15 which remained constant up to 150°C and then increases faster to a value around 900 at 420°C. Within this temperature range no dielectric anomaly was observed. The slow increase at low temperature is due to lattice ionic polarizability and the faster increase in high temperature region is due to space charge polarization. Further no hysteresis loop has been observed at room temperature.

Our results of systematic structural, dielectric, hysteresis loop, spectroscopic studies clearly support the reported centrosymmetric space group.

Acknowledgement

The authors thank the Regional Sophisticated Instrumentation Centre, Indian Institute of Technology, Madras for IR and Raman experiments.

References

[1] B E Warren and W L Bragg, *Z. Kristallogr.* **69**, 168 (1928)
[2] R D Shannon, *Chem. Commun.* **15**, 881 (1971)
[3] R D Shannon and C Clavo, *J. Solid State Chem.* **6**, 538 (1973)
[4] H T Evans and S Block, *Am. Mineral.* **39**, 326 (1954)
[5] M Gaunse, Y Piffard and M Tourncux, *Can. J. Chem.* **52**, 3539 (1924)

[6] O Shinji and Y Ikagaumi, *Inorg. Chem.* **18**, 466 (1979)
[7] F C Hawthorne and C J Clavo, *Solid State Chem.* **22**, 157 (1977)
[8] D M Adams and P A Fletcher, *Spectrochim. Acta* **A44**, 233 (1988)
[9] D Wallde and A M Heyns, *Mater. Res. Bull.* **27**, 129 (1992)
[10] A P Khasid, V V Patil, R Patil and S H Chavan, *Indian J. Pure Appl. Phys.* **29**, 67 (1991)
[11] A P Khasid, V V Patil and S H Chavan, *Indian J. Pure Appl. Phys.* **29**, 64 (1991)
[12] R T Patil, N B Patil, A P Kashid and S H Chavan, *Mater. Res. Bull.* **25**, 57 (1990)

PRAMANA
— journal of
physics

© Printed in India

Vol. 44, No. 3,
March 1995
pp. 225–229

Anomalous variation of thermal lens signal with concentration from rhodamine B in methanol solution

C V BINDHU, S S HARILAL, RIJU C ISSAC, GEETHA K VARIER,
V P N NAMPOORI and C P G VALLABHAN
Laser Division, School of Photonics, Cochin University of Science and Technology, Cochin 682 022, India

MS received 12 September 1994; revised 12 December 1994

Abstract. Thermal lens signals in solutions of rhodamine B laser dye in methanol are measured using the dual beam pump-probe technique. The nature of variations of signal strength with concentration is found to be different for 514 and 488 nm Ar^+ laser excitations. However, both the pump wavelengths produce an oscillatory type variation of thermal lens signal amplitude with the concentration of the dye solution. Probable reasons for this peculiar behaviour (which is absent in the case of fluorescent intensity) are mentioned.

Keywords. Thermal lens; laser dyes.

PACS Nos **42·65; 33·50**

1. Introduction

It is well known that the absorption of electromagnetic radiation by atoms or molecules generates thermal energy in the medium due to nonradiative relaxation of excited states. This deexcitation mechanism has provided the physical basis for the development of thermo-optic spectroscopy which includes photoacoustic spectroscopy [1] and photothermal spectroscopy [2]. In the latter, the change in the values of refractive index due to thermo-optic effect generates a virtual optical element (lens, prism etc.) within the sample, thereby changing the propagation properties of a probe beam. Depending on the experimental configuration, different types of optical effects are produced among which one of the most well known is the thermal lens (TL) phenomenon.

Thermal blooming of laser beam was first observed by Gordon *et al* in 1964 [3]. Absorption of a laser beam followed by nonradiative deexcitation in the sample results in the increase of the temperature of the irradiated region. The temperature distribution of the irradiated region will be the same as the intensity distribution across the beam section which is usually gaussian. Since most liquids have a positive coefficient of thermal expansion, the temperature coefficient of refractive index is negative and consequently thermal lens generated is a divergent one. Another low intensity laser beam can be used to probe the formation of the thermal lens. Thus using a pump-probe method the TL signal can be measured and the data acquired in this manner can throw valuable light regarding the absorption and deexcitation processes taking place in the sample material. In addition to the well-known applications for the estimation of weak optical absorptions [4] the thermal lens technique also allows the measurement of fluorescent quantum yield of dyes [5] and the determination of the quantum yield of photochemical reaction [6]. In the case of samples showing fluorescence emission, thermo-optic effect is highly sensitive to parameters like concentration, pump power and pump-probe configuration. In this paper we report a peculiar concentration dependence of thermal lens effect in the laser dye rhodamine B.

2. Experimental set-up

The experimental set-up (figure 1) used for the present work is that of the dual beam thermal lens technique similar to the one reported previously by Fang and Swofford [7]. The 514 nm excitation from an argon ion laser (Spectra Physics, Model 171) is used as the pump source to generate the thermal lens in the medium. Radiation of wavelength 632·8 nm from a low power intensity stabilized He-Ne laser source (5 mW, Spectra Physics) is used as the probe beam. Absorption coefficient of rhodamine B at 632·8 nm is very small as compared to that at 514 nm and 488 nm and hence the perturbation of refractive index due to the He-Ne probe beam can be neglected. Pump beam is intensity modulated at 7·5 Hz using a mechanical chopper. Solution of rhodamine B in methanol in a quartz cuvette (1·3 cm × 0·7 cm × 3 cm) is kept in the pump beam path. The probe beam is made to pass collinearly through the sample using a dichroic mirror. Spot sizes of both the probe and pump beams are nearly same and are very small as compared to the optical path length of the cuvette and hence paraxial approximation holds good. A filter is placed in the path of the emergent beams which allows only the 632·8 nm wavelength to reach the detector system in which the tip of an optical fibre mounted on a XYZ translator serves as the finite aperture. The fibre is coupled to a monochromator-PMT assembly (which also provides further filtering). The signal output from PMT is processed using a lock-in amplifier (Stanford SR 850).

3. Results and discussion

An accurately weighed amount of rhodamine B is dissolved in methanol to get a concentration of $3{\cdot}45 \times 10^{-3}$ mole/l. From this stock solution, samples with

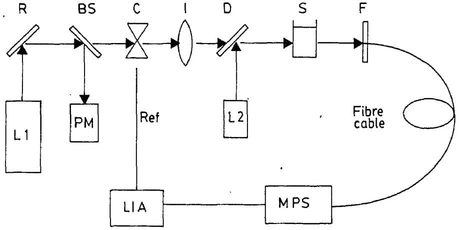

Figure 1. Schematic diagram of the experimental set-up. (L1 – argon ion laser; PM – power meter; C – chopper; l – lens; D – dichroic mirror; S – sample cell; L2 – probe laser; F – filter; BS – beam splitter; R – reflector; LIA – lock-in amplifier; MPS – monochromator-PMT assembly).

different concentrations are prepared. Thermal lens signal strength is measured in the dye solutions at various concentrations ranging from $3{\cdot}45 \times 10^{-3}$ to $8{\cdot}7 \times 10^{-6}$ mole/l. Concentration dependence of thermal lens signal strength is also monitored for different laser powers for 514 and 488 nm excitations from the argon ion laser. Figure 2 shows the variation of thermal lens signal with concentration for different laser powers for 514 nm excitation. This exhibits a type of concentration dependent oscillatory type variation of TL signal strength. With the 514 nm pump wavelength the signal peaks at concentrations of $1{\cdot}16 \times 10^{-3}$ and $4{\cdot}63 \times 10^{-5}$ mole/l. On decreasing the sample concentration from $1{\cdot}16 \times 10^{-3}$ to about $8{\cdot}7 \times 10^{-6}$ mole/l the signal intensity generally decreases. At a concentration of $4{\cdot}63 \times 10^{-5}$ mole/l the signal has a maximum; but on further decreasing the concentration the signal intensity again drops. The depth of this modulation effect is larger at higher laser powers. Concentration dependence of thermal lens signal for 488 nm excitation at various laser powers is shown in figure 3. For the 488 nm excitation the signal strength is small compared to that of 514 nm exciatation at lower laser powers for all concentrations. As the power is increased the signal strength corresponding to 488 nm increases relative to 514 nm. This is an indication of nonlinear optical absorption [8]. At first the signal strength increases up to a concentration of $8{\cdot}7 \times 10^{-4}$ mole/l. The signal intensity slowly decreases in the concentration range $8{\cdot}7 \times 10^{-4}$ to $1{\cdot}16 \times 10^{-3}$ mole/l. On further increasing the sample concentration, the TL signal begins to increase. It may be noted here that this type of peculiar phenomenon is also observed in the case of photoacoustic signal variations in rhodamine 6G solutions [9]. The dependence of the TL signal strength on concentration at powers above 30 mW has not been studied since aberrational effects begin to appear at these power levels.

Concentration dependence of fluorescence which is measured using a front surface geometry does not show (figure 4) the behaviour as observed in TL effect. The reason for this peculiar concentration dependent phenomena is not clear

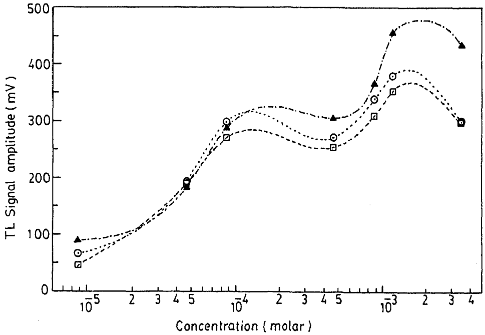

Figure 2. Variation of thermal lens signal strength with concentration at various powers for 514 nm excitation (□ – 15 mW, ○ – 20 mW, ▲ – 25 mW).

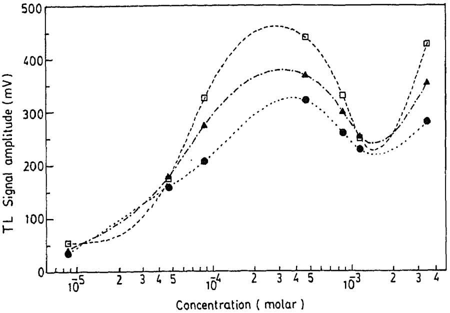

Figure 3. Variation of thermal lens signal strength with concentration at various powers for 488 nm excitation (● – 15 mW, ▲ – 20 mW, □ – 25 mW).

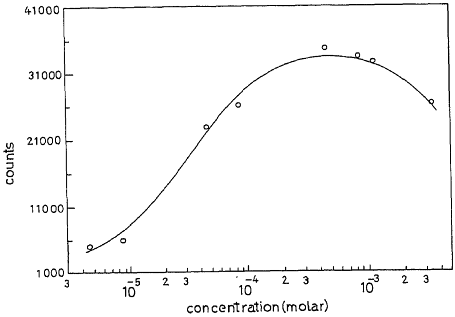

Figure 4. Change in fluorescence intensity with concentration.

at present. It may be attributed to the influence of various complexes formed in the solution at different concentrations and to the probable change in the molecular symmetry of excited states. Usually some deaggregating agents like hexafluoroisopropanol or ammonyx LO are added into the dye solution to reduce the effect of complex formation [10]. In the present case no such deaggregating agents were added and hence we can expect processes like dimerization at higher concentrations. The role of amplified spontaneous emission which has been found to take place within the dye solution both in the longitudinal and transverse directions of the pump beam also becomes important in this context.

Acknowledgements

Authors gratefully acknowledge the financial support from the Department of Science and Technology, India under National Laser Program. The authors (SSH), (CVB) and (GKV) are thankful to CSIR, UGC and Science, Technology and Environment Development (Govt. of Kerala) for their research fellowships.

References

[1] C K N Patel and A C Tam, *Rev. Mod. Phys.* **53**, 517 (1981)
[2] M D Morris and K Peck, *Anal, Chem.* **58**, 811A (1986)
[3] J P Gordon, R C C Leite, R S Porto and J R Whinnery, *J. Appl. Phys.* **36**, 3 (1965)
[4] J P Hanshalter and M D Morris, *Appl. Spectrosc.* **34**, 445 (1991)
[5] J Shen and R P Snook, *Chem Phys. Lett.* **155**, 583 (1989)
[6] K Daree, *Opt. Commun.* **4**, 238 (1971)
[7] H L Fang and R L Swofford, *Ultrasensitive Laser Spectroscopy* edited by D S Kliger (New York, Academic press, 1983)
[8] C V Bindhu, S S Harilal, R C Issac, G K Varier, V P N Nampoori and C P G Vallabhan (to be published)
[9] P Sathy, *Studies on two photon absorptions in certain laser dyes using pulsed photoacoustics and fluorescence techniques*, Cochin University of Science and Technology (1994)
[10] K H Drexhage, in *Dye lasers* edited by F P Schafer (Berlin, Springer, 1973)

PRAMANA
— journal of
physics

© Printed in India

Vol. 44, No. 3,
March 1995
pp. 231–235

Pulsed photoacoustic technique to study nonlinear processes in liquids: Results in toluene

C V BINDHU, S S HARILAL, RIJU C ISSAC, GEETHA K VARIER,
V P N NAMPOORI and C P G VALLABHAN
Laser Division, School of Photonics, Cochin University of Science and Technology,
Cochin 682 022, India

MS received 11 July 1994; revised 12 December 1994

Abstract. Pulsed photoacoustic measurements have been carried out in toluene at 532 nm wavelength using a Q-switched frequency doubled Nd:YAG laser. The variation of photoacoustic signal amplitude with incident laser power indicates that at lower laser powers one photon absorption takes place at this wavelength while a clear two photon absorption occurs in this liquid at higher laser powers. The studies made here demonstrate that pulsed photoacoustic technique is simple and effective for the investigation of multiphoton processes in liquids.

Keywords. Photoacoustics; multiphoton phenomena.

PACS No. 42·62

1. Introduction

The advantages of employing photoacoustic (PA) technique for characterizing various molecular processes have been extensively discussed earlier [1, 2]. The method relies essentially on the study of acoustic waves generated in the sample due to nonradiative transitions following the absorption of light energy. Even though PA approach has become an accepted method to study thermal and optical properties of materials during the last two decades, not much work has been reported in utilizing this effect to investigate multiphoton processes, especially in organic molecules, where efficient nonradiative relaxations $S_n \to S_1$ release a significant amount of thermal energy into the medium.

The identification and analysis of multiphoton absorption (MPA) in nonlinear optical media have been mostly based either on the observation of radiative transitions [3–5] or on the variation in the transmitted beam intensity [6, 7]. However, the latter technique is not very sensitive in all cases especially where variation in transmitted intensity due to MPA is small, while the former is useful only in samples having large fluorescence quantum yield. Measurements of thermo-optic effect is an alternate method to identify MPA in nonlinear media where probability of nonradiative relaxation of excited molecules is large. PA effect is one such thermo-optic phenomenon which can provide useful information regarding the multiphoton processes [8].

Of the several configurations of PA measurements it has been demonstrated that pulsed PA technique [9, 10] is very effective to detect such optical phenomena since one can have sufficient photon density to induce nonlinear effects in the medium and the pulsed PA technique has higher sensitivity as compared to the continuous wave modulation schemes. Because of its high sensitivity, pulsed PA is ideally suited for probing the nonradiative relaxations [11] and the technique has recently been used to study two photon absorption (TPA) process in certain laser dyes [12] as well as in organic vapours [13]. Since organic liquids like toluene are extensively used for various technical applications such as solvents for laser dyes, fullerenes etc., the nonlinear properties of these solvents become a subject of great importance. Considerable interest exists in the study of multiphoton processes in these molecules as it throws much light on the nature of energy levels and other aspects like inter-state coupling and molecular relaxations. Even though TPA in toluene has been reported earlier by several authors, in this communication we demonstrate pulsed PA as an effective and versatile technique to study MPA in liquids.

The pulsed PA signal $q(\nu)$ generated in an absorbing liquid at incident laser frequency ν is given by [14]

$$q(\nu) = AI(\nu)^n \eta(\nu) \tag{1}$$

where $I(\nu)$ is the incident laser power, $\eta(\nu)$ is the quantum yield of the nonradiative transition and n is the number of photons absorbed. The constant A is a function of the cell geometry, acoustic transducer properties and the ultrasonic attenuation in the solution. Equation (1) shows that by monitoring the dependence of PA signal amplitude as a function of laser power, one can identify the occurrence of multiphoton processes if any, in the sample.

2. Experimental set up

The schematic experimental set up is shown in figure 1. The PA cell is made of stainless steel with glass windows for the entry and exit of the laser beam. The acoustic transducer that detects the laser induced PA signals is a lead-zirconate-titanate (PZT) disc of 4 mm thickness and 15 mm diameter, firmly mounted in a stainless steel chamber which is screwed onto the PA cell. The purpose of mounting the PZT cylinder inside the stainless steel casing is to minimize external electrical pick up and to prevent sample contamination by PZT (and vice versa). The diaphragm of the chamber has a thickness of 0·5 mm and it is finely polished. A lead disk followed by a copper disk forms the backing of the PZT which is spring loaded within the chamber. Details of the cell fabrication is given by Sathy *et al* [15].

The second harmonic output beam (532 nm) from a Q-switched pulsed Nd:YAG laser (Quanta-Ray, DCR-11) is focussed using a convex lens (focal length 5 cm) into the PA cell containing spectroscopic grade toluene. The lens position is adjusted so that the beam focus is at the centre of cell which is at a perpendicular distance of

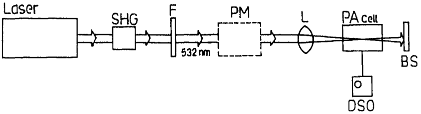

Figure 1. Schematic diagram of the experimental set up. SHG, second harmonic generator; F, harmonic separator; PM, power meter; L, lens; BS, beam stopper; DSO, digital storage oscilloscope.

1·53 cm from the transducer. The spot size at the focal point is measured as 200 μm in diameter. A dichroic filter oriented at 45° to the beam axis separates the fundamental radiation (1064 nm) from the second harmonic. The laser pulse width (FWHM) is ≃ 10 ns and the pulse repetition frequency is 16 Hz. The incident power is monitored using a laser power meter (Scientech model 362) and the transducer output is measured from a digital storage oscilloscope (Iwatsu model DS 8621). The averaged amplitude of the first pulse in the PA signal trace is monitored as a function of the input laser power.

3. Results and discussion

Figure 2 shows the oscilloscope trace of the PA signal produced in toluene. The acoustic signal exhibits a delay of 12 μs with respect to the pump pulse which corresponds to the propagation time of the acoustic signal from the focal region to the piezoelectric detector. This time interval corresponds to the velocity of 1275 m/s which is comparable with the reported value (1300 m/s) of ultrasonic velocity [16] in toluene. From (1) it is clear that TPA process requires a slope two for the log–log plot of PA signal strength against laser power. Figure 3 shows such a plot obtained in the present case. As is clear from figure 3, the slope of log–log plot is nearly unity at low laser power region whereas the slope changes to ≃ 2 at higher laser powers. This shows that at lower laser powers, the optical absorption phenomenon is essentially mediated by one photon process (OPA) while at higher laser powers TPA is favoured.

One photon process in toluene can be explained on the basis of overtone excitation of toluene molecule. CH stretching vibration in toluene has a fundamental frequency (ω_e) at 3100 cm^{-1} with anharmonicity parameter ($\omega_e x_e$) 65 cm^{-1}. The sixth overtone corresponding to $\Delta v = 7$ in toluene lies at 529 nm which is very near to the pump wavelength 532 nm. Thus at lower laser power, excitation of 6th overtone of CH vibration in toluene takes place through OPA resulting into a PA signal which varies linearly with incident laser power.

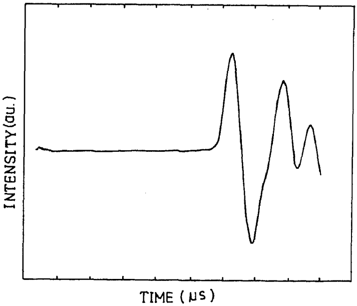

Figure 2. A typical PA signal trace observed on the oscilloscope. The horizontal scale is 2 μs/div.

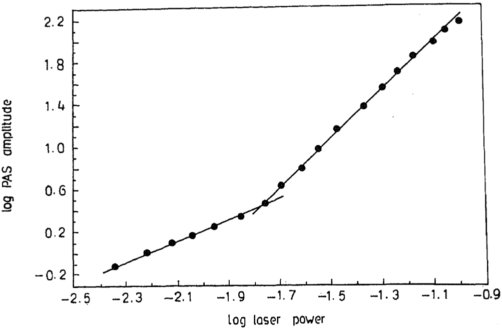

Figure 3. Log laser power plotted against log PA amplitude.

Electronic spectrum of toluene shows a sharp UV band at 274 nm corresponding to $^1A_{1g} - {}^1B_{2u}$ transition which nearly coincides with two photon energy at 532 nm radiation [17]. At higher laser powers, toluene molecules are excited to $^1B_{2u}$ state through TPA. The nonradiative relaxation which follows this process produces the PA signal with characteristic slope two in the log–log plot.

In conclusion we have demonstrated the effectiveness and utility of pulsed PA technique for the study of nonlinear optical processes in liquid medium like toluene. The nature of variation of PA signal amplitude with laser power clearly confirms the occurrence of TPA in toluene at 532 nm. The technique used here is quite suited for experimental investigation of multiphoton processes in liquid media and holds great promise for such studies in many similar organic liquids.

Acknowledgements

Authors are thankful to the Department of Science and Technology, India for financial assistance. The authors (CVB) and (SSH) are grateful to UGC and CSIR for their research fellowships and (GKV) is thankful to Science, Technology and Environment Department for a research fellowship.

References

[1] A C Tam, *Rev. Mod. Phys.* **58**, 381 (1986)
[2] D J Moll, G R Jr Parker and A Kupperman, *J. Chem. Phys.* **80**, 4800 (1984)
[3] N Mikami and M Ito, *Chem. Phys. Lett.* **31**, 472 (1975)
[4] H L B Tang, R J Thrash and U E Luoi, *Chem. Phys. Lett.* **57**, 59 (1978)
[5] C Rulliere and P Kottis, *Chem. Phys. Lett.* **75**, 478 (1980)
[6] A Penzkofer, W Falkenstein and W Kaiser, *Appl. Phys. Lett.* **28**, 319 (1979)
[7] P R Monson and W M Mc Clain, *J. Chem. Phys.* **53**, 29 (1970)
[8] C K N Patel and A C Tam, *Rev. Mod. Phys.* **53**, 517 (1981)
[9] W Lahman and H J Ludwig, *Chem. Phys. Lett.* **45**, 177 (1977)

[10] C K N Patel and A C Tam, *Nature (London)* **280**, 302 (1979)
[11] A C Tam, *Rev. Mod. Phys.* **58**, 381 (1986)
[12] P Sathy, R Philip, V P N Nampoori and C P G Vallabhan, *Opt. Commun.* **74**, 313 (1990)
[13] A V Ravi Kumar, G Padmaja, V P N Nampoori and C P G Vallabhan, *Pramana – J. Phys.* **33**, L621 (1989)
[14] A Rosencwaig, *Photoacoustics and photoacoustic spectroscopy*, (Wiley, New York, 1980)
[15] P Sathy, R Philip, V P N Nampoori and C P G Vallabhan, *J. Phys.* **D27**, 2019 (1994)
[16] E G Richardson, *Ultrasonic Physics*, edited by A E Brown (Elsevile publishing company, New York, 1962)
[17] C N R Rao, *Ultraviolet and visible spectroscopy—chemical applications* (Butterworth and company, London, 1967)

PRAMANA
— journal of
physics

© Printed in India

Vol. 44, No. 3,
March 1995
pp. 237–248

Analysis of mode-locked internally frequency doubled broad-band continuous wave lasers

H K T KUMAR, K APPAJI GOWDA* and K P J REDDY+
Department of Physics, Siddaganga Institute of Technology, Tumkur 572 103, India
*Department of Physics, Bangalore University, Jnana Bharathi Campus, Bangalore 560 056, India
+Department of Aerospace Engineering, Indian Institute of Science, Bangalore 560 012, India

MS received 17 August 1994; revised 25 November 1994

Abstract. Closed-form analysis of pulse evolution in the transient regime in an actively mode-locked internally frequency doubled broad-band continuous wave laser is presented. The analysis enables investigation of the effect of nonlinear crystal inside the laser cavity on mode-locked pulse parameters at the fundamental frequency. It is shown that the presence of internal second harmonic crystal broadens the fundamental mode-locked pulse while accelerating the approach of the system to steady-state. The dependence of pulse parameters on the bandwidth of the tuning element, modulation depth of the active mode-locker and conversion efficiency of the frequency doubler is presented in detailed graphical form.

Keywords. Broad-band lasers; mode locking; Picosecond pulses; frequency-doubling; pulsewidth-band-width product.

PACS Nos 42·55; 42·60; 42·65

1. Introduction

The wide range of applications of wavelength tunable ultrashort light pulses in scientific, medical and industrial research has led to the concentrated efforts towards the development of reliable ultrashort pulse laser sources. Stringent requirements on the stability of laser pulses for these applications have eliminated the usage of conventionally recognised dye laser sources which suffer from photodegradation of the dye solutions. As a consequences tunable broad-band solid state lasers have been recently evolved as alternate sources in the near-infrared and visible region. Among these lasers were the broad-band Ti:Al_2O_3 laser with tunability ranging from 670 to 1100 nm pulses has clearly evolved as an excellent source of ultrashort light pulses for many applications including high resolution spectroscopy [1].

Mode-locking is the chief means of generating ultrashort light pulses from lasers [2]. All the predominant techniques, such as, active [3–5], passive [6], self [7], synchronous [8], additive-pulse [9, 10], resonant passive [11] and coupled-cavity [12] mode-locking, have been employed to generate ultrashort pulses from the broad-band solid state lasers. The shortest pulses of 11 fs duration have been generated in a self-mode-locked Ti: sapphire laser without the help of any additional pulse-compression techniques [13–15].

The operating range of the mode-locked Ti:sapphire laser has been extended into the blue region of 335–550 nm by either intracavity frequency doubling or second harmonic generation outside the laser cavity [16–19].

Although the shortest pulses are obtained from self-mode-locking of broad-band lasers, active mode-locking still holds promise as an important method to generate short pulses with greater stability and tunability from broad-band solid state lasers. The first detailed study of the characteristics of active mode-locking of lasers with broad-band dispersive media, including the effect of band width reducing elements was reported recently [20] based on the theory of active mode-locking developed in [21]. However, the effect of inclusion of SHG crystal inside the broad-band solid state laser cavity is not included in this study, although it is well known that the nonlinear crystal broadens the width of the mode-locked pulse at fundamental wavelength [22–26]. A brief report of the effect of the SHG crystal on the pulsewidth in a mode-locked internally frequency doubled (MLFD) Ti:sapphire laser at steady-state has been reported recently by Reddy [27].

The pulse inside a mode-locked laser builds up from the initial continuous wave oscillations after a lapse of definite time [28–31]. For the design of a laser system it is essential to determine the time interval required to complete the mode-locking process or the time interval required to recover if mode-locked laser is perturbed. The aim of this paper is to present the theoretical analysis of pulse evolution inside an actively mode-locked internally frequency doubled broad-band solid state laser with a special emphasis on Ti:sapphire laser. The pulse evolution dynamics in this system differs from the simple AM mode-locked system studied earlier [28] due to the inclusion of pulse broadening effect by the nonlinear crystal inside the laser cavity. In the case of AM mode-locked system the steady-state is attained when the pulse compression effect of AM modulator is balanced by the pulse broadening due to the bandwidth limiting effect of the laser medium. Whereas in the present system the steady-state is achieved when the pulse compression effect of the modulator is balanced by the combined broadening effects of the laser medium and the nonlinear doubling crystal inside the laser cavity. This may affect the time required for the mode-locked pulse to reach steady-state. The present analysis provides means to compute exact number of round-trips the pulse makes inside the laser cavity to reach steady-state. In addition, the analysis results in an analytic expression for the mode-locked pulsewidth and pulsewidth-bandwidth products in terms of the system parameters, such as, gain bandwidth, tuning element bandwidth and the SHG conversion efficiency of the nonlinear crystal.

2. Analysis

In essence the mode-locked pulse developes from the large number of small pulses present in the initial noise-like emission in the laser cavity. Of many such pulses only one pulse with repetition time defined by the cavity round-trip time survives and undergoes the pulse broadening and compression effects of the elements in each round-trip inside the cavity, ultimately reaching a steady-state. This process of pulse evolution can be analysed by using the self-consistent approach developed by Kuizenga and Siegman [21] for the time-domain description of active mode-locking in solid state lasers. A schematic description of this model is presented in figure 1. As a starting point we assume the existence of an optical pulse inside the laser cavity with an electric field described in the Gaussian form as

$$E(t) = (E_o/2)\exp(-\gamma t^2 + j\omega_p t) \tag{1}$$

where $\gamma = \alpha - j\beta$ is the complex shape factor, ω_p is the centre frequency of the optical pulse and α and β are related to the pulsewidth τ_p and pulsewidth-bandwidth product $\tau_p \Delta f_p$ as

$$\tau_p = [(2 \ln 2)/\alpha]^{1/2} \tag{2}$$

and

$$\tau_p \Delta f_p = (2 \ln 2)/\pi \, [1 + (\beta/\alpha)^2]^{1/2} \tag{3}$$

Thus the parameter α determines the width of the Gaussian pulse in time-domain while the parameter β indicates whether the pulse is chirped or not.

Following the schematic in figure 1, we first consider the passage of the pulse through the amplifier medium. Assuming that the gain medium is homogeneously broadened, the amplitude gain is considered in the Lorentzian form. For operation near the gain peak we can approximate the Lorentzian gain shape with a Gaussian in the form

$$g(\omega) = \exp[g - 4g(\omega - \omega_a)^2/\Delta\omega_a^2] \tag{4}$$

near the line centre (after dropping the phase term). Here g is the saturated round- trip amplitude gain.

Thus, the Gaussian pulse remains Gaussian upon passage through the laser medium with the modified shape parameter

$$\frac{1}{\gamma'} = \frac{1}{\gamma} + \frac{16g}{\Delta\omega_a^2} \tag{5}$$

Hence if the fractional change in γ is small, the net change due to the passage through the amplifier is

$$\Delta\gamma_A = -\frac{16g\gamma^2}{\Delta\omega_a^2} \tag{6}$$

This indicates the broadening of the pulse due to bandwidth narrowing effect of the amplifier.

Next the effect of SHG crystal on the pulse is considered in which it is assumed that the effect of many passes through the crystal is to alter only Gaussian shape parameter and amplitude, while essentially maintaining the Gaussian shape [22]. Thus, the pulse emerging from the crystal after one round-trip will have the field amplitude in the form

$$E'(t) = \left(\frac{E_o}{2}\right) e^{a+\alpha_0} \exp(-\gamma b t^2) \tag{7}$$

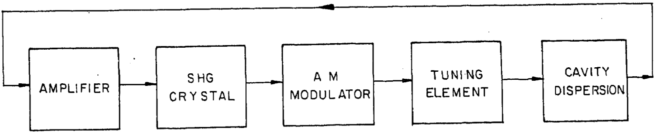

Figure 1. Block diagram of the round-trip model for pulse buildup inside an MLFD laser cavity.

where $a=\sqrt{2}\alpha_s$, $b=1-2\sqrt{2}\alpha_s$, α_s is the average single pass SHG conversion efficiency and α_o is the linear insertion loss of the crystal. Thus the net change in the pulse shape parameter in one round-trip through the doubling crystal is

$$\Delta\gamma_s = -2\sqrt{2}\alpha_s \tag{8}$$

The negative sign in equations (6) and (8) indicate that the passage through the amplifier and the doubling crystal has reduced the magnitude of the shape parameter, which implies broadening of the pulse.

Active mode-locking could be achieved either by an AM or FM modulator inside the laser cavity. The transmission of these modulators can generally by expressed as $\exp[-\delta_g(\omega_m t)^2]$ where $\delta_g = \mp j\delta_c$ for FM modulator and $\delta_g = 2\delta_l$ for the AM modulator, δ_c is the effective single-pass phase retardation of the FM modulator and δ_l is the modulation index of AM modulator [21]. Since both AM and FM active mode-locking process are similar, we consider only AM mode-locking in the present analysis. The pulse shape parameter undergoes a change $\Delta\gamma_{\text{AM}}$ due to a round-trip passage through the AM modulator. This is given by

$$\Delta\gamma_{\text{AM}} = 2\delta_l\omega_m^2 \tag{9}$$

The above equation indicates that the passage of the mode-locked pulse through the AM modulator undergoes an enhancement in the shape parameter leading to the pulse compression.

It is important to note that when the pulse passes through the host media of the amplifier, mode-locker and the frequency doubling crystal, it suffers change due to dispersion effects. These effects are taken into account in the present analysis by considering the transmission function for the bandwidth limiting element such as multiple plate birefringent filter, in the following form [20]

$$\begin{aligned} T(\omega) &= \exp[-j(P|_{\lambda=\lambda_a}\omega/c)]\exp[(j/c)\{\lambda_a^2[\mathrm{d}/\mathrm{d}\lambda(P/\lambda)|_{\lambda=\lambda_a}](\omega-\omega_a)\}] \\ &\quad \times \exp[(-4/\Delta\omega_t^2 - jD/4\pi^2)(\omega-\omega_a)^2] \end{aligned} \tag{10}$$

where P is the round-trip optical path length, c is the speed of light in vacuum, λ_a is the wavelength of light at the gain peak, $\Delta\omega_t$ is the bandwidth of the tuning element, and $D = \left[\frac{\lambda_a^3}{8c^2}\right]\left[\frac{d^2P}{d\lambda^2}\bigg|_{\lambda=\lambda_a}\right]$ represents the round-trip cavity group velocity dispersion.

The operation of this transfer function essentially maintains the Gaussian shape of the mode-locked pulse, while inducing a change in the shape parameter given by

$$\Delta\gamma_{\text{cavity}} = -\left(\frac{16\gamma^2}{\Delta\omega_t^2} + j\frac{4D\gamma}{\pi^2}\right). \tag{11}$$

Thus it can be seen that the bandwidth limiting element enhances the width of the mode-locked pulse while the group velocity dispersion essentially contributes to the chirp of the pulse.

Now we are in a position to estimate the net rate of change in the shape parameter due to a round-trip travel through the cavity elements in an MLFD broad-band laser.

This is achieved by adding Equations (6), (8), (9) and (11), which yields

$$\left(\frac{\Delta\gamma}{\Delta t}\right)=\left[2\delta_l\omega_m^2-2\sqrt{2}\alpha_s\gamma-16\gamma^2\left\{\frac{g}{\Delta\omega_a^2}+\frac{1}{\Delta\omega_t^2}+j\frac{D}{4\pi^2}\right\}\right]\left(\frac{c}{2L}\right)$$

where Δt is the cavity round-trip time interval, and L is the length of the laser resonator.

Assuming the net rate of change of the shape parameter in a single cavity round trip is small, the above equation can be written in the differential form

$$\frac{\mathrm{d}\gamma}{\mathrm{d}t}=\left\{2\delta_l\omega_m^2-2\sqrt{2}\alpha_s-16\left(\frac{g}{\Delta\omega_a^2}+\frac{1}{\Delta\omega_t^2}+j\frac{D}{4\pi}\gamma^2\right)\right\}\left(\frac{c}{2L}\right) \tag{12}$$

where we have replaced $\mathrm{d}\gamma/\mathrm{d}t\equiv\Delta\gamma/\Delta t$, $\Delta t\approx 2L/c$. The slight change in the round-trip time interval due to dispersion effect of the materials inside the laser resonator is neglected.

3. Results and discussion

The evolution of the mode-locked pulse in the transient regime is defined by the first order differential equation (12). However, before solving the equation for transient solution, an estimation of the steady-state pulsewidth can be obtained by assuming very large time parameter. Thus the mode-locking equation yields the solution for γ at steady-state in the form

$$\gamma=\left[16\left(\frac{g}{\Delta\omega^2}+\frac{1}{\Delta\omega_t^2}+j\frac{D}{4\pi^2}\right)\right]^{-1}$$
$$\left\{-\sqrt{2}\alpha_s+\left[\left(\sqrt{2}\alpha_s\right)^2+32\delta_l\omega_m^2\left(\frac{g}{\Delta\omega^2}+\frac{1}{\Delta\omega_t^2}+j\frac{D}{4\pi^2}\right)\right]^{1/2}\right\} \tag{13}$$

where we have assumed $\alpha_s \ll 1$, which is essential to avoid overcoupling of the laser power, and also the pulse spectral width is assumed to be much smaller than the laser linewidth.

This equation is identical to the corresponding equation of Reddy [27] which yields for higher values of SHG conversion efficiency the mode-locked pulsewidth

$$\tau_p=\frac{(\sqrt{2}\ln 2\alpha_s)^{1/2}}{\pi f_m(2\delta_l)^{1/2}}. \tag{14}$$

Hence in the high SHG regime, the mode-locked pulsewidth is independent of the laser gain and the bandwidths of the laser medium and the tuning element while it increases directly with the increase of SHG conversion efficiency.

The steady-state pulsewidth and pulsewidth-bandwidth product are obtained for moderate values of SHG conversion efficiency by separating the real and imaginary parts α and β from (13) which yields

$$\tau_{ps}=(2\ln 2)^{1/2}A^{1/2}\left\{\left(\frac{g}{\Delta\omega_a^2}+\frac{1}{\Delta\omega_t^2}\right)[(r+R)^{1/2}-2\alpha_s]-\left(\frac{D}{4\pi^2}\right)(r-R)^{1/2}\right\}^{1/2} \tag{15}$$

and

$$\tau_{ps}\Delta f_{ps} = (2\ln 2/\pi)$$

$$\left\{1 + \left[\frac{(D/4\pi^2)[(r+R)^{1/2} - 2\alpha_s] - (g/\Delta\omega^2 + 1/\Delta\omega_t^2)(r-R)^{1/2}}{(g/\Delta\omega^2 + 1/\Delta\omega_t^2)[(r+R)^{1/2} - 2\alpha_s] - (D/4\pi^2)(r-R)^{1/2}}\right]^2\right\}^{1/2} \tag{16}$$

where

$$r = (R^2 + I^2)^{1/2},$$

$$R = 2\alpha_s^2 + 32\delta_l\omega_m^2(g/\Delta\omega^2 + 1/\Delta\omega_t^2),$$

$$I = 32\delta_l\omega_m^2(D/4\pi^2)$$

and

$$A = 16\sqrt{2}[(g/\Delta\omega^2 + 1/\Delta\omega_t^2)^2 + (D/4\pi^2)^2].$$

These equations yield the mode-locked pulsewidth and pulsewidth-bandwidth product as functions of the system parameters in an MLFD broad-band laser system at steady-state. These equations can be used to analyse the dependence of pulse parameters on the SHG conversion efficiency, modulation depth and the tuning element bandwidth. However, since the main aim of the present paper is to study the transient evolution of the pulse parameters, we concentrate further discussions on the transient solutions of the mode-locking equation (12), which are in the form

$$\gamma = \gamma_o \tanh[(\sigma + j\Omega)(t + t_o)(c/2L)] - K \tag{17}$$

where

$$\gamma_o = [8\alpha_s^2 + 64\delta_l\omega_m^2(g/\Delta\omega_a^2 + 1/\Delta\omega_t^2 + jD/4\pi^2)]^{1/2}$$
$$[32(g/\Delta\omega_a^2 + 1/\Delta\omega_t^2 + jD/4\pi^2)]^{-1}$$

$$\sigma = \mathrm{Re}[8\alpha_s^2 + 64\delta_l\omega_m^2(g/\Delta\omega_a^2 + 1/\Delta\omega_t^2 + jD/4\pi^2)]^{1/2}$$

$$\Omega = \mathrm{Im}[8\alpha_s^2 + 64\delta_l\omega_m^2(g/\Delta\omega_a^2 + 1/\Delta\omega_t^2 + jD/4\pi^2)]^{1/2}$$

and

$$K = 2\sqrt{2}\alpha_s[16(g/\Delta\omega_a^2 + 1/\Delta\omega_t^2 + jD/4\pi^2)]^{1/2}.$$

Separating real and imaginary parts, equation (17) yields

$$\begin{aligned}\alpha = \{&[(g/\Delta\omega_a^2 + 1/\Delta\omega_t^2)(r+R)^{1/2} + (D/4\pi^2)(r-R)^{1/2}]\sinh(2\sigma M)\\ &- [(g/\Delta\omega_a^2 + 1/\Delta\omega_t^2)(r-R)^{1/2} - (D/4\pi^2)^2(r+R)^{1/2}]\sinh(2\Omega M)\}\\ &[(\cosh(2\sigma M) + \cos(2\Omega M))A]^{-1} - 2\alpha_s(g/\Delta\omega_a^2 + 1/\Delta\omega_t^2)A^{-1}\end{aligned} \tag{18}$$

$$\begin{aligned}\beta = \{&[(g/\Delta\omega_a^2 + 1/\Delta\omega_t^2)(r+R)^{1/2} + (D/4\pi^2)(r-R)^{1/2}]\sin(2\Omega M)\\ &- [(g/\Delta\omega_a^2 + 1/\Delta\omega_t^2)(r-R)^{1/2} - (D/4\pi^2)(r+R)^{1/2}]\sinh(2\sigma M)\}\\ &[(\cosh(2\sigma M) + \cos(2\Omega M))A]^{-1} + 2\alpha_s D/4\pi^2\end{aligned} \tag{19}$$

where $M = (c/2L)(t + t_o)$ is the number of round-trips.

The above equations define the pulsewidth and pulsewidth-bandwidth products of the mode-locked pulse inside an MLFD broad-band laser as a function of number of round-trips inside the laser cavity. For large number of round-trips these equations reduce to the form given in (15) and (16) for steady-state. Also, in absence of SHG the transient regime equations reduce to the form given by Reddy and Tatum [28] for simple active mode-locking case. At steady-state if we assume the case of active mode-locking without frequency doubling, these equations reduce to the form given by Darrow and Jain [20] under the approximations, $g/\Delta\omega_a^2 < 1/\Delta\omega_t^2$ and/or $D/4\pi^2$. Thus the analytical equations (18) and (19) yield the transient solutions for pulsewidth and pulsewidth-bandwidth products which are the most general form of equations to describe the simultaneous mode-locking and internal frequency doubling in broadband laser systems.

For the demonstration of the usefulness of the present theory we apply (18) and (19) to study the pulse evolution in an MLFD Ti:sapphire laser. The system parameters for this laser are given in table 1. The variation of mode-locked pulsewidth as a function of number of cavity round-trips inside the laser cavity is shown in figure 2, for different values of SHG conversion efficiency, and modulation depth of 0·55. In this case we have assumed that the bandwidth limiting element is a two plate briefringent filter. A noticeable feature of the curves in figure 2 is that the pulsewidth approaches steady-state value rather suddenly after few hundred round-trips. For example the steady-state values of 253, 359, 440 and 517 ps, are reached after about 1100, 700, 500 and 400 round-trips for the SHG conversion efficiencies of 0·5, 1·0, 1·5 and 2·0% respectively. This corresponds to the pulse evolution time of 3·66, 2·33, 1·66 and 1·33 μs for a cavity length of 50 cm. Essentially the SHG nonlinear crystal broadens the laser pulse in each transit through the crystal and this broadening effect increases with the increased conversion efficiency. This effect is seen in figure 2, which shows that the steady-state pulsewidth increases with the increase of conversion efficiency of the doubling crystal. One more important effect observed in figure 2 is that the number of cavity round-trips at which the steady-state is approached increases with the decrease of the conversion efficiency. Similar features have been predicted for narrow band solid state lasers [24, 25].

The effect of bandwidth of birefringent tuning element on the pulse evolution time for different SHG conversion efficiencies is shown in figure 3. It is seen that the effect of increasing the bandwidth for a given SHG conversion efficiency is to accelerate the approach of the pulsewidth towards the steady-state. However, the effect of bandwidth variation on the steady-state pulsewidth is negligible.

The variation of the mode-locked pulsewidth with the SHG conversion efficiency is highlighted in figure 4 with modulation depth of the active mode-locking element as

Table 1. System parameters for MLFD Ti:Sapphire laser system.

Parameter	Numerical value
g	0·18
L	0·5 m
Δf_a	197·2 T Hz
Δf_t	56·2 T Hz (Single plate) 13·8 T Hz (Double plate) 3·45 T Hz (Three plate)
D	$[62{\cdot}0 + (18{\cdot}3\,\mathrm{T\,Hz}/\Delta f_t)] \times 10^{-28}\,\mathrm{s}^2$
f_m	160 MHz
δ_l	Variable
α_s	Variable

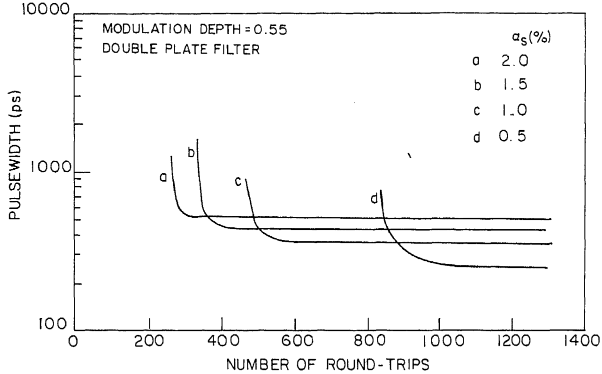

Figure 2. Dependence of the mode-locked pulsewidth on the number of round-trips inside an MLFD laser cavity for different SHG conversion efficiencies.

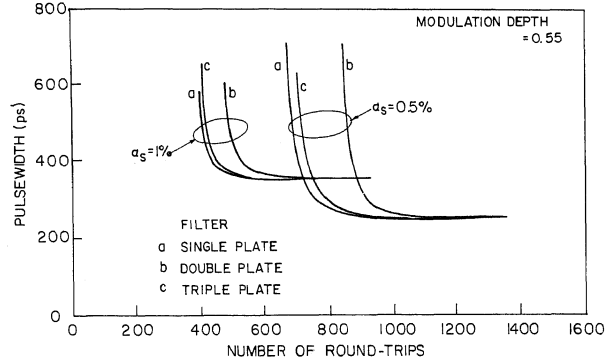

Figure 3. Effect of tuning element bandwidth on the transient evolution of mode-locked pulse inside an MLFD laser cavity.

a parameter. The starting values of all the three curves in this figure are almost identical and correspond to the pure active mode-locking values which were predicted earlier by Reddy and Tatum [28]. As pointed earlier the action of the AM modulator is to compress the pulse while that of the SHG crystal is to broaden the pulse in each transit. Hence it is seen from figure 4 that for a given modulation depth the pulsewidth

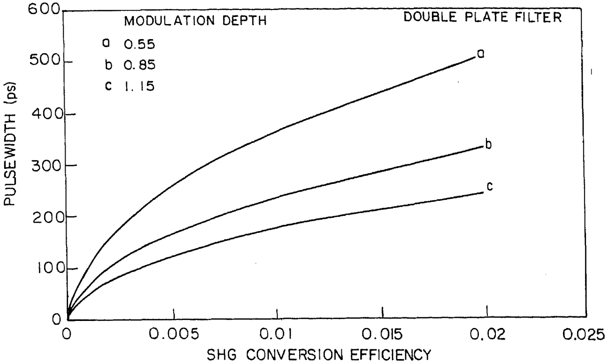

Figure 4. Dependence of the mode-locked pulsewidth at steady-state on the SHG conversion efficiency for different modulation depths of AM mode-locker.

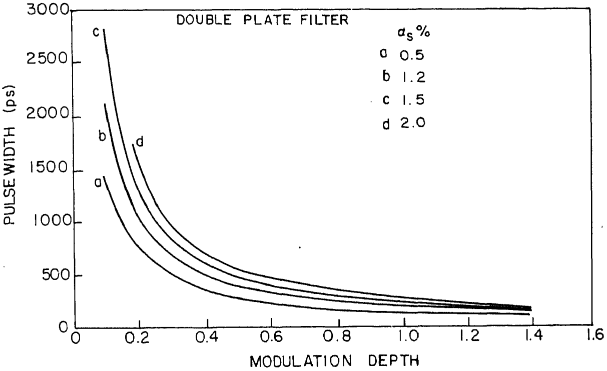

Figure 5. Dependence of the mode-locked pulsewidth at steady-state on the modulation depth of the AM mode-locker for different SHG conversion efficiencies.

increases rapidly with the increase of conversion efficiency and for a given conversion efficiency the pulsewidth decreases with the increase of modulation depth.

The dependence of steady-state pulsewidth on modulation depth of the AM modulator is shown in figure 5 where the curves are plotted for different SHG

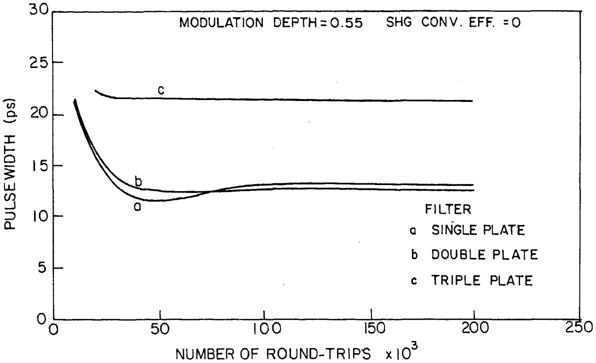

Figure 6. Transient evolution of mode-locked pulsewidth in an AM mode-locked broad-band laser for different bandwidths of the tuning element.

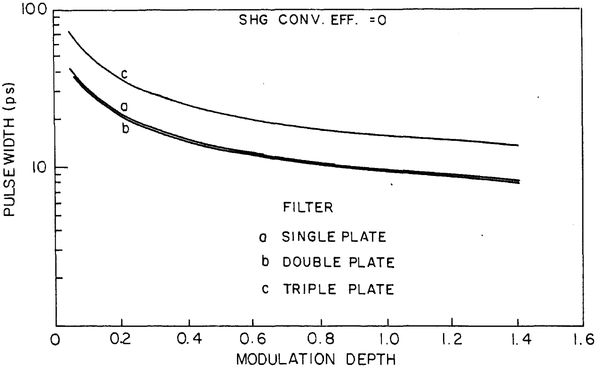

Figure 7. Dependence of steady-state mode-locked pulsewidth on the modulation depth in an AM mode-locked broad-band laser for different bandwidths of the tuning element.

conversion efficiencies. It is seen that the pulsewidth decreases with the increase of the modulation depth and the pulsewidth variation is very sensitive to the changes in the modulation depth for smaller values and becomes insensitive to changes at higher modulation depth. Hence the pulse compression ability of the AM modulator remains nearly constant beyond the modulation depth of ~ 1.

Mode-locked frequency doubled laser

As a final demonstration of the general nature of the present analysis the results of Reddy and Tatum [28] are reproduced from the present analysis assuming zero SHG conversion efficiency. The results are presented in figures 6 and 7. It is seen that the number of round-trips required for the mode-locked pulsewidth to reach steady-state value predicted in the present analysis is of the same order as predicted by Reddy and Tatum [28]. Similarly, the variation of steady-state pulsewidth with the modulation depth for different tuning element bandwidths is identical to the variations shown by Reddy and Tatum [28].

4. Conclusions

Mode-locked broad-band solid state lasers have evolved as reliable sources of picosecond laser pulses in the visible and near infrared regions. The extension of the output wavelength of these lasers to the near ultraviolet region is achieved by frequency doubling. A comprehensive analysis of the mode-locking phenomenon in a mode-locked and internally frequency doubled broad-band laser system is presented here. The analysis enables study of the mode-locked pulse evolution in the transient and steady-state regimes. Pulse evolution studies in the transient regime has shown that the pulsewidth approaches steady-state value within few microseconds. The time taken to reach steady-state increases with the decrease of the second harmonic conversion efficiency. The analysis predicts an order of magnitude increase in the mode-locked pulsewidth due to the inclusion of intracavity second harmonic generator. The dependence of the steady-state pulsewidth on the system parameters is analysed in detail.

Although the results discussed in the present paper include only the width of the mode-locked pulse, the equations given in the paper could be utilized to study the pulsewidth-bandwidth product also. In addition, the present theory can be easily extended for the FM mode-locking in broad-band lasers.

References

[1] C S Adams and A I Ferguson, *Opt. Commun.* **75**, 419 (1990)
[2] J D Simon, *Rev. Sci. Instrum.* **60**, 3597 (1989)
[3] B C Johnson, P F Moulton and A Mooradian, *Opt. Lett.* **10**, 116 (1984)
[4] C P Pinto, C P Yakymyshyn and C R Pollock, *Opt. Lett.* **13**, 383 (1988)
[5] J T Darrow, R K Jain and M Poelker, *Conf. Dig. LEOS*, Wash. DC, OSA paper ME1 (1988)
[6] N Sakura, Y Ishida, H Nakano and Y Yamamoto, *Appl. Phys. Lett.* **56**, 814 (1990)
[7] D E Spence, P N Kean and W Sibbett, *Conf. Dig. LEOS*, Wash. DC, OSA paper PDP10 (1990)
[8] L F Mollenauer, N D Vieira and L Szeto, *Opt. Lett.* **7**, 414 (1982)
[9] P M W French, S M J Kelly and J R Taylor *Opt. Lett.* **15**, 378 (1990)
[10] J Mark, L Y Liu, K L Hall, H A Haus and E P Ippen, *Opt. Lett.* **14**, 48 (1989)
[11] V Keller, W H Knox and H Roskos, *Proc. 7th Int. Conf. Ultrafast Phenom.* edited by C B Harris, E P Ippen, G A Mouron and A H Zewail (Springer-Verlag, Berlin, 1990) 69
[12] L F Mollenauer and R H Stolen, *Opt. Lett.* **9**, 13 (1984)
[13] D E Spence, P N Kean and W Sibbett, *Opt. Lett.* **16**, 42 (1991)
[14] M T Asaki, C P Huang, D Garvey, J Zhou, H C Kapteyn and M M Murnane, *Opt. Lett.* **18**, 977 (1993)
[15] P Curley, C Spielmann, T Brabec, F Krausz, E Wintner and A Schmidt, *Opt. Lett.* **18**, 54 (1993)

[16] C S Adams and A I Ferguson, *Opt. Commun.* **90**, 89 (1992)
[17] V Petrov, D Georgiev and U Stamm, *Appl. Phys. Lett.* **60**, 1550 (1992)
[18] R J Ellingson and C L Tang, *Opt. Lett.* **17**, 343 (1992)
[19] S Backus, M T Asaki, C Shi, H C Kapteyn and M M Murnane, *Opt. Lett.* 19, 399 (1994)
[20] J T Darrow and R K Jain, *IEEE J. Quantum Electron.* **27**, 1048 (1991)
[21] D J Kuizenga and A E Siegman, *IEEE J. Quantum Electron.* **QE-6**, 694 (1970)
[22] J Falk, *IEEE J. Quantum Electron.* **QE-11**, 21 (1975)
[23] M Yamashita, K Yamada and T Sato, *IEEE J. Quantum Electron.* **QE-18**, 95 (1982)
[24] K P J Reddy, *J. Appl. Phys.* **53**, 7076 (1982)
[25] T Damm, U Stamm, K P Stolberg and B Wilhelmi, *Ultrafast phenom. Spectroscopy, Springer Proc. in Phys.* edited by E Klose and B Wilhelmi (Springer, Berlin, 1990) **49**, 23
[26] L R Marshall, A Kaz, A D Hays and R L Burnham, *Opt. Lett.* **17**, 1110 (1992)
[27] K P J Reddy, *J. Appl. Phys.* **74**, 5913 (1993)
[28] K P J Reddy and J A Tatum, *IEEE J. Quantum Electron.* **29**, 1407 (1993)
[29] J Goodberlet, J Wang and J G Fujimoto, *Opt. Lett.* **15**, 1300 (1990)
[30] Y Ishida, N Sarukura and H Nakano, *Conf. Dig. CLEO*, Wash. DC, OSA paper JMB2 (1991)
[31] C L Pan, J C Kuo, K H Wu, J M Shieh, C D Hwang and C S Chang, *Opt. Lett.* **17**, 334 (1992)

PRAMANA
— journal of
physics

© Printed in India

Vol. 44, No. 3,
March 1995
pp. 249–256

Self tapering and uptapering of a self guided laser beam in an absorbing/gain medium with nonlinearity

SARANG MEDHEKAR, S KONAR* and RAJKAMAL
Institute of Computer Science, Electronics and Instrumentation, Devi Ahilya Vishvavidyalaya, Khandwa Road, Indore 452 001, India
*School of Energy Studies, Devi Ahilya Vishvavidyalaya, Khandwa Road, Indore 452 001, India

MS received 19 April 1994; revised 11 October 1994

Abstract. The absorption/gain induced self tapering and uptapering of a self guided Gaussian laser beam when the beam propagates in a saturable nonlinear medium has been discussed. Using the WKBJ and abberationless paraxial ray approximation a beam width equation has been derived. Conditions for tapering/uptapering for both cases i.e., for absorption and gain have been discussed. The beam width of tapered/uptapered beam depends on the rate of absorption/gain, and the length of absorption/gain region along the beam propagation direction. The importance of the present study is pointed out.

Keywords. Self focusing; self tapering; uptapering; saturable nonlinearity; paraxial ray approximation.

PACS No. 42·65

1. Introduction

There has been considerable interest in guiding [1], bending [2, 3] and manipulating light by light without any intermediate structure i.e. lens, mirror or fabricated waveguide. This is achieved through self guided beams in a Kerr nonlinear medium. Recently, Snyder *et al* [4], have pointed out another possibility, i.e. optically controlling the width of a self guided beam. In particular, they have shown that by introducing material gain in a bulk Kerr nonlinear medium, it is possible to taper adiabatically a self guided beam. Moreover, the amount of tapering can be controlled externally by varying the gain through the intensity of the pump beam. Recently, using the theory of steady state self focusing we have generalized Snyder's work in a saturable nonlinear medium [5]. In the present paper we have extended the works of [4, 5]. A significant difference between our results and that of Snyder *et al* [4] is that tapering can be induced not only by gain in the bulk nonlinear medium but also by absorption in the medium; obviously this is possible only in a saturable nonlinear medium. Moreover we have shown that not only tapering but also uptapering can be achieved by introducing gain or absorption in the nonlinear medium.

2. The process

Consider a laser beam of Gaussian intensity distribution along its wave front propagating in a medium with intensity dependent nonlinearity. Along the propagation direction the medium is divided into three regions A, B and C (see figure 1). In regions A and C, the laser beam can propagate without absorption or gain. In region B, the

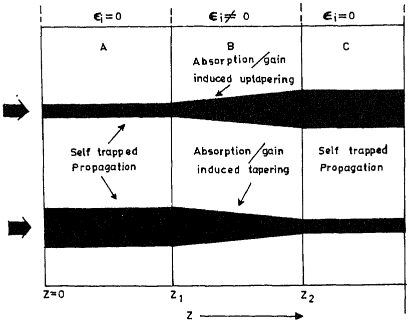

Figure 1. Schematics of tapering uptapering of the laser beams. Beam 1 shows uptapering in region B while beam 2 shows self tapering in region B.

laser beam either lose or grain power as it propagates in this region. If the beam enters region A, as a self trapped mode, and if the gain/absorption in region B is very small, the beam can be tapered/uptapered in this region. Thus in region C the beam will propagate as a self trapped mode. However this is possible only for low gain or absorption. What follows is a brief discussion on how this happens using the theory of self focusing with paraxial ray and Wentzel-Kramers-Brillouin-Jeffreys (WKBJ) approximation.

3. Effective dielectric constant of the medium

Consider the propagation of a Gaussian laser beam along the z-direction in an inhomogeneous absorbing/gain medium with saturating nonlinearity. The initial intensity distribution of the beam at $z = 0$ can be written as

$$EE^*|_{z=0} = E_0^2 \exp(-r^2/r_0^2), \tag{1}$$

where r_0 is the initial beam width and r is the radial co-ordinate of the cylindrical co-ordinate system. As has been shown later the intensity distribution of the beam inside the medium can in general be expressed as [6]

$$EE^* = \frac{E_0^2}{f^2}\exp(-r^2/r_0^2 f^2)\left(\frac{k(0)k^*(0)}{k(f)k^*(f)}\right)^{1/2}\exp\left[i\int\{k(f) - k^*(f)\}\,\mathrm{d}z\right] \tag{2}$$

where f is the dimensionless beam width parameter defined later in (11) and k is the propagation constant defined later in (7).

In the presence of the laser beam the effective dielectric constant of the medium may be written as

$$\varepsilon(EE^*) = \varepsilon_0 + i\varepsilon_i + \phi(EE^*) \tag{3}$$

where ε_0 and $\phi(EE^*)$ are linear and nonlinear part of the dielectric constant respectively, ε_i is a measure of gain or absorption; a positive ε_i signifies amplification, while a negative ε_i is for absorption, and we assume $\varepsilon_i \ll \varepsilon_0$; furthermore $\varepsilon_i = 0$ in regions A and C and $\varepsilon_i \neq 0$ in region B. Typically $\varepsilon_0 \sim 1$ and $\varepsilon_i \sim 10^{-8} - 10^{-10}$ hence, refraction at the interfaces of A and B, and B and C may be ignored. It is known that the simplest intensity dependent dielectrics are Kerr nonlinear medium which do not saturate. However, for any nonlinear medium there exists a maximum change in the intensity dependent dielectric constant. Hence, for saturable nonlinearity ϕ is assumed to be of the form $\phi = \varepsilon_s\{1 - \exp(-\alpha EE^*)\}$, α and ε_s are two positive constants. At this stage we want to make it clear that, another form of saturating nonlinearity, i.e. $\phi(EE^*) = (\alpha\varepsilon_s EE^*)/(1 + \alpha EE^*)$, will give similar results. The qualitative behaviour of these two forms of ϕ with EE^* are same, however they differ in quantitive values [7]. In the paraxial ray approximation one can in general expand ϕ around its value at $r = 0$. In order to do so $\varepsilon(EE^*)$ may be rewritten as

$$\varepsilon(EE^*) = \varepsilon_0 + i\varepsilon_i + \left[\phi\left(\frac{E_0^2}{f^2}\gamma\right) + \phi(EE^*) - \phi\left(\frac{E_0^2}{f^2}\gamma\right)\right] \tag{4}$$

$$\varepsilon(EE^*) = \varepsilon_0'(f) + \psi(r,f) - \varepsilon_2(z)r^2$$

where

$$\varepsilon_0'(f) = \varepsilon_0 + i\varepsilon_i + \phi\left(\frac{E_0^2}{f^2}\gamma\right),$$

$$\psi(r,f) = \left[\phi(EE^*) - \phi\left(\frac{E_0^2}{f^2}\gamma\right)\right] \ll \varepsilon_0'(f)$$

and

$$\gamma = \left[\frac{k(0)k^*(0)}{k(f)k^*(f)}\right]^{1/2} \exp\left[i\int\{k(f) - k^*(f)\}\mathrm{d}z\right]$$

Employing E from (2) in the expression of ϕ and using paraxial ray approximation, ϕ can be expanded by Taylor's expansion as

$$\phi(EE^*) = \phi\left(\frac{E_0^2\gamma}{f^2}\right) - \frac{E_0^2\gamma r^2}{r_0^2 f^4}\phi'\left(\frac{E_0^2\gamma}{f^2}\right)$$

where the prime over ϕ signifies derivative with respect to the argument. Therefore $\varepsilon(EE^*)$ may be rewritten as

$$\varepsilon(EE^*) = \varepsilon_0'(f) - \varepsilon_2' r^2$$

where

$$\varepsilon_2' = \frac{E_0^2\gamma}{r_0^2 f^4}\phi'\left(\frac{E_0^2\gamma}{f^2}\right). \tag{5}$$

4. Theory of self focusing

The wave equation governing the electric vector of the beam in the medium can be written as

$$\nabla^2 E + \frac{\omega^2}{c^2}\varepsilon E = 0 \tag{6}$$

In writing eq. (6) the term $\nabla(\nabla\cdot E)$ has been neglected which is justified when $\frac{c^2}{\omega^2}\left|\frac{\nabla^2 \ln\varepsilon}{\varepsilon}\right| \ll 1$; for the set of parameters of the present paper this inequility is valid. Using WKB approximation and following Akhmanov *et al* [8] and Sodha *et al* [9] one can write

$$E(r,z)=A(r,z)\left(\frac{k(0)k^*(0)}{k(f)k^*(f)}\right)^{1/4}\exp\left\{-i\int k_r\mathrm{d}z\right\} \tag{7}$$

where

$$k(f)=k_r(f)-ik_i(f)=(\omega/c)[\varepsilon_0'(f)]^{1/2},$$

$$k(0)=(\omega/c)[\varepsilon_0'(f=1)]^{1/2}$$

and

$$k_i(f)=(\omega/c)\left[\frac{\varepsilon_i}{2[\varepsilon_0+\phi(EE^*)|_{r=0}]^{1/2}}\right].$$

Substituting for E and ε in (6) one obtains

$$-2ik_r(f)\frac{\partial A}{\partial z}+\frac{\partial^2 A}{\partial r^2}+\frac{1}{r}\frac{\partial A}{\partial r}-k_r^2A-\frac{\omega^2}{c^2}\varepsilon(f)r^2A=0. \tag{8}$$

Putting $A=A_0(r,z)\exp\{-i\int k_r(f)\mathrm{d}S\}$ in (8) and separating real and imaginary parts one obtains

$$2\frac{\partial S}{\partial z}+\left(\frac{\partial S}{\partial r}\right)^2+\frac{\omega^2\varepsilon_2'(f)}{c^2k_r^2(f)}=\frac{1}{k_r^2(f)A_0}\left(\frac{\partial^2 A_0}{\partial r^2}+\frac{1}{r}\frac{\partial A_0}{\partial r}\right) \tag{9}$$

$$\frac{\partial A_0}{\partial z}+\frac{\partial S}{\partial r}\frac{\partial A_0^2}{\partial r}+A_0^2\left(\frac{\partial^2 S}{\partial r^2}+\frac{1}{r}\frac{\partial S}{\partial r}\right)+2k_iA_0^2=0. \tag{10}$$

Solutions of (9) and (10) can be written as [3]

$$\left.\begin{aligned}&S=(r^2/2)\beta(z)+\eta(z)\\&A_0^2=\frac{E_0^2}{f^2}\exp(-r^2/r_0^2f^2)\exp[i\{k(f)-k^*(f)\}\,\mathrm{d}z]\\&\beta(z)=(1/f)(\partial f/\partial z).\end{aligned}\right\} \tag{11}$$

It can be seen from above that β represents the inverse of radius of curvature of the wave front and r_0f is the width of the beam. In geometrical optics approximation $r=r_0f(z)$ represents a ray in a plane containing the z-axis. Substituting for S from (11) in (9) and using the paraxial ray approximation (i.e. $(r/r_0f)^4\ll 1$), equating the coefficients of r^2 in both sides of the resulting equation and substituting for β one obtains

$$\frac{\partial^2 f}{\partial\xi^2}=\frac{\omega^2}{c^2k_r^2(f)f^3}-\frac{\omega^4r_0^2\alpha E_0^2\gamma\varepsilon_3\exp(-\gamma\alpha E_0^2/2f^2)}{2k_r^2(f)c^4f^3} \tag{12}$$

where

$$\xi=\frac{zc}{\omega r_0^2}.$$

The condition for $\frac{\partial^2 f}{\partial \xi^2} = 0$ in regions A and C comes out to be,

$$f^2 = \Omega\alpha E_0^2/2 \log[2c^2/(\omega^2 \Omega\alpha E_0^2 r_0^2 \varepsilon_s) \tag{13}$$

where

$$\Omega = [k(0)k^*(0)/k(f)k^*(f)]^{1/2}.$$

5. Results and discussion

Variation of f with αE_0^2 using (13) is shown in figure 2. For a given f the required power for $\partial^2 f/\partial \xi^2 = 0$ can be easily obtained from figure 2. We divide the curve of figure 2 into two segments in the following way: X is the minimum point of f in figure 2. We draw a verticle line XY passing through X. The portion of the curve lying in the right side of XY is defined as region I and that to the left side is region II. The objective of doing this will be clear soon. We choose $\varepsilon_0 = (1{\cdot}6276)^2$ (corresponds to CS_2), $\varepsilon_s = 0{\cdot}73 \times \varepsilon_0, \omega = 2{\cdot}7 \times 10^{15}$ rad/s, $r_0 = 250\,\mu$m and find out the corresponding values of αE_0^2 from figure 2 for $r_0 = 250\,\mu$m we get two values of αE_0^2 i.e. $\alpha E_0^2 = \alpha E_{01}^2$ and $\alpha E_0^2 = \alpha E_{02}^2$. The first value lies in region II while the second value lies in region I of figure 2. We carry numerical analysis of (12) using $r_0 = 250\,\mu$m, $\alpha E_0^2 = \alpha E_{01}^2 = 38{\cdot}11$, $f = 1$ and $\partial f/\partial \xi = 0|_{\xi=0} = 0$. The variation of f with ξ [using (12)] in the three regions A, B and C is shown in the figure 3 for different values of ε_i. The upper branch

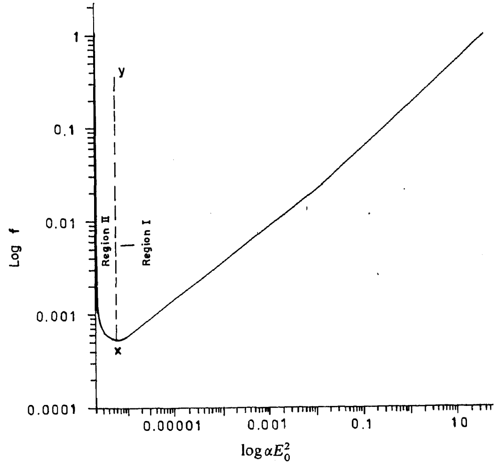

Figure 2. Variation of f with αE_0^2 for $\partial^2 f/\partial \xi^2 = 0$.

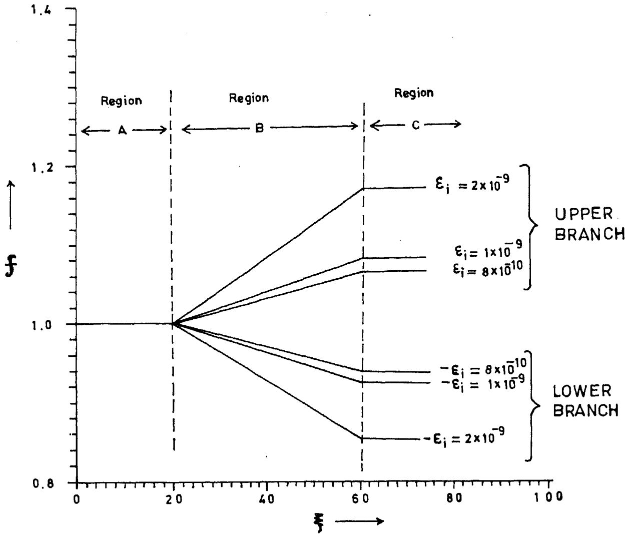

Figure 3. Variation of f with ξ in regions A, B and C. Upper branch shows uptapering by gain (positive ε_i) while lower branch shows tapering by absorption (negative ε_i).

is for gain and lower branch is for absorption. It is clear that in region B the upper branch is uptapered while the lower branch is tapered. In region B, f of the beam changes with ξ which is clear from the figure. Also, because of finite absorption in this region, αE_0^2 changes with ξ. It is interesting to note that though αE_0^2 and f of the beam keep changing in region B, a plot of f and $\alpha E_0^2\gamma$ of region B [calculated from (12)] always coincides the curve in region I of figure 2. Thus in region B, the beam satisfies the condition $\partial^2 f/\partial\xi^2 = 0$, also $\partial f/\partial\xi \sim 0$ for small values of ε_i. This observation suggests that the beam should propagate as a self trapped mode in region C. Curves in region C of figure 3 confirm this. Moreover, the curve in region I of figure 2 suggests uptapering of the beam in case of gain and tapering in case of absorption. Curves in region B of figure 3 also confirm this. For a given length of gain absorption region, radius of the tapered beam increases/decreases with the increase in ε_i. However, for higher values of ε_i tapering/uptapering does not take place and the beam starts oscillating between regions B and C. At this stage it is worth examining the linear behaviour of f with ξ in region B for small values of ε_i. It must be pointed out that tapering/uptapering is a combined effect of variation of electric field intensity due to absorption/amplification (which is almost exponential in nature) and the variation of f (for $\partial^2 f/\partial\xi^2 = 0$) with the electric field intensity. Due to this combined effect, for small values of ε_i, beam tapers/uptapers almost linearly with ξ while for higher values it tapers/uptapers in exponential manner with oscillations superimposed on it.

The behaviour of the beam for higher values of ε_i, is shown in the figure 4 where we have chosen ε_i and the length of B region such that in each case the final tapered/uptapered beam width is almost the same. It is clear from this figure that tapering is possible only for small values of ε_i, as we go on increasing the value of ε_i, the beam deviates more and more from the curve of region I and hence its width starts oscillating in region C. We expect similar behaviour of the beam in region II if we choose the value of αE_0^2 from region II, except that in this region the tapering/uptapering of the beam is induced by gain/absorption in contrast to the absorption/gain in region I, which is obvious because of the fact that in this region the curve in figure 2 has opposite slopes. Also the slope of the curve in region II is much higher than that in region I, hence we expect that a much lower value of ε_i would induce the same amount of tapering/uptapering in region I. Here we want to make it clear that just for numerical appreciation of (12) and (13) we have chosen the parameters of CS_2 but the observations given here are equally useful for any other saturable nonlinear

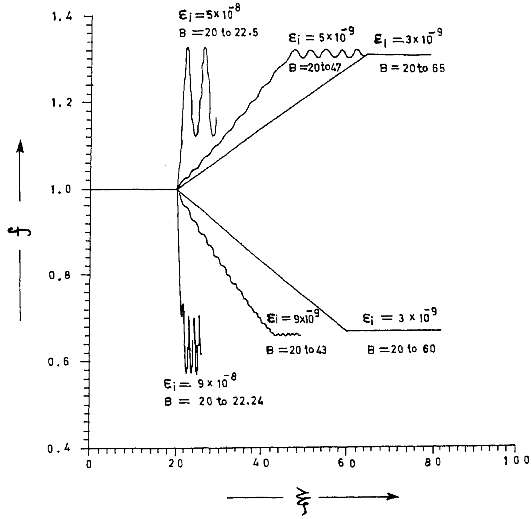

Figure 4. Variation of f with ξ for different length of the B region and different values of ε_i.

medium.

In conclusion, a saturating nonlinear medium with gain or absorption allows for the tapering or uptapering of a self guided beam. If the initial beam is chosen in region I, then we obtain tapering by absorption and uptapering by gain, whereas, if the initial beam is chosen in region II of figure 2, then we obtain tapering by gain and uptapering by absorption. The degree of tapering/uptapering can be controlled by changing the amount of gain or absorption. This phenomena allows us to optically control the width of the self guided beam. The tapered/uptapered beam will induce a tapered/uptapered waveguide, which may be useful in inducing tapered mismatched (linear) couplers [4].

Acknowledgements

This work is supported by OPTEL, Bhopal, India. The authors acknowledge the valuable suggestions of Prof. M S Sodha. They are indebted to Mr Ashutosh Saxena for computational aid and also would like to thank the referee for valuable suggestions.

References

[1] R de la Fuente, A Barthelemy and C Froehly, *Opt. Lett.* **16**, 793 (1991)

[2] J S Aitchison, A M Weiner, Y Silberberg, D E Leaird, M K Oliver, J K Jackel and P W E Smith, *Opt. Lett.* **16**, 15 (1991)

[3] L Poladian, A W Snyder and D J Mitchell, *Opt. Commun.* **84**, (1991)
A W Snyder, L Poladian and D J Mitchell, *Directing one beam of light by another beam*, presented at the fifteenth annual meeting of the Australian Conference on Optical Fiber Technology, Sydney, Australia, December 2–6, 1990
T Thawaites, *New Sci.* **1751**, 14 (1991)

[4] A W Snyder, L Poladian and D J Mitchell, *Opt. Lett.* **17**, 267 (1992)

[5] M S Sodha, S Medhekar, S Konar, A Saxena and Rajkamal, *Opt. Lett.* **19**, 1110 (1994)

[6] S Medhekar, A Saxena and Rajkamal, *Indian J. Pure Appl. Phys.* **31**, 609 (1993)

[7] V E Wood, E D Evans and R P Kenan, *Opt. Commun.* **69**, 156 (1988)

[8] S A Akhmanov, A P Sukhorukov and R V Khokhlov, *Sov. Phys. Usp.* **10**, 609 (1968)

[9] M S Sodha, A K Ghatak and V K Tripathi, *Prog. Opt.* **13**, 169 (1976)

PRAMANA
— journal of
physics

© Printed in India

Vol. 44, No. 3,
March 1995
pp. 257–262

The evolution of the resonant mode in plasma-maser interaction

BIPULJYOTI SAIKIA and S BUJARBARUA
Centre of Plasma Physics, Saptaswahid Path, Dispur, Guwahati 781 006, India

MS received 18 February 1994; revised 16 January 1995

Abstract. We study the evolution of the resonant waves considering its interaction with the nonresonant waves and the plasma particles due to plasma-maser effect. The nonlinear dielectric function of the resonant wave is calculated and is found to consist of two parts: the direct and the polarization coupling terms. On the other hand, the nonlinear dielectric function of the nonresonant wave consists only of the direct coupling term. The significance of our results is discussed.

Keywords. Mode-mode coupling; nonlinear interaction; resonant and nonresonant waves; dielectric function.

PACS No. 52·35

1. Introduction

Since the prediction of the plasma-maser effect [1, 2], also known as the induced Bremsstrahlung radiation, the theory has been applied to expalin numerous radiation phenomena occurring in space [3]. The plasma-maser effect occurs when nonresonant as well as resonant waves are present in a plasma. The resonant waves are those for which the Cherenkov resonance condition ($\omega - \mathbf{k}.v = 0$) is satisfied (in a magnetized plasma we have the cyclotron resonance), while the nonresonant waves are those for which the Cherenkov resonance and the scattering resonance conditions are not satisfied [$(\Omega - \mathbf{K}.v \neq 0)$ and $(\Omega - \omega - (\mathbf{K} - \mathbf{k}).v \neq 0)$]. Here $\omega, \mathbf{k}$ and $\Omega, \mathbf{K}$ are frequencies and wave numbers of the resonant and the nonresonant waves respectively. The most important characteristics of the plasma-maser interaction is its efficiency for up-conversion of wave energy from a turbulent low frequency resonant mode to a high frequency nonresonant mode through resonant interaction with the particles.

In most of the earlier works on the plasma-maser, only the evolution of the nonresonant waves were studied, and the nonlinear dielectric function of the nonresonant modes were derived to obtain growth rate [4, 5]. There are also works which studied the simultaneous effect of the resonant and the nonresonant waves on the particle distribution function [6]. It is demonstrated that in a plasma where energy-momentum sources are available (open system), a test nonresonant mode is highly unstable due to plasma-maser effect; while in a closed system, where there is no energy-momentum sources, the growth due to plasma-maser is exactly equal and opposite to the reverse absorption effect due to nonstationarity of the system [7, 8]. Thus in a closed system the number of nonresonant quanta is conserved. Recently, the energy-momentum conservation and the Manley-Rowe relations were investigated for unmagnetized [9] and magnetized systems [10].

In the present paper, we investigate the evolution of the resonant mode in plasma-maser interaction. We obtain an expression for the nonlinear dielectric function of the resonant mode, and its basic differences with the nonlinear dielectric function of the nonresonant mode is pointed out. We obtain nonlinear dielectric function of the resonant (ion sound) wave in presence of the nonresonant (Langmuir) wave. For simplicity of calculations we assume one dimensional unmagnetized plasma with $k_e > k > K$, where k_e is the electron Debye wave number, and k and K are the respective wave numbers of the resonant and nonresonant modes.

Here we must mention that there are two competing processes which potentially give the same order contribution as that of plasma-maser. The first v one is the nonlinear Landau resonance [11]. The condition is $\Omega \pm \omega = (\mathbf{K} \pm \mathbf{k})\cdot v$. This gives the resonance velocity $v = \omega_{pe}/(K \pm k)$ for $\Omega \sim \omega_{pe} \gg \omega$. Accordingly, for $k_e \gg K$ and $k_e \gg k$, the resonance velocity is much larger than the electron thermal velocity ($v \gg v_e$). The second process is the resonant decay interaction [12]. The relevant conditions are $\Omega(\mathbf{K}) \pm \omega(\mathbf{k}) = \Omega'(\mathbf{K}')$ and $\mathbf{K} \pm \mathbf{k} = \mathbf{K}'$. In addition, to identify the plasma wave as the high frequency mode, we need $\Omega > \omega_{pi}$, where ω_{pi} is the ion plasma frequency. Thus the resonant decay interaction is kinematically possible only when $\omega_{pe} \sim kc_s$ (where c_s is the ion sound velocity). This condition obviously does not coexist with our earlier assumption that $k_e > k > K$. Thus, at least for $k_e > k > K$ considered in this paper, we can rule out the two competing processes: nonlinear Landau resonance and the resonant three wave decay process. Furthermore, both these processes are energy down conversion processes, whereas the plasma-maser is basically an energy up-conversion process.

The paper is organized in the following fashion. In §2, the nonlinear dielectric function of the resonant mode is derived. The growth (damping) rate of the resonant mode is considered and compared with that of nonresonant mode in §3. Section 4 contains a brief discussion of our work and its importance in nonlinear wave-particle interaction.

2. Nonlinear dielectric function

We use the Vlasov-Poisson system of equations to obtain the nonlinear dielectric function of the ion sound mode as,

$$\varepsilon_{\omega,k} = \varepsilon^0_{\omega,k} + \varepsilon^d_{\omega,k} + \varepsilon^p_{\omega,k} \tag{1}$$

where $\varepsilon^0_{\omega,k}$ is the linear part given by,

$$\varepsilon^0_{\omega,k} = 1 + \frac{\omega_{pe}^2}{k}\int \frac{1}{\omega - kv + i0}\frac{\partial}{\partial v} f_{0e}\,\mathrm{d}v + \frac{\omega_{pe}^2}{k}\int \frac{1}{\omega - kv}\frac{\partial}{\partial v} f_{0i}\,\mathrm{d}v. \tag{2}$$

$\varepsilon^d_{\omega,k}$ is the direct nonlinear coupling term given by,

$$\varepsilon^d_{\omega,k} = \frac{\omega_{pe}^2}{k}\left(\frac{e}{m}\right)^2 \sum_{\Omega,K} \left|E_{\Omega,K}\right|^2 \int \frac{1}{\omega - kv + i0}\frac{\partial}{\partial v}\frac{1}{\omega - \Omega - (k-K)v}$$

$$\times \frac{\partial}{\partial v}\left(\frac{1}{\Omega - Kv} + \frac{1}{kv - \omega - i0}\right)\frac{\partial}{\partial v} f_{0e}\,\mathrm{d}v. \tag{3}$$

$\varepsilon^p_{\omega,k}$ is the polarization coupling term,

$$\varepsilon^p_{\omega,k} = -\frac{\omega^2_{pe}}{k}\left(\frac{e}{m}\right)^2 \sum_{\Omega,K} \left|E_{\Omega,K}\right|^2 \frac{1}{(k-K)\varepsilon^0_{\omega-\Omega,k-K}} A \times B \tag{4}$$

where

$$A = \int \frac{1}{\omega - kv + i0}\frac{\partial}{\partial v}\left(\frac{1}{\omega - \Omega - (k-K)v} + \frac{1}{\Omega - Kv}\right)\frac{\partial}{\partial v} f_{0e}\,\mathrm{d}v \tag{5}$$

and

$$B = A(\omega \leftrightarrow \omega - \Omega, k \leftrightarrow k - K, \Omega \leftrightarrow -\Omega, K \leftrightarrow -K). \tag{6}$$

Thus we see that the nonlinear growth (or damping) rate of the resonant waves due to plasma-maser interaction originates from two processes: the direct coupling term and the polarization coupling term, which can be written as,

$$\gamma_{\omega,k} = -\frac{\mathrm{Im}\varepsilon^d_{\omega,k} + \mathrm{Im}\varepsilon^p_{\omega,k}}{\dfrac{\partial}{\partial\omega}\mathrm{Re}\varepsilon^0_{\omega,k}} \tag{7}$$

Here Re and Im show the real and imaginary parts of the respective dielectric function.

It is to be noted here that in a closed system, an additional imaginary part of the dielectric function proportional to $|E_{\omega,k}|^2$ due to nonstationarity of the system is to be taken into account in evaluating the growth (damping) rate of the nonresonant wave. This corresponds to the quasilinear interaction of the particles with the resonant waves. But the nonresonant waves give no contribution proportional to $|E_{\Omega,\mathbf{K}}|^2$ to the quasilinear interaction owing to the assumption $\Omega - \mathbf{K}\cdot v \neq 0$. In case of the nonresonant waves it can be shown that this term is equal and opposite to the imaginary part of the direct nonlinear coupling term of the dielectric function in closed system. However, in this paper we are primarily concerned with the contribution of the polarization coupling term in respect of resonant and nonresonant waves. Further, we assume the system to be open where constant particle distributions are maintained.

3. The growth (damping) rate of the resonant mode

Assuming Maxwellian distribution for unperturbed distribution function, we evaluate the imaginary part of the direct nonlinear term (3) to obtain the damping rate as,

$$\frac{\gamma^d_{\omega,k}}{\omega} = -2\sqrt{\frac{\pi m}{M}}\sum_{\Omega,K} W_L \frac{k}{|k|} \tag{8}$$

where $W_L = |E_{\Omega,K}|^2/4\pi N T$ is the normalized energy of the nonresonant mode. Here we take the real part of the linear dispersion function of the resonant (ion sound) mode as,

$$\mathrm{Re}\,\varepsilon^0_{\omega,k} = 1 + \left(\frac{k_e}{k}\right)^2 - \left(\frac{\omega_{pi}}{\omega}\right)^2 \tag{9}$$

Next, we evaluate the damping rate due to the polarization coupling term (4). From (5) and (6), we obtain,

$$A = -\frac{k}{\Omega^2}\int \frac{1}{\omega - kv + i0}\frac{\partial}{\partial v} f_{0e}\mathrm{d}v \tag{10}$$

and

$$B = -\frac{(k-K)}{\Omega^2}\int \frac{1}{\omega - kv - i0}\frac{\partial}{\partial v} f_{0e}\mathrm{d}v \tag{11}$$

which gives,

$$\mathrm{Im}(A \times B) = 2\sqrt{\frac{\pi m}{M}}\left(\frac{m}{T}\right)^2 \frac{(k-K)}{\Omega^4 |k|}. \tag{12}$$

Thus the damping rate due to the polarization term reduces to,

$$\frac{\gamma^p_{\omega,k}}{\omega} = -\sqrt{\frac{\pi m}{M}}\sum_{\Omega,K} W_L \left(\frac{k_e}{k}\right)^2 \frac{k}{|k|} \tag{13}$$

In evaluating (13), we use

$$\frac{1}{\varepsilon^0_{\omega-\Omega,k-K}} \approx -\left(\frac{k_e}{k}\right)^2.$$

This result is markedly different from the results obtained for nonresonant waves. For nonresonant waves, the imaginary part of the polarization term of the dielectric function vanishes irrespective of the modes of the coupling waves in unmagnetized system [4,5]. Following ref. [4] we obtain the polarization term of the dielectric function for the nonresonant waves as,

$$\varepsilon^p_{\Omega,K} = \frac{\omega^2_{pe}}{K}\left(\frac{e}{m}\right)^2 \sum_{\omega,K} |E_{\omega,k}|^2 \frac{\omega^2_{pe}}{(K-k)\varepsilon^0_{\Omega-\omega,K-k}} C \times D \tag{14}$$

where

$$C = \int \frac{1}{\Omega - Kv}\frac{\partial}{\partial v}\left(\frac{1}{\Omega - \omega - (K-k)v} + \frac{1}{\omega - kv + i0}\right)\frac{\partial}{\partial v} f_{0e}\mathrm{d}v \tag{15}$$

and

$$D = C(\Omega \leftrightarrow \Omega - \omega, K \leftrightarrow K - k, \omega \leftrightarrow -\omega, k \leftrightarrow -k) \tag{16}$$

It is straightforward to show that,

$$C \propto \int \frac{1}{(\Omega - Kv)(\Omega - \omega - (K-k)v)(\omega - kv + i0)}\frac{\partial}{\partial v} f_{0e}\mathrm{d}v$$

$$D \propto \int \frac{1}{(\Omega - \omega - (K-k)v)(\Omega - Kv)(\omega - kv - i0)}\frac{\partial}{\partial v} f_{0e}\mathrm{d}v = -C^* \tag{17}$$

Here * represents the complex conjugate. Thus $\mathrm{Im}[C \times D] = 0$, and accordingly, the imaginary part of the polarization coupling term of the dielectric function of the nonresonant wave for an unmagnetized plasma becomes zero. Thus we see that the polarization term gives non-zero contribution in case of resonant waves for the breaking symmetry of the term (i.e., $B \neq -A^*$).

The growth rate of the nonresonant wave comes only from the direct coupling term, which can be written as [13],

$$\frac{\gamma^d_{\Omega,K}}{\omega_{pe}} = \frac{1}{2}\sqrt{\frac{\pi m}{M}} \sum_{\omega,k} W_S \frac{kK}{k_e^2}. \tag{18}$$

As an illustration, we give a numerical comparison of the growth (damping) rates of the nonresonant and resonant waves in plasma-maser interaction. If we assume $k \sim K$, $k_e/k \sim 10$ and $\omega/\omega_{pe} \sim \sqrt{m/M}$, we obtain from (8) and (13) $|\gamma^d_{\omega,k}| \sim 10^{-3} W_L$ and $|\gamma^p_{\omega,k}| \sim 10^{-2} W_L$, respectively. Taking the nonresonant wave as test wave, we obtain from (18) $\gamma^d_{\Omega,K} \sim 10^{-4} W_S$ and $\gamma^p_{\Omega,K} = 0$. Thus it is clearly seen that the total wave energy $(W_S + W_L)$ decreases due to the absorption of energy by the resonant particles in the plasma-maser instability.

4. Discussion

We have obtained the nonlinear dielectric function and the evolution of the resonant waves considering its interaction with nonresonant waves and particles due to plasma-maser effect. It is found that in contrast to the growth rate of the nonresonant waves, which comes only from the direct nonlinear coupling of the waves, the damping rate of the resonant waves comes from both the direct and the polarization coupling terms. This result is significant, because the question of energy exchange in the plasma-maser interaction is important. Furthermore, the conservation of the energy in plasma-maser interaction [9, 10] indicates an effective energy variation of the resonant mode. It can also be expected that under certain conditions, the plasma-maser can also lead to the increase of energy of the resonant mode. This may occur, for instance, in presence of an external current. In presence of an external current, the unperturbed distribution function can be written as,

$$f_{0e} = \left(\frac{m}{2\pi T}\right)^{1/2} \exp\left[-\frac{m(v - v_0)^2}{2T}\right],$$

where v_0 is the drift velocity of the electrons. Then, under the condition $v_0 > \sqrt{m/M}\, v_e$, the energy of the resonant mode may increase for positive phase velocity of the nonresonant mode $(\Omega/K > 0)$. The physical reason is that the drifting electrons carry some extra free energy from the beginning.

Acknowledgement

The work of BS is supported by the Council of Scientific and Industrial Research, India.

References

[1] M Nambu, *Phys. Rev. Lett.* **34**, 387 (1975)
[2] V N Tsytovich, L Stenflo and H Wilhelmsson, *Phys. Scr.* **11**, 251 (1975)
[3] See, for example, the review paper: M Nambu, *Space Sci. Rev.* **44**, 357 (1986)

[4] M Nambu, S Bujarbarua and S N Sarma, *Phys. Rev.* **A35**, 798 (1987)
[5] B J Saikia, B K Saikia, S Bujarbarua and M Nambu, *Pramana-J. Phys.* **42**, 435 (1994)
[6] V S Krivitskii and S V Vladimirov, *Comm. Plasma Phys. Controlled Fusion* **13**, 219 (1990)
[7] S B Isakov, V S Krivitskii and V N Tsytovich, *Sov. Phys. JETP* **63**, 545 (1986)
[8] B J Saikia and S Bujarbarua, *Phys. Scr.* **51** 277 (1995)
[9] M Nambu and T Hada, *Phys. Fluids* **B5**, 742 (1993)
[10] B J Saikia, M Nambu and S Bujarbarua, *Phys. Plasmas* (communicated, 1995)
[11] A T Lin, P K Kaw and J M Dawson, *Phys. Rev.* **A8**, 2618 (1973)
[12] R C Davidson, in *Methods in nonlinear plasma theory* (Academic, New York, 1972)
[13] M Nambu, *J. Phys. Soc. Jpn.* **53**, 1594 (1984)

PRAMANA
— journal of
physics

© Printed in India

Vol. 44, No. 3,
March 1995
pp. 263–270

Dynamic sheath expansion and ion current in transient ion sheath experiments

S MUKHERJEE, K AVINASH and P I JOHN
Institute for Plasma Research, Bhat, Gandhinagar 382 424, India

MS received 5 December 1994; revised 4 February 1995

Abstract. Experimental results on the measurement of current collected by an electrode immersed in a plasma for a pulsed negative bias are presented. The measured current is compared with a model based on the concept of an expanding capacitor. The scaling laws predicted by the model are verified for the measured current which agree each other. The paper emphasizes the role of displacement current in an expanding ion sheath.

Keywords. Transient sheath evolution; displacement current; dynamic capacitor.

PACS No. 52·40

1. Introduction

Plasma sheaths are rather ubiquitous in laboratory plasmas; occurring under a variety of conditions; e.g. probes [1], dusty plasmas [2], radio frequency (RF) antenna plasma interactions [3], etc. The recent upsurge of interest in the study of transient and equilibrium ion sheaths is motivated by the necessity to understand their role in technological applications. In plasma source ion implantation [4] (PSII) which is relatively new and a non-line of sight technique for surface modification of materials, the sheath physics plays a crucial role. In this technique a large negative potential is applied to the target immersed in a plasma. On a time scale short compared to the inverse of ion plasma frequency (f_{pi}^{-1}) the electrons are repelled away from the electrode exposing stationary ions thus forming on ion matrix sheath. On a larger time scale compared to (f_{pi}^{-1}), the ions are accelerated towards the target while the sheath expands away from the target.

The transient sheath evolution resulting from an instantaneous pulse of negative voltage applied to the electrode has been widely studied in PSII literature. Widner *et al* [5] have found the sheath propagation by experiments and numerical calculations using fluid equations. In the case of mercury arc rectifiers, Chester [6] applied the Child–Langmuir law quasi-statically to describe the sheath expansion. Liberman [7] and Scheurer *et al* [8] have developed analytical models for instantaneous pulse application. Stewart *et al* [9] have extended the model analytically to cases with finite rise time of the pulse. The basic assumption in all these models is that the conduction current is continuous across the sheath, i.e. the charge uncovered by the expanding sheath is equal to the implantation current. Recently Wood [10] has reexamined this assumption on the basis of numerical simulation. He has shown that in an expanding sheath the displacement current due to changing electric field is significant. The presence of finite displacement current in PSII experiments has also been noticed. The general conclusion seems that in the rising part of the pulse the contribution from the displacement current is substantial.

In this paper we report an experimental study to ascertain the role of displacement current in the sheath expansion. In the experiment a large negative bias is applied to a disc electrode immersed in a uniform plasma and the attention is focussed on the flat top phase of the pulse where the applied voltage is constant. The total current collected by the electrode is recorded as a function of time. The results are explained in terms of a model where the expanding sheath is regarded as a variable capacitor. Our results show that even during the flat top phase of the pulse the contribution of the displacement current is substantial and it reduces the total current to the electrode. Apart from this we have also explored the parameter space in order to verify the various scaling laws relating the electrode current to the plasma density and peak voltage.

2. Experimental set up and measurement techniques

The experimental set up [figure 1] consists of a stainless steel cylindrical chamber of length 120 cm and diameter 50 cm and is pumped down to $1{\cdot}0 \times 10^{-5}$ torr by using a combination of rotary and diffusion pumps. Argon gas is filled is the chamber to a pressure of $1{\cdot}0 \times 10^{-4}$ torr. Filaments located at the ends of the chamber are heated to give thermionic electrons. The electrons are accelerated into the chamber where they impact ionize the argon atoms to produce a plasma. Langmuir probe measurements show, that the plasma produced has densities in the range of 10^{8-9} per cc and T_e of 2 eV. In the centre of the chamber a disc of diameter 20 cm and thickness 1 mm is kept on which a pulsed negative bias is applied. The bias applied on the disc has a rise time of 50 to 70 ns depending on the amplitude of the bias applied. Thereafter the bias is maintained at its peak value for 3 μs and is made to go to zero in 2 μs.

The pulse described above is made by discharging a charged coaxial cable into its characteristic impedance [11]. Between the disc electrode and the characteristic impedance (50Ω) a $0{\cdot}1\,\mu$F capacitor is kept so that the disc is initially floating. A Pearson current transformer is kept in between the capacitor and disc to measure the current. The capacitor also ensures that there is no dc current through the current transformer [figure 2]. The peak voltages are varied from 350 V to 5 kV.

In figure 3 we show the general nature of the applied bias and the current as measured by the current transformer. In the subsequent figures the time $t = 0$ ns corresponds to the time when the voltage has reached its peak. Figures 4 and 5 are the typical nature of the experimental current measured as function of time in the flat top phase of the pulse, and it decreases monotonically as a function of time.

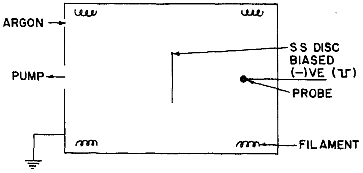

Figure 1. Experimental set up.

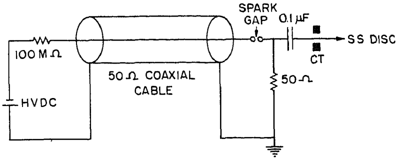

Figure 2. Pulse forming network, CT is the Pearson current transformer.

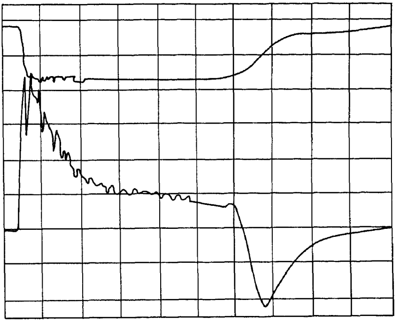

Figure 3. A typical oscilloscope trace for the applied bias (top) and the corresponding current through current transformer (bias). Top trace has y-axis 2000 V/div and x-axis 500 ns/div. Bottom trace has y-axis 100 mA/div and x-axis 500 ns/div. Plasma density $6{\cdot}26 \times 10^8$ per cc. Note the current behaviour in the flat top of the applied bias. The model predicts the current in this portion.

3. Model and comparison with experimental data

The results can be understood in terms of a simple model which represents the sheath as dynamic capacitor. We consider a planar, one dimensional model where at a time $t = 0^+$ a voltage pulse of $V = -V_0$ is applied on the planar electrode. The electrons respond instantaneously and are driven away. The exposed ions form an ion matrix sheath. On a longer time scale the ions move towards the electrode while the sheath expands in the other direction to supply the extra ions. We assume,

a) the ions while going through the sheath does not undergo any collisions.
b) the transit time of ions through the sheath is much faster than the rate of sheath expansion.
c) at each instant of time the current flow in the sheath satisfies Child's law
d) the applied bias is much larger than T_e.

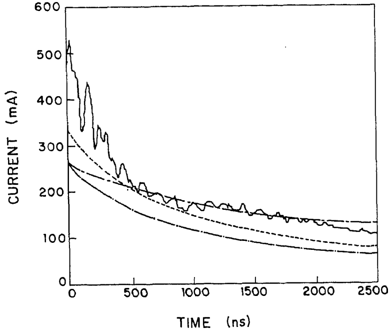

Figure 4. Comparison between the current obtained in (i) experiment (——) (ii) the model [Eq. (7)] (—·—) (iii) conduction current [Eq. (2)] (——·——) (iv) model [Eq. (7)] and contribution from the emitted secondary electrons (----). Applied bias is 3010 V and plasma density is 9·4 × 10^8/cc.

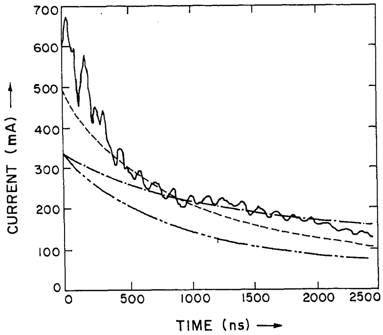

Figure 5. Comparison between the current obtained in (i) experiment (——) (ii) the model [Eq. (7)] (—··—) (iii) conduction current [Eq. (2)] (——·——) (iv) model [Eq. (7)] and contribution from the emitted secondary electrons (-----). Applied bias is 4900 V and plasma density is 9·4 × 10^8/cc.

The first assumption allows the ions to impinge on the electrode with the energy corresponding to the entire potential difference existing between the electrode and the dynamic sheath plasma interface. The third assumption is a consequence of the second assumption being valid. The fourth assumption neglects the effect of the electron dynamics on the transient sheath properties.

Dynamic sheath expansion

We first neglect the displacement current and calculate the electrode current with the assumption that the conduction current is continuous across the sheath. This requires that the Child's law current density is equal to the charge crossing the sheath boundary per unit time, i.e.,

$$[(4/9)\varepsilon_0(2e/M)^{1/2}V^{3/2}]/x^2 = en(\mathrm{d}x/\mathrm{d}t + u_0) \tag{1}$$

where x is the sheath position, M is the ion mass, n is the number density while u_0 is the speed with which the ions enter. Following Wood and Liberman we assume that since the sheath thickness is much small compared to the final equilibrium sheath, the term u_0 is small compared to $\mathrm{d}x/\mathrm{d}t$ and hence can be neglected. The resulting equation can be solved for $x(t)$, with the following boundary condition,

$$x(0) = (2\varepsilon_0 V_0/ne)^{1/2},$$

where $x(0)$ is the ion matrix sheath thickness. The value of $x(0)$ when substituted in (1) gives the conduction current as

$$I = (2/9)A(2e/M)^{1/2}en V^{1/2}/(1 + (2/3)w_{pi}t)^{2/3} \tag{2}$$

where A is the area of the electrode. In figures 4 and 5 we plot $I(t)$ obtained from (2). Initially it is smaller than the experimental $I(t)$ while at later times it is in excess. This clearly shows the inadequacy of the assumption of the continuity of the conduction current across the sheath. This also indicates, that if the pulse duration is increased more, keeping the applied bias as constant, the difference between the experimental current and the current predicted by (2) would also increase.

In an expanding sheath the electric field changes with time (even when the applied voltage is constant, because the sheath plasma interface penetrates in the plasma starting from the ion matrix sheath thickness) and the effect of the resultant displacement current must be taken into account. This implies that we must assume the continuity of the total current (conduction current + displacement current) rather than that of the conduction current alone. As shown by Wood this can be elegantly done by considering the sheath as a variable capacitor with varying thickness. Wood has considered the effect when the voltage at the electrode is a function of time ($\mathrm{d}V/\mathrm{d}t \neq 0$), and found the expression for the current. But his general prescription (Eq. (9) of Ref. 10) is valid as long as the net charge (Q) in the dynamic sheath is a function of time. The total charge collected by the electrode is $Q = CV$ so that the total electrode-current at constant voltage is,

$$I = \mathrm{d}Q/\mathrm{d}t = C\mathrm{d}V/\mathrm{d}t + V\mathrm{d}C/\mathrm{d}t = V\mathrm{d}C/\mathrm{d}t. \tag{3}$$

The capacitance of the sheath is greater than that of the vaccum capacitor with same parameters, because of space charge effect. This problem has been considered in detail by Bull [12] who has shown that space charge limited capacitance is roughly twice the value of the vacuum capacitance. We assume that the result holds for an expanding sheath as well, so that,

$$C = \frac{2\varepsilon_0 A}{x}. \tag{4}$$

Then

$$I = -\frac{2\varepsilon_0 A V}{x^2}(\mathrm{d}x/\mathrm{d}t). \tag{5}$$

The sheath expansion velocity is given by,

$$\frac{\mathrm{d}x}{\mathrm{d}t} = \frac{4}{9}\varepsilon_0\left(\frac{2e}{M}\right)^{1/2}\frac{V_0^{3/2}}{enx^2}. \tag{6}$$

Substituting (6) in (5) we have,

$$I = [(2/9)A(2e/M)^{1/2}en V^{1/2}]/(1 + (2/3)w_{pi}t)^{4/3}. \tag{7}$$

In figures 4 and 5, $I(t)$ obtained from (7) is also plotted as a function of time. It can be seen that the current obtained from (7) is smaller than that obtained from (2). This is clear because of the contribution of the displacement current. From figures 4 and 5 we see that in this case the general agreement with the experimental current, as far as the shape is considered, is better. There is a consistent residual difference. This residual difference is because of a number of factors not included in our model. These factors will be discussed at the end.

To find the validity of the scaling laws that is predicted from the model, we assume that the measured current has $I \propto V^b$ for constant t and n. The value of b is obtained by curve fitting techniques and is tabulated in table 1. The experimental data used to find b is at a time $t = 2000$ ns). From the table it is seen that the value of b is around 0·5 which agrees with the model. To see the scaling with density for constant bias and time we again assume that $I \propto n^c$. A dependence like this is valid when the denominator in our model is close to unity. The experimental data used to find c is at a time $t = 50$ ns. The value of c is obtained by curve fitting techniques and is tabulated in table 2. The value of c is closer to 1 indicating the validity of the scaling laws predicted by our model.

4. Discussion

To summarize we have experimentally measured the electrode current as a function of time during the flat top of the voltage pulse. It is also shown that even during this phase the contributions from the displacement current in the sheath are significant.

Table 1. Tabulated values of b for various plasma densities, where $I_{\text{experiment}} \propto (\text{bias})^b$; $t = 2000$ ns; the model predicts $b = 0{\cdot}5$.

Density (10^8/cc)	Value of b
1·56	0·63
3·13	0·58
4·69	0·55
6·26	0·53
7·83	0·55
9·38	0·52

Table 2. Tabulated values of c for various applied bias, where $I_{\text{experiment}} \propto (\text{density})^c$; $t = 50\,\text{ns}$, model predicts $c = 1$ when denominator in (7) is unity.

Bias (V)	Value of c
380	1·078
1130	1·088
2130	1·095
3010	1·236
4900	1·275

Following Wood the results are interpreted in terms of a variable capacitor model which elegantly takes into account the effect of displacement current.

The experimental conditions satisfy the requirements of the model. The applied pulse has a rise time of the 50 to 70 ns which is much faster than the inverse of ion plasma frequency. Thus the concept of initial formation of the ion matrix sheath is valid. The current generated by the expansion of the ion matrix sheath during this rise time is not computed in the present work, as it has been dealt already in [10]. Secondly, the model assumes that the sheath starts developing from the ion matrix sheath thickness, and this assumption is satisfied when the pulse reaches its flat top. The model cannot be extrapolated to the limits of $t = 0$ and $t = \infty$. The second limit gives the current for the equilibrium sheath. Thus our model is valid in the limit when the sheath is expanding. Wood has also shown that in about 3 to 4 ion plasma periods, equilibrium flow of ions is established. The experiment is stopped before that so that the assumptions made in the model does not break down.

We now comment on the factors which are responsible for the residual difference between experimental and theoretical current. One of the reasons is the secondary electron emission from the disc, giving an additional current which is to be added to the current predicted by the model (Eq. (7)). It has been proved experimentally [13], that the current generated by the secondary electrons can be substantial and it is necessary to add this current to the current generated by the sheath motion. Thus the net current to the electrode increases by a factor of 1·1 to 1·4 [14] to that predicted by the model depending on the bias voltage. In figures 4 and 5 we also plot the total current as a function of time, where total current is a sum of current generated by (7) and contribution from secondary electron emitted from the electrode. The total current thus obtained, is in better agreement with the experimental current. If the contribution of the secondary electrons is added to the conduction current, then it is obvious that the resultant current will be much larger than the measured current.

The other source of error in the model can be the assumption made regarding the expansion of the sheath. It is assumed, that the sheath expands with sheath plasma interface parallel to the disc. Expansion in any other direction is neglected. This assumption may not be true at later times of the evolution. If the sheath expands in other directions more ions will be exposed to the sheath electric field and the net current will increase. It has been shown by Malik *et al* [15] that the sheath formed by a disc takes a spherical shape. Hence the current created by the two dimensional expansion of the sheath, can add to the total current and make even better agreement with the experiment.

Apart from this there are a few prominent peaks seen in the initial part of the measured current. These peaks are initially large and gradually decrease in amplitude with time. The model which is presented does not explain this observation. A recent simulation by Calder *et al* [16], where a negative bias is applied on an electrode immersed in a plasma, the current collected also shows oscillatory behaviour. The simulation indicates, that the electrons which are displaced by the negative bias overshoot their dynamic equilibrium position and then oscillate about this position. As the sheath expands the centre of oscillation also shifts with it. As the sheath thickness approaches its equilibrium value, the oscillations damp in amplitude. This picture can qualitatively explain the peaks observed in the experimental current. When the sheath expands, the sheath edge is not uniquely defined because of the presence of these oscillations at the sheath edge. Hence the sheath thickness also oscillates, though its mean value is always increasing. As the current to the electrode is defined by (3), the current also oscillates because the oscillating sheath edge changes the sheath capacitance. The shifting of the mean position defines the sheath expansion which gives rise to the current which the model tries to explain. On top of this current is a small oscillatory current created by the sheath edge oscillation. A detailed study of the problem is in progress.

Acknowledgement

The authors are grateful to the referee for critical evaluation of the paper and for important suggestions.

References

[1] N Hershkowitz in *Plasma diagnostics – discharge parameters and chemistry* edited by O Auciello and D L Flamm (Academic Press, New York, 1989) Vol. 1, p. 113

[2] T J Sommerer, M S Barnes, J H Keller, M C McCaughey and M J Kushner, *Appl. Phys. Lett.* **59**, 638 (1991)

[3] M J Mayberg, R I Pinster, C C Petty, M Porkolab, S C Chiu, W P Cory and R Prater, *Nucl. Fusion,* **33**, 267 (1993)

[4] M Shamim, J T Scheuer and John R Conrad, *J. Appl. Phys.* **69** 2904 (1991)

[5] M Widner, I Alexeff, W D Jones and K E Longreen, *Phys. Fluids.* **13**, 1245 (1969)

[6] J K Chester, *J. Sci. Tech.* **37**, 2 (1970)

[7] M A Liberman, *J. Appl. Phys.* **66**, 2926 (1989)

[8] J T Scheuer, M Shamim and J R Conrad, *J. Appl. Phys.* **67**, 1241 (1990)

[9] R A Stewart and M A Liberman, *J. Appl. Phys.* **70**, 3481 (1991)

[10] Blake P Wood, *J. Appl. Phys.* **73**, 4770 (1993)

[11] F B A Frungel, *High speed pulse technology,* (Academic Press, New York, 1965) Vol. 1

[12] C S Bull, *Proc. of the Institution of Electrical Engineers,* **B104**, 374 (1957)

[13] M M Shamim, J T Scheuer, R P Fetherson and J R Conrad, *J. Appl. Phys.* **70**, 4756 (1991)

[14] S C Brown, *Basic data of plasma physics,* (MIT Press, Cambridge, 1967)

[15] S M Malik, R P Fetherson, K Sridharan, and J R Conrad, *Plasma Sources Sci. Technol.* **2**, 81 (1993)

[16] A C Calder, G W Hulbert and J G Laframboise, *Phys. Fluids.* **B5**, 674 (1993)

PRAMANA
— journal of
physics

© Printed in India

Vol. 44, No. 3,
March 1995
pp. 271–277

Static structure factor of electrons around a heavy positively charged impurity in a one-component quantum rare plasma

S P TEWARI and HIRA JOSHI
Department of Physics and Astrophysics, University of Delhi, Delhi 110 007, India

MS received 26 December 1994

Abstract. An expression for the static structure factor, $g^{+-}(r)$, of electrons at a distance r from an infinitely heavy positively charged particle in a one component quantum rare plasma has been obtained in linear response theory using an appropriate quantum dielectric function of the rare plasma. The expression is a complicated function of the electron plasma frequency, Debye screening length and r, but reduces to that of classical plasma when quantum corrections are neglected. For $r < r_s$ ($2r_s$ being the mean distance between two electrons), the temperature dependent $g^{+-}(r)$ has larger values in quantum case in comparison to that in classical situation and keeps increasing with decrease in r, more so at low temperatures when de-Broglie wavelength becomes larger and a considerable fraction of r_s.

Keywords. Static structure factor; charged impurity; one component quantum rare plasma.

PACS Nos 71·45; 73·20; 72·30

1. Introduction

An expression for the static structure factor of electrons around a massive positively charged particle, such as a proton or an heavy ion in a one component classical rare plasma which one encounters in semiconductors, ionosphere and intergalactic space to name a few examples, has been derived taking into account nonlinear effects [1]. The expression is dependent upon certain distance r_0, the distance of closest approach of electrons to the impurity, which is to be judiciously chosen. Since $r_0 \gg \lambda_{\text{th}}$ (thermal de Broglie wavelength of electrons), no quantum correction is needed. However, if the electrons build up close to the impurity, that is $r \sim \lambda_{\text{th}}$, is to be studied one would have to use an appropriate quantum dielectric function. In the present communication we report the results of such an investigation of static structure factor of electrons around a heavy positively charged impurity in one component quantum rare plasma in the linear response theory.

2. Mathematical formalism

The expression for the static structure factor is given as

$$g^{+-}(r) = 1 + \frac{1}{(2\pi)^3}\int \nu^{\pm}(\bar{q})\exp(-i\bar{q}\cdot\bar{r})\overline{\mathrm{d}q}. \tag{1}$$

When the density of positive charge introduced in the system is small then $\nu^{\pm}(q)$ [2] is given by

$$\nu^{\pm}(\bar{q}) = -\frac{Z}{n^{-}}\mathrm{Re}\left(\frac{1}{\varepsilon^{--}[\bar{q},(\hbar q^2/2m)]} - 1\right) + \frac{z}{n^{-}}\frac{2}{\pi}\int_0^{\infty} \mathrm{d}\omega\, \mathrm{Im}\left(\frac{1}{\varepsilon^{--}(\bar{q},\omega)}\right) P\left[\frac{\hbar q^2/2M}{\omega^2-(\hbar q^2/2M)^2}\right], \tag{2}$$

where $\varepsilon^{--}(q,\omega)$ is the dielectric function of the plasma, z is an integer, n^{-} is the number density of electrons of the system, $\omega, \bar{q}$ are the angular frequency and wave-vector respectively and M is the mass of positively charged impurity.

Since, we are considering $M=\infty$, $\nu^{\pm}(q)$ reduces to

$$\nu^{\pm}(\bar{q}) = -\frac{z}{n^{-}}\mathrm{Re}\left[\frac{1}{\varepsilon^{--}(\bar{q},0)} - 1\right]. \tag{3}$$

Using the quantum two particle distribution function in one component rare plasma assembly having Maxwellian momentum distribution funtion, the expression for quantum dielectric function at zero frequency [3, 4] is given as

$$\varepsilon_q(0) = 1 + \frac{1}{q^2 d^2}\left[\frac{z'+g(z')}{z'+1}\right], \tag{4}$$

$$z' = q\lambda_{\mathrm{th}}/2,$$

where

$$g(Z') = \exp(-z')^2 \int_0^1 \exp(z'^2x^2)\mathrm{d}x, \tag{5}$$

and

$$d^2 = V^2/\omega_p^2(z'+1).$$

Substituting $\sqrt{\alpha}x = iu$ in (5) and integrating [5] we get

$$g(z') = \exp(-z')^2\left[1 - \frac{(\sqrt{\alpha}/i)^2}{3} + \frac{(\sqrt{\alpha}/i)^4}{10} - + \dots\right] \tag{6}$$

which in the case of $z'^2 < 1$ reduces to

$$g(z') = 1 - \frac{2}{3}z'^2 - \frac{7}{30}z'^4 - \dots \tag{7}$$

Using (7) in (4) we get

$$\varepsilon_q(0) = \left[1 + \frac{\omega_p^2}{q^2\,V^2} + \frac{1}{2\sqrt{2}}\frac{h\omega_p}{k_{\mathrm{B}}\,T}\frac{\omega_p}{qV} + \frac{1}{24}\left(\frac{h\omega_p}{k_{\mathrm{B}}\,T}\right)^2 + \dots\right], \tag{8}$$

where h is Planck's constant; $\omega_p(=(4\pi n^{-}e^2/m)^{1/2})$ is the angular plasma frequency, e and m_e are the charge and mass of electrons respectively; $V(=(k_B\,T/m)^{1/2})$ is the thermal velocity of electron, k_{B} is the Boltzmann's constant and T is the temperature of the plasma.

When $h \to 0$ (8) reduces to the well-known classical expression for $\varepsilon_q(0)$ [1, 4–8],

$$\varepsilon_q(0) = 1 + \frac{\omega_p^2}{q^2\,V^2}. \tag{9}$$

Equation (8) represents the quantum mechanical dielectric function of the plasma in which contributions up to h^2 have been taken into account. One can go to higher order terms in h using further terms in (8).

It may be pointed out here, that these quantum corrections appear only because the rare plasma has become mildly degenerate so that consideration of Fermi-Dirac statistics which appear when the plasma becomes strongly degenerate, is not required. That is, one continues to use the Maxwellian distribution function with modified linear momenta only.

We can write down $\varepsilon_q(0)$ given by (8) in the following alternate form

$$\varepsilon_q(0) = D + \frac{c}{q} + \frac{a^2}{q^2}, \tag{10}$$

where

$$a^2 = \frac{\omega_p^2}{V^2} = \frac{1}{\lambda_{\mathrm{D}}^2};\ \lambda_{\mathrm{D}} \text{ is the Debye screening length,}$$

$$c = a^2 \lambda_{\mathrm{th}}/2 = a\mu/2,\ \lambda_{\mathrm{th}} = \frac{h}{(2mk_{\mathrm{B}}\,T)^{1/2}},$$

$$D = 1 - \frac{1}{6}\mu^2 \text{ and } \mu = \lambda_{\mathrm{th}}/\lambda_{\mathrm{D}}.$$

Substituting (10) in (3) we get for

$$v^{\pm}(q) = \frac{z}{n^-}\left[\frac{a^2 + (\mu q/2)(a - \frac{1}{3}\mu q)}{a^2 + q^2 + (\mu q/2)(a - \frac{1}{3}\mu q)}\right]. \tag{11}$$

Using $v^{\pm}(q)$ given above in (1), performing θ and ϕ integrations and some mathematical manipulations we get an expression for the static structure factor as

$$g^{+-}(r) - 1 = \frac{z}{2\pi^2 r n^-}\left[a^2 \frac{\mathrm{d}}{\mathrm{d}r}\int_0^\infty \frac{(-\cos qr)\mathrm{d}q}{a^2 + q^2 + (\mu q/2)(a - \frac{1}{3}\mu q)}\right.$$

$$+ \frac{a\mu}{2}\frac{\mathrm{d}^2}{\mathrm{d}r^2}\int_0^\infty \frac{(-\sin qr)\mathrm{d}q}{a^2 + q^2 + (\mu q/2)(a - \frac{1}{3}\mu q)}$$

$$\left. - \frac{1}{6}\mu^2 \frac{\mathrm{d}^3}{\mathrm{d}r^3}\int_0^\infty \frac{\cos qr\,\mathrm{d}q}{a^2 + q^2 + (\mu q/2)(a - \frac{1}{3}\mu q)}\right]. \tag{12}$$

After decomposing the various terms in partial fractions, integrations can be performed and finally taking the appropriate spatial derivatives of various terms one gets an expression for $g^{+-}(r)$ as

$$\begin{aligned} g^{+-}(r)-1 = -\frac{z}{n^{-}}\frac{6-\mu^2}{3\pi^2 a\sqrt{3{\cdot}\bar{6}\mu^2-16}} \times \\ \Big\{ e^{ir\alpha}\Big[a^2 A+\frac{a\mu}{2}B+\frac{1}{6}\mu^2 C\Big] \\ + e^{-ir\alpha}\Big[a^2 A^*+\frac{a\mu}{2}B^*+\frac{1}{6}\mu^2 C^*\Big] \\ + e^{ir\beta}\Big[a^2 E+\frac{a\mu}{2}F+\frac{1}{6}\mu^2 G\Big] \\ + e^{-ir\beta}\Big[a^2 E^*+\frac{a\mu}{2}F^*+\frac{1}{6}\mu^2 G^*\Big]\Big\} \end{aligned} \tag{13}$$

where

$$A=\Big[-\frac{1}{2r^2}-\frac{\alpha^2}{4}+(0{\cdot}423i-1{\cdot}57)\frac{\alpha}{2r}+\frac{ri\alpha^3}{24}+0{\cdot}0069r^2\alpha^4+\dots\Big],$$

$$B=\Big[-\frac{i}{2r^3}-\frac{\alpha}{r^2}+(0{\cdot}923i-1{\cdot}57)\frac{\alpha^2}{2r}-\frac{\alpha^3}{6}+\frac{r\alpha^4 i}{48}+\dots\Big],$$

$$C=\Big[-\frac{1}{r^4}+\frac{3\alpha i}{2r^3}+\frac{3\alpha^2}{2r^2}+(1{\cdot}57-i1{\cdot}256)\frac{\alpha^3}{2r}+\frac{0{\cdot}25}{2}\alpha^4+\dots\Big],$$

$$E=\Big[\frac{1}{2r^2}+\frac{\beta^2}{4}+\frac{\beta}{2r}(1{\cdot}57-0{\cdot}423i)-\frac{r\beta^3 i}{24}-0{\cdot}0069r^2\beta^4+\dots\Big],$$

$$F=\Big[\frac{i}{2r^3}+\frac{\beta}{r^2}+(1{\cdot}57-0{\cdot}923i)\frac{\beta^2}{2r}+\frac{1}{6}\beta^3-\frac{r\beta^4 i}{48}+\dots\Big],$$

$$G=\Big[\frac{1}{r^4}-\frac{3\beta i}{2r^3}-\frac{3}{2}\frac{\beta^2}{r^2}+(-1{\cdot}57+1{\cdot}256i)\frac{\beta^3}{2r}-0{\cdot}125\beta^4+\dots\Big],$$

$$A^*=[A]^*,\ B^*=[B]^*,\ C^*=[C]^*$$

$$E^*=[E]^*,\ F^*=[F]^*,\ G^*=[G]^*$$

with

$$\alpha=-\frac{a\mu}{4-0{\cdot}\bar{6}\mu^2}+\frac{a}{4-0{\cdot}\bar{6}\mu^2}(3{\cdot}\bar{6}\mu^2-16)^{1/2}$$

and

$$\beta=\frac{-a\mu}{4-0{\cdot}\bar{6}\mu^2}-\frac{a}{4-0{\cdot}\bar{6}\mu^2}(3{\cdot}\bar{6}\mu^2-16)^{1/2}.$$

3. Results and discussion

When $h=0$, $\mu=0$, the roots of the quadratic equations occurring in the denominators of (12) get simplified and the expression for $g^{+-}(r)$ reduces to the well-known classical expression of $g^{+-}(r)$ [1] i.e.

$$g^{+-}(r) = 1 + \frac{z}{n^-}\frac{a^2}{4\pi}\frac{e^{-ra}}{r}. \tag{14}$$

As is evident, the expression (13) for the distribution of electrons around a heavy positively charged impurity is quite complicated when one considers quantum corrections to the classical dielectric function up to h^2. When $h = 0$, it reduces to the simple classical expression given by (14). Equation (13) exhibits that the static structure factor in the present case is dependent, in a quite involved way, on the temperature, plasma frequency of the electrons and the distance r from the impurity. Equation (13) can be grouped into three types of terms: (i) independent of μ (ii) proportional to μ and (iii) dependent on μ^2. In each group there is a complicated dependence on r. However, one can observe that for a given temperature and electron density, as $r \to 0$, $g^{+-}(r)$ increases quite sharply.

We have also made computations on $g^{+-}(r)$ for a plasma having the electron density $n^- = 10^{15}\,\mathrm{cm}^{-3}$ and different temperatures 1200, 300, 60 and 30 K when $z = 1$, $n^- \lambda_{\mathrm{th}}^3 \ll 1$ in each of the cases, implying small degeneracy. The results of the calculation, omitting the terms of the form e^{ra} which lead to unphysical sharp build up of electrons for large r, have been shown in figure 1. Y-axis represents the ratio R, of $g^{+-}(r)_Q$ (the calculations using (13)) and $g^{+-}(r)_{\mathrm{cl}}$ (the calculations based on (14)) i.e. $R = g^{+-}(r)_Q / q^{+-}(r)_{\mathrm{cl}}$, while the X-axis represents r, the distance from the impurity in terms of r_s (r_s in this case $\sim 620\,\text{Å}$). As r is decreased and approaches zero, the ratio R, increases first slowly and then somewhat sharply for very small r. For r nearly equal to r_s, R is nearly equal to one for temperatures greater than 60 K implying thereby that no quantum corrections are needed for $r > r_s$. Further, the quantum corrections as one would expect become increasingly important for $r < r_s$ but the degree of their contribution is significantly dependent on the temperature. For example, as is clear from the figure for $r = 0{\cdot}25 r_s$, say, the value of R is equal to 1·25, 1·45 and 2·40 for $T = 1200$, 300 and 60 K respectively. This is what is expected because as we decrease temperature while λ_{th} increases, λ_D decreases resulting in somewhat large increase in μ. For r still smaller, the quantum correction for high temperatures becomes first comparable and then larger than the classical values implying thereby that when electrons are close to impurity, quantum nature of plasma plays a dominant role in the determination of their distribution around the impurity. In the figure we have also shown calculations for $T = 30$ K ($n^- \lambda_{\mathrm{th}}^3 \simeq 0{\cdot}014$). In this case the ratio R does not approach the value one even at $r = 2r_s$ as is shown in the inset (1a) of the figure.

If one neglects h^2 dependent terms and calculates the ratio, R, one finds that for $T = 1200$ K there is hardly any change in the ratio for all r from the one shown in figure 1. However, as the temperature is decreased, h^2 terms contribute. For example when $T = 60$ K, the ratio R with the neglect of h^2 terms, is shown in figure 1b by solid line and on comparison with figure 1, one finds that the contribution of h^2 is quite large for $r < 0{\cdot}3 r_s$. For $T = 30$ K, the contribution of h^2 is still more significant as can be seen by comparing the plots of R, as given in the inset (1b) with that given in the main figure. In the inset (1b), R does not take into account h^2 terms.

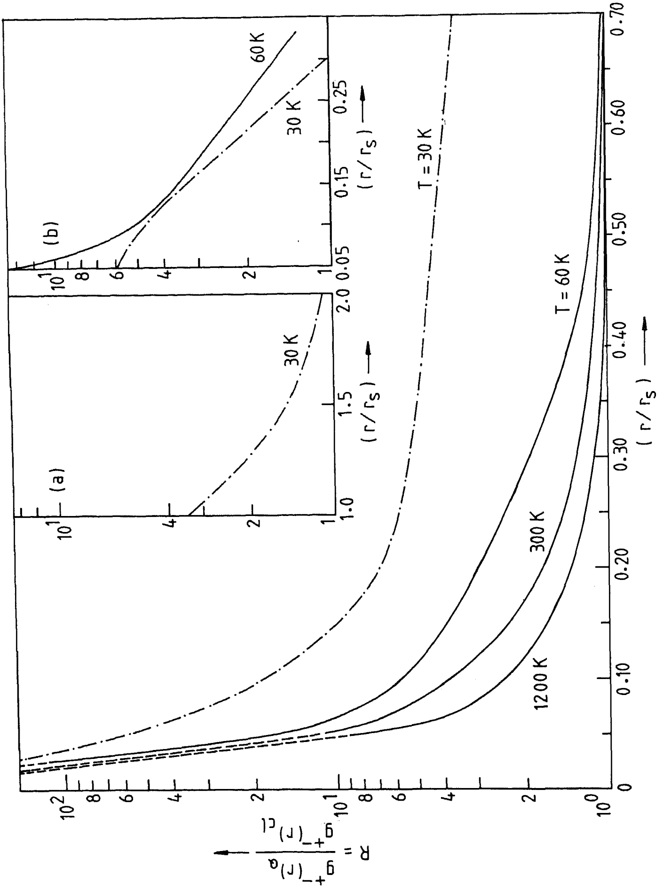

Figure 1. The variation of the temperature dependent ratio R of the quantum mechanical static structure factor, $g^{+-}(r)_Q$, of electrons around a massive positively charged impurity to the classical static structure factor, $g^{+-}(r)_{\mathrm{cl}}$, in one component quantum rare plasma with distance r from the impurity expressed in units of r_s, at 1200, 300, 60 and 30 K when the density of electrons = $10^{15}\ \mathrm{cm}^{-3}$. In inset (a) is shown the variation of R at 30 K for $1{\cdot}0 < r/r_s < 2{\cdot}0$.

In inset (b) are shown the variation of R at 60 and 30 K when the terms having μ^2 as cofactor in the expression of $g^+(r)_Q$ have not been taken into account.

4. Conclusions

From our study we conclude that the derived expression of the static structure factor for the electrons around a massive positively charged impurity in a rare plasma taking into account the quantum corrections is quite different from the one given the classical approach. The quantum corrections become increasingly important for distances close to the impurity and at low temperatures when the thermal de Broglie wavelength of electrons becomes a significant fraction of the mean interelectron distance and μ acquires a finite non negligible value.

The results of our work can be checked by performing suitable scattering experiment from a doped semiconductor kept at an appropriate temperature. Explicit values of $g^{\pm}(r)$ for a one component weakly degenerate plasma which can be easily obtained in a doped semiconductor, have been reported in the preceding discussion in order to check these values experimentally. Scattering of low energy photons (0 to 40 μm) from such a plasma have been performed and reported [9]. Our study may also be useful to assess plasma density in intergalactic space by observing the build up of mobile light mass charge carriers of the plasma around a heavy charged impurity.

References

[1] B Biswas and S P Tewari, *J. Phys.* **C12**, L273 (1979).
[2] A Sjolander and M J Stott, *Phys. Rev.* **B5**, 2109 (1972)
[3] B A Trubnikov and V F Elesin, *Sov. Phys. JETP* **20**, 866 (1965)
[4] S P Tewari and H Joshi, *Phys. Lett.* **A173**, 160 (1993)
[5] I S Grandshyteyn and I W Rhyzik, *Tables of Integrals, Series and Products* (Academic Press, New York and London, 1965) Fourth Edn. p. 1058
[6] B Biswas and S P Tewari, *J. Phys.* **C16**, 901 (1983)
[7] S P Tewari and P K Yadav, *Phys. Lett.* **A58**, 347 (1976)
[8] L Landau, *J. Phys.* **10**, 25 (1946)
[9] W G Spitzer and H Y Fan, *Phys. Rev.* **106**, 882 (1957)

Corrigendum

New answer to the solar neutrino problem

MARC DIXMIER

(*Pramana – J. Phys.*, **43**, pp. 453–465, December 1994)

p. 453, line 9 of § 1: of earth should read: on earth

p. 454, line 11: [10, 11a] should read [10, 11, 11a]

p. 463, second line before formula (A1): l'_{ν_e} should read l_{ν_e}

p. 464, second line after formula (A2): the expression slowing-down should be between quotation marks (since only the energy of the particles is altered in the interaction, not their velocity, contrary to the case of neutrons or charged particles interacting with matter).

RAMAN RESEARCH INSTITUTE
BANGALORE - 80.
CLASS NO.
ACC NO. 26997